Sheffield Hallam University

A Sheffield Hallam University thesis

Fabrication of Solution-processed Photoactive Polymer- and Halide Perovskite-based Solar Cells

Yaqub Shayi Rahaq

A thesis submitted in partial fulfilment of the requirements of

Sheffield Hallam University

for the degree of Doctor of Philosophy

2017

Declaration

I hereby declare that this thesis submitted for the degree of PhD is the result of my own research and that this thesis has not been submitted for higher degree to any other university or institution.

Yaqub Shayi Rahaq

Dedication

To my father and my mother, your sacrifices won't be forgotten

To my beloved wife (Kalthom), and my children (Jumana, Yousef, Abdulrahman, Zain

and Omar)

This effort is a small gift to all of you

Yaqub Shayi Rahaq

Acknowledgement

First and foremost, I would like to express my sincere gratitude to my supervisor Dr. Heming Wang for his valuable guidance, continued support and enlightenment during the journey of my PhD.

I would appreciate his great attention that he paid to my research throughout the past four years as I gained encouragement and support to complete the work. I would also like to thank my second supervisor, Dr Aseel Hassan for his support, assistance and consideration on revising my thesis. Also, I would thank all the member of staff for their support; Prof. Alan Smith, Prof. Doug Cleaver, Dr. Nicholas Farmilo, Dr. Hywel Jones, Dr. Danial Loch, Dr. Francis Clegg, Dr. Fares alnaemi, Dr Akram Khan and Dr. Abbas Hashim.

I would thank my PhD colleagues and friends who have helped me in the labs: Dr. Vikas Kumar, Dr. Burak Khadem, Abubaker, Magdi, Ronak, Dr. Nayef Alenezi, Faraj, Abdusalam, Olly, Kalid Shahriar, Salim, Eman, Amani, Mirjam, Hisham, Olu, Madugu, Mohammed, Abdullah, Ali, Hadi, Ojo, Ibrahim, Dignesh and. Mathew.

Deep gratitude to all MERI staff and technicians who were constantly of assistance.

Finally, heartfelt thanks to my Father, Mother, Wife, children and my siblings, for their support, guidance, patience and encouragement.

Abstract

In the current work, different architectures and photoactive materials have been investigated in order to fabricate low-temperature solution-processed solar cells using dip and spin coating methods.

Inverted bulk heterojunction structure has been utilised in fabrication of polymer solar cells using dip coating method. In this structure, all layers except electrodes were deposited using dip coating method, which demonstrated an excellent potential to produce large-scale area PV devices. Formulation of solutions (using different solvents) of hole transport layer, active layer, and electron transport layer play a key role in producing uniform thin films as well as compatibility with dip coating method. The best PV device achieved ~ 3.4% power conversion efficiency.

On the other hand, planar heterojunction structures have been employed to produce perovskite-based solar cells using one and two step spin coating methods (OSSCM & TSSCM). Thorough investigations of controlling the morphology of the perovskite films have been carried out using low-temperature processing methods. It was found that it is difficult to control the morphology via OSSCM without additives or using solvent engineering. Controlling the morphology of the perovskite films was achieved via TSSCM after optimizing process parameters such as the concentration of methylammonium iodide (MAI), allowed reaction time (Art), and thermal annealing.

In this work it has been established that the best morphology of the perovskite film was achieved when the 1.0 wt% MAI solution was loaded at 60 sec on top of the pre-coated PbI_2 followed by thermal annealing for two hours.

Furthermore, a novel route for fabrication of solar radiation absorbers has been developed by blending a photoactive conjugated polymer with an organolead halide perovskite to create a composite photoactive layer for solar light harvesting. The photoactive polymer did not only contribute to generation of charges, but also enhanced stability of solar cells by providing a barrier protection to halide perovskites.

List of Abbreviation

AFM   atomic force microscopy

Art   allowed reaction time

AM   air mass

BHJ   bulk heterojunction

BCP   Bathocuproine

CB   conduction band

CIGS   Copper indium gallium diselenide

CB   Chlorobenzene

DI   deionised (water)

DSSC   dye sensitized solar cell

DMF   Dimethylformamide

DCB   Dichlorobenzene

DIO   1,8-diiodooctane

EQE   external quantum efficiency

EA   electron affinity (χ_s)

Eb   exciton binding energy

ETL   electron transporting layer

FF   fill factor

HTL   hole transport layer

HOMO   highest occupied molecular orbital

ITO   Indium tin oxide

IP   ionisation potential

IR   infrared light

ICL   interconnecting layers

IPA   Isopropanol

Jsc   short circuit current

J-V   current density-voltage (characteristics)

KB   Boltzmann's constant

k   extinction coefficient

LUMO   lowest unoccupied molecular orbital

L_D exciton diffusion length

MAI   Methylammonium iodide

Ms   mesoporous

NREL   National Renewable Energy Laboratory

OPV   organic photovoltaic

OSSCM   one-step spin coating method

P3HT   poly(3-hexylthiophene-2,5-diyl)

PCE   power conversion efficiency

PEDOT: PSS   poly(3,4-ethylenedioxythiophene)-poly(styrenesulfonate)

PL   photoluminescence

PCBM   [6,6]-phenyl-C61-butyric acid methyl ester

PHJ   planar heterojunction

PbI_2 Lead iodide

PSC   polymer solar cells

PTB7   poly[[4,8-bis[(2-ethylhexyl)oxy]benzo[1,2-b:4,5-b′]dithiophene-2,6-diyl][3-fluoro-2-[(2-ethylhexyl)carbonyl] thieno[3,4-b]thiophenediy

rpm   revolutions per minute

SEM   scanning electron microscopy

SPPDs   solution-processable photovoltaic devices

P Max   Maximal power output

Spiro-MeOtad   2,2',7,7'-tetrakis-(N,N-di-p-methoxyphenylamine)9,9'-spirobifluorene

TF   tolerance factor

TSSCM   two-step spin coating method

UV-Vis   ultraviolet-visible

VB   valance band

XRD   X-ray diffraction

VASP   vapor-assisted solution process

Voc   open circuit voltage

λ   wavelength

List of Publication

Publications

- ❖ **Rahaq, Y**., Wang, H., & Kumar, V. (2014). Fabricating the solution-processable inverted photovoltaic devices by the dip-coating method. Organic Electronics, 15(5), 984-990.

- ❖ Wang, H., **Rahaq, Y**., & Kumar, V. (2016). A composite light-harvesting layer from photoactive polymer and halide perovskite for planar heterojunction solar cells. Scientific Reports, 6, 29567.

Patent

- ❖ I have patent pending: UK Patent application No. 1600577.9. Photovoltaics polymer-perovskite Composite Materiale, 2016

Conference presentations

- ❖ Blending photoactive polymer with halide perovskite as light harvesting layer for solar cells to enhance stability of devices. Valencia, Spain March 2017. The International Conference on Perovskite Thin Film Photovoltaics (ABXPV17) (oral presentation)

- ❖ A highly efficient planar hetrojunction solar cells based on hybrid halide perovskite fabricated via sequential method. London South bank University. The UK, July 2016. Photovoltaics (PV): strategic alternative energy source for Egypt; from cell to grid connected PV arrays (oral presentation)

❖ Investigation of morphologies and crystallisation of the organometallic halide perovskites for photovoltaic devices. UK Semiconductor 2015. Sheffield July 2015. (Poster presentation).

❖ Utilizing Dip Coating method to fabricate the solution processable inverted photovoltaic devices. Sheffield Hallam University Symposium March 2014. (oral presentation).

❖ Promotion of crystallisation for the organometal halide perovskite via a chemical catalyst at low temperature. HOPV2015, Rome Italy, May 2015. International Conference on Hybrid and Organic Photovoltaics 2015 (HOPV15) (poster presentation).

❖ Enhancement of the processing stability in fabricating organolead halide perovskite solar cells by a modified two-step method and improvement of the device stability by introducing a stable sol-gel/ PEDOT:PSS layer. HOPV2016, Swansea University, July 2016. International Conference on Hybrid and Organic Photovoltaics (HOPV16) (poster presentation).

❖ Novel Composite Photoactive Layers for Light-Harvesting in Hybrid Organic-Inorganic Solar Cells. Sheffield Hallam Symposium, December 2016. (poster presentation) (awarded 2nd prize among 110 posters).

Table of Contents

List of Figures

List of Tables

Chapter 1 - Introduction

1.1 Background

The demand for energy has been significantly increased due to the rapid development of the world population and industrialisation. The global market energy consumption rapidly rises by 49 % from 2007 -2035 according to the international energy outlook 2010. Worldwide energy increased from 495 quadrillion British thermal unit (Btu) in 2007 to 739 quadrillion Btu in 2035 as shown in Figure 1.1 [1].
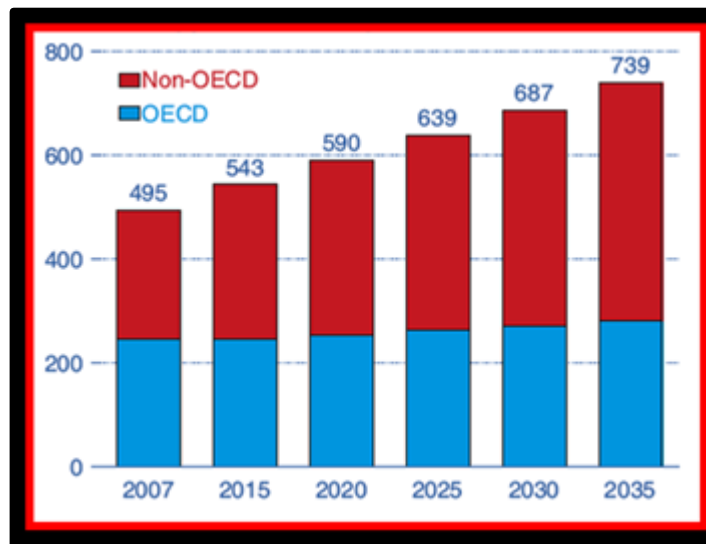
Figure 1.1 World marketed energy consumption, 2007-2035 (quadrillion Btu) [1]**.**

Sources that meet the demand in global energy consumption are classed as either renewable energy and non-renewable energy sources, which are strongly distinguished by their long-term sustainability. Renewable energy sources including solar, geothermal and wind energy sources are defined as naturally-produced resources that can continually be renewed without depletion [1].

On the other hand, non-renewable energy resources are defined as being finite by nature as they deplete long-accumulated fossil-based materials such as oil, natural gas and coal as well as natural elements which are used to generate nuclear energy.

Figure 1.2 shows that fossil fuel are still the greatest source for energy production and are dependent upon the requirments of the expanding energy demand between 2007 and 2035, which may lead to a depletion of these resources after a finite period. In addition to the factor of being finite, the increase in carbon dioxide emissions as a result of burning fossil fuels is further raising concerns on global climate changes which results in increasing hazard to human beings worldwide.
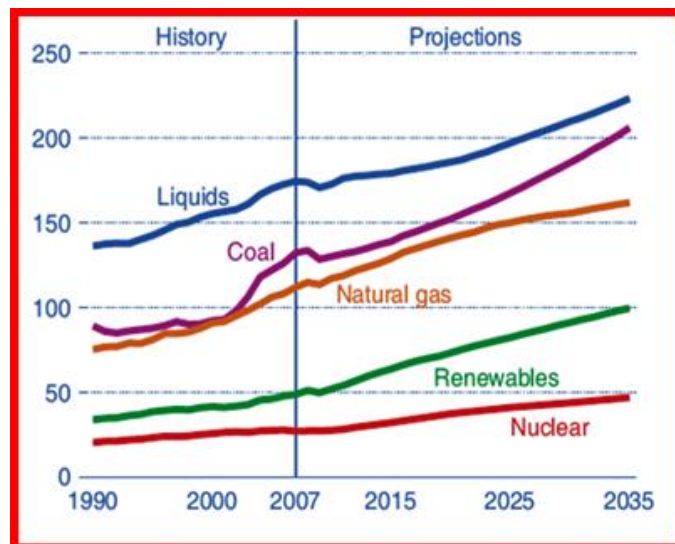
Figure 1.2 World marketed energy use by fuel type, 1990-2035 (quadrillion Btu) [1]

When compared to traditional forms of fossil fuels, nuclear energy is the most feasible alternative as very large amounts of energy can be generated without producing CO_2 emissions. However, the presence of potential leakage among nuclear plants and the disposal of nuclear waste is always an ongoing concern to worldwide energy producers. By contrast, alternative renewable energy sources are non-destructive to the environment and unlike fossil fuel sources, they cannot be

depleted. These include solar, wind, and geothermal energy sources. The use of fully renewable sources presents an enormous opportunity to preserve the environment and positively impact on human health. As one of these renewable sources, solar energy is promising and has attracted a significant of attention during the last decade due to its following favourable advantages:

1. Abundance, sustainability of the source, and non-destructive impact on the environment.

2. It has the lowest demand of maintenance and guarantees a long-term performance of up to 20-25 years for Si-based solar cells.

3. The potential to install solar cells at remote locations, rendering it unnecessary to be connected to the national grid.

4. Significant cost-reduction seen in solar panels, from $76/Watt in 1977 to only 0.35 cent/Watt in 2015 as shown in Figure 1.3.
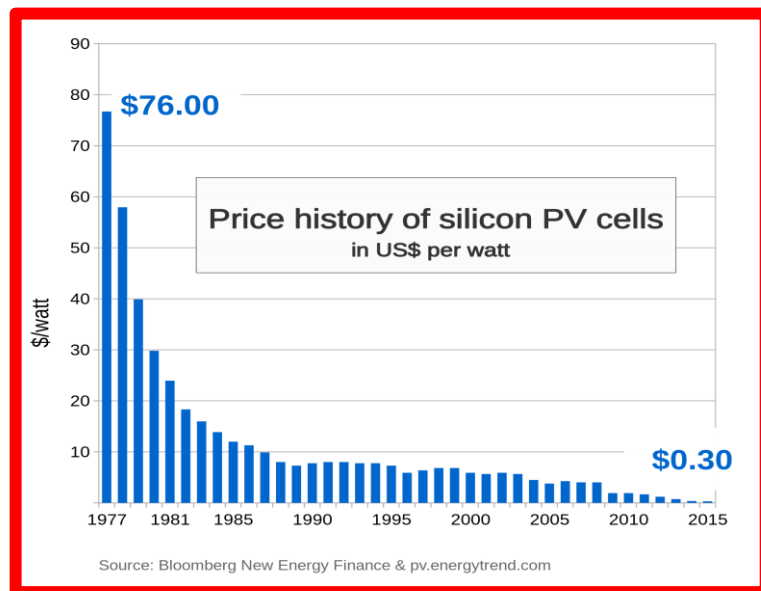
Figure 1.3 Price history of silicon PV cells in US$ per watt [2]

1.2 The solar radiation and air mass

The sun, being our closest star, is a spherical body emitting large amounts of solar radiation onto the earth surface via the void of empty space. The approximate distance between the sun and the earth is 2.4×10^{11} Km. It has been calculated that the sun supplies energy to the earth at 1.08×10^{17} W [3,4], whilst the yearly global energy consumption is calculated at approximately 1.78×10^{13} W [5] . Based on these calculations, only a very small proportion of the energy emitted by the sun is required to meet a year's global energy demand.

The solar spectral distribution is defined as the feasible relationship between the intensity of solar radiation and the wavelength [6]. Moreover, the solar spectral distribution is altered when the radiation penetrates the earth's atmosphere through scattering and absorption [6].

However, before the sun's radiation reaches the surface of the earth, this process begins with the fusion of hydrogen and helium at the sun's interior, creating a core temperature of approximately 1.5×10^7 K. Furthermore, as this process moves through the layers of the star, the solar radiation emitted from the sun's surface layer and close to that emitted out into space has a temperature of around 6000 K [7]. The spectrum of electromagnetic solar radiation includes γ rays, X-rays, ultraviolet radiation, visible light, infra-red radiation, radio waves and radar waves [8]. From these emissions, two main properties of the sun may directly impact on the solar cells units; irradiance which is the proportion of fallen radiation on the surface per unit area; and the characteristic spectra of the radiation [9]. Furthermore, it should also be mentioned that the sun's position continuously changes each day, subsequently changing the distance of the sun's irradiance between the sun and the

earth's surface. Because of this fluctuation, the level of attenuation can vary drastically. This factor is determined by the air mass.

Air mass (AM) could be defined as the required distance for solar radiation to travel to the earth's atmosphere, which impacts on both the irradiance and solar spectral distribution [10] as shown in Figure 1.4.

AM0 refers to the solar radiation spectrum outside of earth's atmosphere meaning that the path length within the atmosphere is zero [11].

AM1 refers to the distance of the solar radiation spectrum required to reach the earth's surface when the sun is directly at an overhead position relative to the earth. AM 1.5 occurs when the solar radiation has a solar zenith angle (z) at 48.2° from the overhead position. Moreover, the Solar Zenith angle (z) could be defined as the angle between the sun and the vertical [10].
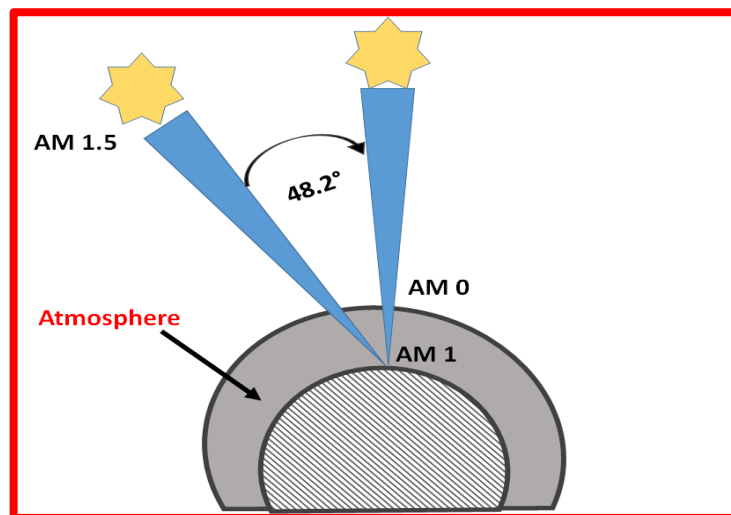
Figure 1.4 The path length, in units of Air Mass (AM) measured at a condition AM0, AM1 and AM 1.5

1.3 Motivation for research

The first and second generation of solar cells based on the mono-crystal silicon and thin film silicon respectively have a very high efficiency making them commercially viable for a long time. However, their high fabrication cost as well as technology complexity lead to numerous investigations on lower cost solar cell technologies that could provide inexpensive and efficient alternative PV devices [12]. Recently, a new generation of solution-processable photovoltaic devices (SPPDs) has become prominent which mainly includes dye-sensitized solar cells [13], quantum-dot solar cells [14], polymer solar cells (PSC) [15], and very recently perovskite solar cells [16]. They have the required features of ease of fabrication, cost effectiveness, possibility of using flexible substrates, and large area device processing using roll to roll (R2R) technology or other simple solution manufacturing methods [17–20]. The simplicity of the fabrication processing technologies of SPPDs potentially results in a sharp reduction in the cost of large-scale photovoltaic devices.

Amongst these solar cell technologies, PSCs appear to be one of the most promising candidates in the competition to achieve low-cost photovoltaic devices due to their advantage of being lightweight, ability of deposition on flexible substrates and simplicity of fabrication process. However, in spite of these promising advantages, the performance of PSCs does not exceed 11.7% for the single bulk heterojunction [21]. Furthermore, hybrid organometal halide perovskite has recently received substantial consideration as an inexpensive photoactive alternative material to the conventional Si-based solar cells. Amongst the superior properties of this material are its direct band gap, high absorption coefficient and long electron-hole diffusion length with the highest efficiency of more than 22% [22]. In spite of the excellent performance of perovskite solar cells, further investigations are still required to

solve the major issues of stability of the perovskite materials and the toxicity of lead (Pb).

1.4 Aims and objectives

The primary aim of this research is to develop low cost, highly stable, and highly efficient solution-processed photovoltaic devices using both dip- and spin- coating methods. The current research objectives are focussed on fabricating three different structures of solar cells based on photoactive polymer, organometal halide perovskite, and hybrid photoactive polymer-perovskite composite using solution processed techniques via either dip- or spin- coating methods. Dip-coating technique has been used to fabricate high performance photoactive polymer solar cells. The solutions for each layer in the polymer solar cells were modified in order to be compatible with the dip-coating method for producing PV devices.

On the other hand, two step spin coating method (TSSCM) has been employed to produce high-efficiency perovskite solar cells using [6,6]-phenyl C61 butyric acid methyl ester (PCBM)-based planar heterojunction structures. Moreover, three step spin coating method (THSSCM) has been used to fabricate a novel photoactive composite structure based on perovskite-PTB7 materials to achieve high performance with enhanced stability compared to solar cells fabricated from the pristine perovskite. Several techniques have been utilised in this research in order to analyse the produced thin films and devices; these include:

- UV-vis spectroscopy and X-ray diffraction patterns are used to examine the optical and structural properties of the thin films respectively.

- Atomic force microscopy (AFM) and scanning electron microscope (SEM) are used to investigate the surface morphologies of the produced thin films.

- FTIR and photoluminescence PL are utilised to examine the internal structures of the composite perovskite and optical properties respectively.

- Current density-voltage (J-V) characterisation and external quantum efficiency (EQE) measurements are carried to identify the performance of produced solar cells.

1.5 Outline of the thesis

This thesis is organised as follows:

- ❖ In Chapter 2, a literature review is carried out to better understand current technologies, manufacturing and developing of solar cells. Basic architectures of solar cells and fabrication methods are reviewed. Furthermore, present issues with solar cell technologies and methods to combat these issues are also presented.

- ❖ Chapter 3 introduces the selection and preparation of materials used in this thesis (i.e. photoactive materials, electron transport materials, hole transport materials, and electrodes), and study of their features and their characteristics. This chapter also introduces the principles of various characterisation techniques used in this work.

- ❖ In chapter 4, the fabrication of polymer solar cells using dip coating method is discussed. AFM is used to investigate the morphology of the photoactive layer, hole transport layer and electron transport layer fabricated using either

dip or spin coating method, separately. UV-Vis absorption spectroscopy and X-ray diffraction measurements are also be used to examine the optical and structural properties of the photoactive layer.

❖ Chapter 5 explains the use of the one-step spin deposition method (OSSDM) to fabricate perovskite materials. The top surface morphology, the optical and crystal structure properties of the perovskite film fabricated via OSSCM will be studied. The two-step static deposition method (TSSDM) is used to fabricate the perovskite thin films. Extensive investigations are carried out to examine the perovskite films morphologies and crystallisation behaviour by altering different parameters. Moreover, the prepared perovskite films will be characterised using UV-Vis absorption and X-ray diffraction tests to understand their optical and structural properties. The impact of thermal annealing treatment on the perovskite films will be examined using the optimized parameters.

❖ Building on the ideal parameters identified in the previous Chapter, Chapter 6 investigates the fabrication of highly efficient reproducible perovskite solar cells with varying concentrations of Methylammonium iodide (MAI) solution using TSSCM. The optical and structural properties of the perovskite films will be examined when different concentrations of the MAI are used. Moreover, the cross section and the top surface morphologies of the perovskite films under these concentrations of the MAI solution will be assessed.

❖ In Chapter 7, a novel photoactive material based on conjugated photoactive polymer and a nanocomposite halide perovskite is developed. This new light

harvesting layer employs to fabricate highly efficient hybrid solar cells. Blending the conjugated photoactive polymer with the perovskite extends its light absorption and significantly enhances the solar cells' stability up to 940 hours inside the glovebox compared to the pristine perovskite-based solar cells. Their optical and structural properties examine using UV-Vis absorption and photoluminescence as well as X-ray diffraction. The surface and cross section morphologies of the novel photoactive absorber studies using AFM and SEM. Additionally, stability of solar cells fabricated from the pristine perovskite and the novel composite material investigates under the condition of storing in a glovebox for a time period.

❖ Lastly, Chapter 8 presents conclusions derived from this work and the implications for future research will also be addressed.

Chapter 2 - Literature Review

2.1 Introduction to solar cells

Photovoltaic (PV) technologies may trace back to more than one hundred years ago. In 1839 French scientist Edmond Becquerel [23] first noticed the photovoltaic effect after two metal electrodes were placed in an electrolyte. In 1873 and 1876 respectively, Smith and Adams discovered the photoconductivity of a solid material known as selenium [24]. Although the selenium did not work as a PV material, there was an important benefit derived from this experiment which showed that solid materials might convert light into electricity without heating. More than seven decades later, the first photovoltaic cell based on silicon p-n junction was revealed in 1954 in the Bell labs in the United States [25].

Chapin, Fuller, and Pearson observed the sensitivity of silicon doped with an impurity to light [26,27] which has resulted in power conversion efficiency (PCE) of ~6%. Since then, scientists have endeavoured to implement a series of developments for manufacturing high-efficiency Si-based solar cells with a high degree of stability. As a result, the highest efficiency of solar cells reached 25% and they have since dominated the market [28].

However, the production of high-purity Si requires high-temperature, a very clean environment, and high-cost equipment. As a result, there was an urgent necessity to find alternative materials which can be manufactured at low cost without employing complicated fabrication processes. Although amorphous silicon, cadmium-telluride, copper indium gallium diselenide (CIGS) thin films-based solar cells fabricated by vacuum deposition methods were discovered with lower fabrication cost than Si-

based solar cells. The PCEs of solar cells produced from these materials are still smaller than that of bulk Si-based solar cells. Their highest reported efficiencies were ~10.1%, ~16.7%, and ~19.4%, respectively [28].

Compared to the vacuum-based methods, solution-processed solar cells have significantly reduced cost using R2R method and showed potential to revolutionise thin film-based solar cells. Polymer-based, organometal halide perovskite-based, and kesterite-nanoparticles-based (e.g. $Cu_2ZnSn(S,Se)_4$) solar cells are able to be fabricated by the solution-processed method. The PCE for polymer-based and kesterite-nanoparticles-based solar cells has increased to around 11% [21]. Halide lead perovskites presented very promising results for light harvesting, which led to a significant achievement PCE of better than 20% in a short period [29]. Semiconductive polymers such as poly (sulphur nitride) and polyacetylene were first investigated in solar cells in the 1980s [27]. However, the achieved PCE was limited to less than ~0.1%. In 1986, a significant transformation occurred when Tang used heterojunction structures (copper phthalocyanine (CuPc) as a donor and a perylene tetracarboxylic derivative as an acceptor) in one cell [30] with PCE increasing significantly to ~1%. This transition opened the door of exploring the use of cheap, lightweight, and flexible materials to produce solar cells. Progress was realized in 1995 when the first bulk heterojunction (BHJ) PV device from semiconductive polymers was invented by Heeger's group and Friend's group separately [31,32]. Since then, studies have been carried out and efforts have been intensified over the past twenty years to developing PSCs.

This chapter will review different photoactive materials which were used to fabricate low cost solution processed solar cells mainly including semi-conductive

polymers with fullerene derivatives and organolead halide perovskites. Different fabrication methods, architectures, and solar cells development will be reviewed.

2.2 Generation of solar cells

The first-generation of solar cells were based on wafers of the monocrystalline or polycrystalline silicon. Currently, they still dominate nearly 90% of the commercial solar cell market [27]. They typically exhibit features of high stability and efficiency (PCE of ~25% for monocrystalline Si-based solar cells and ~20% for poly-crystalline Si-based solar cells respectively [28]. However, there are some limitations for Si-based solar cells including their high installation costs, the costly production of high purity silicon wafers and relatively low visible light absorption if compared with other semiconductors.

Drawbacks within the first generation solar cells led to the development of the second-generation PV devices that were based on the thin film solar cell technologies [25]. The candidate materials for the second-generation solar cells are amorphous silicon, cadmium telluride (CdTe) and copper indium gallium selenide (CIGS). The fabrication processes for the second-generation PV devices including sputtering, physical and/or chemical-vapour deposition methods have been widely used [33]. The attainable PCE of around 15-20% was achieved for the laboratory prototype PV devices, demonstrating their potential to compete with the silicon-wafer-based PV devices [33].

Despite the significant reduction in the cost of thin film solar cells, the PCE of the second-generation solar cells is still lower than that of the first- generation solar cells [34]. One of the main disadvantages for the second-generation solar cells based on (CdTe) and (CIGS) is either the high-temperature fabrication or the need for high

vacuum technology. Additionally, some raw materials used in the second-generation solar cells are scarce, expensive (e.g. indium), very toxic (e.g. cadmium), and unstable [35].

Because of these drawbacks, a so-called third-generation of solar cells by the solution-processed methods has emerged [36]. The benefits of the first and second-generation PV devices are still in the foreground, which attracts the global market due to their high degree of stability and high performance. Nevertheless, because of limitations of the complicated production processes and excessive cost, they are not able to compete with low-cost electricity generated by burning fossil fuels. Thus, it is necessary to develop inexpensive PV devices to compete with the fossil fuels energy.

Solution-processed solar cells have the potential to be produced at very low-cost. Polymer-based semiconductive materials have the potential to be used to fabricate PV cells at low temperature through the high throughput solution-processed method [37]. Polymers are typically considered the cheapest materials and have high absorption coefficients, allowing them to form very thin films, typically a few hundreds of nanometres [38]. By using these materials, the cost of PV cells will be reduced considerably; however, the performance needs to match their first and second-generation counterparts. The highest achieved power conversion efficiency of polymer solar cells is currently at ~11.7% [21]. Very recently, a new-type of solution-processed organic-inorganic hybrid halide perovskites have been developed and an efficiency of ~22.1% has been achieved [39].

2.2.1 Operational mechanisms of photovoltaic solar cells

The mechanisms of absorbing photons in semiconducting polymer based solar cells and generation of free charge carriers followed by their collection at both electrodes could be categorized into six main steps as shown in Figure 2.1 [40].

These steps are:

1- Absorption of photons and creation of excitons

2- Exciton diffusion

3- Exciton dissociation

4- Charge carriers separation

5- Charge migration

6- Charge collection at the electrodes
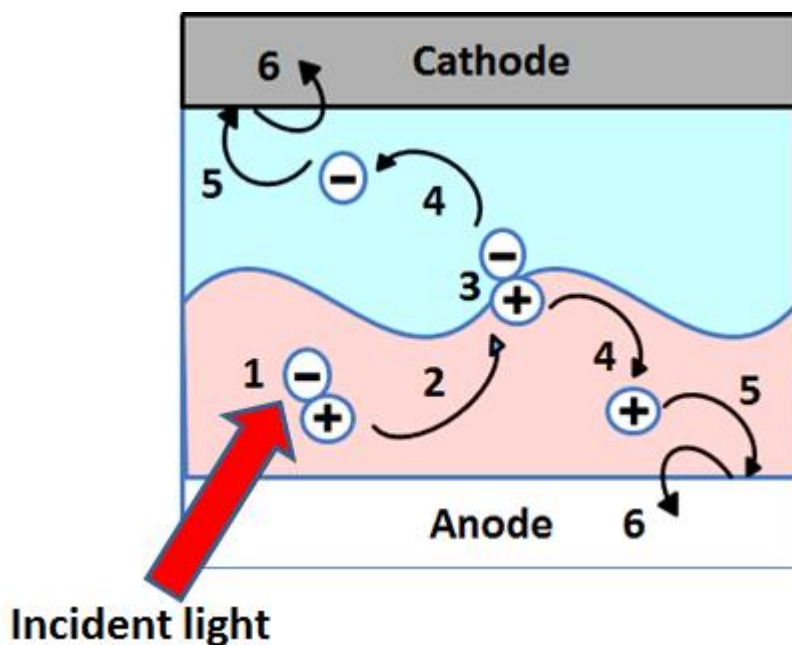
Figure 2.1 Schematic diagram of the main steps of the photocurrent generation in polymer-based solar cells

The working mechanism of polymer and organometallic halide perovskite solar cells is shown in Figure 2.2. Typically, when the photovoltaic devices is exposed to the incident sun light, the photons will penetrate through the different transparent layers (e.g. ITO and PEDOT:PSS) before reaching the photoactive layer. Several factors affect the proportion of generated excitons which are successfully dissociated and collected by the corresponding electrodes including, the thickness of the photoactive layer, the band gap of the photoactive layer, optical and other physical characteristics of the hole and/or electron transport layers [41].

Among those factors, the band gap of the polymer or organometal halide perovskite materials is the most important factor which determines the portion of incident photons that will be absorbed by the active layer. For example, the band gap of the photoactive layer of a organometal halide perovskite material is roughly 1.52-1.59 eV resulting in absorbed proportion of nearly 60% of the incident photons [42].
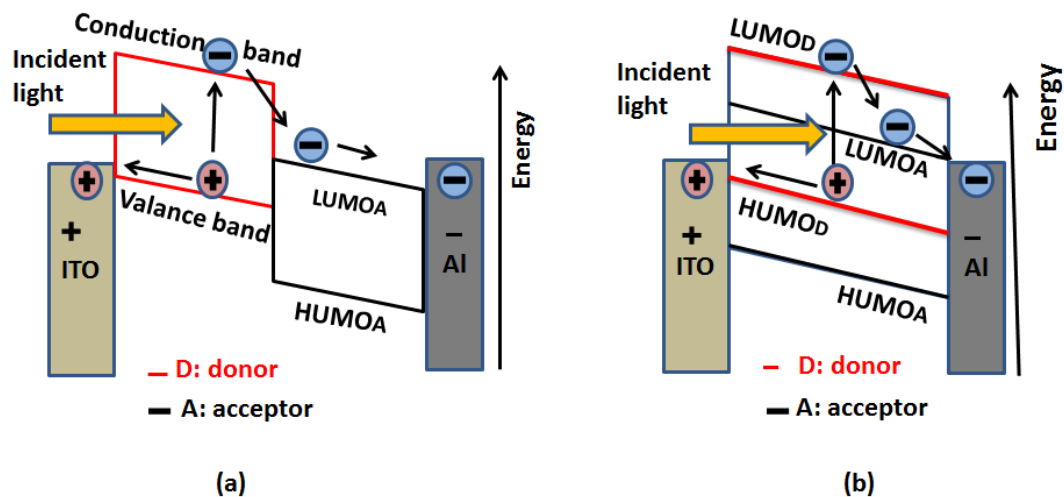
Figure 2.2 The processing mechanism of conversion photons into electricity in: a) Planar heterojunction Perovskite, b) Bulk heterojunction polymer solar cell

Only 30% of the incident photons are absorbed by a polymer-based photoactive layer owing to the band gap of the majority of semiconducting polymers being

higher than 2 eV [43]. Moreover, absorption coefficients of polymer materials and organometal halide perovskites are high $\sim 10^5$ cm^{-1} and 1.5×10^4 cm^{-1} at 550 nm respectively [44].

The high absorption coefficient allows very thin film of the photoactive material at $\sim$ 100-300 nm of thickness to absorb most incident photons [40].

As a result of photons absorption in the photoactive layer of polymer with energy $\geq$ the band gap (Eg), electrons will be induced from the HOMO level to the LUMO level forming a strong electrostatically bond electron-hole pair known as Frankel excitons. On the contrary, in perovskite based solar cells, free charge carriers will generate directly after absorbing photons in the photoactive layer with energy $\geq$ than the band gap (Eg) of the active layer [45]. The excitons created in halide perovskites are called Mott-Wannier which has very low binding energy at $\sim$2 meV [46] unlike photoactive polymer materials which has the Frankel exciton with high binding energy at $\sim$ 0.5 eV [40].

The Frankel exciton diffuses to the interfacial layer between the donor and the acceptor. The diffusion length in polymer materials is in the range of 10-20 nm, which leads to the requirement of bulk heterojunction structures between the donor and the acceptor for efficient PV devices to prevent the recombination of free electrons and holes. On the contrary, it is unnecessary to have bulk heterojunction in halide perovskite-based solar cells and planar heterojunction structures are used to obtain efficient PV devices. The halide perovskite materials have long diffusion lengths of excitons of $\sim$100 nm for $CH_3NH_3PbI_3$ and $\sim$1 μm for $CH_3NH_3Pb_{3-X}I_X$ [47,48]. The generated excitons in polymer materials which diffused to the interface

between the donor (D) and the acceptor (A) remain electrostatically bond together and an additional force is required to break the excitons into free charges [34].

The dissociation of charges at the D/A interface in polymer materials requires a driving force due to high binding energy of excitons in polymers. The required driving force for exciton dissociation is the internal electric field that can be determined from the gradient in the potentials of electrons and holes in the D/A interface. This internal electric field depends on the offset between the HUMO of the donor and the LUMO of the acceptor [49]. The difference in work functions of electrodes creates an external driving force to move and collect the free charge carriers to the corresponding electrodes [50].

2.3 Polymer-based solar cells

2.3.1 Development of polymer solar cells

The first attempt to produce polymer solar cells was in 1959 when an anthracene single crystal was used [51]. Since then, considerable efforts have been made and studies have been carried out to find highly efficient and inexpensive materials for PV devices which can compete with solar cells based on inorganic materials. The polymer materials have various desirable characteristics including high flexibility and simple fabrication processes using lightweight, low-cost and simple to produce raw materials [17–20]. Moreover, polymer materials have very high absorption coefficient compared with inorganic materials such as Si, which offer an opportunity to produce very thin film devices [38]. The active layer in polymer solar cells is based on donor and acceptor materials. The donor has a low ionisation potential, and the acceptor has a high electron affinity (χ_s) [34]. In the last decade, two types of materials have been used extensively in the preparation of PV cells active layer.

These are P3HT and PCBM as the electron donor and the electron acceptor materials, respectively. Their outstanding performance and high stability make them distinct obvious choice for a current scientific research [52]. In photoactive polymer materials, the optical band gap is in the range between ~1.4 eV to ~2 eV [53].

The solution processed polymer-based solar cells have attracted outstanding attention as a favourable alternative to the classical inorganic Si-based solar cells due to their lightweight, inexpensive raw materials, and the possibility of producing solar cells on a large-scale R2R technique. Following the emergence of bulk heterojunction structures in polymer solar cells in 1995 [31], many researchers were focused on the development of increasing the PCE of polymer solar cells. Shaheed *et al*. claimed a bulk heterojunction structure when he applied the mixture of poly[2-methyl,5-(3*,7**dimethyl-octyloxy)]-p-phenylene vinylene (MDMO-PPV):PCBM as an active layer. He used the spin coating method to deposit the active layer and a PCE of ~2.5 % was achieved [54]. The blend of P3HT:PCBM as a photoactive layer in the polymer solar cell was presented by Chirvase *et al*. in 2003. They mixed P3HT: PCBM at the weight ratio of 1:4 as a photoactive layer and ~0.2% PCE was obtained [55]. Pandinger and co-workers increased this PCE performance to ~3.5% when they blended P3HT:PCBM at 1:1 weight ratio. The performance of the device was enhanced after thermal annealing was applied for several minutes to the whole device [56]. Over the years, the power conversion efficiency had remained between 3-5% [57] until 2011 when Mitsubishi Chemical manifested a high PCE of ~10.0% [58]. However, no details regarding the photoactive materials and the device architecture were given [58]. In 2013, a high fill factor between 75-80 % and PCE of 8.7% was achieved for the single junction structure by using poly[5-(2-hexyldodecyl)-1,3-thieno[3,4- c]pyrrole-4,6-dione-alt-

5,5-(2,5-bis(3-dodecylthiophen-2-yl)-thio- phene)] (PTPD3T) or poly[N-(2-hexyldodecyl)-2,2′-bithio-phene-3,3′-dicarboximide-alt-5,5-(2,5-bis(3-decylthiophen-2-yl)- thiophene)] (PBTI3T) as donor polymers blending with $PC_{71}BM$ as the acceptor material. The enhanced fill factor and performance of the highly ordered BHJ bicontinuous networks give optimum vertical phase gradation and very close packing. These contributions result in higher extraction and life time [59].

In the same year, Yang and co-workers claimed a high PCE of polymer solar cells of 10.6% via using tandem structure under the standard conditions [60]. They mixed a low band gap polymer poly{2,6′-4,8-di(5-ethylhexylthienyl)benzo[1,2- b;3,4-b]dithiophene-alt-5-dibutyloctyl-3,6-bis(5-bromothiophen-2-yl)pyrrolo[3,4-c]pyrrole-1,4-dione} (PBDTT-DPP) with PCBM for the front photoactive layer and P3HT:ICBA in the back photoactive layer. In 2015, J.D Chen *et al*. claimed a high PCE for a single junction polymer solar cell, surpassing 10%. They utilised nanoimprinting technology to blend deterministic aperiodic nanostructures (DANs) into the single-junction polymer solar cells for broadband self-enhanced light absorption with enhance charge collection. Blending of poly[4,8-bis(5-(2-ethylhexyl)thiophen-2-yl)benzo[1,2-b:4,5-b′] dith- iophene- co -3-fluorothieno[3,4-b]thiophene-2-carboxylate]:[6,6]-phenyl-C71-butyric acid methyl ester (PTB7): $PC_{71}BM$ was used as a photoactive layer [61].

Also in 2015, Z. He *et al*. reported a high PCE (over 10%) for a single junction [62]. This high PCE was produced by controlling the tail state density under the conduction band of the electron acceptor and the disorder stage of the mix produced from a newly designed semiconducting polymer with a low band gap (1.59 eV) and $PC_{71}BM$. The narrow band gap semiconducting polymer was synthesized from 1.59

poly [[2,6′-4,8-di(5-ethylhexylthienyl)benzo[1,2-b;3,3-b] dithiophene] [3-fluoro-2[(2-ethylhexyl)carbonyl]thieno[3,4-b]thiophenediyl]] (PTB7-Th) and mixed with $PC_{71}BM$ as a photoactive layer [62]. Very recently, Prof Yan's group from South Korea achieved a certified PCE of 11.5% and 11.7% in 2016 using an environmentally friendly hydrocarbon solvent-based system [21] . To date, the bulk heterojunction structure remains one of the most auspicious configurations of the polymer-based solar cells.

2.3.2 Architectures of polymer solar cells

2.3.2.1 Bi-layer junction architectures

In 1986, C.W. Tang used two different materials as the donor and the acceptor with different ionization potentials and electron affinities in the bi-layer heterojunction structure as shown in Figure 2.3 [30,32]. Copper phthalocyanine (CuPc) was used as the donor and perylene tetracarboxylic derivative as the acceptor. The required electric field that contributes to dissociate charge carriers effectively was created by the band offset at the donor-acceptor interface. The power conversion efficiency of this device was only ~1%. After excitons diffuse to the interface between donors and acceptors and dissociated electrons and holes will migrate in the opposite direction to their respective electrodes, which requires a long carrier life time so that they can reach the electrodes before recombination [63].
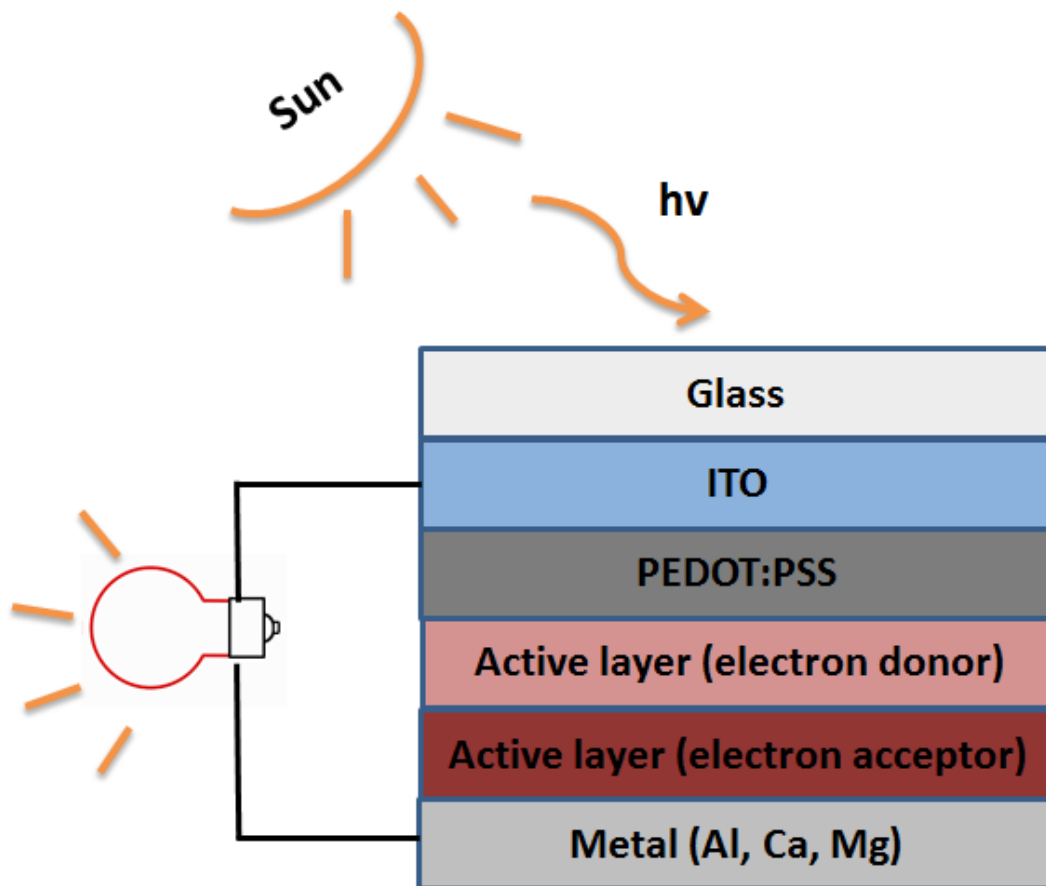
Figure 2.3 Schematic diagram of the planar heterojunction structure

2.3.2.2 Bulk heterojunction

In the bilayer heterojunction of PSCs, the short circuit current and power conversion efficiency are usually very low because most charge carriers decay or recombine before collection by electrodes. The reason is that free charge carrier mobility and exciton diffusion length in photoactive polymers are much lower compared with that in inorganic materials [51]. This led to the discovery of the concept of bulk heterojunction structures by Yu *et al*. in 1995 [31].

The idea of bulk heterojunction structures is based on increasing the interfacial area between donors and acceptors in tens-nanoscale phase separation and reducing the dissociation length of charge carriers. After its discovery, substantial progress was

made in the development of polymer solar cells [32]. The bulk heterojunction structure is formed after an interpenetrating donor mixes together with the bicontinuous network of the acceptor as shown in Figure 2.4. Excitons can then be created anywhere in the active layer, resulting in an increased number of arising pathways in the donor and acceptor from their interfaces to the corresponding electrodes. Consequently, an excessive number of charge carriers will percolate to both electrodes via the introducion of charge transport pathways. It is very important that a percolating pathway is required in the bulk heterojunction structure of PSCs in order to facilitate the transition of the separated charges to both electrodes [64].
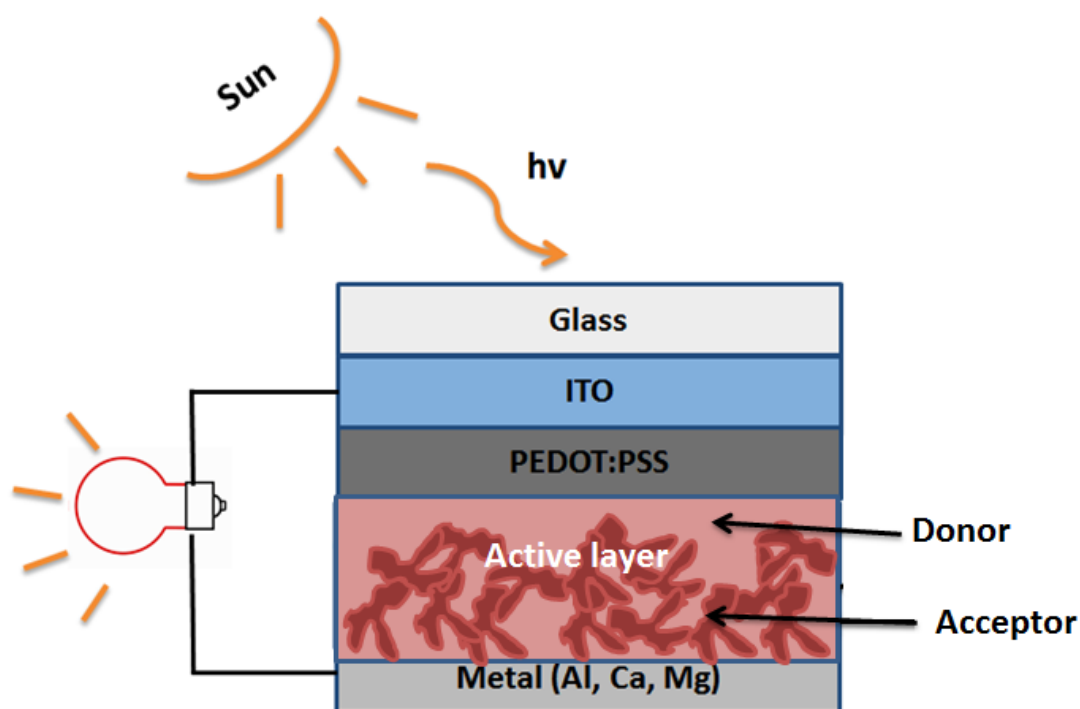
Figure 2.4 Schematic diagram of the bulk heterojunction organic solar cells

The introduction of BHJ structures in PSCs contributes to increase short-circuit current and fill factor, which leads to an increase in the PCE. After many efforts have been exerted, an important factor has been studied in the PSCs, which is morphology of the active layer. The latter plays the main role in optimising the

properties of the active layer and thus enhancing the performance of the solar cells. There are many aspects affecting the morphologies of bulk heterojunction between donor and acceptor materials; these include type of solvents used, ratio of compounds between donors and acceptors, and layers annealing method [65]. One of the most investigated materials in the field of BHJ polymer solar cells is P3HT as the donor and PCBM as the acceptor due to their good performance and high degree of stability [52]. The use of bulk heterojunction structures in PSCs has dramatically increased the performance of solar cells. The PCE increased from ~5% in 2008 for the single BHJ device to 11.7% by employing hydrocarbon-based processing system in 2016 by Yan's group [21] that is deemed more environmentally friendly compared to the use of halogenated solvents.

2.3.2.3 Tandem solar cells

Considerable loss of energy is inevitable in a single BHJ PSCs stemming from an inability to absorb photons with smaller or larger energy than the band gap of the materials. Such loss can be reduced by using tandem solar cell architecture. The concept of tandem solar cells is based on making the most from absorbing different wavelengths of photons in the solar light spectrum while increasing light harvesting. In contrast, a single active layer relies on absorbing photons in a specific wavelength of the solar light spectrum. Tandem solar cells have a potential to acquire a wider range of solar radiation by using materials with various absorption bands. The architecture of tandem solar cells practically contains two separate subcell layers connected in series. The open circuit voltage of tandem solar cells can be calculated by summing the voltage value of each cell while the current is the same. Between two active layers, there exists an interconnecting layer (ICL) which is a combination of an electron transport layer (e.g. metal oxide) and a hole transport layer (e.g.

PEDOT:PSS) as shown in Figure.2.5. The ICL must be a strong protection layer to prevent solvents from the upper layer penetrating into the lower layer. With the invention of different low band gap photoactive polymers presenting wide absorbance including near infrared light, the tandem structure is applicable and 10% barrier in PCE has been transcended. In 2008, 8.62% PCE was achieved by Yang's group for the tandem polymer solar cells, which has been further increased to 10.6% in 2012 [60]. Four years later, the PCE of tandem polymer solar cells was increased to over 11 % by Prof. Hou's group [66] after developing a new low band gap polymer poly(2,5-bis(2-decyltet- radecyl)- pyrrolo[3,4-c]pyrrole-1,4(2H,5H)-dione-3,6-diyl- alt - 3″,4′-difl uoro-2,2′:5′,2″:5″,2‴-quaterthiophene-5,5‴-diyl (PDPP4T-2F) used in a double junction tandem structure with either $PC_{61}BM$ or $PC_{71}BM$.
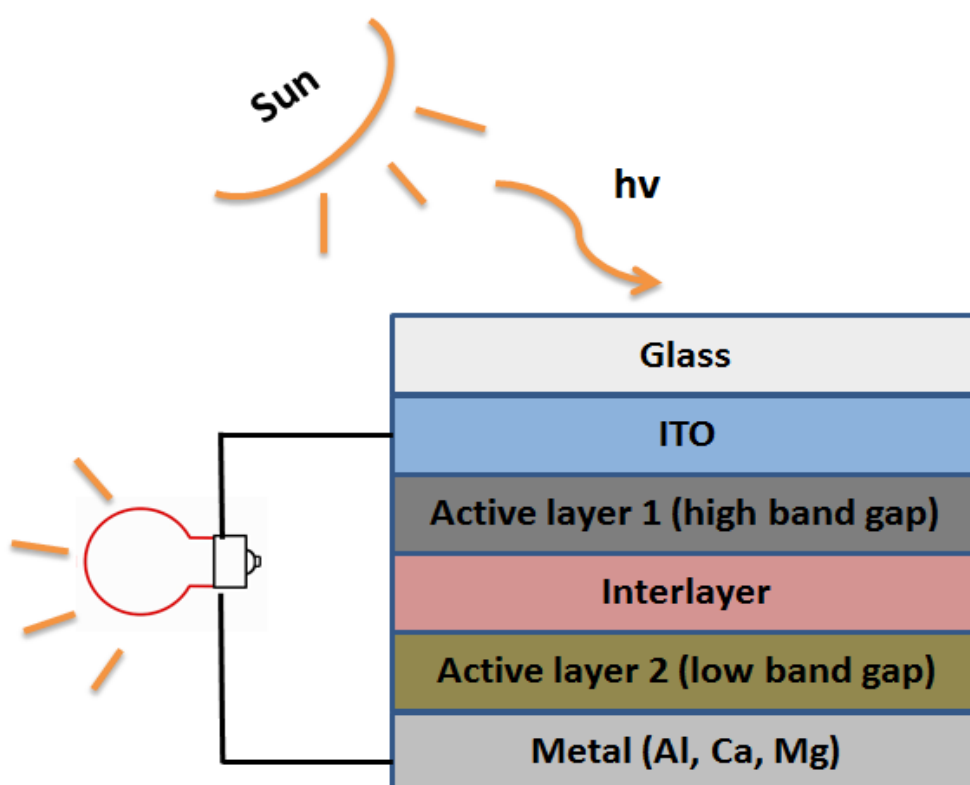
Figure 2.5 A schematic diagram of the tandem bulk heterojunction structure

2.3.3 Fabrication methods of solution-processed solar cells

The first stage of transforming organic or organic-inorganic solution -processed solar cells from the lab scale to commercialisation is to determine the deposition methods that will offer mass production and low-cost. The roll-to-roll techniques to fabricate polymer solar cells on low-priced and flexible substrates have a great potential to significantly reduce the cost of solar cells. Currently, various techniques including spin, doctor blade, spray, slot die, and other thin film coating methods have been investigated in the lab scale. Future efforts will be made to transfer the lab scale PV devices to industrial mass production. Different deposition methods have their own advantages and disadvantages.

The spin-coating method is one of the most famous fabrication methods, which is commonly used in the lab to fabricate solution-processed solar cells due to its simplicity, low-cost, and repeatability. As shown in Figure 2.6, a limited amount of solution with specific concentration drops onto the centre of the substrate during rotation with a selected rotating rate. The solvents evaporate forming a uniform thin film. The main advantage of the spin-coating method is that a very uniform and homogenous thin film is produced while the solvents are drying. Several factors can affect the thickness of thin films including spinning rate, solution viscosity, and temperature [67].
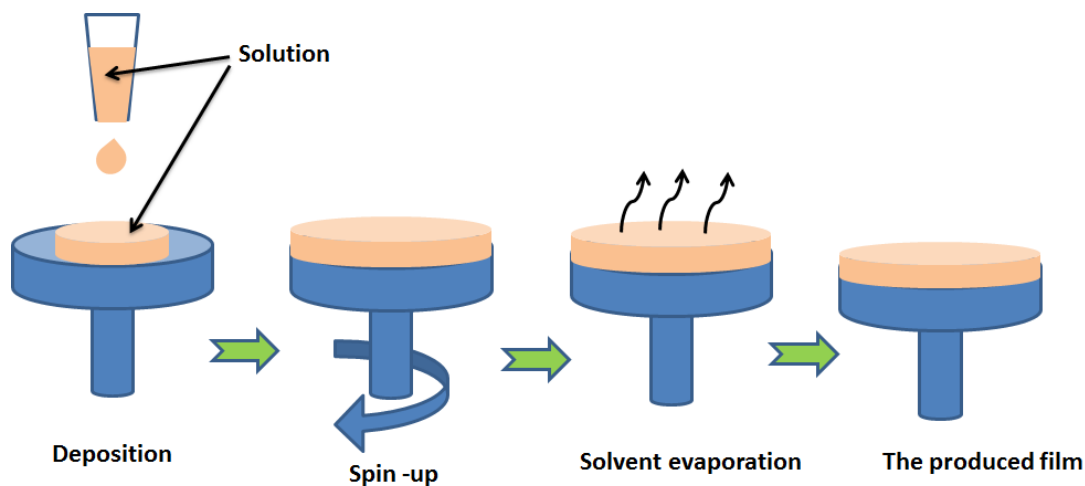
Figure 2.6 Schematic of spin-coating process

The main limitations of using the spin-coating method relate to high levels of wasted solution and the small-scale thin films are produced. Consequently, it is not favourable for mass production [18].

Blade coating also called doctor blading or knife coating, is widely used to fabricate large-scale thin film coating, as illustrated in Figure 2.7. There are several parameters that can be adjusted to control the film thickness produced by blade coating technique including blade gap, blade coating speed and concentration of the solution [68]. The main advantages of using the blade coating technique are that it gives large-scale surface uniformity, fewer waste materials, avoids interlayer dissolution and it is compatible with (R2R) technique. However, the major obstacles of using the blade coating technique are the complex chemistry of ink formulations and the contact effects when the followed layer is applied on the previously formed film [69].
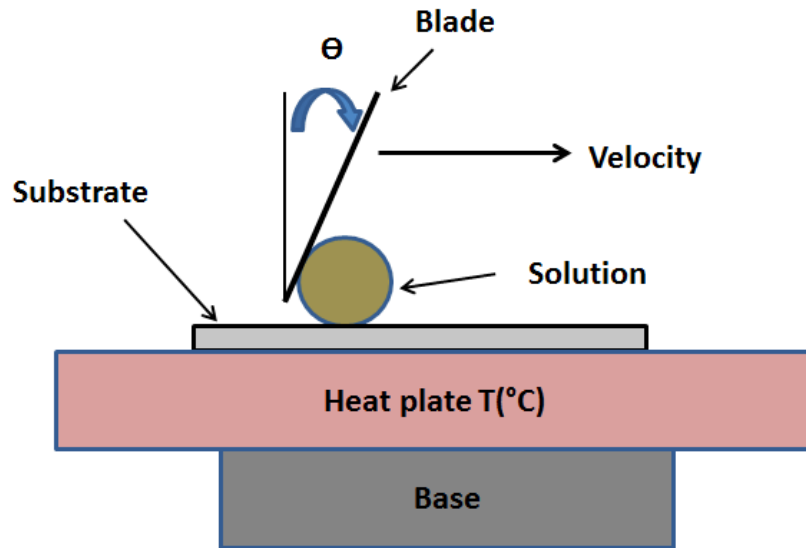
Figure 2.7 Schematic of blade-coating process

Spray coating is a well known method which is extensively used in industry to paint car parts and other tools as shown in Figure 2.8. Spray technique requires forcing the printing ink via a nozzle in order to produce a fine aerosol. The thin film formed using spray coating technique can be controlled by optimizing different parameters such as solution concentration, type of solvents, the working distance between the nozzle and the substrate, substrate temperature and the nozzle's flow rate [18,70].
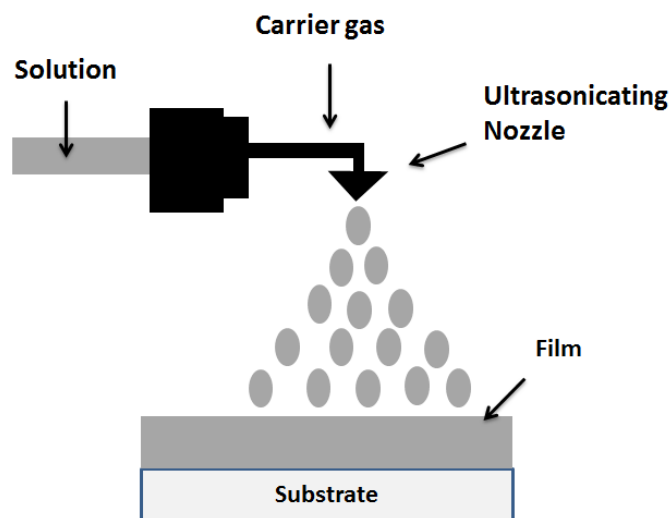
Figure 2.8 Schematic of spray-coating process.

The main advantages of using the spray coating technique are that it can be carried out at a great production speed, and it has the potential to be used with different substrates as there is no direct contact between the nozzle and the substrate [71]. However, the spray-coating method does require precise control of the nozzles and the liquid droplets can splash to the previously coated areas affecting the properties of the photovoltaic (PV) devices [69].

The dip-coating process on the other hand is a simple, high-productivity, high accuracy method of depositing a uniform film on a large-scale area as shown in Figure 2.9.
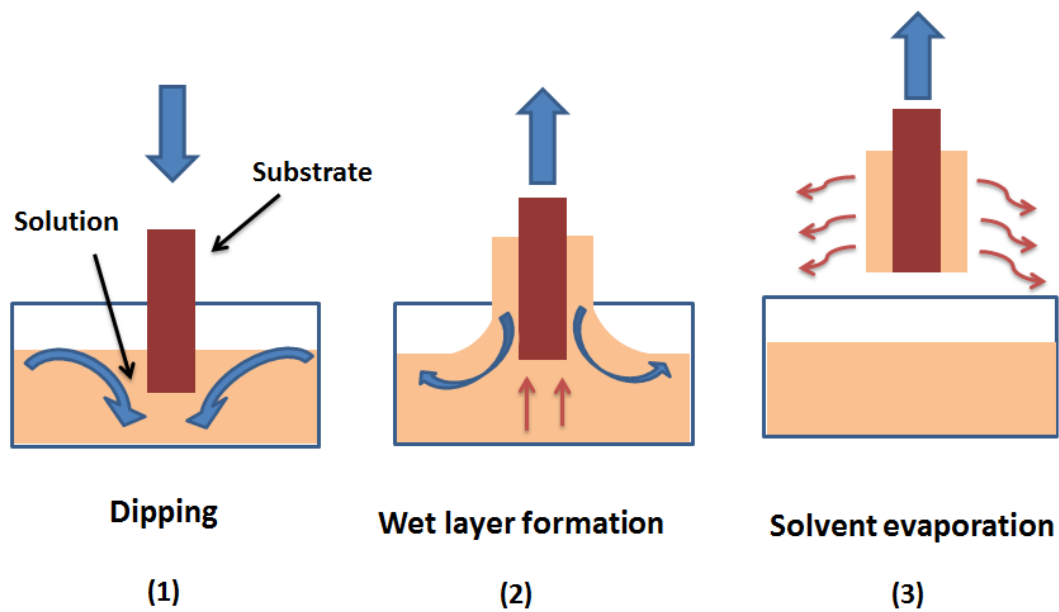
Figure 2.9 Schematic of dip-coating process

The dip coating method has a potential to be used as a promising alternative for fabricating large area solution processed polymer solar cells on an industrial scale. Historically, the dip-coating process is a very old method of producing sol-gel thin films, which was invented by Jenaer Glaswerk Schott & Gen. in 1939 for silica films [72].

Nowadays, many commercial optical functional sol-gel thin films on glass have been manufactured by the dip-coating method with a large area of several square meters. Moreover, the dip-coating method significantly reduces the number of wasted materials during processing and could be used to fabricate two PV devices at the same time. The main disadvantage of the dip-coating method is that only rigid substrates can be used.

Furthermore, different printing techniques have been developed after the printing press evolved by Johannes Gutenberg in 1440 [17]. Although these printing techniques have their own positive and negative aspects, they depend on the similar process of moving the ink solution to the substrates [17].

(R2R) method is one of the important printing techniques which can be used for commercial production of solar cells. Slot-die coating and knife coating are the two most common techniques which incorporate the R2R method as shown in Figure 2.10. In the knife coating method, the ink tank is placed before the knife that acts to provide the meniscus with new ink. When the substrate moves, the fixed knife drives the ink in front of it only allowing ink that fits below the edge to pass through. The two main parameters that could affect the thickness of the film produced by the knife coating method are; i) the distance between the knife and the substrate and ii) the speed rate of the roll. The knife coating method is appropriate for coating large scale areas without any pattern [73].
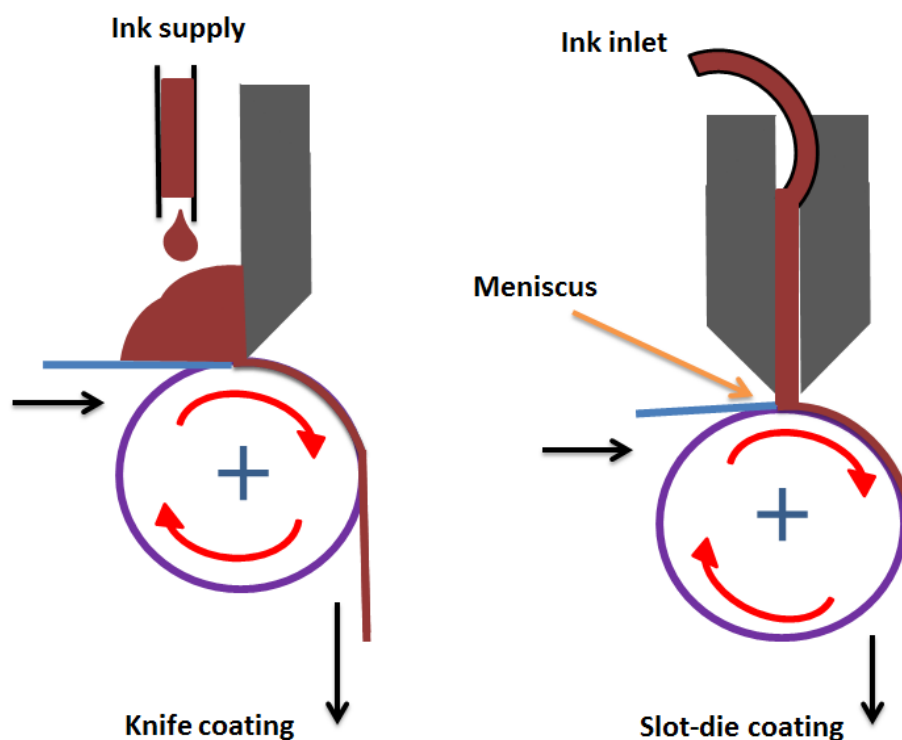
Figure 2.10 Schematic of knife-coating process and slot-die coating

In the slot-die coating the coating head is placed very near to the substrate without contacting it. The ink is injected via the fixed coating head into the moving substrate creating a continuous coat on the large scale substrates [18]. It is possible to coat different width of stripes using slot-die coating methods [18]. However, web speed is limited during the operation of slot-die coating when applying the ink composition. Exceeding this limit will stop the coating process [73].

2.3.4 Current limitations of polymer solar cells

Although the distinguished properties including inexpensive raw materials, solution processed methods, and fabricating solar cells on flexible substrates make polymer photoactive semiconductors privileged competitors with light-absorbing materials of the first and second generation solar cells, - currently some limitations have hindered their potential to achieve this goal. One of the main obstacles is the lower

power conversion efficiency when compared with the first and second-generation solar cells. Moreover, the life span of polymer solar cells is short (less than one year) compared with Si-based solar cells that have a life span of 25 years [74].

2.4 Organic-inorganic halide perovskite solar cells

2.4.1 Development of halide perovskite solar cells

Meeting the increasing energy demand is essential with the daily global growth and development. Various PV technologies have emerged and gained a significant attention as the promising energy sources including; dye-sensitized solar cells (DSCs), polymer solar cells (OPV), and quantum dot (QT)-based solar cells. Nevertheless, these solution-processed PV devices present much lower performance when compared with the Si-based solar cells. The power conversion efficiency of these solar cells were around 11% [45].

 A promising candidate called organometal halide perovskites has recently emerged as a novel and strong competitor in the PV community. It can be produced by the solution-processed technique on flexible substrates [16]. The PCE of perovskite-based solar cells jumped dramatically from ~3.9 to ~22 % just in a few years [75]. Currently, different fabrication techniques and configurations were used to fabricate high efficiency perovskite solar cells. Miyasaka's group first utilised hybrid organic-inorganic halide perovskites of $CH_3NH_3PbBr_3$ with I^-/I_3^- electrolyte in 2006, reaching a PCE of 2.2%. The power conversion efficiency was improved in 2009 to 3.8% when they replaced Br with I [76,77].

Two years later, Im et al. increased the power conversion efficiency to 6.5% by applying the spin-coated nanocrystalline perovskites onto the nanocrystalline TiO_2

surface in the liquid electrolyte cells [78]. However, the lifetime of the liquid-electrolyte-based perovskite solar cells was just a few minutes due to the prompt decomposition of the perovskite material into the liquid electrolyte. This led to new concept of replacing the liquid electrolyte by a solid-state hole transport material. This was accomplished by Park and Gratzel in 2012 when they introduced the solid-state solar cell instead of the liquid electrolyte [79]. They used spiro-MeOTAD as a hole transporting material (HTM), the highest efficiency of 9.7% was obtained and the stability of the devices was higher than that of the liquid electrolyte based solar cell [79].

After replacing the liquid electrolyte, the power conversion efficiency of the halide perovskite-based solar cell ($CH_3NH_3PbI_2Cl$) reached over 10% as it adopted a mesoporous structures [80,81]. Gratzel *et al*. developed a new structure of halide perovskite solar cells with free hole transport material in the same year. The halide perovskite acts as an absorber as well as a hole conductor. The structure was ($FTO/CH_3NH_3PbI_3/ TiO_2/Au$) and PCE of 7.3% was achieved [82]. Snaith *et al*. reported a new meso-supersaturated structure using mixed halide perovskite $CH_3NH_3PbI_{3-x}Cl_x$ as a light absorber and electron transporter. Replacing mesoporous TiO_2 by alumina oxide which worked as scaffold layer only, obtained a PCE of 10.9% [80].

Further improvement of PCE in the subsequent year was achieved when Gratzel *et al*. presented the so-called sequential deposition technique of the perovskite active layer within the porous metal oxide layer achieving a PCE of 15% [83]. At the same year, Snaith and co-workers introduced very uniform morphologies of mixed halide perovskite $CH_3NH_3PbI_{3-x}Cl_x$ using a vacuum deposition technique. They obtained thin film of perovskite directly on the substrate after controlling the evaporation

speed of two separate sources of thin film ($PbCl_2$ and CH_3NH_3I); the produced solar cell was shown to yield PCE of 15.7% [84].

The first certified PCE of halide perovskite solar cells of 14.1% was presented by Gratzel in 2013. It was confirmed by two independent sources; solar cell efficiency Tables compiled by Green *et al*. [85] and the National Renewable Energy Laboratory (NREL)'s chart of research cell efficiency records. Furthermore, positive results based on improving the structure of halide perovskite solar cells and enhancing the morphologies of the photoactive films were reported. The certified result jumped to 21.1% in 2015 by the Gratzel's group. Very recently, better power conversion efficiency of 22.1 % was certified by NREL [86].

2.4.2 Properties of halide perovskites as light absorbers

2.4.2.1 Crystal structures of halide perovskites

Halide perovskites represent any material that has similar crystal structures to calcium titanate ($CaTiO_3$). In 1839, this mineral was discovered in Russia by Gustav Rose and is named after the Russian mineralogist Lev Perovskite (1792-1856) [85,87,88].

The general formula of a pure perovskite family is ABX_3 as shown in Figure 2.11, where A indicates a large cation and is located at the corners of the unit cell, B indicates a smaller metal cation surrounded by six halide anions, creating six-fold proportionate octahedrons, and X is an anion halide existing at the face centre [89,90]. The initial discovery of halide based perovskites was in 1958 by Moller. He found that the caesium lead halides ($CsPbX_3$) have the perovskite structure [91]. Two decades later, the organic methylammonium cation appeared in halide based perovskite structures produced by Weber and Naturforsch [92].
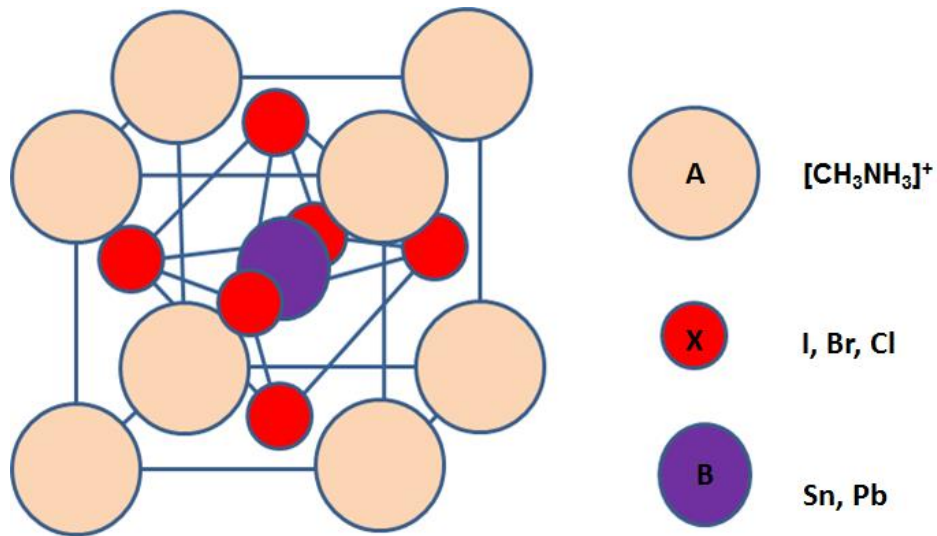
Figure 2.11 Crystal structure of halide perovskites

The perovskite crystal structure might be approximated by the tolerance factor (TF) [87,93] which is identified as the proportion of the distance between A-X to the distance between B-X; It could be given as [94]:

$$TF = \frac{R_A + R_B}{\sqrt{2}\,(R_B + R_X)} \quad \dots\dots\dots\dots\dots\dots\dots\dots\dots\dots\dots\dots\dots\dots\dots\dots \quad (2)$$

where R_A, R_B, and R_X correspond to atomic radii of A, B and X respectively. The ideal cubic geometry of perovskite could be obtained if TF =1 [95]. On the other hand, if TF is less than 1, the octahedron [BX6] tends to be distorted to a low-symmetry structure in order to keep the stability of the structure [95]. This degree of distortion of the crystal structure could determine numerous physical features; magnetic, electronic, and dielectric properties in particular [85].

The tolerance factor (TF) represents the essential guidance of stability, distortion, and tuning of radii size of the perovskite structure [93]. In addition to tolerance factor, chemistry and bonding play an important role on the formability and stability of the perovskite structure [87,93]. The crystalline formation of perovskites possibly

depends on the temperature; for instance, the orthorhombic phase is formed at a low temperature, which consecutively changed into the tetragonal and cubic structures after increasing the temperature [96].

The perovskite materials show a direct band gap of ~1.5 eV for $CH_3NH_3PbI_3$ to 2.2 eV for $CH_3NH_3PbBr_3$, which might be tuned in an extensive range [97]

2.4.2.2 Electronic structure

Recent studies on the cubic phase of halide perovskite at room temperature have disclosed that the characteristics of Pb-X determine the electronic structure of halide perovskites [96]. The electronic structure of halide perovskites have indicated that the valence band minimum (VBM) consists of σ antibonding states of Pb 6s and xp orbitals and the conduction band maximum (CBM) primarily consists of σ-antibonding states of Pb 6p orbitals and xs orbitals [98]. The contribution of MA toward the electronic properties are too small as a result of the deep level of MA structure within the valence and conduction band [99].

The cubic phase of $MAPbX_3$ demonstrates that its electronic structure is mainly controlled by the characteristics of the Pb-X bonds. The generalised gradient approximation was used by Baikie's group to measure the band structures for three phases of $MAPbI_3$; i.e. cubic, tetragonal and orthorhombic phases [100]. It was found that $MAPbI_3$ has a direct band gap of 1.3 eV at the R point for a cubic structure, 1.43 eV at the T point for tetragonal structure, and 1.61 eV at the T point for the orthorhombic structure [100].

2.4.2.3 Optical structure and band gap

The prominent features of halide perovskites are the direct band gap and strong optical absorption coefficient which render them highly attractive for use as competitive absorbers in solar cells [82,101–103].

The perovskite materials present a broad absorption spectrum along the entire visible to near-infrared range and have a large absorption coefficient compared to conventional semiconducting materials. The absorption coefficient of organometal halide perovskites is approximately 1.5×10^4 cm^{-1} at 550 nm [79]. The absorption properties of the MAPbI$_3$ thin film was assessed and compared with other inorganic semiconducting materials such as GaAs, CdTe, and CIGS which have the absorption coefficient of up to 10^4-10^5 cm^{-1} [104]. The absorption onset edge of the perovskite was nearly similar to these materials [104].

The band gap of the CH$_3$NH$_3$PbI$_3$ was calculated to be 1.5-1.55 eV, resulting in a limited absorption range of 800 nm or less. Consequently, tuning the band gap of CH$_3$NH$_3$PbI$_3$ is required to increase the absorption of photons of longer wavelengths without affecting the absorption coefficient.

Absorbance of halide perovskites can be extended via tuning the band gap of perovskite in order to enhance the performance of the halide perovskite-based PV devices [85,104]. One of the strategies of tuning the band gap is to change (CH$_3$NH$_3$I) MA with other organic or inorganic cations. For instance, by replacing methylammonium with formamidinium which results in reducing the band gap by 0.07 eV [104]. Another way to achieve band gap tuning is to replace Pb with another metal (partially or completely). For example, partially substituting Pb with Sn and

varying the ratio of Sn: Pb tunes the band gap between 1.17 eV and 1.55 eV in the synthesis process of halide perovskites [105].

2.4.2.4 Key parameters for PCE of halide lead perovskite-based solar cells

Exciton binding energy (Eb) is one of the major factors that contribute to the photovoltaic mechanism in organometal halide perovskite solar cells. The exciton binding energy is controlled by the dielectric constant of the materials [106]. It is noted that dielectric constant is very high in organolead halide perovskites compared with photoactive polymers. Dielectric constant is nearly 32 [107] for halide perovskites and is ~ 3 for photoactive polymers [108]. There are many ways to determine the exciton binding energy including theoretical analysis [46], optical absorption [109], magneto- absorption [110] and temperature dependence [111].

A theoretical analysis was used by Hirasawa in 1994 to calculate the exciton binding energy in $CH_3NH_3PbI_3$. He found that the exciton binding energy was estimated to be 37meV [110]. Low binding energy in $CH_3NH_3PbI_3$ suggests that excitons in $CH_3NH_3PbI_3$ are Mott-Wannier type excitons. On the contrast, the photoactive polymers have high exciton binding energy which is estimated in the range of (0.3-0.5 eV) [112] suggesting that excitons in photoactive polymers are of Frankel type. Theoretical studies suggested that the Mott-Wannier excitons yield free charge carriers at room temperature owing to the optical phonons and collective rotational motion of the organic cations[113].

Consequently, low binding energy of solar light harvesting materials plays an important role in achieving high PCE solar cells. Another important feature for halide lead perovskites is their long carrier diffusion length related to charge transportation properties compared with short diffusion length in photoactive

polymers. The long diffusion length can contribute directly to high-performance in solar cells. The charge transport properties of $CH_3NH_3PbI_3$ and $CH_3NH_3PbI_{3-X}Cl_X$ were studied separately by Xing *et al*. and Stranks *et al*.[47]. Each of these groups conducted time-resolved photoluminescence (TRPL) and transient absorption spectroscopy respectively. According to their results, it was estimated that the charge diffusion length in $CH_3NH_3PbI_3$ is ~100 nm and ~1 μm for $CH_3NH_3Pb_{3-X}I_X$ compared with photoactive polymer materials with diffusion length of ~10 nm [47]. Bai *et al*. suggested that the charge carrier diffusion length of organometal lead iodide is significantly reliant on the processing conditions and the deposition techniques [114]. Two main factors determine the value of the diffusion length(L), which are diffusion coefficient (D) and carrier life time (τ) according to the Einstein relation [115]

$$L = \sqrt{D\tau} \dots\dots\dots\dots\dots\dots\dots\dots\dots\dots\dots\dots\dots\dots\dots\dots\dots \text{(3)}$$

$$D = \mu\frac{KT}{q} \dots\dots\dots\dots\dots\dots\dots\dots\dots\dots\dots\dots\dots\dots\dots\dots \text{(4)}$$

Where (μ) is the carrier mobility, (K) is Boltzmann constant, (T) is absolute temperature and (q) is the charge of carriers.

2.4.3 Architectures of halide perovskite solar cells

2.4.3.1 TiO$_2$-based solar cell structures

TiO$_2$-based solar cell structures could be divided into three types; these are mesoporous, meso-supersaturated, and planar heterojunction structures. In the mesoporous structure, nanoparticles of perovskites percolate over the mesoporous titanium oxide (TiO$_2$) film. In this specific architecture, organometal halide perovskite was firstly utilised to sensitize mesoporous titanium oxide (TiO$_2$) within

a liquid electrolyte in dye-sensitized solar cells (DSSCs) as shown in Figure 2.12a. The organometal halide perovskite nanocrystals $CH_3NH_3PbX_3$ (X=I, Br) as sunlight absorbers were fabricated for the first time by Kojima's group in 2009, generating a PCE of 3-4% [77]. It presented a large area in contact between the sensitizer perovskite and the TiO_2 layer within the liquid electrolyte-based solar cell. The main obstacle with this configuration is that the organometal halide perovskite can dissolve or decompose into the liquid electrolyte rapidly [79,116].
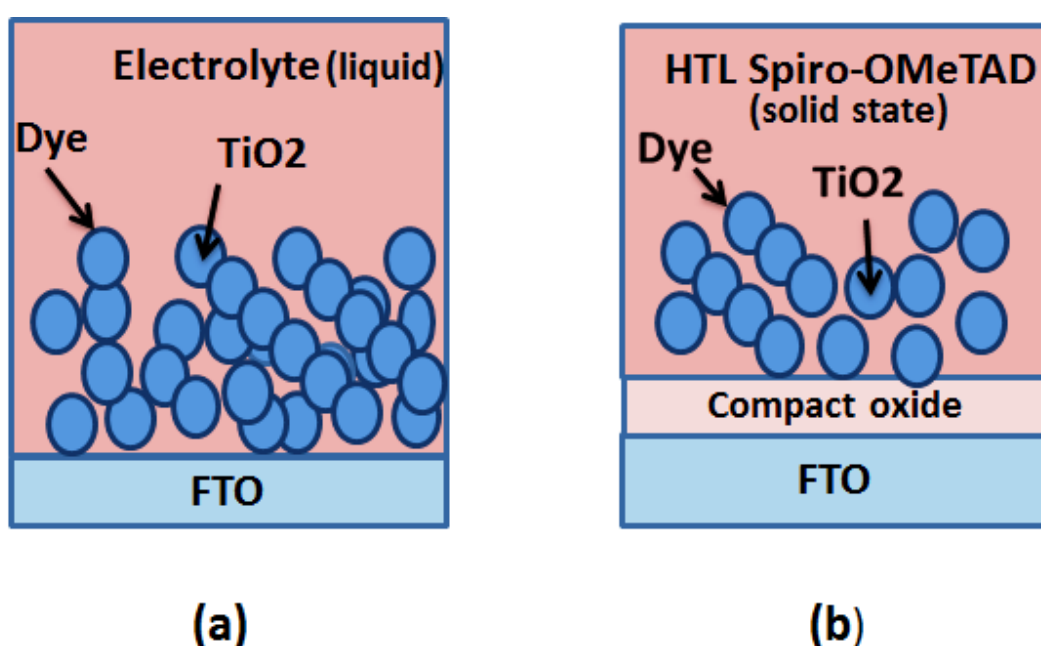
Figure 2.12 Schematic of halide perovskite-based solar cells: (a) with liquid electrolyte; (b) with solid HTL

In 2012, the liquid-electrolyte-based mesoporous structure was converted into another type of mesoporous structure that was based on introducing a solid-state hole transport layer commonly named as spiro-MeOTAD [79]. Figure 2.12(b) shows a schematic diagram of the solid-state mesoporous TiO_2-based halide perovskite solar cell wherein it consists of FTO/compact-mesoporous TiO_2 (as ETL)/$CH_3NH_3PbX_3$ (as absorber)/Spiro-MeOTAD (as HTL)/top electrode. The

compact TiO$_2$ layer is deposited by the spray-coating method on top of the fluorine-doped tin oxide (FTO) coated glass substrate, then the mesoporous TiO$_2$ layer is produced by either the screen-printing or spin-coating technique, followed by deposition of the halide perovskite harvesting layer. The hole transport layer of commonly spiro-MeOTAD is fabricated on top of this layer and finally the top metal electrode is deposited [117]. The compact TiO$_2$ layer and mesoporous layer act as n-type electron transport layer in order to transfer and collect electrons, which are generated in the photoactive perovskite layer to the corresponding electrode [45,118]. A significant number of papers have been published with perovskite based solar cells adopting this type of structure [45].
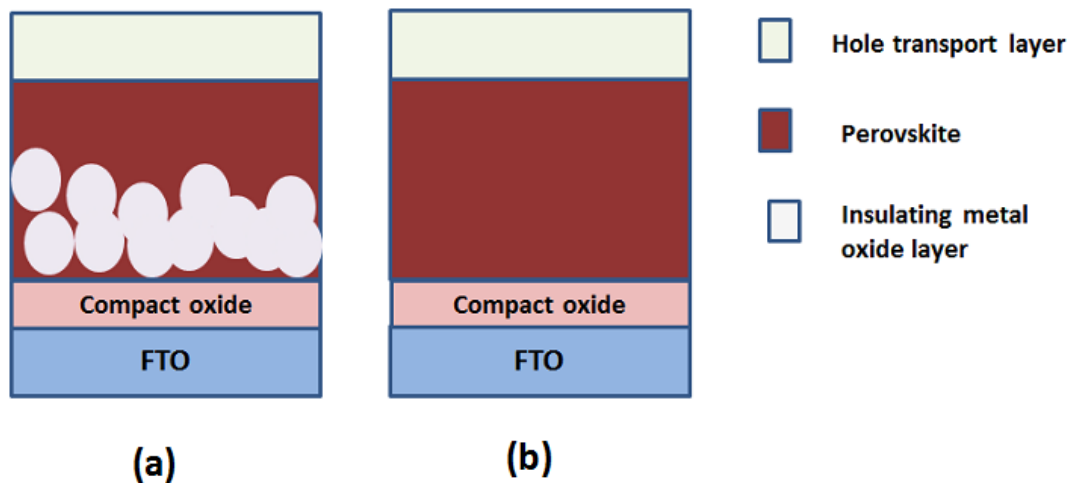
Figure 2.13 TiO$_2$ based halide perovskite solar cells: (a) meso-superstructured; (b) planar heterojunction

In the mesoporous TiO$_2$ based solar cells, the photogenerated electrons have serious possibility of being captured by traps. These are caused by the oxygen vacancies, which are formed as a result of the noticeable degradation of mesoporous TiO$_2$ particles under ultraviolet illumination [119]. Consequently, scaffold metal oxide such as Al$_2$O$_3$ was introduced into the mesoporous structure in order to significantly enhance stability of the devices [120].

This type of TiO$_2$-based solar cell is classified as a mesoporous supersaturated structure as shown in Figure 2.13 (a). Snaith *et al*. used meso-superstructured to fabricate organometal halide perovskite-based solar cells in 2012, achieving a PCE of 10.9% [80]. Insulating Al$_2$O$_3$ was used instead of pure mesoporous TiO$_2$, and the Al$_2$O$_3$ nanoparticles act as a scaffold layer to improve the quality of the perovskite layer. The Al$_2$O$_3$-formed scaffold does not collect and transfer electrons coming from the perovskite absorber because of its wide band energy [118,121]. The role of collecting and transporting electrons is achieved by the compact TiO$_2$ layer. Free electrons have to travel much longer distance to reach the electrode for collection in the meso-superstructured based perovskite solar cells compared to the mesoporous solar cells. This results in increased demand for high-quality halide perovskites to obtain a long diffusion length for free electrons.

The main disadvantage for mesoporous TiO$_2$-based solar cells is the high-temperature sintering requirement (heat treatment at ~500°C) of TiO$_2$ for efficient photovoltaic devices [118], which limits its potential applications on flexible substrates. Adding to production costs, a large hysteresis is observed in the J-V characterisation of the mesoporous and meso-superstructured solar cells [118]. Other concerns in mesoporous TiO$_2$-based solar cells are infiltration of the perovskite nanoparticles and charge recombination caused by the short distance between the hole transport layer and the mesoporous TiO$_2$ layer [89]. Therefore, low-temperature planar heterojunction (PHJ) structures were developed without using the mesoporous TiO$_2$ film in the TiO$_2$-based halide perovskite solar cells. TiO$_2$-based PHJ solar cells exhibited lower recombination rates than the mesoporous TiO$_2$-based halide perovskite solar cells, while the charge transport rate in both structures was the same [122]. Snaith *et al*. first studied this structure in 2013 wherein they used the

PHJ of FTO/compact TiO_2/$CH_3NH_3PbI_{3-x}Cl_x$/Spiro-MeOTAD/Ag, and a PCE of 15.4% was obtained [84].

A successful effort was further obtained by Liu and Kelly when they prepared planar heterojunction perovskite-based solar cells at room temperature. They showed that high-performance perovskite-based PHJ PV devices can be realised without using the mesoporous scaffold structure. They applied ZnO nanoparticles as the electron transport layer, and high-performance PV devices of ~15.7% PCE was achieved [123].

2.4.3.2 Carbon fullerene-based solar cells

Planar heterojunction structure (PHJ) without mesoporous layer; i.e. mesoporous TiO_2 (Ms TiO_2 layer) has emerged as a new way to fabricate organometal halide perovskite-based solar cells. This structure creates additional choices in utilising various hole and electron transport materials for stability enhancement of solar cells as shown in Figure 2.14a. Another important feature in PHJ structure is that it has the potential to produce efficient perovskite-based solar cells in two different configurations; i.e. with normal or inverted structures [124]. The normal configuration of PHJ structures has been mentioned in the TiO_2-based PHJ solar cells in Figure 2.13b. In the inverted configuration, other semiconductive materials were utilised as HTL (PEDOT:PSS) [125], ETL (PFN and BCP) [22,126], and photogenerated exciton acceptor (C60, $PC_{61}BM$, $PC_{71}BM$, and ICBA). The solution-processed roll-to-roll method is easy to be adapted in the fabrication of efficient perovskite-based solar cells in the inverted PHJ structure [126].

The first report of fabricating the inverted PHJ solar cells was presented by Chen and co-workers in 2013 [127]. They used the PHJ structure consisting of

glass/ITO/PEDOT:PSS(as HTL)/ $CH_3NH_3PbX_3$ (as light absorber)/C_{60}(as exciton acceptor) /bathocuproine (BCP)(as buffer layer)/Al (as top electrode). However, the PCE of their PV devices was limited to ~3.9%. The thickness reduction of the photoactive layer caused a reduction in the magnitude of J_{sc} [127]. The PCE of the inverted PHJ was significantly enhanced to ~7.41% by Sun *et al*. in 2014. They used $CH_3NH_3PbX_3$ and $PC_{61}BM$ as an electron donor and acceptor respectively and the thickness of the photoactive layer was less than 100 nm [111]. Chen *et al*. claimed high-performance PV devices using the sequential vacuum deposition technique to deposit halide perovskite. The inverted PHJ structure of ITO/PEDOT:PSS/ $CH_3NH_3PbI_{3-x}Cl_x$/C_{60}/bathophenanthroline (Bphen)/Ca/Ag was used in their solar cells, and ~15.4% of PCE was obtained[128]. Chiang *et al*. reported the fabrication of high-quality perovskite by the low-temperature solution processed two-step method. They utilised the PHJ inverted structure consisting of ITO/PEDOT:PSS/$CH_3NH_3PbI_3$/PCBM/Ca/Al and ~16.4% of PCE was achieved [129]. Lately, the inverted PCBM-based planar heterojunction structure to fabricate perovskite solar cells has been widely used in the perovskite society due to the simple solution-processed method at low-temperature processing of solar cells.

Very recently, planar heterojunction structures have been modified to optimise the performance of perovskite-based solar cells using a bulk heterojunction layer (BHJ) in the inverted PCBM based PHJ structure as illustrated in Figure 2.14 b& c. Additives have also been doped into the perovskite layer to enhance their properties.
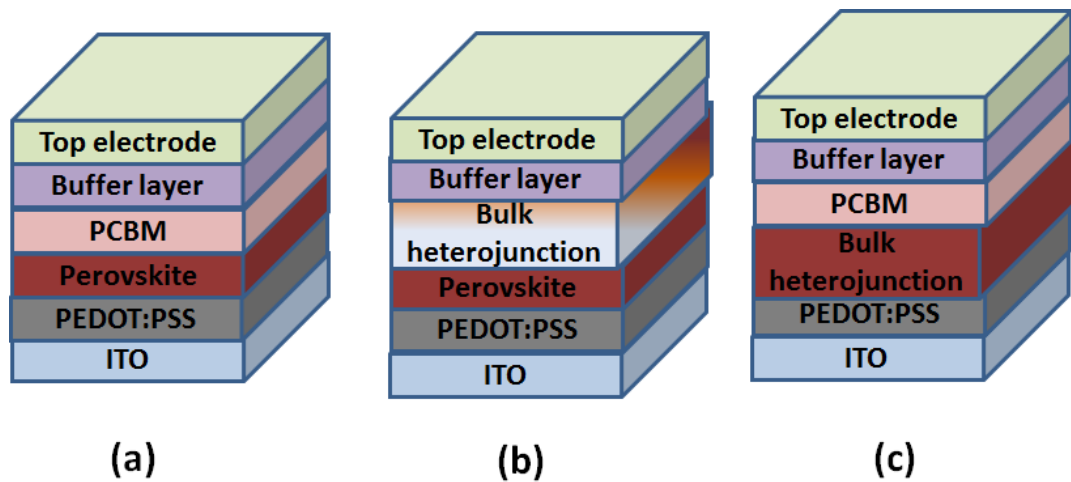
Figure 2.14 Schematic of PCBM-based perovskite solar cells: a) general planar heterojunction; b & c) modified with PHJ by a photoactive polymer BHJ

Chiang *et al*. presented a bulk heterojunction perovskite structure by doping a tiny amount of PCBM within the perovskite layer [130]. His architecture consists of ITO/ PEDOT:PSS/ $CH_3NH_3PbI_3$–PCBM/PCBM/Ca/Al. A significant improvement in fill factor of 0.82 was achieved by filling the pinholes and vacancies between the perovskite's grains, resulting in increased grain perovskite crystals. Gong *et al*. used bulk heterojunction layer in the perovskite solar cells. They mixed perovskite with fullerene derivatives ($CH_3NH_3PbI_3:A_{10}C_{60}$) to produce 300 nm of perovskite film followed by coating 200 nm of $PC_{61}BM$. The PCE of this new structure was 22% higher than the normal inverted planar heterojunction solar cells [75].

Yang *et al*. applied two photoactive layers in his solar cells including $CH_3NH_3PbI_{3-x}Cl_x$ and a bulk heterojunction layer of a wide bandgap small molecule DOR3T-TBDT with $PC_{71}BM$ [131]. Light harvesting by the photoactive layers increased from UV to near IR region, improving short circuit current at ~21 mA/cm^2, and ~14.3% of PCE was achieved [131]. In addition, Ding *et al*. used a bulk heterojunction structure on the top of the perovskite layer. They used ITO/PEDOT/ $CH_3NH_3PbX_3$/(PDPP3T–$PC_{61}BM$)/Ca/Al in this solar cell and they achieved PCE of

~ 7.5-9.5% by changing the thickness of the PC$_{61}$BM [132]. Moreover, low band gap polymer (PCE-10) was used as one of the light absorbers with (PC$_{71}$BM) in the tandem based perovskite configuration. The front subcell contains PHJ of a PC$_{61}$BM/CH$_3$NH$_3$PbI$_3$ and the back subcell contains BHJ of blending of (PCE-10: PC$_{71}$BM). High PCE of ~ 16% was achieved with V$_{oc}$ and FF of 1.8 V and 77% respectively [133].

2.4.4 Fabrication methods of halide lead perovskites

2.4.4.1 One step spin-coating method

Different processing techniques have been developed to fabricate organometal halide perovskites. Examples of fabricating CH$_3$NH$_3$PbX$_3$ (X=I, CLand Br) will be discussed for various deposition methods. Solution-processed one-step spin-coating method is one of the most used methods for the deposition of organometal halide perovskites, owing to the ease of the fabrication processes and low-cost compared to other coating methods. As illustrated in Figure 2.15a, metallic halogen (MX$_2$) and organic compound methylammonium halide (AX) are dissolved in a common polar solvent including N, N-dimethylformamide (DMF), gamma-butyrolactone (GBL), n-methyl-2-pyrrolidone (NMP), and/or dimethyl sulfoxide (DMSO). The prepared solution is applied onto the substrate for the deposition of perovskites layers. Finally, heat treatment is carried out to obtain crystalline perovskites [16,111,134]. The major pertinent parameters in the spin-coating method are type of solvents used, spin-rate, concentration of the solution, and heat treatment after coating. However, obstacles exist in the one-step spin-coating method, e.g. difficulties of obtaining large-area uniform and/or discontinuous thin films, which results in poor film morphologies and hence very poor performance of solar cells [83,135]. The poor film morphologies are caused by rapid crystallisation of perovskites, which is

generated through the solvent evaporation and intensive ionic interaction between metal cations and halides [118,127,136].
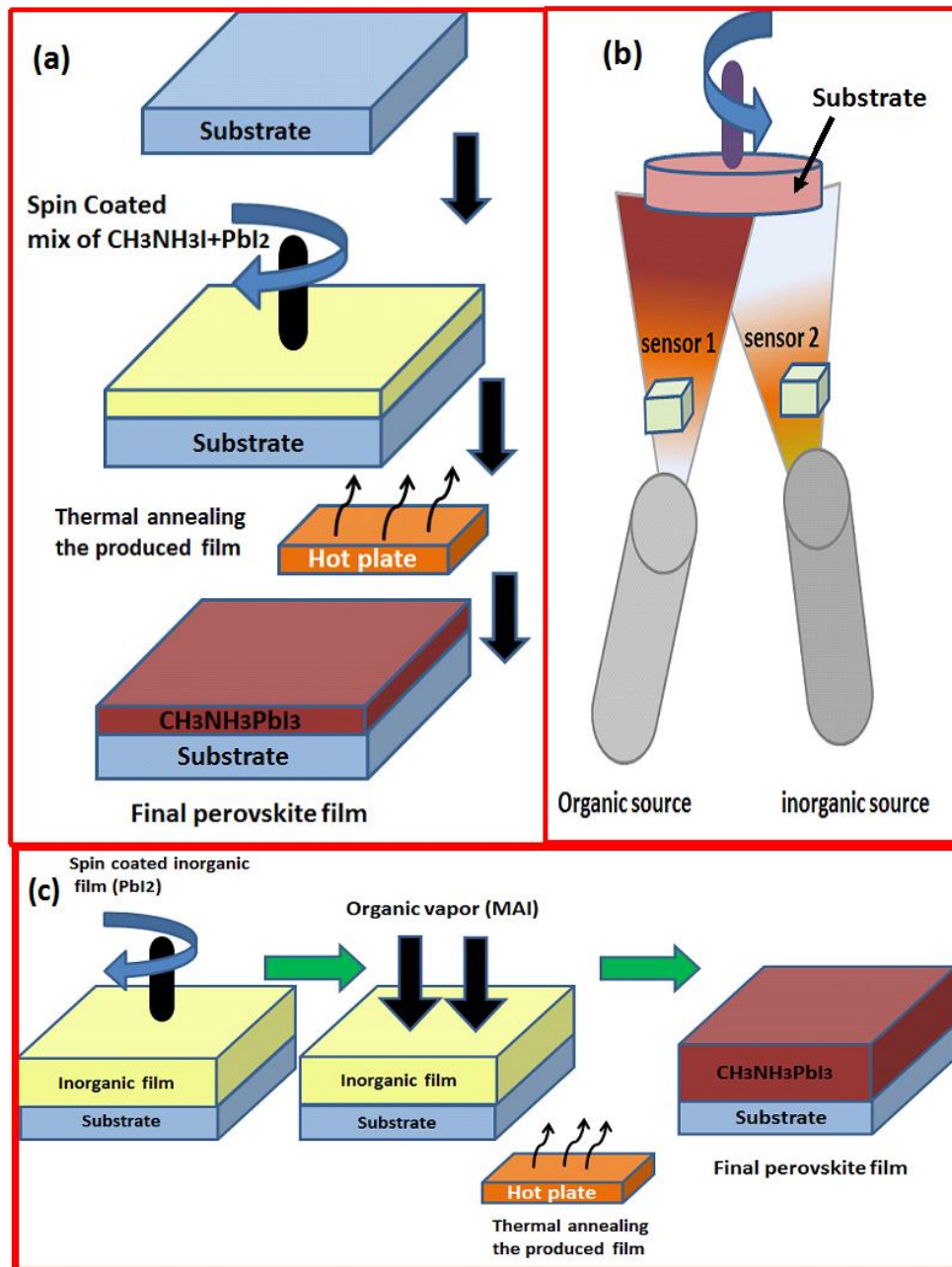
Figure 2.15 One-step fabrication method: a) one-step spin-coating method; b) one-step vapour deposition method; c) vapour assisted solution-processed method

2.4.4.2 Co-evaporation method

Although most researchers have used the solution processed techniques to produce halide perovskite-based solar cells, the vapour deposition technique has the auspicious potential to fabricate very high-quality perovskite thin films, [137] with the advantages of full coverage surface, uniform thin film [138] and capability of preparing multi- layers within sizable areas [84].

The evaporation-based technique might be divided into two common methods; these are dual source vapour deposition method and vapour assist spin-coating method [22]. In the dual source vapour deposition method as illustrated in Figure 2.15b, two separate sources of organic and inorganic vapours are installed into the nitrogen glovebox with a flow rate which can be adjusted to control the composition thickness. In 1997, Era *et al.* first used the dual-source vapour deposition technique by supplying the vapour of lead iodide and organic ammonium iodide to fabricate the perovskite thin film [139]. Snaith and co-workers presented planar heterojunction based solar cells using the vapour deposition method to deposit $CH_3NH_3PbI_{3-x}Cl_3$ onto the TiO_2 thin film on top of the FTO film on glass. Smooth and uniform films were created, resulting in a PCE of 15.4% [84]. Mankiewicz *et al.* revealed another example of using the thermal evaporation method to fabricate $CH_3NH_3PbX_3$ with PEDOT:PSS and PCBM layers in their solar cells, achieving a PCE of 12.4% [140]. However, the vapour deposition method requires high vacuum and demands a huge amount of energy [104]. In order to overcome this disadvantage, another deposition method (the vapor-assisted solution process (VASP)) was developed by Yang's group [138]. They used the solution-processed method to deposit PbI_2 layer and the thermal evaporation method to provide the

MAI source for fabrication of perovskites layer as shown in Figure 2.15c. Compact and uniform PbI_2 films were obtained leading to a PCE of ~12.1% [138].

2.4.4.3 Sequential deposition method

One of the main handicaps of utilising one-step spin deposition method to fabricate perovskite solar cells is the rapid reaction between AX and MX_2, creating pin holes and uncovering the surface of the perovskite. This poor morphology creates shunts paths and reduces the light absorption of the perovskite solar cells [134,141]. Furthermore, disadvantages of using the dual vapour thermal deposition method are high vacuum equipment requirement, consumption of large amount of energy and poor thermal stability of the halide perovskite layer as well as the difficulty of controlling the source temperature and the precursor evaporation rate [142].

The so-called sequential deposition method or two-step method was developed as an alternative to the one step method in the manufacture of halide perovskite. One of the most important features offered by the two-step method compared with the one-step method is that it provides better control on the crystallisation of the perovskite film [143], giving superior morphologies and interfaces [141]. Moreover, the two-step method has a potential to fabricate high-efficient perovskite-based solar cells at low temperature [125]. This technique has been widely used in both TiO_2- and PCBM-based planar heterojunction solar cells, obtaining a full coverage perovskite thin film with pin-hole-free, and homogenous thin films.

In the two-step method, there are various deposition processes used in the fabrication of perovskite films. Typically, metallic halogen (MX_2) was first deposited by the spin-coating method whilst methylammonium halide (AX) was then applied on the top of MX_2 by different second methods including dynamic or

static spin-coating method and dip-coating method as illustrated in Figure 2.16. In the dynamic spin-coating method, the AX solution is directly added on the top of the MX_2 film during the rotation. In contrast, in the static spin-coating method the AX solution is applied on the top of the MX_2 film for a period of time (reaction time) and then followed by the spin- coating process. In the dip-coating technique, the MX_2 film is immersed into the AX alcoholic solution. The obtained perovskite film is then thermally annealed on a hotplate for a limited time. Thermal annealing is required as it plays a significant role in transforming the formed intermediate phase of perovskite into its fully crystallised perovskite phase.

The two-step dynamic spin-coating method was claimed by Chiang *et al*. to fabricate high-quality perovskite ($CH_3NH_3PbI_3$)films. They utilised planar heterojunction structures with an inverted configuration of ITO/PEDOT:PSS/ perovskite/$PC_{71}BM$/Ca/Al and a PCE of ~16.3% was obtained [125]. The two-step static spin-coating method was reported by Park and his co-workers. They deposited the PbI_2 thin film onto the mesoporous TiO_2 layer, followed by applying the MAI solution on the PbI_2 thin film for 45 s and then heated the perovskite film at 100°C for 5 min. They found that the pre-heating process of the substrate before applying the PbI_2 solution is essential to achieve high PCE of ~15% [144]. Burschka *et al*. used the two-step dip-coating method to fabricate high-performance perovskite film of $CH_3NH_3PbI_3$ onto the mesoporous TiO_2 film. High reproducibility of solar cells was obtained and a PCE of ~15% was obtained [83].
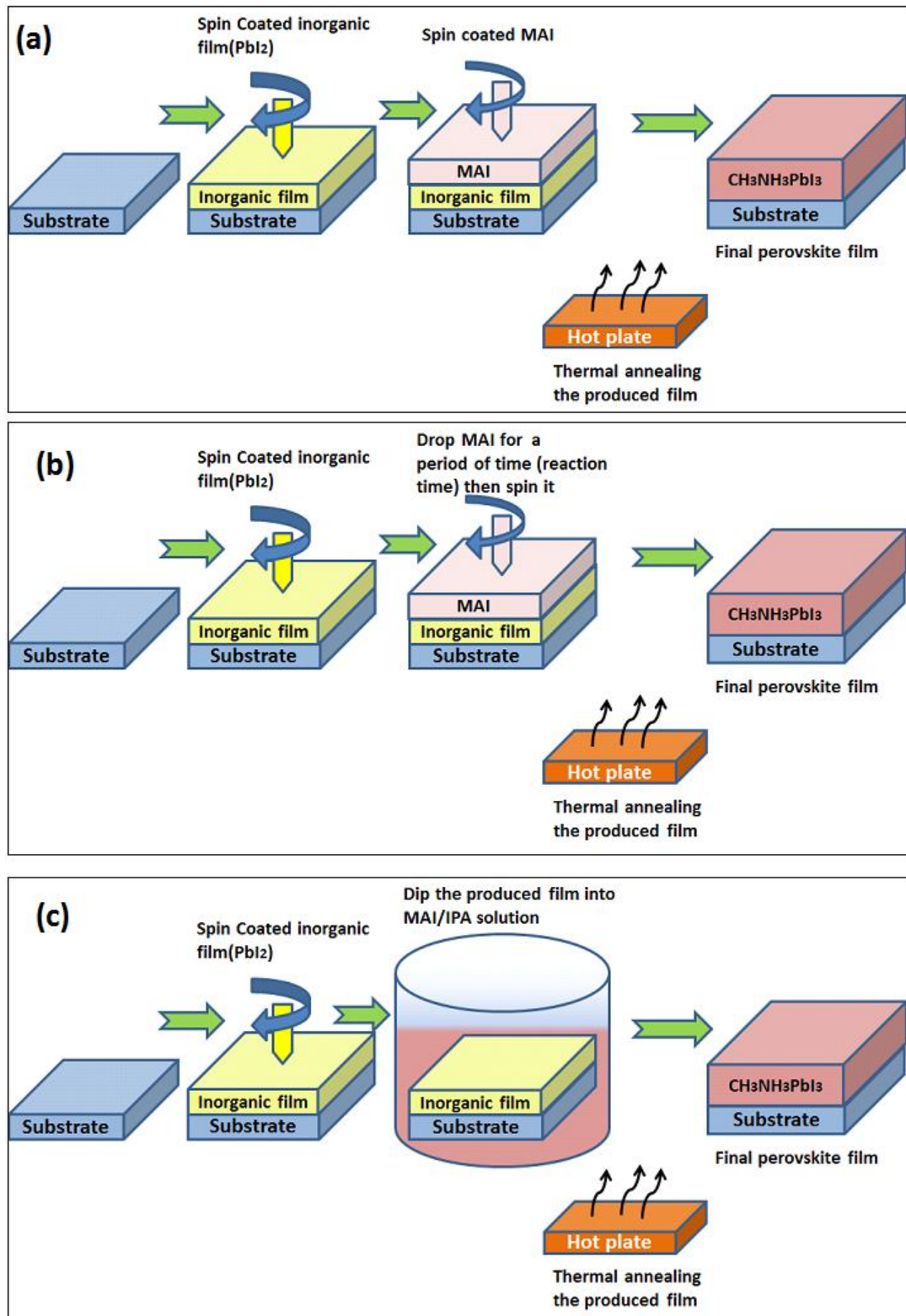
Figure 2.16 Schematic diagram of the fabrication processes of the perovskite film by: (a) a two-step dynamic spin-coating method; (b) a two-step static spin-coating method; (c) two-step dip-coating method

2.4.5 Morphologies of halide perovskites

One of the main challenges in obtaining high-performance perovskite-based solar cells is the control of the perovskite thin film morphology [145]. Physical characteristics of halide perovskites including light absorption, charge carrier transport, and diffusion length are highly reliant on the degree of crystallinity of the perovskite thin film [134,146,147]. The crystallinity of the perovskite thin film depends extremely on many factors such as deposition process, composition of materials, perovskite structure, the used solvents and additives, annealing treatment (thermal and solvent annealing), and humidity during preparation [47,134]. The crystallisation process comprises two major processes; i.e. nucleation and crystal growth [76].

The poor perovskite morphology arises from pinholes and incomplete surface coverage which results in low-resistance shunting path and decreasing light absorption. It is feasible to optimise morphologies of perovskite thin films by selecting efficient techniques to manipulate nucleation and crystal growth in the perovskite thin film. Several efforts have been exerted to optimise the morphologies of the perovskite layer. The deposition method is one of the most significant factors which impact on the morphology of the perovskite thin film. In the one-step deposition method, the crystallisation process of perovskite crystals is very fast, creating very poor surface morphology with pinholes in the film and discontinuous film [118,134].

Different morphological control methods are presented in Table 2.1. Optimisation of perovskite crystals in the films was achieved by Spiccia and co-workers using the one-step deposition method. They deposited $CH_3NH_3PbI_3$ thin film and then followed by inducing a fast crystallisation process via exposing the perovskite film

to chlorobenzene. Smooth and homogenous thin films were produced with large grain structure. A mean PCE of 13.9±0.7 was obtained in their solar cells [135]. It is suggested that the morphology of the perovskite film fabricated by the spin-coating technique could be influenced through two main factors; i.e. thermodynamic and kinetic impact. Both thermodynamic and kinetic influences play their crucial functions in the growth of perovskite thin film's morphologies [148]. The thermodynamic effects are determined by fundamental characteristics of the composition and concentration of the solutions which are utilised to fabricate the perovskite thin film. These include, the proportion of (AX) to (MX_2), degree of interaction and solubility of the perovskite components. Kinetic factors on the other hand are related to average solvent evaporation, post-treatment, and incorporation of additives.

The two-step deposition method is an important technique which has its potential to govern the crystallization in the perovskite film [83,149,150]. Park and co-workers utilised the two-step spin-coating method to fabricate the $CH_3NH_3PbI_3$ thin film in TiO_2-based planar heterojunction solar cells [151]. They identified that the cuboids crystal in the perovskite exceptionally depended on the concentration of the CH_3NH_3I solution. They optimised and controlled the cuboids crystals using a low concentration of the CH_3NH_3I solution (0.038M), resulting in larger cuboids of perovskite (~720 nm) and achieving a high PCE of ~17.01% for the solar cells [151].

Furthermore, doping additives into the precursor's solution is an alternative to control the morphology of the perovskite film. Joen *et al*. have shown that the morphology of the perovskite film can be controlled by adding a limited amount of N-cyclohexyl-2-pyrrolidone (CHP) into DMF solvent. A uniform film with

complete coverage surfaces was obtained after the additive remained on the surface during the formation of the perovskite film due to the high boiling point and low vapour pressure of the N-cyclohexyl-2-pyrrolidone (CHP) [152]. In addition, Liang *et al.* improved the crystallization process of the perovskite film by combining 1,8-diiodooctane (DIO) into the precursor solution of perovskite, showing very smooth surface and continuous thin film. The effect of additives in the precursor solution not only enhances homogeneous nucleation but also changes the kinetic growth mechanism of perovskite crystals [145].

Solvent annealing is another method to optimize the morphology of the perovskite film when it's deposited in a saturated ambient environment containing solvent vapour. It is a common technique which was widely used to optimize the morphology of the photoactive polymer films in polymer-based photovoltaic devices. Xiao *et al.* first used the solvent annealing method to optimize crystallinity and grain size in the perovskite film by annealing the perovskite film in a saturated environment of DMF vapour. The DMF vapour can assist the diffusion and rearrangement of the precursor's molecules and ions due to high degree of solubility of PbI_2 and CH_3NH_3I in DMF, giving the opportunity of perovskite crystals to grow intensively [153].

Solvent engineering technique (SET) was used by Seok *et al.* in order to obtain homogenous and very dense perovskite thin films. Two types of solvents, (γ-butyrolactone and dimethylsulphoxide (DMSO) (7:3v/v)) were mixed with the perovskite precursor solution to produce $MAPb(I_{1-x}Br_x)_3$ perovskite film. Toluene then dropped on the perovskite film during the spin-casting process of the perovskite film, which led to the formation of a dense and uniform perovskite layer. [154]. High power conversion efficiency PCE of ~16.2% was achieved.

Table 2-1 **A summary of methods to control the morphology of perovskite solar cells and corresponding high power conversion efficiency**

Deposition method	Method	Structure	PCE (%)	Ref
One-step spin method	FDC	FTO/bI TiO$_2$/MAPbI$_3$/Spiro-MeOTAD/Au	13.9	[135]
One-step spin method	Additive (CHP)	ITO/PEDOT: PSS/CH$_3$NH$_3$PbI$_3$/PCBM/Al	10.0	[152]
One-step spin method	Additive (DIO)	ITO/PEDOT:PSS/CH$_3$NH3Pb$_3$-$_x$Cl$_x$/PCBM/C$_{60}$/Ag	11.8	[145]
One-step spin method	Solvent engineering	FTO/bI- TiO$_2$/mp- TiO$_2$/MAPb(1-xBrx)$_3$/PTAA/Au	16.7	[154]
One-step spin method	Solvent engineering	ITO/PEDOT:PSS/CH$_3$NH$_3$PbI$_3$/PC$_{61}$BM/LiF/Al	14.1	[155]
One-step spin method	Solvent engineering mix solvent	ITO/PEDOT:PSS/CH$_3$NH$_3$PbI$_3$/PCBM/Al	6.16	[156]
Two-step spin method	Solvent annealing	ITO/PEDOT:PSS/CH$_3$NH$_3$PbI$_3$/PC$_{61}$BM/C$_{60}$/BcP/Al	15.6	[153]
Two-step spin method	Growth perovskite cuboids and controlled size	FTO/bI TiO$_2$/mp-TiO$_2$/MAPbI$_3$/Spiro-MeOTAD/Au	17.0	[151]
Two-step spin method	Thermal annealing	ITO/PEDOT:PSS/CH$_3$NH$_3$Pb$_3$-xCl$_x$/PC$_{61}$BM/Al	7.5	[148]

2.4.6 Current limitations of halide perovskite-based solar cells

2.4.6.1 Stability of halide perovskite-based solar cells

The rapid degradation of organometal halide perovskite can be considered one of the main challenges encountered by researchers in the perovskite photovoltaic community. Poor long term stability is the major limitation for commercialisation of halide perovskite-based solar cells. The degradation mechanism of halide perovskite-based solar cells has not been fully investigated in the past five years; most studies have been focused on enhancing the performance of the perovskite - based solar cells [142]. The degradation mechanism for the perovskite-based PV devices could be divided into three types; i.e. chemical, thermal, and environmental degradation. The chemical degradation is caused by adjacent components such as solvents, solutes, and additives which were used in numerous processing procedures [76]. The thermal decomposition of halide perovskite is caused by exposing the perovskite-based PV devices from low temperature to high temperature for a period of time, which leads to decomposition of halide perovskite. The halide perovskite film can convert gradually into the PbI_2 film at increased temperature. It was suggested that the thermal stability could be influenced by minor changes in the synthetic processes and the precursors used [157]. The environmental degradation is caused by exposing the unsealed perovskite-based PV devices to light, moisture and oxygen. Due to their ionic nature, degradation of halide perovskite crystals shows a high degree of sensitivity to light, moisture and oxygen [158,159]. High moisture content in air can break the lattice structure between molecules and cause elements to decompose [93]. Thereafter crystal structures of the perovskite film change to metal halide. It was found that methylammonium lead iodide ($CH_3NH_3PbI_3$) is more

sensitive to humidity compared with methylammonium lead bromide (CH$_3$NH$_3$PbBr$_3$) [160].

Noh *et al*. revealed that exposing methylammonium lead iodide to ~50% humidity can result in decomposition, showing a colour change from dark brown to yellow. However, the stability is remarkably enhanced after doping Br into perovskite material to produce MAPb(I$_{1-x}$Br$_x$)$_3$, where x=0.2 and 0.29 [161]. It was well known that the perovskite-based liquid electrolyte structural PV devices have very poor stability and a very short life span. The efficiency of the PV devices could degrade in a few minutes because of high solubility of perovskite into the liquid electrolyte [162]. The stability of the perovskite solar cells based on the liquid electrolyte was greatly improved by changing the liquid electrolyte with a solid-state hole transport layer [163].

Later, different techniques were used to enhance the stability of perovskite-based solar cells as presented in Table 2.2. Burschka and his colleagues found that the fabrication of perovskite solar cells by the two-step method retains more than 80% of the performance of the encapsulated devices under illumination and increases the life time of the sealed devices to ~500 h [83]. Kim *et al*. enhanced the environmental stability of perovskite-based devices when they improved the morphology of the perovskite layer using the blade-coating method. They demonstrated that the morphology of the perovskite crystal thin films significantly improved after solvents evaporated from the surface during the blade-coating process, resulting in the formation of a large and compact crystalline domain in the perovskite layer [164]. There are other ways to enhance the stability of the perovskite-based solar cell which adopts a proper electron and/or hole transport layer. It was found that mesoporous TiO$_2$ in the case of acting as the electron transport layer affects the

stability of the PV devices because TiO$_2$ is unstable under UV illumination [93]. Using Al$_2$O$_3$ or ZnO nanorods instead of TiO$_2$ elongate the life time of PV devices [158,165]. Three different hole transport materials were explored by T. Park's group [166] to investigate the impact of 20% humidity on the long-term stability over 1000 hours. They used Poly[2,5-bis(2-decyldodecyl)pyrrolo[3,4-c]pyrrole-1,4(2H,5H)-dione-(E)-1,2-di(2,20-bithiophen-5-yl) ethene] (PDPPDBTE), P3HT, and Spiro-MeOTAD as HTLs separately on top of TiO2/CH$_3$NH$_3$PbI$_3$-based devices and deduced that the semiconductive polymers HTLs maintained better performance of the PV devices over the period of testing than Spiro-MeOTAD. The outstanding stability of the polymer HTLs based perovskite devices was due to hydrophobicity of the semiconductive polymers of PDPPDBTE and P3HT, which decreased the infiltration of water into the perovskite surface [166]. Snaith *et al*. presented a novel HTL of polymer-functionalized single-walled carbon nanotubes (SWNTs) for replacement of PEDOT:PSS on top of CH$_3$NH$_3$Pb$_{3-x}$Cl$_x$ thin film. The perovskite devices showed unparalleled thermal stability and moisture resistance after the devices were exposed to 80 °C in air for 96 h [167]. Snaith and co-workers replaced the compositions of halide perovskites; for instance; replacing methylammonium with formamidinium or iodide with bromide leads to increasing the stability of the perovskite. FAPbI$_3$ and CH$_3$NH$_3$BrX$_3$ have better stability compared with MAPbI$_3$ [168,169]. Mei *et al*. presented highly stable unsealed devices for 1008 h in the normal environmental condition e.g., (AM1.5), light intensity at 100 mW cm^{-2} and room temperature. They applied modified perovskite materials (5-AVA)$_x$(MA)$_{1-x}$PbI$_3$ with free hole transport materials and obtained a certified PCE of ~12.8% after the perovskite layer was protected by a carbon layer which acted as a back contact [170]. A low-temperature solution-processed material of PhNa-1T was used

instead of PEDOT:PSS as a hole transport layer, demonstrating that the stability of PV devices was enhanced under ambient conditions of 25°C and 40% relative humidity compared with devices using PEDOT:PSS. The device structure was PEN/ITO/PhNa-1T /$CH_3NH_3PbI_3$/$PC_{61}BM$/Ag. It revealed higher resistance within a replicate mechanical stress [171]. Zhao *et al*. claimed a novel configuration by inserting a polymer as an insulated scaffold material, which led to enhancing the stability to ~300 h in an ambient environment with 70% relative humidity. The unsealed devices show a PCE of ~16%. This structure not only improved the stability but also exhibited robust self-sealing or humidity-resistance, showing that the perovskite devices could offer power conversion efficiency recovery after water vapour attached on the surface and then evaporated [172].

Table 2-2 A summary of methods to enhance the stability of perovskite and corresponding high power conversion efficiency

Structure	Method	Device structure	Life time	PCE (%)	Ref
TiO2 based PHJ	Doping Br into CH3NH3PbI3	FTO/Bl-TiO2/Ms TiO2/ $CH_3NH_xPbBr_{3-x}$	_	12.3	[161]
TiO2 based PHJ	Applying HTMs	FTO/Bl-TiO2/Ms TiO2/ $CH_3NH_3PbI_3$/ (HTMs)	1000	9.2	[166]
PCBM based PHJ	Using blade coating technique	ITO/PEDOT:PSS/$CH_3NH_3PbI_3$/PCBM/C_{60}/Ag	268	12.21	[164]
ZnO based PHJ	Using ZnO as ETL	FTO/ZnO/$CH_3NH_3PbI_3$/spiro-MeOTAD/Ag	500	5	[165]
TiO2 based PHJ	Using Al_2O_3 as scaffold	FTO/BI-TiO2/Al_2O_3 $CH_3NH_3PbI_3$/spiro-MeOTAD/Ag	18	4.6	[173]
TiO2 based PHJ	Using HTL PDPPDBTE	FTO/Bl-TiO2/MsTiO2/ $CH_3NH_3PbI_3$/ (HTMs : P3HT,PDPPDBTE and spiro-MeOTAD)/Au	1000	9.2	[166]
TiO2 based PHJ	Using formamidinium lead iodide as photoactive layer	FTO/BI-TiO2/$FAPbI_3$/spiro-MeOTAD/Au	_	14.2	[168]
PCBM based PHJ	Using HTL PhNa-1T	ITO/HTL(PhNa-1T) /$CH_3NH_3PbI_3$/PCBM/Ag	300	14.7	[171]

2.4.6.2 Toxicity of lead in halide perovskites

High PCEs of halide perovskite-based solar cells are currently only realised in organic-inorganic hybrid lead halide perovskites. However, lead is very toxic and not environmentally friendly [174]. Efforts have been made to search for an alternative of lead-free halide perovskites. Hao *et al* firstly fabricated lead-free hybrid halide perovskite solar cells based on tin iodide perovskite. They achieved ~5.7% using $CH_3NH_3SnI_{3-x}Br_x$ as an absorber layer [42]. Then, Snaith and co-workers reported lead free $CH_3NH_3SnI_3$ perovskite solar cells and ~6.4% PCE was reached [175]. However, Sn-based halide perovskite shows poor stability. The decomposition starts just in 2 h after preparation and attains a total decomposition after one day [42].

Chapter 3 - Materials Preparation and Characterisation

3.1 Introduction

In this chapter, preparation of photoactive materials, hole and electron transport materials, and bottom and top electrodes for fabrication of the solar cells in this thesis will be explained. This will include details of experimental techniques used to characterise the photoactive polymer, halide perovskite, and photoactive polymer-perovskite composite materials.

In this thesis, three different configurations and photoactive materials were employed. The first photoactive layer is P3HT that is blended with PCBM in the bulk heterojunction-based solar cells. The second photoactive layer is halide perovskite of methylammonium lead iodide in PCBM-based planar heterojunction solar cells. The third photoactive layer is a composite of methylammonium lead iodide perovskite and photoactive polymer PTB7 in PCBM-based planar heterojunction solar cells. Typically, the active layer is sandwiched between two electrodes in all three solar cells architectures. The first electrode should be at least semi-transparent, which allows sunlight passing through to reach the photoactive layer.

Usually, indium doped tin oxide (ITO) or fluorine doped tin oxide (FTO) are used and the opposite electrode is typically a thin film of metal including aluminium, silver, gold, etc.

3.2 Materials preparation and properties

3.2.1 Photoactive materials for polymer solar cells

The bulk heterojunction structure was used to fabricate solution-processed polymer solar cells. The photoactive layer consists of a blend of the conjugated polymer poly (3-hexylthiophene) (P3HT) as the electron donor and a small molecule material (fullerene derivatives) of PCBM semiconductor as the electron acceptor. The P3HT has been broadly used in a variety of applications including solar cells, OLEDs and transistors [176]. The mixture of P3HT:PCBM has attracted a significant attention in the last decade [177]. The performance of polymer solar cells relies on the quality of the crystallinity and the regioregularity of the polymer [178]. Amongst various conjugated polymers, P3HT is notably recognised to exhibit a high degree of crystallinity and displays comparatively excellent charge transport properties [179]. In turn, the crystallinity of the photoactive layer is linked with the regioregularity of the conjugated polymer. In many cases, P3HT is observed to have more than 90% regioregularity, which increases the level of crystallinity of the active layer.

Some other factors such as the weight ratio between the donor and the acceptor, the type of solvents used, the thermal annealing treatment, and the thickness of the photoactive layer have significant impact on the performance of OPV devices [180]. Among the fullerene additives, PCBM is considered as one of the most attractive variants, which has been widely used as the electron acceptor. This is due to its solubility in chlorobenzene, which subsequently enables the use of solution-processed method to deposit the active layer.
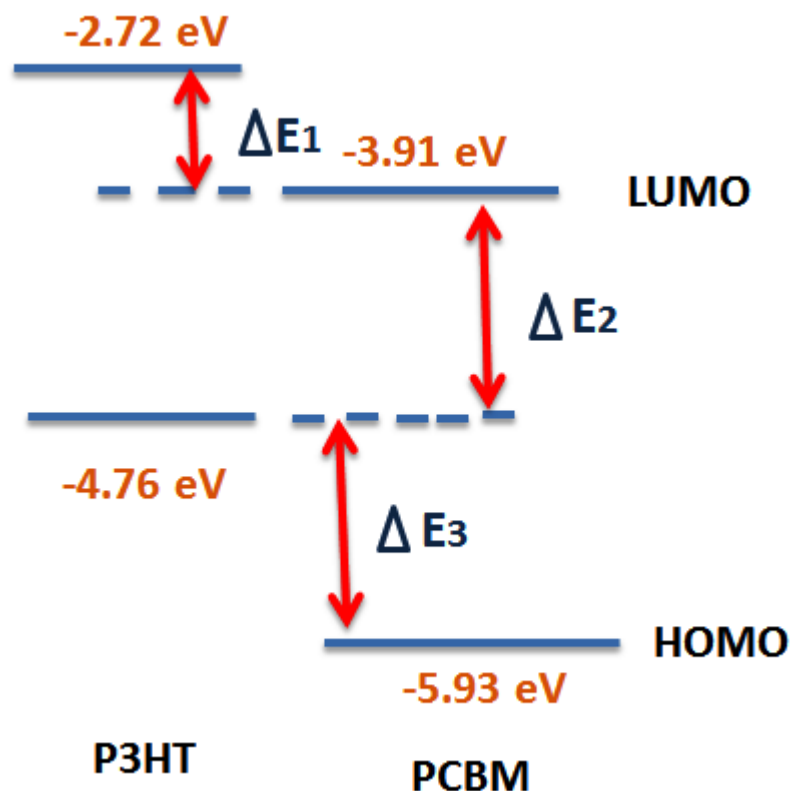
Figure 3.1 The energy level of P3HT:PCBM [177]

Furthermore, the blending of P3HT:PCBM is shown to absorb photons in the wavelength range of 380-670 nm, implying that the exciton in the active layer is generated by the absorption of photons with energies between 2.0 and 3.3 eV [177]. Figure 3.1 illustrates the energy levels of P3HT:PCBM. In order to achieve an efficient charge separation in the solar cells, the HOMO and LUMO of the donor must be 0.2-0.3 eV larger than the HOMO and LUMO of the acceptor [177]. In the case of a smaller or larger offset, it may be difficult to acquire an effective charge separation as most of the energy will dissipate [177]. However, when the energy of photons is higher than 2.0 eV, a small proportion will be absorbed by the photoactive layer of P3HT:PCBM and 70% of the remaining energy of photons will be wasted in heat [43]. Therefore, in order to minimise the loss of energy as much as

possible, doping the donor and acceptor components is crucial to the assembly process.

3.2.1.1 Preparation of polymer photoactive layers

P3HT used in the current research was purchased from Merck (Lisico) and has a regioregularity of more than 94%. PCBM was purchased from Solenne BV and has a purity of 99.5%. 30 mg concentration of the blend with an equal molar ratio of P3HT to PCBM was dissolved in 1 mL of chlorobenzene and stirred overnight on a hotplate. The mixture was then filtered by the 0.45 μm PTFE filter to remove large particles.

3.2.2 Photoactive materials of halide perovskites for solar cells

Methylammonium halide perovskite ($MAPbI_3$) was selected as the photoactive layer for the PCBM-based planar heterojunction solar cells. This type of material has attracted great deal of attention due to some unique characteristics that distinguish it from other solar cell materials. It has a narrow band gap of ~1.55 eV, outstanding performance of high efficiency, and ability to harvest a high number of the incident photons from the visible range up to 800 nm [85]. The methylammonium halide perovskite consists of two main materials: lead iodide (PbI_2) and methylammonium iodide (MAI). The PbI_2 powder was purchased from Sigma-Aldrich while the MAI salt was synthesised in our lab according to the procedure described later in this chapter.

$MAPbI_3$ thin films were fabricated via two deposition methods: i) (OSSCM), and ii) (TSSCM). In OSSCM, PbI_2 was firstly mixed with MAI using appropriate solvents such as DMF or dimethyl sulfoxide (DMSO). In TSSCM, PbI_2 in DMF solvent was firstly applied on top of HTMs, and then MAI in the IPA solvent was applied onto

the pre-coated PbI$_2$ film, followed by thermal annealing at 100°C for a period of time to complete the reaction and thus the perovskite thin film was produced. Figure 3.2 shows the energy level of the perovskite structure. MAPbI$_3$ acts as a donor material which has a HOMO at -5.43 eV and a LUMO at -3.93 eV, respectively. PCBM was used as an acceptor material in the planar heterojunction PV structures with a HOMO at -6.0 eV and LUMO at -4.2 eV.
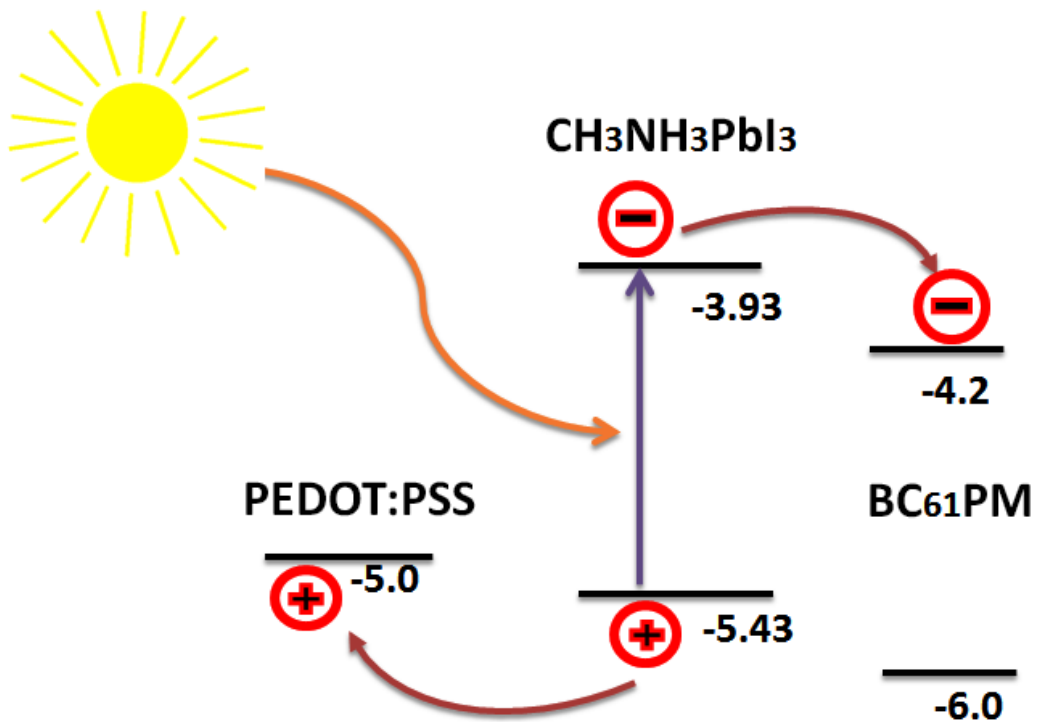
Figure 3.2 Energy level of perovskite structure [181]

3.2.3 Photoactive polymer-perovskite composite for solar cells

A novel composite photoactive layer is used to fabricate organic-inorganic hybrid solar cells. The composite consists of methylammonium halide perovskite MAPbI$_3$ and PTB7 polymer. Figure 3.3 shows the energy levels of the photoactive polymer-perovskite composites. Similar energy levels were used for the MAPbI$_3$ and PCBM, while PTB7 polymer is shown to act as a donor in addition to MAPbI$_3$ and has a HOMO at -5.3 eV and LUMO at -3.5 eV respectively.
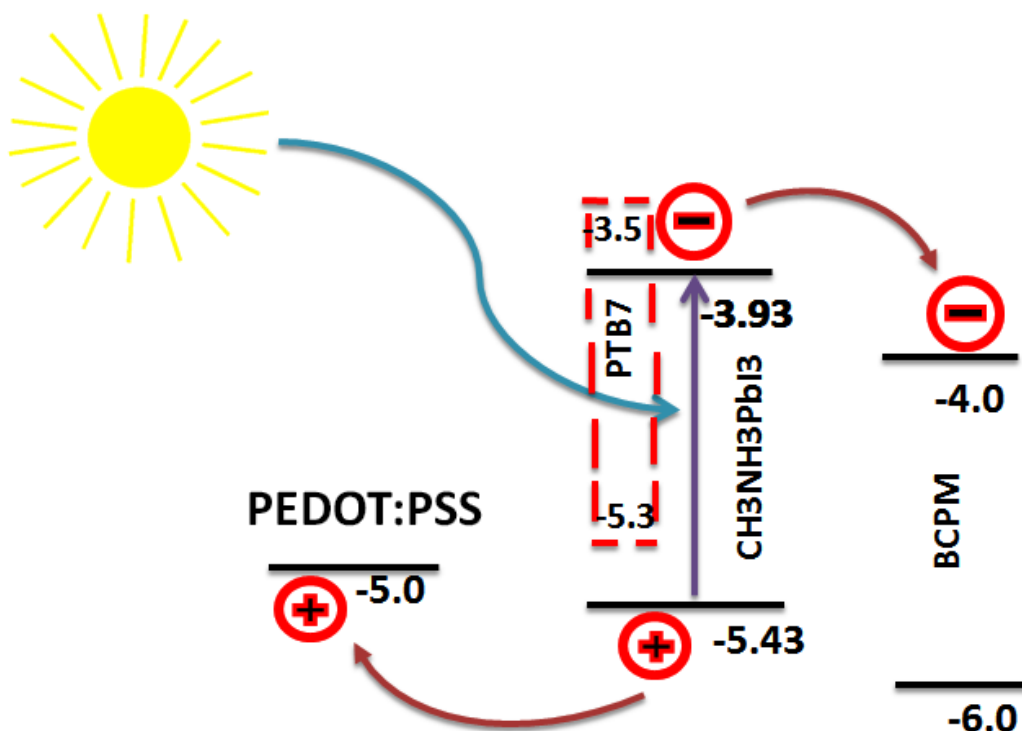
Figure 3.3 Energy levels of the photoactive polymer-perovskite composite

3.2.3.1 Preparation of perovskite materials

MAI was synthesised in the ambient atmosphere at room temperature via the chemical reaction of 27 ml methylamine solution (CH_3NH_2, 40 wt.% in methanol, TCI) with 30 ml of hydriodic acid (HI 57 wt.% in water, Aldrich) in a round bottomed flask. This process was carried out at 0°C in an ice bath for two hours. The methylamine solution was added first into the round-bottomed flask and then hydroiodic acid (HI) was dropwise added in during stirring. White precipitate of MAI was collected after the mixture in the solution was transformed into a rotary evaporator and heated at 50°C for one hour. The white precipitate was washed three times with diethyl ether and finally dried in vacuum for 24 h.

The PbI_2 solution was prepared by dissolving 1 mole PbI_2 in 1 ml DMF solvent and then 20 μl of DIO was added into the solution to promote the dissolution of PbI_2.

The PbI$_2$ solution became clear after continuous stirring at 70°C overnight as shown in Figure 3.4.
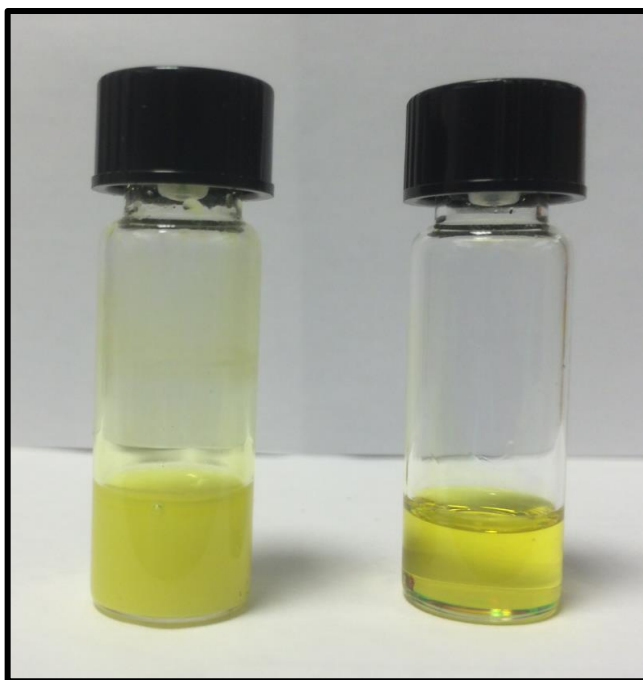
Figure 3.4 PbI$_2$ solution; left) before adding DIO, right) after adding DIO

3.2.4 Electron transport layer

Electron transport materials play a critical role in the polymer and perovskite solar cells allowing for the transport of electrons and blocking of holes. The ohmic contact aligning between the LUMO of the donor material and the electron collecting electrode is an essential factor which impacts on the transport and collection of the electrons. Furthermore, the high electron affinity is required to facilitate the pathway of electrons proficiently and to stop holes transport in the photovoltaic devices [52,182]

In the polymer PV devices, ZnO thin film was chosen as the electron transport material due to numerous beneficial features, such as high transparency, high electron mobility, and wide bandgap. Moreover, the ZnO film can be fabricated by

the sol-gel solution method, which has the potential of providing a highly wetting surface and good adhesion with the photoactive layer of the polymer [183].

In the pure perovskite and photoactive polymer-perovskite composite devices, PCBM was used as the electron transport material. PCBM is a prominent competitor as an alternative to TiO_2 in the perovskite's solar cells due to its simple fabrication process, enabling it to be deposited in a normal environment at low temperatures [93]. Furthermore, PCBM has a high electron affinity and high degree of solubility in chlorobenzene, dichlorobenzene, and chloroform, which allows the film to be deposited by the solution-based processing techniques of the spin- or dip- coating method.

3.2.4.1 Preparation of ZnO and PCBM solutions

The sol-gel method was used to prepare the ZnO colloid solution. 0.1 M of the precursor zinc acetate dihydrate was dissolved in 2-methoxyethanol. Ethanolamine was then added into the solution in order to adjust the pH value to less than 7. The molar ratio of Zinc acetate to ethanolamine is at 1:1. The solution was then stirred for 1 hour in air. The fullerene derivative [6,6]-phenyl-C61-butyric acid methyl ester (PCBM) is broadly utilised as an acceptor material in solar cells by either blending PCBM with P3HT in the polymer solar cells or depositing as a separate thin film on top of the perovskite film in the planar heterojunction perovskite solar cells. Two diffrenet concentrations of PCBM (30 mg and 40 mg) were dissolved in 1 ml chlorobenzene and stirred on a hotplate at 70°C for 2 hours, and then the solution was filtered using 0.45 µm PTFE filter to obtain very high purity PCBM solution.

3.2.5 Selection of the cathode buffer layer

Bathocuproine (BCP) was selected as the cathode buffer layer. The main benefit of inserting the cathode buffer layer between the acceptor material and the cathode is to enhance the extraction and collection of the negative charge carriers [112]. Furthermore, (BCP) plays a key role in providing protection to the photoactive layer and contributing to obtain ohmic contact with the top electrode [74]. Theoretically, the low work function electrode is required to extract the negative charge carriers in the inverted structure. However, high work function electrodes such as Au can also effectively provide electrons extraction layer in many cases [112].

3.2.5.1 Preparation of the cathode buffer layer (BCP)

To prepare a solution-processed bathocuproine buffer layer, 2 mg (BCP) was dissolved into 1 mL methanol and then sonicated for 10 minutes. The solution was then stirred for 30 min on a hot plate at 40°C followed by passing the solution through the 0.45 µm PTFE filter to obtain a pure BCP solution.

3.2.6 Hole transport laye

Different HTMs have been used in the polymer and perovskite solar cells such as MoO_3, V_2O_5, PEDOT:PSS and spiro-MeOTAD. In the perovskite-based solar cells, spiro-MeOTAD is a common material which has been widely utilised as the hole transport material. However, the complicated processes for the synthesis of the material leads to a very high commercial cost [117].

The selected hole transport material in this thesis is PEDOT:PSS for all configurations due to its highly valued advantages of low-cost, ease of applying as thin film, superb transparency, chemical stability and high hole conductivity [76]. PEDOT:PSS was employed between the active layer and the opposite electrode. The

essential factor of the hole transport layer (PEDOT:PSS) is that the material's energy levels are suitable to facilitate the holes transport and blocks the electrons transport. An efficient hole transport layer should produce an ohmic contact with the electrode and match the Fermi level of the donor to enhance the transport of holes and effectively block the passage of electrons.

In this thesis, PEDOT:PSS was applied on top of the blend of P3HT:PCBM and at the bottom of the perovskite layer or the composite perovskite/PTB7 layer, respectively. The PEDOT:PSS can be uniformly deposited on the ITO-coated glass substrate. However, it is hard to obtain a uniform thin film of PEDOT:PSS on the top of the P3HT:PCBM film due to hydrophobic feature of the blend film. Different treatments were utilised to overcome this issue in order to deposit uniform film; these are i) adding a surfactant [184], and ii) using co-solvents [185].

3.2.6.1 Preparation of PEDOT:PSS

Poly(3,4-ethylenedioxythiophene): poly(styrene sulfonate) (PEDOT:PSS) (1.3-1.7 wt% in water) was purchased from Ossila which has a work function of ~ 5.1 e V. The PEDOT:PSS solution was filtered using 0.45 μm PVDF filter before use in order to remove any large-sized particles. Different surfactants (e.g., Triton or Zony) were added to the PEDOT:PSS solution at 1% X-100 in volume to enhance the wettability of the hydrophobic blend film in the photoactive layer [186]. Dip- and spin- coating methods were respectively utilised to fabricate the thin films of PEDOT:PSS, followed by the thermal annealing at 140°C for 15 min.

3.2.7 Electrode materials

In this thesis, all fabricated devices were applied onto glass substrates coated with indium tin oxide (ITO) thin film. Indium tin oxide (ITO) is one of the most broadly used materials as an anode or cathode [12], with the work function of ITO at - 4.8 eV. Au (with the work function of -5.1 eV) is used as the top electrode in this thesis. The PVD sputtering coating technique was used to deposit the thin film of Au on the PV cells.

3.2.8 Cleaning procedure

Indium-tin-oxide (ITO) coated glasses were cut into small slides of 2×2.5 cm^2. The etching process was used to pattern the ITO-coated glasses by applying a mixture of Zn powder and hydrochloric acid (HCl). Cleaning the substrates before fabricating solar cells is an essential step to remove any sorts of impurities on the substrates. The patterned ITO substrates were firstly cleaned by the soap solution and washed by deionized (DI) water. Then, the substrates were sonicated separately in acetone and isopropanol for 10 min, followed by washing the substrates by DI water. Finally, the substrates were blown dry using N$_2$. The same procedure was applied to clean any other glass substrates for materials analysis using SEM, AFM, UV-Vis FTIR and PL.

3.3 Characterisation methods

3.3.1 Characterisation of the PV devices

J-V characterisation was performed under the simulated AM 1.5G irradiation (100 mW /cm^2) using Keithley 2401 sourcemeter under ambient environment. A Schott KG5 colour-filtered Si diode (Hamamatsu S1133) was utilised to calibrate light intensity of the solar light simulator before J-V measurements were carried out. An

aperture of aluminium mask was applied on the PV devices to obtain an active area of 0.04 cm² and to prevent any contribution from externally fallen light on the devices. External quantum efficiency (EQE) spectra were measured by a home-built spectral response measurement set-up. X-ray diffraction (XRD) patterns were obtained using Philips X'PERT MPD with Cu-Kα X-ray source of wavelength 1.54 Å and with operational parameters of 40 kV tube voltage and 40 mA tube current. Scanning electron microscopy (SEM) was used to investigate the morphologies of the perovskite thin films using Nova Nano Microscopic instrument. Reflectance FTIR spectra were recorded in the frequency range of 800-4000 cm^{-1} using Nexus FTIR instruments (Thermo Nicolet Corp, USA) with ATR-FTIR spectrometer. FTIR samples were prepared on the Au-coated glass slides. Atomic Force Microscopy (AFM) images were obtained by Bruker multimode. Steady-state Photoluminescence (PL) spectra were recorded by the Varian cary eclipse fluorescence spectrophotometer upon excitation 400 and 620 nm, separately.

3.3.2 Current-Voltage (I-V) Characterization

One of the most important methods to determine the performance of PV devices is the I-V characterization. The measurements were carried out by employing source meter and a solar simulator. I-V curves of the investigated devices will be drawn as a result of applying different values of voltage within a specified range and recording the corresponding current values. Tests are conducted either in the dark or under illumination in order to derive the PV device parameters, including V_{oc}, I_{sc}, FF, serious resistance, shunt resistant, and PCE as shown in Figure 3.5.
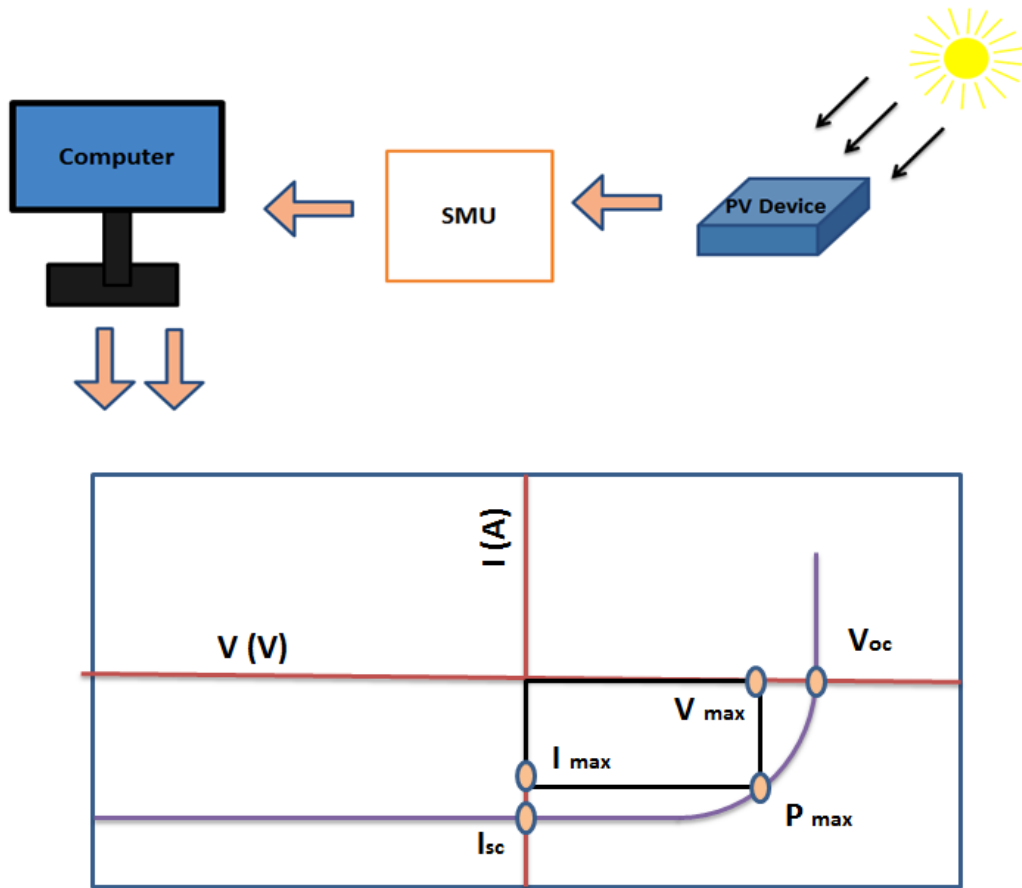
Figure 3.5 Experimental setup for I-V characterisation of solar cells

Standard conditions were applied to test the performance of the PV devices in the I-V characterisation; i.e. one sun of the irradiance of 1000 W/m² and air mass of 1.5, at temperature of 25 C°.

The maximum power of solar cells (P_{max}) corresponds to the product of ($V_{max}.I_{max}$) as shown in Figure 3.5.

The power conversion efficiency (PCE) of solar cells is defined as the ratio between the maximium electric power delivered by the solar cell and the power of incident light with a given active area [12] :

$$PCE = \frac{(I.V_{max})}{P_{light}*A} = \frac{V_{oc} * I_{sc} *FF}{P_{light} *A} \quad \ldots\ldots\ldots\ldots\ldots (1)$$

where fill factor (FF) is defined as

$$FF = \frac{(I.V_{max})}{V_{oc} * J_{sC}} \dots \dots \dots \dots \dots \dots \dots \dots (2)$$

where V_{oc} is the open circuit voltage, I_{sc} is the short circuit current, and P_{light} is the intensity of incident light.

3.3.3 Atomic Force Microscopy (AFM)

AFM was used to identify the surface topography of the materials with high resolution using tapping mode. In this type of sample scanning, a sharp probe is installed on the cantilever of the tip taps over the surface of the sample during scanning. The cantilever tip is stimulated to oscillate near the resonance frequency (~300 kHz). Different distances between the tip and the surface of the sample recorded changes in the surface topography as shown in Figure 3.6.
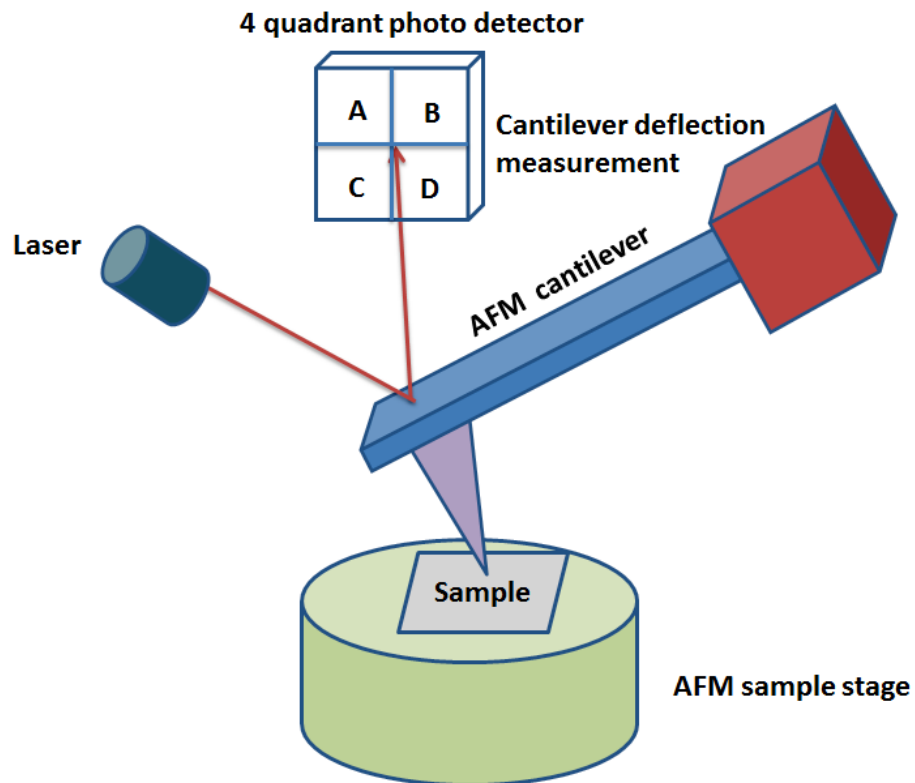
Figure 3.6 Schematic diagram of the atomic force microscopy (AFM)

Analytic software was then used to analyse those variations which are measured by the photodetector. Several types of operation modes have been used in AFM including the contact mode where the probe contacts the surface constantly and the tapping mode where the probe intermittently taps the surface or the probe hovers over the surface. The tapping mode is widely used in AFM characterization due to its high resolution and sample protection (friction causes damage in other modes).

3.3.4 Scanning Electron Microscope (SEM)

The scanning electron microscope has been used to form a significantly magnified image with great visibility and high resolution of the surface morphology of specimens. In this instrument, as shown in Figure 3.7, the electron gun located at the top of the SEM instrument produces a beam of electrons by heating the metallic filament of tungsten. This beam of electrons vertically moves down through electromagnetic lenses. When the beam hits the sample, electrons and X-rays are dispersed and ejected from the sample and are then collected by the detector. The detector converts these electrons into signals which are sent to the computer and finally the SEM image is obtained. SEM operates inside a vacuum chamber using high-energy electron source (2-25 KV). The samples were coated by a thin film of Au to eliminate surface charging.
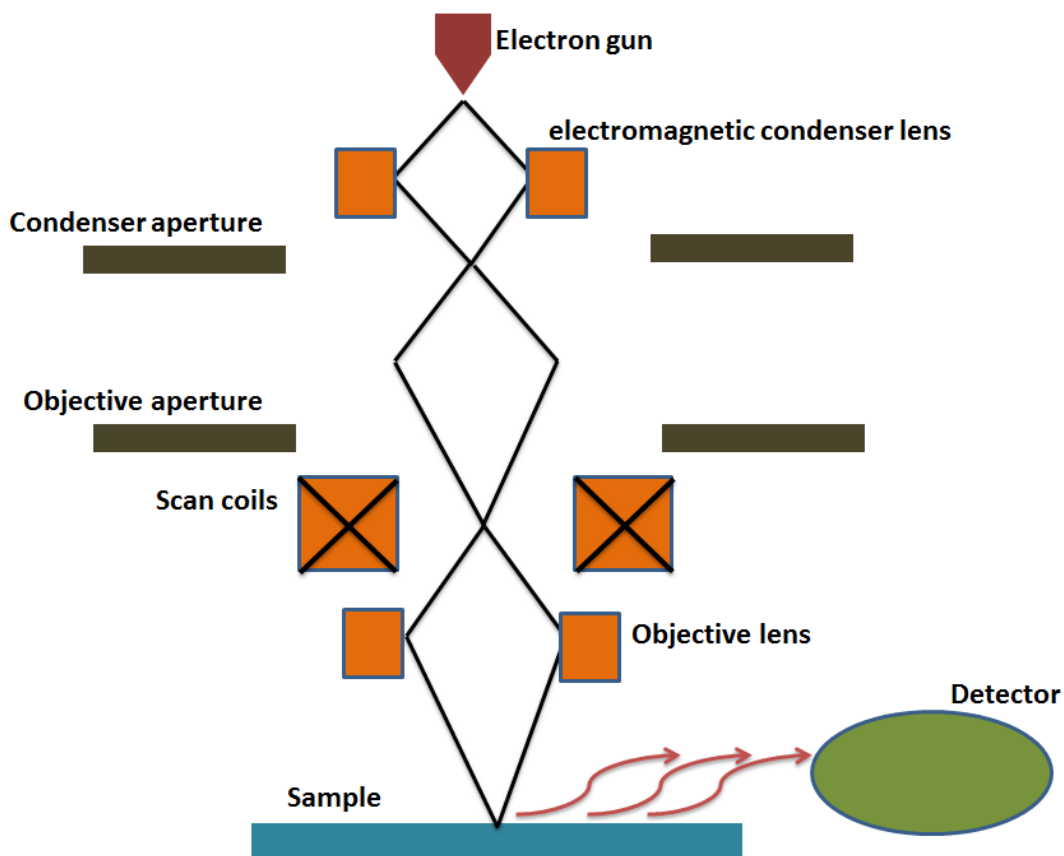
Figure 3.7 Schematic diagram of the principle of SEM

3.3.5 UV-Vis Spectroscopy

UV-Vis spectroscopy is one of the oldest techniques that contribute to identify the organic structure, orientation and ordering structure of molecules. Commonly, organic molecules and halide perovskite absorb light in the spectral region between ~ 300-800 nm. The photons energy might be absorbed by molecules in specific units or quanta units, that is compatible with the energy difference between HOMO and LUMO levels. Light absorption usually happens when the light radiation falls on the active layer with sufficient energy to cause electron transition from the bonding σ, π and the nonbonding (n) orbitals to the antibonding σ^* and π^* orbitals respectively as shown in Figure 3.8 [187].
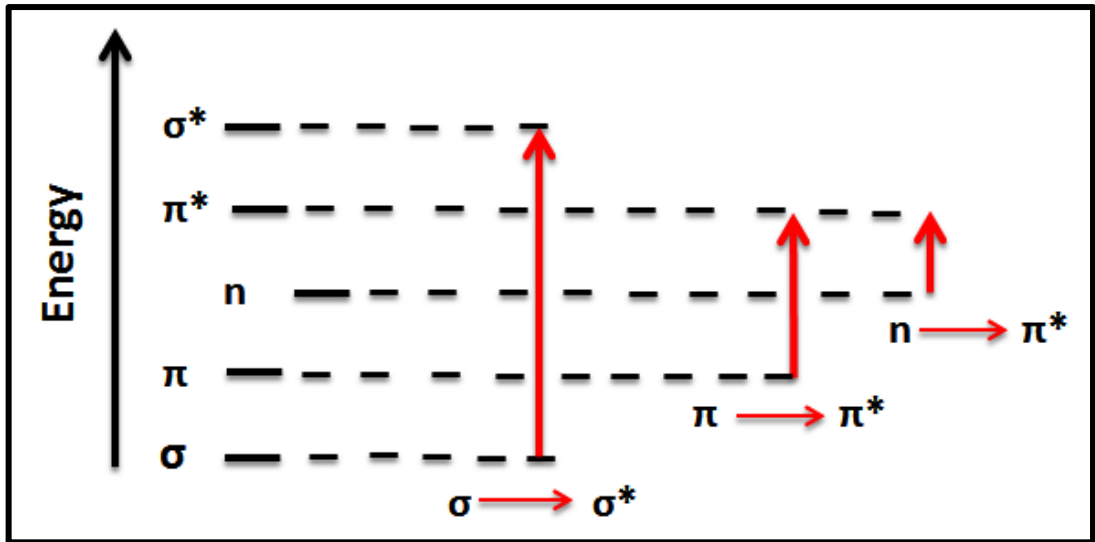
Figure 3.8 Schematic diagram of electronic transition level

There is a widely used formula regarding absorption and transmittance (T) which is the Beer-Lambert's law. It depicts that the absorption of incident light when passes through a medium is proportional to the thickness of the medium. It's intensity decreased exponentially in the formula [187,188]:

$$I = I_o \, e^{-\alpha x} \text{ ... ...(3)}$$

or

$$ln \, {}^{I_o}/_I = \alpha x \text{ ....(4)}$$

where I_o is the intensity of incident light, I is the intensity of light after passing through the sample at a thickness x, α is a constant (absorption coefficient) as shown in Figure 3.9.
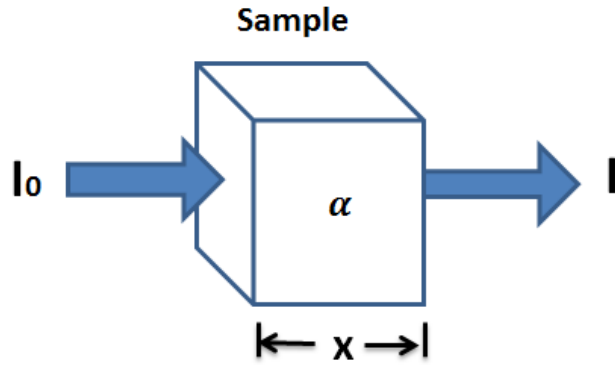
Figure 3.9 Graphical illustration of the Lambert-Beer law

When using common logarithms (base10), equation (3) will become:

$$I = I_o \times 10^{-kx} \ldots\ldots\ldots\ldots\ldots\ldots\ldots\ldots.(5)$$

or

$$\log {I_o}/{I} = kx \ldots\ldots\ldots\ldots\ldots\ldots\ldots\ldots..(6)$$

where k= α/2.303 is the extinction coefficient. Beer's law depicts that the absorption is proportional to the concentration of the medium, where k = εC, ε is the extinction coefficient for unit concentration (L mol^{-1} cm^{-1}), c is molar concentration (mol /L), and x is path length of the sample (cm). By combining Lambert's and Beer's law, the new formula is

$$A = \log {I_o}/{I} = \varepsilon cx \ldots\ldots\ldots\ldots\ldots\ldots\ldots\ldots..(7)$$

The logarithm term (${I_o}/{I}$) is known as absorbance (A), which is plotted in the UV-spectrum versus to the wavelength (λ).

The concept of the absorption method can be summarised by shedding monochromatic light through the surface of the film and collecting the corresponding data of the transmitted light. Consequently, we can calculate the absorption of light at each wavelength. The working principle of UV-Vis spectrum is shown in Figure 3.10
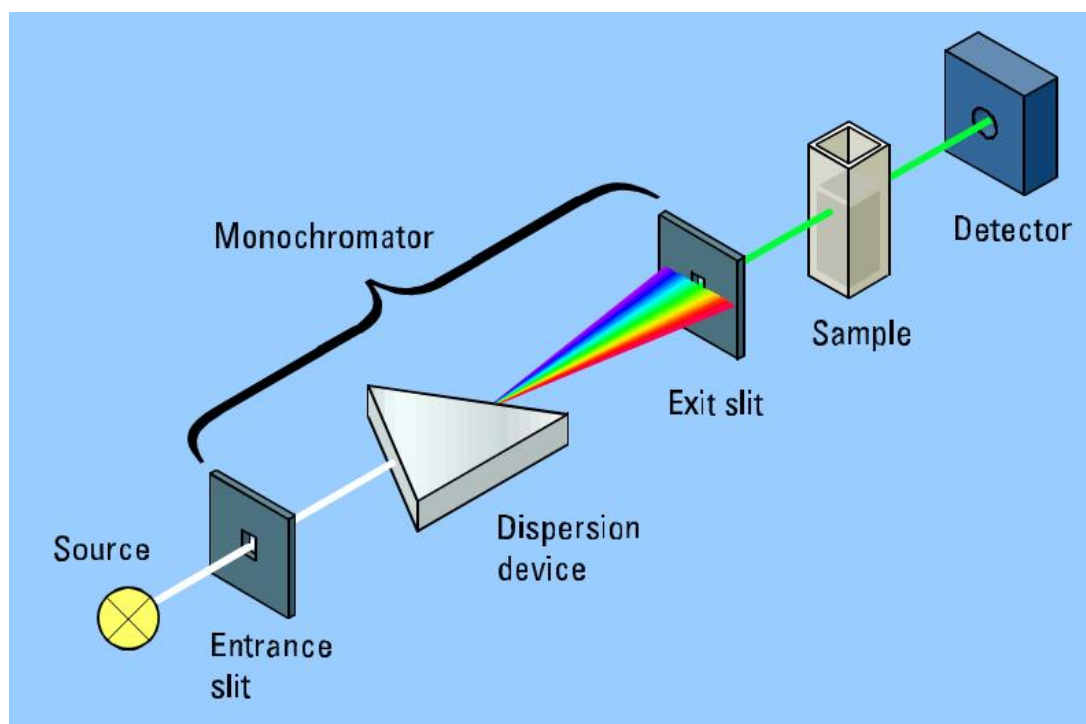
Figure 3.10 The principle of UV-Vis spectroscopy

3.3.6 Photoluminescence (PL)

Photoluminescence spectroscopy is a contactless and non-destructive technique for the study of the electronic structure of materials. The photo-excitation process caused by absorption of incident photons by the electrons within the sample, which results in exciting the electrons to higher electronic state and then the surplus energy will release by emission of light or luminescence [189].
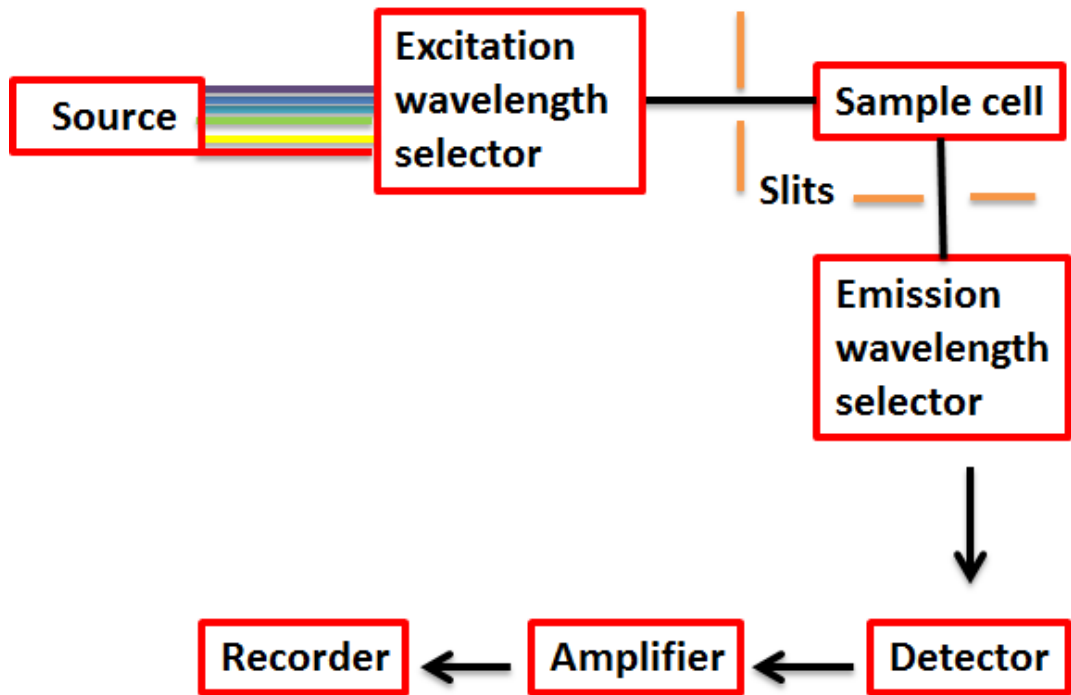
Figure 3.11 Schematic diagram of the photoluminescence setup

The phenomenon of photo-excitation is identified as photoluminescence, and it is schematically described in Figure 3.11. This technique is usually utilised to determine the performance of the excited charges splitting up at the interface among the donor and acceptor materials [190]. In the case of interface between perovskite and PCBM, once the donor material absorbs photons, it will release lights via the photoluminescence procedure. When the acceptor materials applied on top or mixed with the donor, a quenching of photoluminescence occurs indicating that many excitons are separated to free charges. As the separation ratio of free charges increases, quenching of photoluminescence will increase. Further, quenching of photoluminescence will take place as a result of applying the HTL and ETL to the photoactive layer [106].

3.3.7 X- Ray Diffraction (XRD)

One of the most familiar techniques for the characterisation of crystallinity of materials is the non-destructive XRD technique. Figure 3.12 shows the principle of X-ray diffraction measurements. A diffraction pattern which is produced by diffraction from different planes contains information about internal structures of the materials, degree of crystal orientations, phases and average grain sizes [191]. XRD peaks have been produced after overlapping of a monochromatic beam of x-rays dispersed at a specific angle for each lattice plane of the sample [192]. The peak intensities are identified through distribution of atoms inside the lattice planes. The number of peaks depends on the structure of the material. For instance, single crystal (one orientation in structures) will produce only one peak in the diffraction pattern while the polycrystalline samples which contain many differently oriented crystallites will produce many peaks [193].
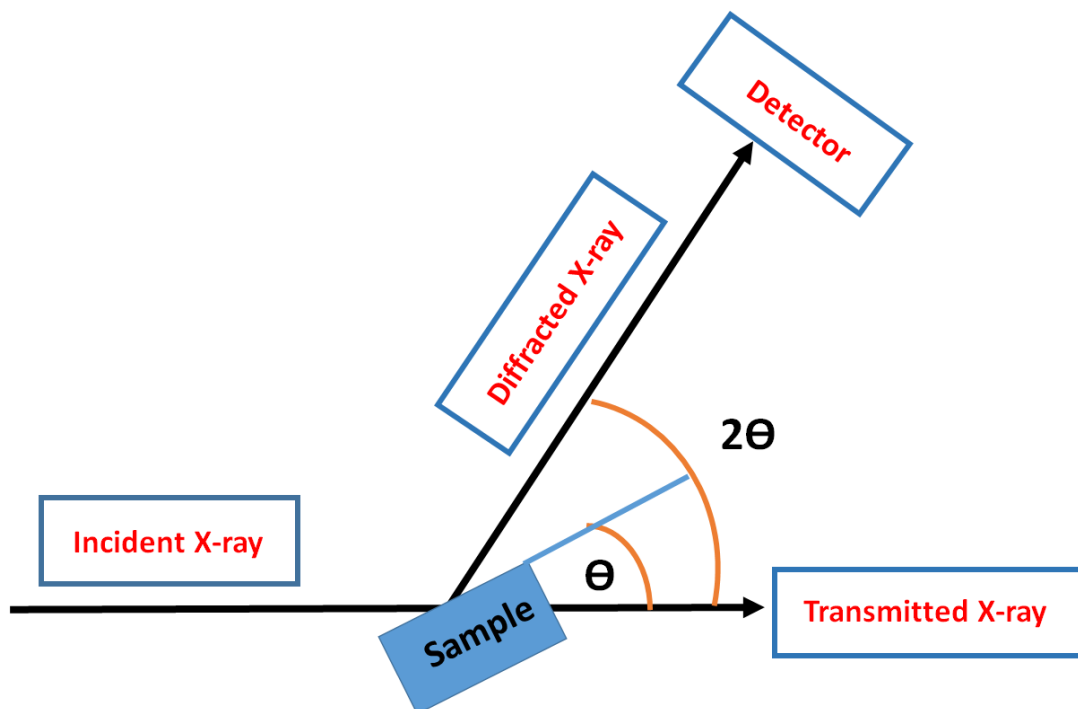
Figure 3.12 Schematic diagram of the X-ray diffraction measurement system

Figure 3.13 schematically demonstrates the Bragg's law of diffraction. Bragg's law is typically used to determine the required conditions for diffraction, as described by the following equation [194]:

$$n\lambda = 2d\sin(\Theta)\ldots\ldots\ldots\ldots\ldots\ldots\ldots(7)$$

where, n is an integer (1, 2, 3), λ is the wavelength of the X-rays, Θ is the angle between the incident rays and the surface of the crystal, and d is the spacing between layers of atoms.
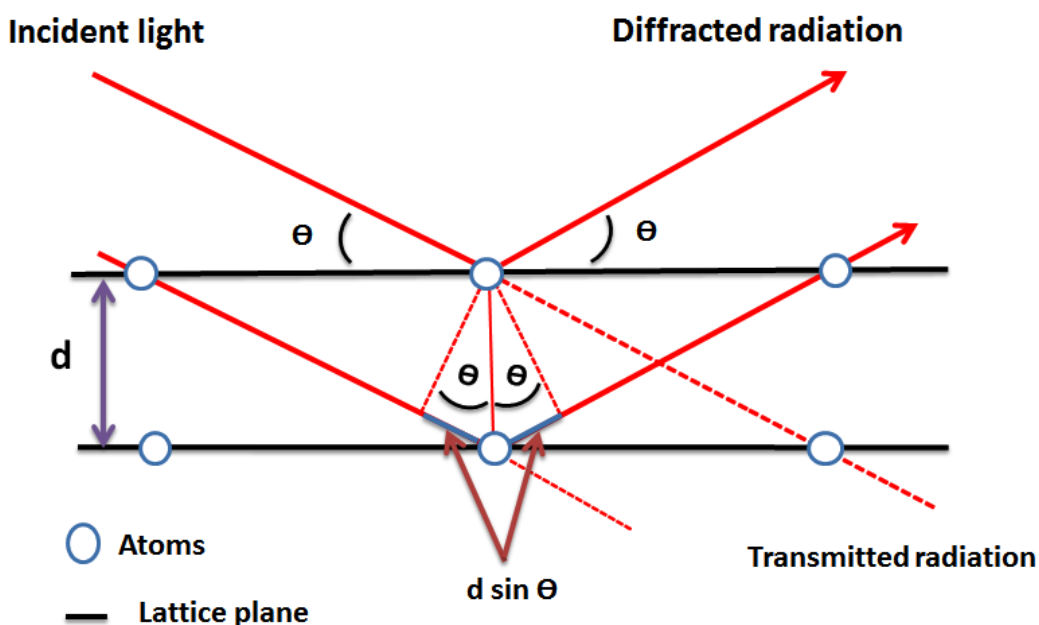
Figure 3.13 Schematic diagram of Brag's law of diffraction

3.3.8 Fourier transform infrared spectroscopy (FTIR)

Infrared spectroscopy is a beneficial characterisation method which is widely used to identify the compound structure of organic or inorganic materials. The process of infrared spectroscopy is similar to that for UV-vis spectroscopy in the absorption measurement except it works in the infrared region as illustrated in Figure 3.14 [52]. When the sample's irradiated by the infrared light, the absorbed spectrum can be

analysed by linking a specific characteristic frequency to the functional group and therefore determining the composition of the sample [52].

The infrared spectroscopy measurements can take place using absorption, emission, and reflection. Infrared spectroscopy is a technique which depends on the vibrations of the molecules as its energy is not adequate to induce electron transitions from the valence band to the conduction band. Alternatively, infrared photons excite vibrational and rotational motion in the molecules [195]. Typically, an infrared spectrum is attained by passing the infra radiation through the substrate and then identifying the portion of the incident radiation which is absorbed at a specific energy. The energy at any position of peak in the absorption spectrum refers to the frequency of the vibration of an element of the sample molecule [195].
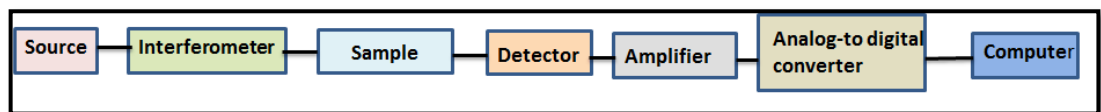
Figure 3.14 Schematic diagram of the Fourier transform infrared spectroscopy

3.3.9 External quantum efficiency

The external quantum efficiency is the proportion of charge carriers gathered by the solar cell to the quantity of photons of a given energy incident on the solar cell. Consequently, both the absorption of photons and the collection of free charges play an important role in determining the external quantum efficiency. Electron-hole pairs which are created as a result of absorbing incident photons by the PV active layer. This pair should be separated to free charges and then collected by the corresponding electrodes to reduce the possibility of recombination. Charge recombination will cause reduction in the external quantum efficiency(EQE) [177]:

$$EQE = ŋ_A \cdot ŋ_{Diff} \cdot ŋ_{Diss} \cdot ŋ_C \quad \ldots\ldots\ldots\ldots\ldots\ldots (7)$$

where, $ŋ_A$ is the efficiency of the incident photons absorption, $ŋ_{Diff}$ is the efficiency of the photo-induced exciton diffusion at heterojunction, $ŋ_{Diss}$ is the efficiency of the exciton dissociation at the heterojunction and $ŋ_C$ is the efficiency of charge carrier transport and collection at the electrodes.

In addition, the internal quantum efficiency (IQE) is defined as the proportion of charge carriers gathered by the solar cell to the quantity of photons of a given energy incident on the solar cell and absorbed by the cell. The transmitted and reflected lights are out of consideration to calculate the IQE [196]

$$IQE = \frac{EQE}{1-R-T} \quad \ldots\ldots\ldots\ldots\ldots\ldots\ldots\ldots\ldots\ldots\ldots .(8)$$

where, R is reflectance and T is the transmittance.

Chapter 4 - Fabrication of P3HT:PCBM heterojunction solar cells by the dip-coating method

4.1 Introduction

The solution-processable photovoltaic devices (SPPDs) mainly, including dye-sensitized TiO2 [197], quantum-dot nanoparticles [14], organic semiconducting polymers [198], and very recently perovskites [16] represent great opportunities and advantages of simple fabrication, cost effectiveness, devices on flexible substrates, and large area devices by the roll to roll (R2R) technology [17–19] or other simple solution manufacturing methods [199]. The solution-processed methods may be classified as spin-coating, spray-coating, dip-coating, doctor-blading, screen (or ink-jet) printing methods, etc. [73,200]. Spin coating is one of the most efficacious techniques and has been widely used in laboratories for fabrication of SPPDs due to its advantages of ease of use and high-degree of regularity for film forming. In the fabrication of SPPDs, spin coating is the most commonly used method as reported in the published literature. Nevertheless, there is a significant limitation to the spin-coating method that is it is only suitable for small-scale fabrication or small area devices, and is not compatible with the commercial applications for large-scale devices. Other methods have their advantages and drawbacks [18].

The spray-coating method needs precise control on the nozzle and the liquid droplets may splash onto the previously coated areas affecting the properties of the photovoltaic (PV) devices [69].

The doctor-blading or the printing methods can easily realise the R2R manufacturing of PV devices. However, their disadvantages could include complicated chemistry of ink formulations and contact effects when the latter layer is applied on the previously formed film [69].

The dip coating method has its own features and potential to be used as a promising alternative for fabricating large area SPPDs on industrial scale. Historically, the dip-coating process is a very old technology of producing sol–gel thin films, which was invented by Jenaer Glaswerk Schott & Gen. in 1939 for silica films [72]. A schematic diagram is shown in Figure 4.1 for the dip-coating process. The substrate is pulled vertically from the coating bath at a constant speed (V_ρ). The entrained liquid by the moving substrate splits into two at the free surface (point S in Figure 4.1) in a viscous boundary layer, returning the outer layer to the bath. When the upward moving flux is balanced above the stagnation point S due to evaporation of the solvents, a continuing and position-stable film is formed with respect to the coating bath surface.
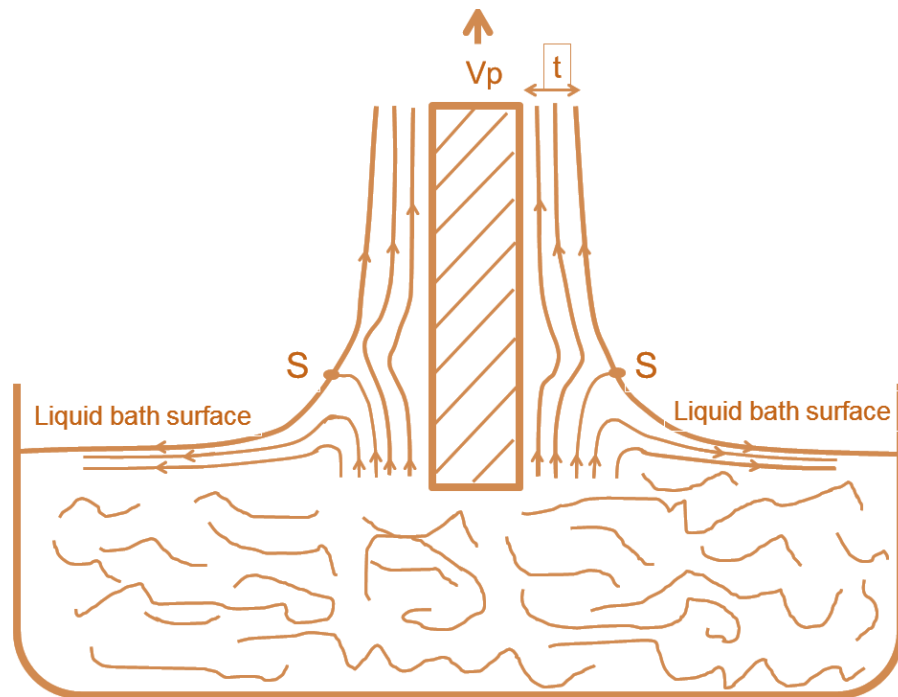
Figure 4.1 Schematic diagram of the dip-coating technology

Within the drying process, the colloids are progressively concentrated by evaporation, leading to aggregation, gelation, and final drying to form a type of a dry gel or xerogel film. When the substrates' speed (V_ρ) and liquid viscosity (n) are low, e.g. in the case of the sol–gel coating,

the thickness of the wet film can be written as:

$$t = [0.94(n \times V_\rho)^{2/3}]/[{\gamma_S}^{1/6}(p \times g)^{1/2}] \ldots\ldots\ldots\ldots\ldots\ldots (1)$$

Where γ_S is the liquid–vapour surface tension, p is the liquid density and g is the acceleration of gravity [201]. Dip-coating process is a simple high productivity technique with a high accuracy to deposit a uniform film on a large-scale area. Nowadays, many commercial optical functional sol–gel thin films on glass have been manufactured by the dip-coating method with a large area of several square metres. Moreover, the dip-coating method owns the advantages of significantly reducing the amount of wasted materials during the processing and the potential capability of depositing two PV devices at the same time. Polymer photovoltaic devices (PPVs) have attracted considerable interests in the last decade due to their potential advantages of the solution-processable manufacturing. Power conversion efficiency (PCE) has increased after bulk heterojunction (BHJ) structures were introduced in the devices [31], where the donor (organic polymers) blends together with the accepter (fullerene derivatives) in a thin combined film placed between the electron transport layer (ETL) and the hole transport layer (HTL) that are connected to the electrode layers separately. In the past few years, 8% PCE has been obtained in a single BHJ device using the new low band gap material [202–205]. Very recently, the PCE achieve a giant leap up to 11.5% for the single BHJ [21].

Although these significant achievements have pushed the technology of PPVs further towards the application of commercial products, there are still huge challenges to be overcome with much effort including large area high-PCE devices and long-term stability of the devices.

Dabirian *et al*. investigated the properties of the dip-coated PCBM [206]. Xue *et al*. produced bundles of P3HT nanorods by using the dip-coating method [207]. Hu *et al*. has published a study to deposit the active layer of PPV devices in the conventionally structural devices [208].

In this chapter, we report the deposition of all layers except the electrodes in the inverted PPVs by dip-coating technology. The blend of the active layer based on the chlorobenzene-dispersed P3HT:PCBM has been modified and transformed it into a sol–gel-like solution by adding petroleum ether. Figure 4.2 shows a gel of the P3HT:PCBM blend with a high concentration of petroleum ether after stored in a closed bottle in the glovebox for two days. The blend can also form a gel much faster with the evaporation of chlorobenzene than that it is stored in the closed environment, which is compatible with the use of the dip-coating process in order to fabricate a uniform active layer for PPV devices. The dip-coating method has also been used to produce the ETL and HTL layers. Efficient devices with a PCE around 3.4% were obtained. This exploration demonstrates that the dip-coating method has its own potential and advantages to be used as an industrial scale method for fabrication of all layers of SPPDs.

Figure 4.2 Photos of the P3HT:PCBM blend: left) a gel formed from the modified blend; right) the liquid blend of the unmodified P3HT: PCBM in chlorobenzene

4.2 Experimental

4.2.1 Material preparation for the PPV devices

ITO coated glasses were bought from Vision Tek system. Ltd., (UK) with sheet resistance of (12–15 $\Omega/\square$). The ZnO thin film was selected as the ETL layer, which was prepared according to the procedure in section (3.2.4.1). The solution for the active layer was obtained by adding P3HT:PCBM (at the ratio of 1:1) into the chlorobenzene solvent. The blend was then stirred and heated overnight at 70°C. Petroleum ether was then added into the P3HT:PCBM chlorobenzene solution, enabling to form the sol–gel-like blend for the dip-coating of the active layer. The ratio of chlorobenzene to the petroleum ether was kept below 1:1 in volume to avoid the immediate formation of the particulate gel at room temperature. The concentration of the P3HT in the whole mixed solvent was 15 mg/ml. The PEDOT:PSS thin film was used as the HTL layer. To improve the compatible property of the aqueous PEDOT:PSS solution for the dip-coating, 2-propanol was added to modify the aqueous PEDOT:PSS solution. The volumetric ratio between PEDOT:PSS and 2-propanol was at the ratio of 10:2. To further improve the wettability of the aqueous PEDOT:PSS solution to the P3HT:PCBM layer, 1% Triton X-100 in volume was added into the final PEDOT:PSS solution.

4.2.2 Fabrication of PPVs by the dip-coating process

Pre-structured ITO-coated glass substrates with the size of 20 x 25mm were cleaned by soap water and then washed by deionised (DI) water. After N_2 blow dry, the samples were ultrasonically cleaned in acetone and 2-propanol separately and then followed by N_2 blowing them dry. Figure 4.3 illustrates a schematic diagram of the fabrication process of polymer solar cells via the dip-coating processes.
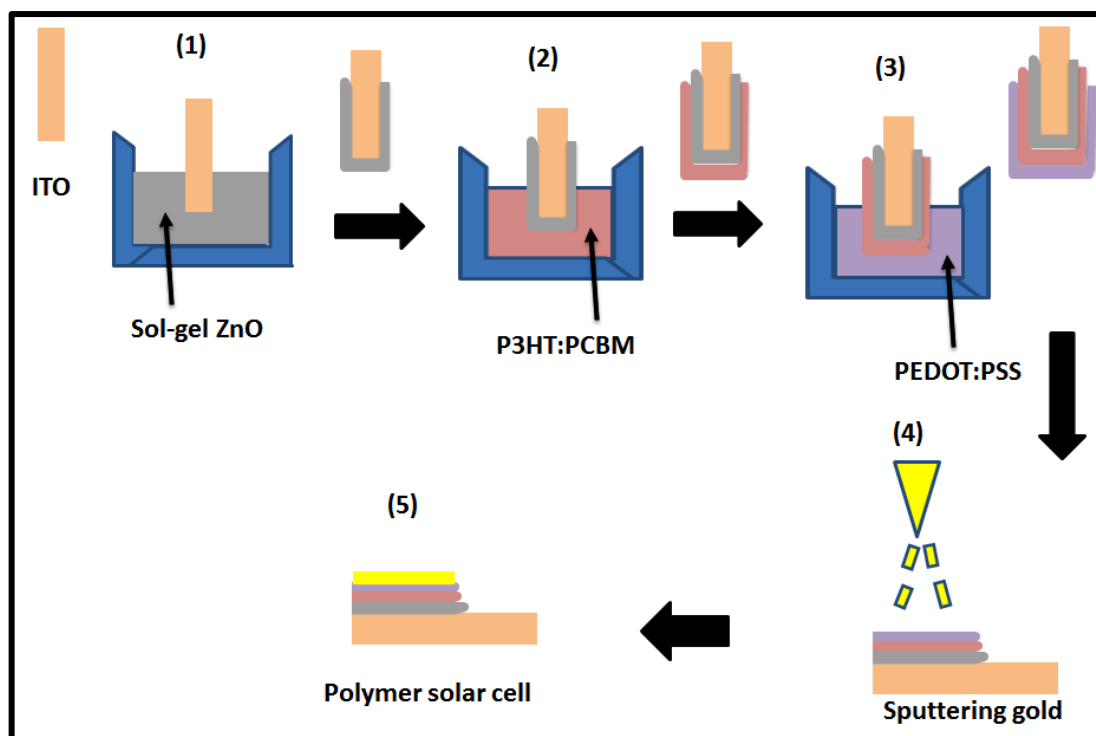
Figure 4.3 A schematic diagram of the fabrication processes for P3HT:PCBM solar cells via the dip-coating method

The cleaned ITO coated slides with more than half of its area was immersed in the modified solution of ZnO-based sol for 10 sec, then withdrawn at the rate of 20 mm/s. The sol– gel ZnO coated sample was heated on a hot plate at 150°C for 5 min and then at 250°C for another 5 min. The ITO glass coated with the ZnO layer was then immersed in the modified solution of the active layer for 15 sec and then pulled out at the rate of 21 mm/s. Two different drying methods were carried out for the active layer. In one method, the dip-coated sample was kept for a period of time over the top of the container containing the evaporated solvent, which extended the drying time. In the other method, the dip-coated sample was quickly removed out of the container and then was kept drying in the normal ambient environment which led to a faster drying rate. The drying process was observed by monitoring the colour change of the film until a purple colour appeared. The active layer was either un-annealed or annealed at 140°C for 5 min in the glovebox. Finally, the device was submerged into the 2- propanol diluted PEDOT:PSS aqueous solution for 15 sec, then

91

withdrawn at the average rate of 7 mm/s and cured at 140°C for 15 min. Finally top Au electrode layer was fabricated by vacuum deposition method as the positive electrode.

4.2.3 Formulations of the photoactive, electron transport and hole transport layers

In this experiment, different attempts were undertaken to optimise the solutions of the photoactive layer, electron transport layer and hole transport layer, in order to effectively deposit the uniform films by the dip-coating method as shown in Tables 4.1, 4.2, and 4.3 respectively. In the first-stage of experiment, various concentrations of methanol were added separately or also with 2-propanol into the 30 mg P3HT: PCBM blend within 1mL chlorobenzene. In this instance, the withdrawal rate was fixed at 21 mm/sec resulting in non-uniform films.

Table 4-1 Parameters used to modify the formulation of P3HT:PCBM by the dip-coating method

Formulations of the active layer P3HT:PCBM	Withdraw rate	Solvent additive	Results
30 mg of P3HT:PCBM/1 mL chlorobenzene	21 mm/sec	1 mL of Methanol	non-uniform film
30 mg of P3HT:PCBM/1 mL chlorobenzene	21 mm/sec	1.5 mL of Methanol	Non-uniform film
30 mg of P3HT:PCBM/1 mL chlorobenzene	21 mm/sec	1 mL of Methanol +0.75 mL 2-prpoanol	Non-uniform film
30 mg of P3HT:PCBM/1 mL chlorobenzene	21 mm/sec	1 mL of Methanol +1 mL 2-prpoanol	Non-uniform film
30 mg of P3HT:PCBM/1 mL chlorobenzene	21 mm/sec	0.5 mL of Petroleum ether	Slightly improved
30 mg of P3HT:PCBM/1 mL chlorobenzene	21 mm/sec	0.75 mL of Petroleum ether	Slightly improved
30 mg of P3HT:PCBM/1.5 mL chlorobenzene	21 mm/sec	0.75 mL of Petroleum ether	Slightly improved
30 mg of P3HT:PCBM/ 2 mL chlorobenzene	21 mm/sec	0.75 mL of Petroleum ether	Slightly improved
30 mg of P3HT:PCBM/ 2 mL chlorobenzene	21 mm/sec	1 mL of Petroleum ether	Slightly improved
30 mg of P3HT:PCBM/ 2 mL chlorobenzene	21 mm/sec	1.5 mL Petroleum ether	Slightly improved
30 mg of P3HT:PCBM/ 2 mL chlorobenzene	21 mm/sec	1.9 mL of Petroleum ether	Homogeneous film

Thereafter, petroleum ether with various concentrations was added into the P3HT:PCBM chlorobenzene solutions. A homogenous photoactive layer of P3HT:PCBM was achieved after 1.9 mL of this solvent was then introduced into the blending process.

Additionally, in order to form thin films of PEDOT:PSS using the dip-coating method, the withdraw rate was fixed at 7 mm/sec and 10 μl of triton was added to the 1 mL PEDOT:PSS to enhance the surface wetting.

Table 4-2 Parameters used to modify the formulations of PEDOT:PSS by the dip-coating method

Formulation of Electron transport layer PEDOT:PSS	Withdraw rate	solvent additive	Results
1 mL of PEDOT:PSS	7 mm/sec	1 mL of 2-propanol +drops of Triton	Many defects
1 mL of PEDOT:PSS	7 mm/sec	1.5 mL of 2-propanol +drops of Triton	Non-uniform film
1 mL of PEDOT:PSS	7 mm/sec	2 mL of 2-propanol +drops of Triton	Non-uniform film
1 mL of PEDOT:PSS	7 mm/sec	0.5 mL of 2-propanol +0.2 μl of NMP +drops of Triton	Slightly improved
1 mL of PEDOT:PSS	7 mm/sec	0.2 mL of 2-propanol 0.2 μl of NMP+ drops of Triton	Homogeneous film

Various concentrations of 2-propanol were added into the PEDOT:PSS solutions. A uniform film of PEDOT:PSS was only achieved when both 0.2 mL of 2-propanol and 0.2 μl of N-Methyl-2-pyrrolidone (NMP) were added into 1 mL of PEDOT:PSS solution.

Furthermore, 20 mL of the prepared sol-gel ZnO was used with a fixed withdraw rate at 20 mm/sec for the deposition of the ZnO film. Various concentrations of Petroleum ether were added to the sol-gel ZnO with or without 0.5 mL of methanol, resulting in different

dewetting degrees of the coating on the substrate. Only a uniform and wetted ZnO film was successfully obtained when 1 mL of the Petroleum ether was introduced to the ZnO solution.

Table 4-3 Parameters used to modify the formulation of the ZnO film by the dip-coating method

Formulation of Electron transport layer ZnO	Withdraw rate	solvent additive	Results
20 mL of ZnO (sol-gel)	20 mm/sec	0.5 mL of Petroleum ether	Dewetted
20 mg of ZnO (sol-gel)	20 mm/sec	0.5 mL of Petroleum ether +0.5 Methanol	Not fully wetted and not uniform
20 mg of ZnO (sol-gel)	20 mm/sec	0.75 mL of Petroleum ether	Still not fully wetted
20 mg of ZnO (sol-gel)	20 mm/sec	1 mL Petroleum ether	Uniform and wetted surface

4.3 Results and discussion

4.3.1 Performance of the PPV devices

Figure 4.4 illustrates the J–V characteristics of three types of devices; i.e. (1) Device A represents the PPV device with the annealed active layer that dried in the ambient air environment; (2) Device B is the PPV device where the active layer dried in the solvent-containing environment inside glovebox but without annealing and then followed applying the PEDOT layer by the dip-coating method; (3) Device C represents the PPV device with the active layer that dried in the solvent- containing environment followed by heat treatment at 140°C inside glovebox before dip-applying the PEDOT:PSS layer.
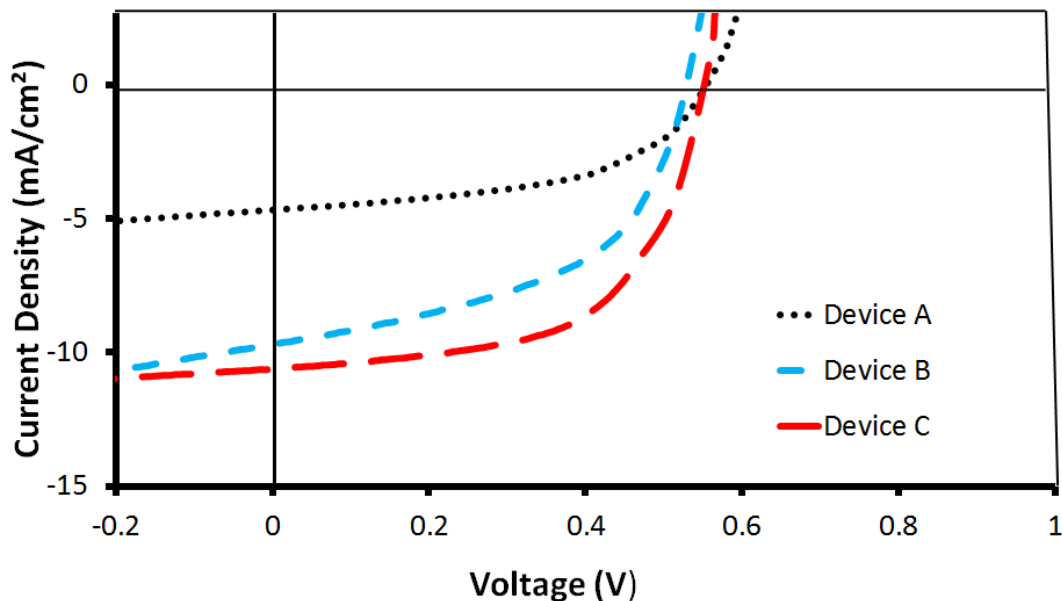
Figure 4.4. J-V characteristics of three types of devices; 1) Device A for the dip-coated active layer dried at the normal air environment; 2) Device B for the dip-coated active layer dried at the solvent-containing environment without annealing; 3) Device C for the dip-coated active layer dried at the solvent-containing environment followed by annealing

Summary of the performance parameters is listed in Table 4.4. Device A exhibits a low PCE of 1.32% mainly because of the low short current density of 4.67 mA/cm^2 and the low fill factor (FF) of 51%. This result is much lower than that of the PPV devices which produced by the spin-coating method inside the glovebox [209].Two potential reasons can be assigned that caused the reduction of PCE; (1) oxidation of the active layer when it dried in the normal air condition compared with those devices produced inside the glovebox; (2) moisture effects on the active layer due to the aqueous PEDOT:PSS solution applied by the dip-coating method. When the active layer was placed in the solvent-containing environment for drying, Device B had an improved PCE of 2.61% due to the significantly increased short current density at 9.7 mA/cm^2. The morphology of the active layer has been altered by the extended drying rate, which enhanced the PCE of PPV devices. The PCE of Device C further reached to 3.46% when the dip-coated active layer was annealed at 140°C before the PEDOT:PSS layer was applied. Heat treatment increased the moisture resistance of the active layer. The enhanced current density and FF are the main reasons for the

improved PCE, reaching 10.61 mA/cm^2 and 59% respectively for Device C. Devices A and B have displayed a close performance in their FF. However, Device A dried in air but annealed at high temperature while Device B dried in the solvent-containing environment without annealing. The interesting results may be worth carrying out further investigation in order to fully understand the reasons behind the different characteristics of the three types of devices.

Table 4-4 Photovoltaic performance of the PPV devices; (1) Device A for the dip-coated active layer dried in the normal air environment; (2) Device B for the dip-coated active layer dried in the solvent-containing environment without annealing; (3) Device C for the dip-coated active layer dried at the solvent-containing environment and followed by annealing

OPV devices	V_{oc} (V)	J_{sc} (mA/cm^2)	FF (%)	PCE (%)
Device A	0.55	4.67	51.0	1.32
Device B	0.54	9.70	49.8	2.61
Device C	0.55	10.61	59.0	3.46

4.3.2 Characterisation of the active layer

Figure 4.5 indicates the UV–Vis absorption spectra of the P3HT:PCBM active layers deposited by the dip-coating technique. The P3HT:PCBM active layer for Device B exhibits little higher light absorption intensity than that for Device A. They all show the characteristic absorbing peaks at around 520, 550, and 610 nm for the P3HT polymer. A light absorption increase was obtained after the dip-coated active layer dried in the solvent-containing environment was followed by the cure at 140°C.
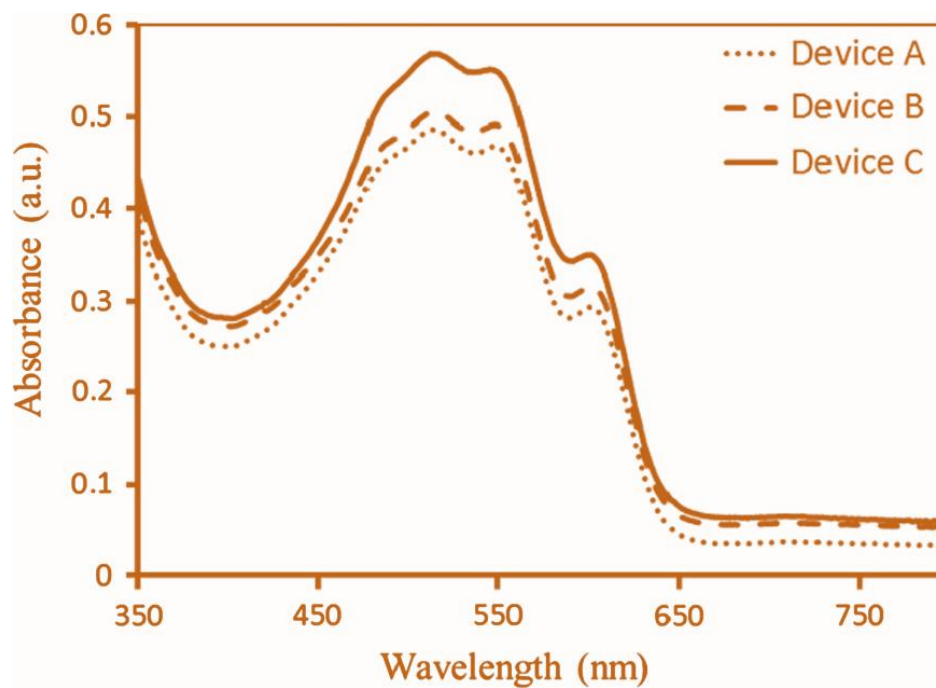
Figure 4.5 Light absorption spectra of the P3HT/PCBM blend of the devices; 1) Device A for the dip-coated active layer dried in the normal air environment; 2) Device B for the dip-coated active layer dried in the solvent-containing environment without annealing; 3) Device C for the dip-coated active layer dried in the solvent-containing environment and followed by annealing

Three peaks, one at 510 and two shoulders at 550 nm and 610 nm separately show the enhanced absorption in comparison with the active layer without the thermal annealing. The increase in light absorption is one of the main reasons that contributes to the increased short current density and hence the PCE for Device C. The X-ray diffraction (XRD) measurements were further performed to characterise the structure of the active layers; the obtained XRD patterns of the P3HT:PCBM films are shown in Figure 4.6.
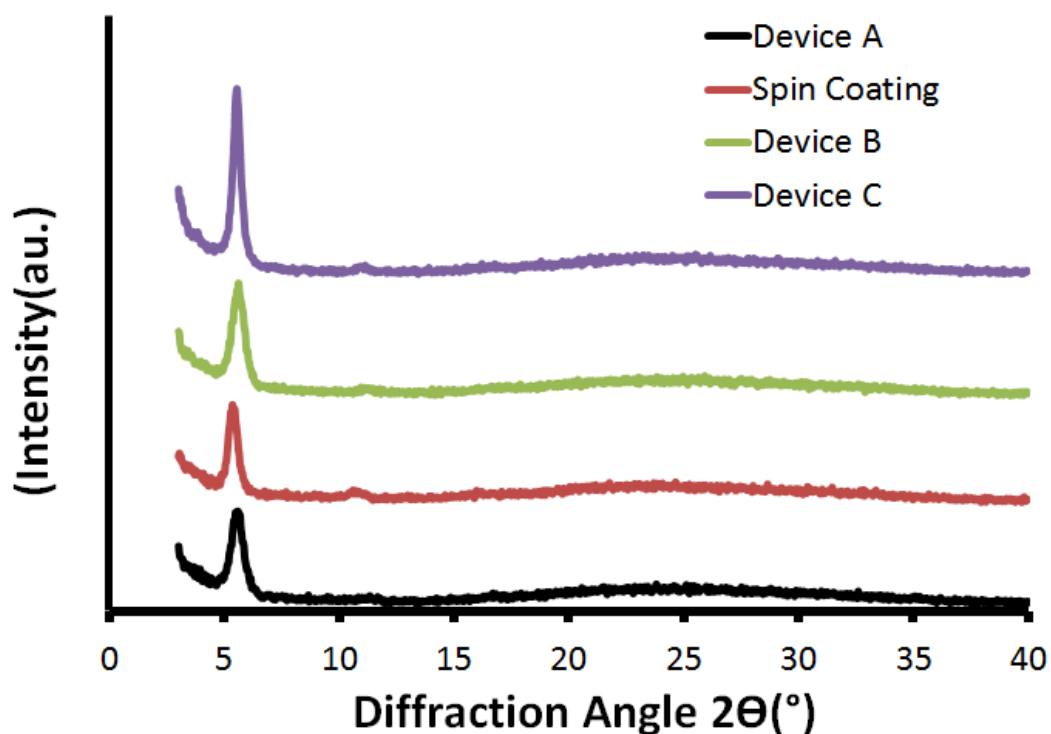
Figure 4.6 XRD patterns of the P3HT:PCBM films; 1) Device A for the dip-coated active layer dried in the normal air environment; 2) spin-coating derived active layer with annealing as a reference ; 3) Device B for the dip-coated active layer dried in the solvent-containing environment without annealing; 4) Device C for the dip-coated active layer dried in the solvent-containing environment and followed by annealing

A strong peak at around 5.40° appears for all types of the P3HT:PCBM active layer fabricated by different methods. The XRD pattern of the active layer by the spin-coating method in the glovebox is also presented in Figure 4.6 as a reference. Device A illustrates slightly smaller intensity of the peak at 5.40° than that of the spin coated sample. As shown in Figure 4.4 since Device A exhibits much lower PCE value than that of the spin-coating derived device, it can be inferred that the reduced PCE could be caused by moisture which results from the following PEDOT:PSS dip-coating. Device B shows increased peak intensity at 5.40° compared with Device A, which confirms that the crystallinity of the active layer was improved by the extended drying rate of the active layer, leading to the increased PCE. The intensity of the diffraction peak of the active layer at 5.40° further increased after heat treatment of device C, demonstrating more oriented structures formed between the inter-chain spacing of the P3HT polymers after the parallel layers that are

associated with the interdigitated alkyl chains. This result corresponds to the increased light absorption and thus improved the PCE of Device C.

4.3.2.1 Morphologies of the active layer

AFM measurements were also carried out in order to investigate the morphologies of the surfaces of the three types of active layers and to better understand the mechanism behind the different performance of the studied PPV devices; the obtained AFM results are shown in Figure 4.7. It appears from Figure 4.7a that the surface of the active layer for Device A is rougher than that of Device B and C when it dried in the normal air condition. The faster drying rate caused the active layer to become solid thin film more quickly. The fast solidification of the active layer did not allow enough time for even distribution within the film, leading to a rougher morphology in comparison with that of Device B and C, as shown in Figure 4.7a. The root mean square roughness derived from the AFM image of the active layer of Device A is 3.71 nm. Active layer of Device B was dried in the environment of organic solvents, which has led slower drying rate. The AFM image of the active layer for Device B shows improved roughness compared to that of Device A as shown in Figure 4.7b. As a result the root mean square roughness in this layer has reduced to 3.31 nm. The extended drying time of the active layer has allowed the interpenetrating networks more mobility to arrange regularly to form a uniform film. Figure 4.7c displays the morphology of the active layer for Device C. Subjecting the active layer to thermal annealing has further smoothed the surface morphology of the active layer. The donor and acceptor were more evenly arranged in the blend and the dense interpenetrating networks have formed. This is evidenced by the reduced z-axis from 26.8 nm in the case of Device A to 18.6 nm for Device C as shown in Figure 4.7c where the root mean square roughness becomes 3.09 nm. AFM images confirm that the morphologies of the active layers have been modified with different processing methods, which has contributed to the improved PCE of the PPV devices.
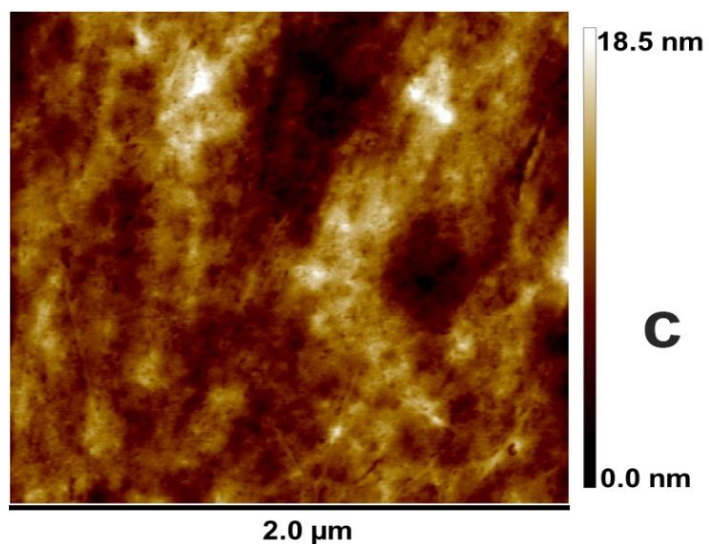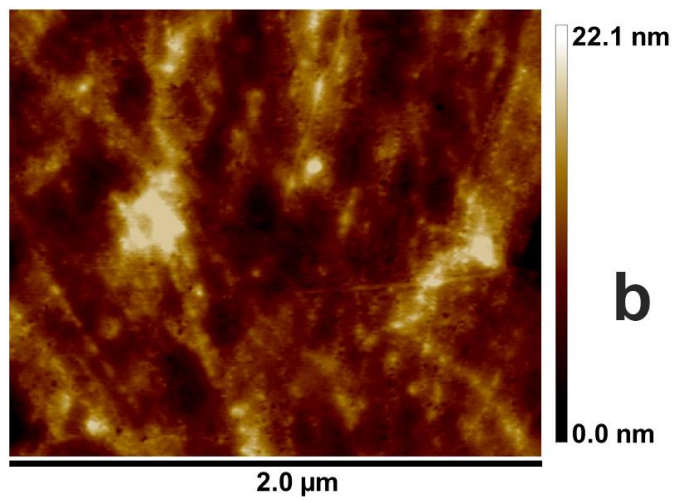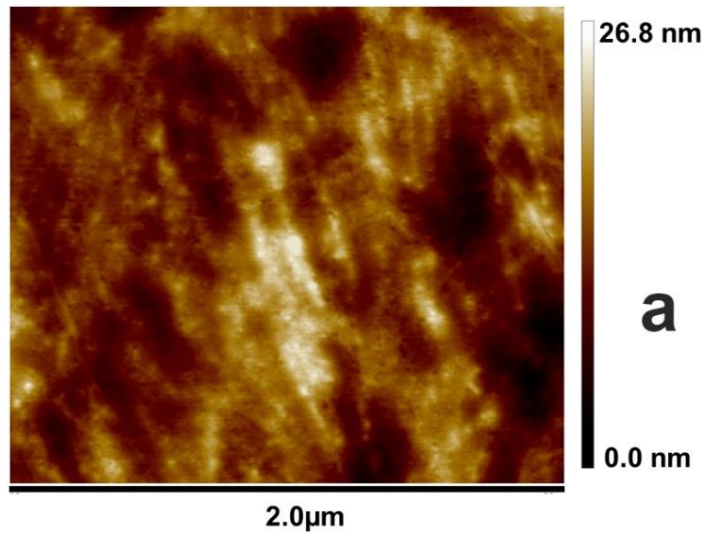
Figure 4.7 AFM images of the active layers for a) Device A; b) Device B; c) Device C

4.3.2.2 Morphologies of HTLs and ETLs

Morphologies of the spin and dip coated ZnO and PEDOT:PSS layer were compared separately using the AFM measurements. The spin and dip coated ZnO and PEDOT:PSS layers shown to exhibit quite different features, as illustrated in Figure 4.8&4.9. The spin-coated ZnO in Figure 4.8a presents a slightly smoother surface as depicted from the height colour changes while the dip coated ZnO thin film in Figure 4.8b shows a smaller-nanoparticles- bonded denser thin film.
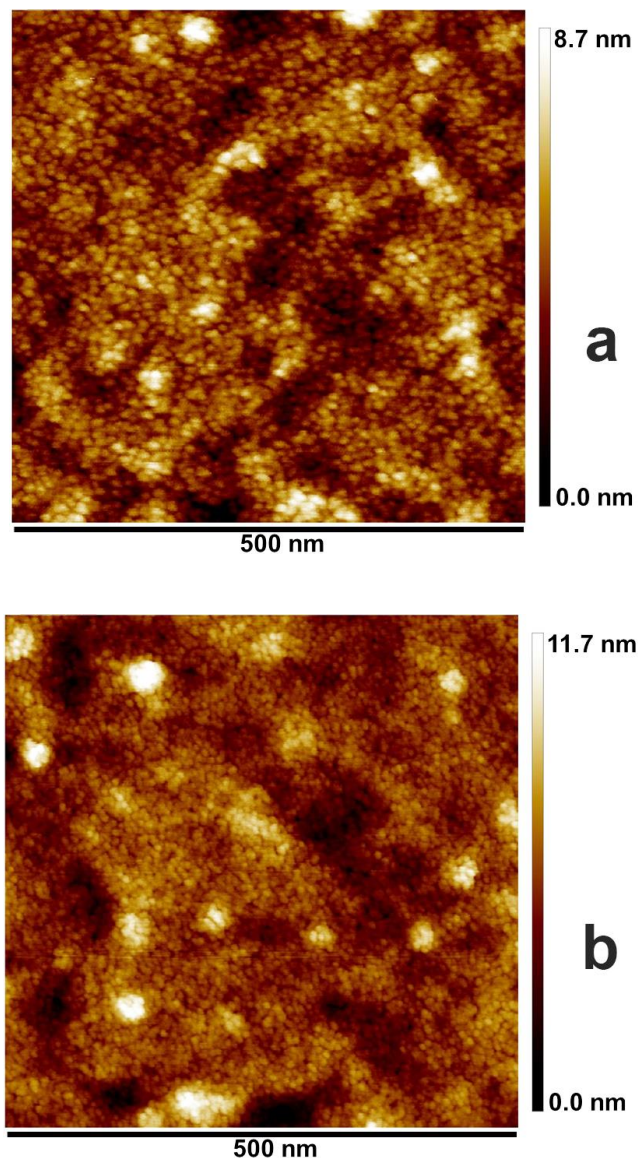
Figure 4.8 AFM images of the ZnO thin films; a) by the spin coating method; b) by the dip-coating method

Compared to the spin-coated ZnO thin film, the dip-coated ZnO thin film had a slower drying rate, which explains the formation of the denser thin film. Both films also show some valleys in height in their morphologies and different sized nanoparticles owing to different formulation of both solutions. Figure 4.9 shows the morphologies of the PEDOT:PSS layers obtained by the two coating methods. In comparison with the ZnO thin film, the spin-coated PEDOT:PSS thin film in Figure 4.9a demonstrates the same smoother surface than the dip-coated PEDOT:PSS layer.
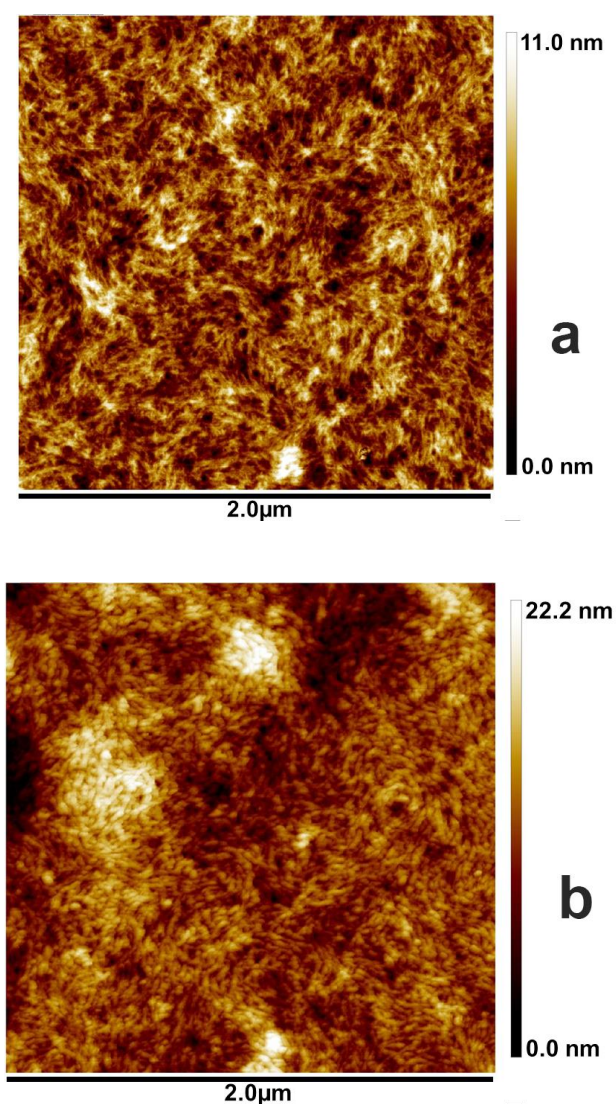
Figure 4.9 AFM images of the PEDOT:PSS thin films; a) by the spin coating method; 2) by the dip-coating method

However, the spin-coated PEDOT:PSS thin film demonstrates a fully different morphology than the dip-coated PEDOT:PSS layer in Figure 4.9b. It appears to exhibit a nano-wire or fibre-like constituted thin film, nevertheless, the dip-coated PEDOT:PSS thin film demonstrates larger sized- nanoparticles formed morphology. The root mean square roughness of the spin-and dip-coated PEDOT:PSS is 1.56 nm and 2.91 nm, respectively. The difference in morphologies of the PEDOT:PSS thin films by different coating methods may affect the charge transport resistance of the PEDOT:PSS HTL.

4.4 Conclusion

Solution processed inverted PPV devices were produced by the dip-coating method. The best P3HT:PCBM inverted PPV device achieved a PCE of 3.4%. The drying method of the P3HT:PCBM active layer significantly affected the performance of the fabricated PPV devices after the sample was withdrawn from the solution. When the active layer dries at a slower rate, it presents smoother morphologies and more oriented structures. Thermal annealing can further improve its surface roughness and also enhance its crystallinity. The aqueous solution of the PEDOT:PSS has its effect on the pre-deposited P3HT:PCBM active layer. The spin and dip-coating PEDOT:PSS thin films present significantly different morphologies owing to different solvents used and different processing which might impact on the performance of the PV devices.

Chapter 5 - Morphological studies of perovskite solar cells

5.1 Introduction

In the past few years, organometal halide perovskite ($CH_3NH_3PbI_3$) has emerged as one of the most prominent candidates for photovoltaic devices due to its distinguished optical and electrical properties [171]. These materials can be fabricated using solution-processing methods at low cost and ease of procedure compared to the Si-based solar cells [133,210–212]. The power conversion efficiency (PCE) of perovskite solar cells has been aggressively approaching that of crystalline silicon solar cells [134]. Very recently, the certified performance of perovskite solar cells dramatically increased to 22.1 %, making them a potential competitor to the Si-based solar cells [213].

Currently, a planar heterojunction structure is widely used to fabricate typical perovskite solar cells via the co-evaporation method or solution-processed deposition method [124]. The expensive fabrication cost and process complexity of the vacuum deposition method [142] lead to broad interests in the solution-processed method. However, one of the biggest challenges that dominates the performance of the solution-processed perovskite solar cells is to control the morphologies of the perovskite films [118]. It is closely linked to many physical properties in solar cells including exciton diffusion length, charge carriers dissociation efficiency, and charge transport to the electrodes [156]. Also, photons absorption efficiency and shunting paths are reliant on the morphology and the quality of the perovskite films [117]. The crystallization behavior of the perovskite films is affected by many factors such as using one-step or two-step methods, the precursor concentrations, additives in the one-step method, thickness of the pre-

coated lead iodide (PbI_2), allowed-reaction-time (Art) between PbI_2 and methylammonium iodide (MAI) in the two-step method before casting the mixture into perovskite thin films, and thermal annealing [118]. Although many efforts have been explored to obtain high-quality perovskite thin films, there are still extensive studies need to be carried out in order to achieve highly reproducible defect-free perovskite thin films.

In this chapter, investigations into control over the morphology of the perovskite films using the low-temperature (TSSCM) were presented. (OSSCM) was also studied for comparison with the TSSCM. The morphologies of the produced perovskite thin films will be demonstrated and discussed in detail. The perovskite films by both methods were characterised using scanning electron microscopic (SEM), UV-vis spectroscopy, and X-ray diffraction (XRD) measurements. Different concentrations of the MAI solutions and different allowed-reaction-times (Art) between PbI_2 and MAI, and various thermal annealing methods were investigated.

5.2 Experimental methods for perovskite films and solar cells by OSSCM

The one-step spinning deposition method (OSSCM) was used to fabricate the perovskite thin film samples for various purposes including study of the produced solar cells properties and crystallisation behaviour of the perovskite films. The PHJ PV structure was schematically presented in Figure 5.1, where it contained thin films of ITO/PEDOT:PSS/$CH_3NH_3PbI_3$/PCBM/BCP/Au, respectively. Pre-structured ITO-coated glass substrates with sizes of ~ 20 x 25 mm were cleaned according to the procedure which was presented in section 3.2.8. The cleaned ITO substrates were spin-coated at 3000 r.p.m by the PEDOT:PSS solution and followed by heating at 140°C for 10 min.
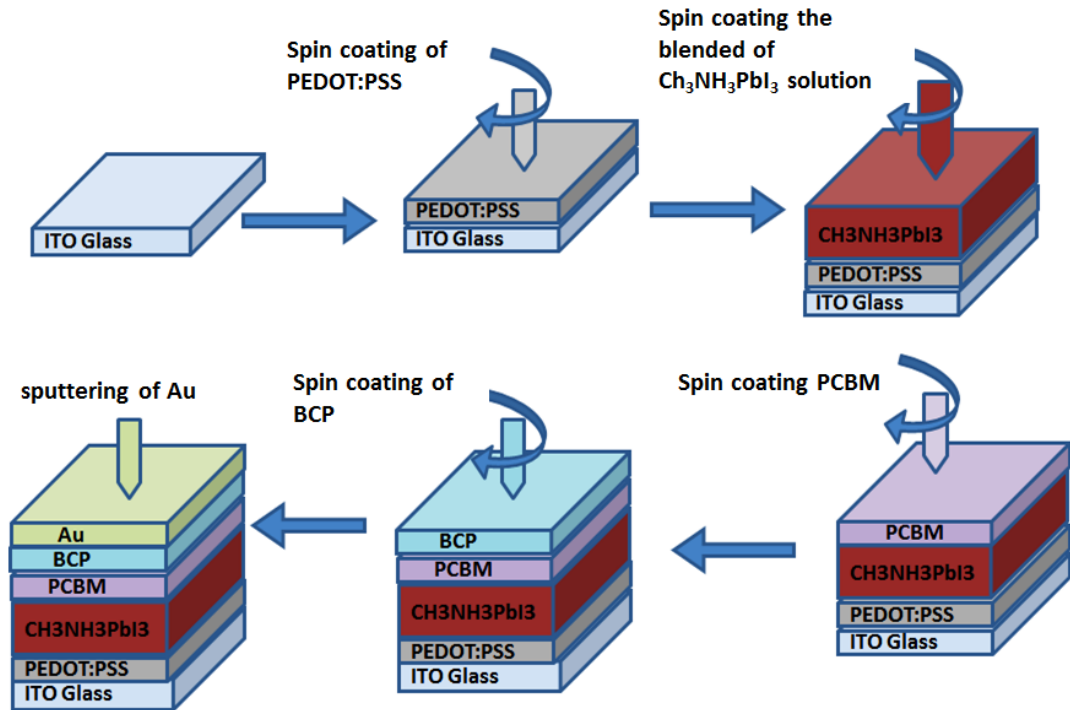
Figure 5.1 Schematic diagram of the fabrication processes of each layer of the perovskite solar cells using OSSCM

The halide perovskite precursor solution was produced by blending lead iodide (PbI$_2$) and methylammonium iodide (MAI) at the molar ratio 1:1 in anhydrous N, N -dimethylformamide (DMF) solvent. Then, 30 μl of the blended solution (PbI$_2$ and MAI) was spun at 5000 r.p.m for 20 sec. The obtained thin films were subjected to heat treatment at 100°C for two hours. The PCBM film was then deposited by the spin-coating method from the PCBM solution on top of the formed perovskite thin film at 2000 r.p.m followed by heat treatment at 100°C for 30 min. A thin film of BCP (~10 nm) was deposited by the spin-coating method on top of the BCPM film as the electron buffer layer prior to the deposition of Au thin film of ~100 nm as the top electrode by the vacuum sputtering method.

5.3 Results and discussion

5.3.1 Morphological studies of the CH₃NH₃PbI₃ film fabricated via OSSCM

The morphology of the $CH_3NH_3PbI_3$ thin film produced by the OSSCM was examined using SEM measurements. Figure 5.2 illustrates porous fabric structures of the perovskite thin films. It was suggested that the porous structure is owing to the prompt reaction between the two precursors of MAI and PbI_2 and a rapid crystallisation of the formed intermediate phase by the subsequent thermal annealing processes[134].
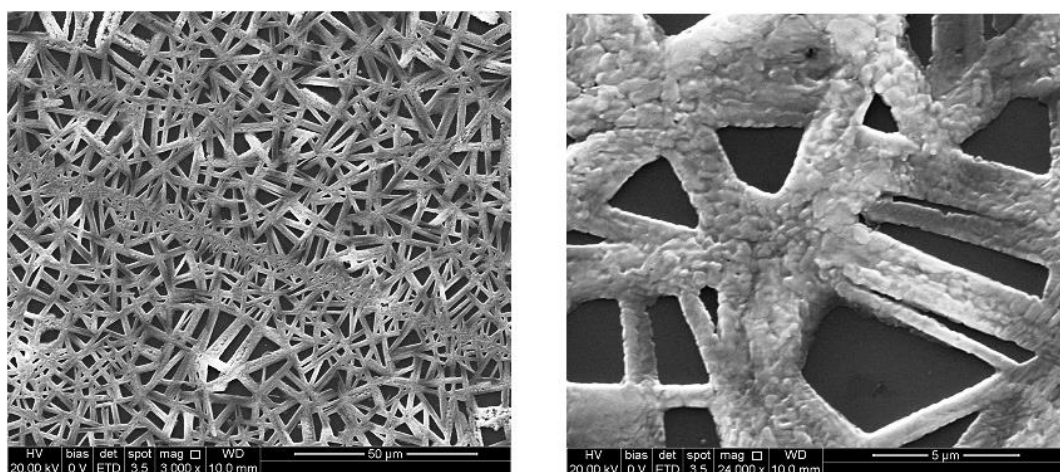
Figure 5.2 SEM images of the perovskite film fabricated via OSSCM

5.3.2 Light absorption and crystal structures of the CH₃NH₃PbI₃ films fabricated via OSSCM

The UV-Vis absorption spectra and X-ray diffraction measurements were carried out to investigate the optical properties and crystal structures of the $CH_3NH_3PbI_3$ thin film obtained by OSSCM respectively. Figure 5.3 shows a typical light absorption spectrum of the obtained perovskite film in the wavelength range 350 to 800 nm. The absorption onset appears at 800 nm which is in agreement with the reported

optical bandgap of ~ 1.52 eV for methylammonium halide perovskite $CH_3NH_3PbI_3$ [80,214,215].
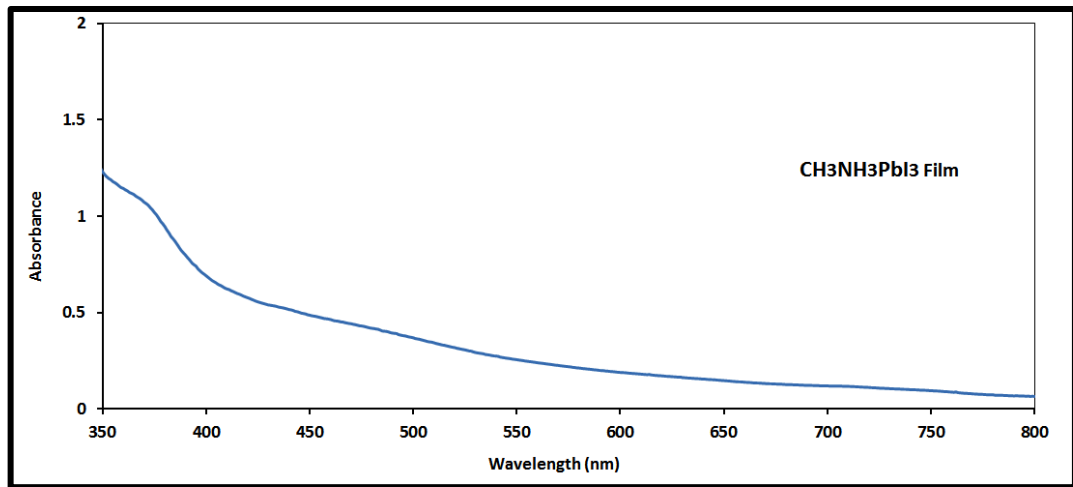
Figure 5.3 UV-Vis absorption spectrum of the $CH_3NH_3PbI_3$ film fabricated via OSSCM

Figure 5.4 shows the X-ray diffraction pattern measured for the $CH_3NH_3PbI_3$ thin film produced by the OSSCM. Two main peaks at 2Θ of 14.2° and 28° in addition to other peaks at 19°, 24°, 31°, 41° and 43° are presented, confirming the formation of the perovskite structure.
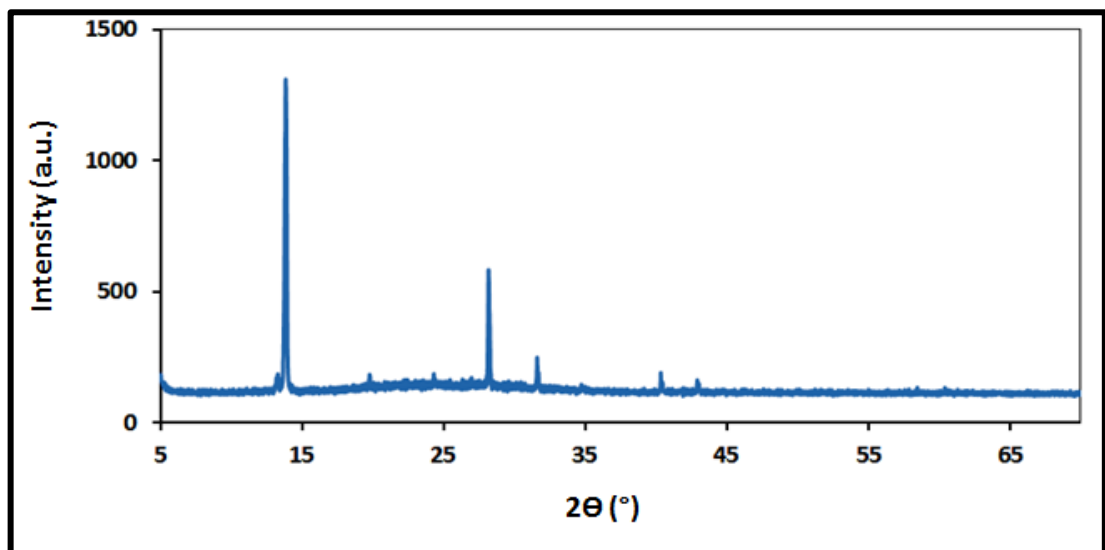
Figure 5.4 X-ray diffraction pattern of the $CH_3NH_3PbI_3$ film fabricated via OSSCM

5.3.3 Performance of the perovskite solar cells fabricated via OSSCM

In total, 30 solar cells based on $CH_3NH_3PbI_3$ thin film produced by the OSSCM were studied and have all shown a very poor performance. The best power conversion efficiency (PCE) of 3.45% was achieved as a result of short circuit current (J_{sc}), open circuit voltage (V_{oc}) and fill factor (FF) of 9.97 mA, 0.933 mV and 0.37 respectively. Figure 5.5 illustrates the current-voltage (J-V) characteristics of the best-performing perovskite device fabricated by OSSDM. Table 1 summarises the obtained photovoltaic parameters of the perovskite solar cells fabricated by OSSDM.

The poor performance of the perovskite devices was mainly due to their porous structures in morphologies of the perovskite films, resulting in the reduced light absorption and the current leakage in solar cells as a result of shunt paths formation.
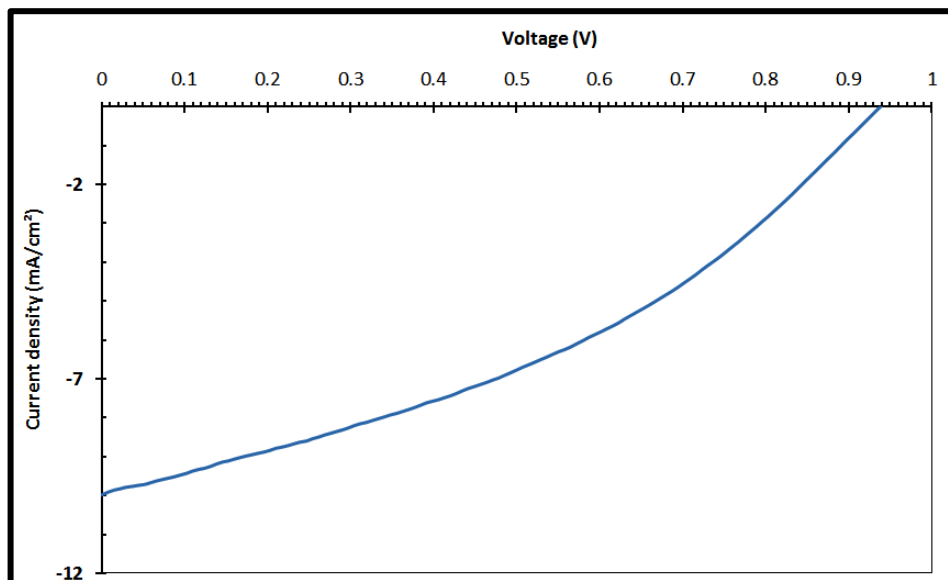
Figure 5.5 J-V characteristics of the CH$_3$NH$_3$PbI$_3$ solar cell fabricated via OSSCM

Table 5-1 Summary of parameters for the best CH$_3$NH$_3$PbI$_3$ solar cells fabricated by OSSCM

Perovskite solar cell device	J$_{sc}$ (mA/cm^2)	V$_{oc}$ (mV)	FF	PCE (%)
The best device	9.97	0.933	0.37	3.45

5.4 Morphological studies of the perovskite films using (TSSCM)

5.4.1 Morphology study of PbI$_2$ thin films

Figure 5.6 shows the surface morphology of the PbI$_2$ thin film produced from the lead iodide (PbI$_2$) in DMF solution with the DIO additive. The PbI$_2$ is shown to exhibit a connected and uniform needle-like nano-crystalline structure. This unique structure allowed the PbI$_2$ phase to react with the added MAI in the following stage to form the halide perovskite thin films.
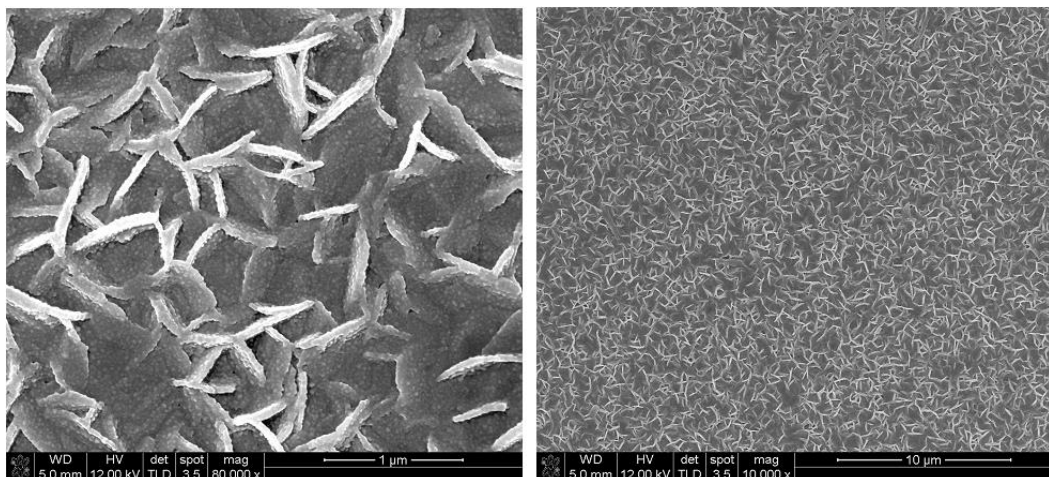
Figure 5.6 SEM image of PbI$_2$ based DIO film

5.4.2 The morphology of the CH₃NH₃PbI₃ films fabricated via TSSCM with different concentrations of the MAI solution.

The growth behaviour of the perovskite crystals was investigated using different MAI concentrations and different allowed reaction time (Art) between MAI and PbI_2 by the two-step method. Thermal annealing of the perovskite thin films was carried out at 100°C for 2 hours.

Figure 5.7 shows the colour change of the applied MAI solution that was kept on top of the pre-coated PbI_2 film at different extended reaction time between MAI and PbI_2. As can be observed, the colour of the solution gradually changed from yellow to brown and finally to dark brown as the reaction time increased from one sec to one minute.
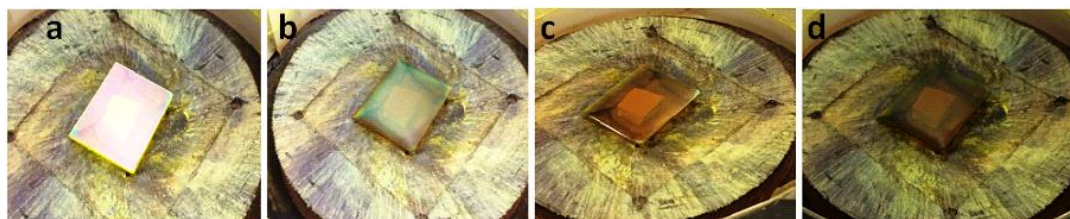
Figure 5.7 Pictures of the PbI₂ film (left, centre left) and the MAI solution after being applied onto the pre-deposited PbI₂ thin film with different extended reaction time between MAI and PbI₂: b) 1 sec, c) 20 sec and d) 60 sec

The perovskite films were fabricated by the procedures as followed; a super saturated solution of PbI_2 was deposited onto the glass slides and then thermally annealed at 70 °C for 8 min. Subsequently, a 120 μl of the MAI solution was deposited onto the cured PbI_2 layer following different reaction time and then followed by thermal annealing at 100 °C for 120 min.

A processing model to describe the formation of the perovskite thin films with various concentrations of the MAI solutions (0.5, 0.8, 1.0 and 1.2 wt %) is

schematically presented in Figure 5.8. When the MAI solution reached the pre-coated PbI_2 crystals, nucleation of an intermediate phase of perovskites only happened in those areas where the MAI concentration must be greater than a concentration threshold (C_k). Lower concentrations than C_k did not result in the intermediate perovskite phase for the crystal growth. Reaction time between MAI and PbI_2 allows the growth of an intermediate phase of perovskite. This intermediate phase is then transformed into full perovskite phases after thermal annealing at 100°C. When a low concentration of the MAI solution 0.5 or 0.8 wt % was applied onto the pre-formed PbI_2 film as shown in Figure 5.8, only a perturbation in concentration led to some areas with a locally high concentration of the MAI, which resulted in the formation of a sporadically distributed intermediate phase of $CH_3NH_3PbI_3$. Only when the concentration of the MAI solution increased to 1.0 wt %, the distributed amount of MAI on the whole surface area of the PbI_2 film was maintained at larger than the concentration threshold, and a gradually controlled crystal growth happened. After maintaining the structure for about one minute, the thin film with a uniform intermediate perovskite phase was formed. Longer growth time (60 sec) and higher concentration of MAI (1.2 wt%) will lead to the lift-off of the intermediate perovskite phase from the substrate, which then reduced the thickness of the final perovskite film by the subsequent spin-coating process.
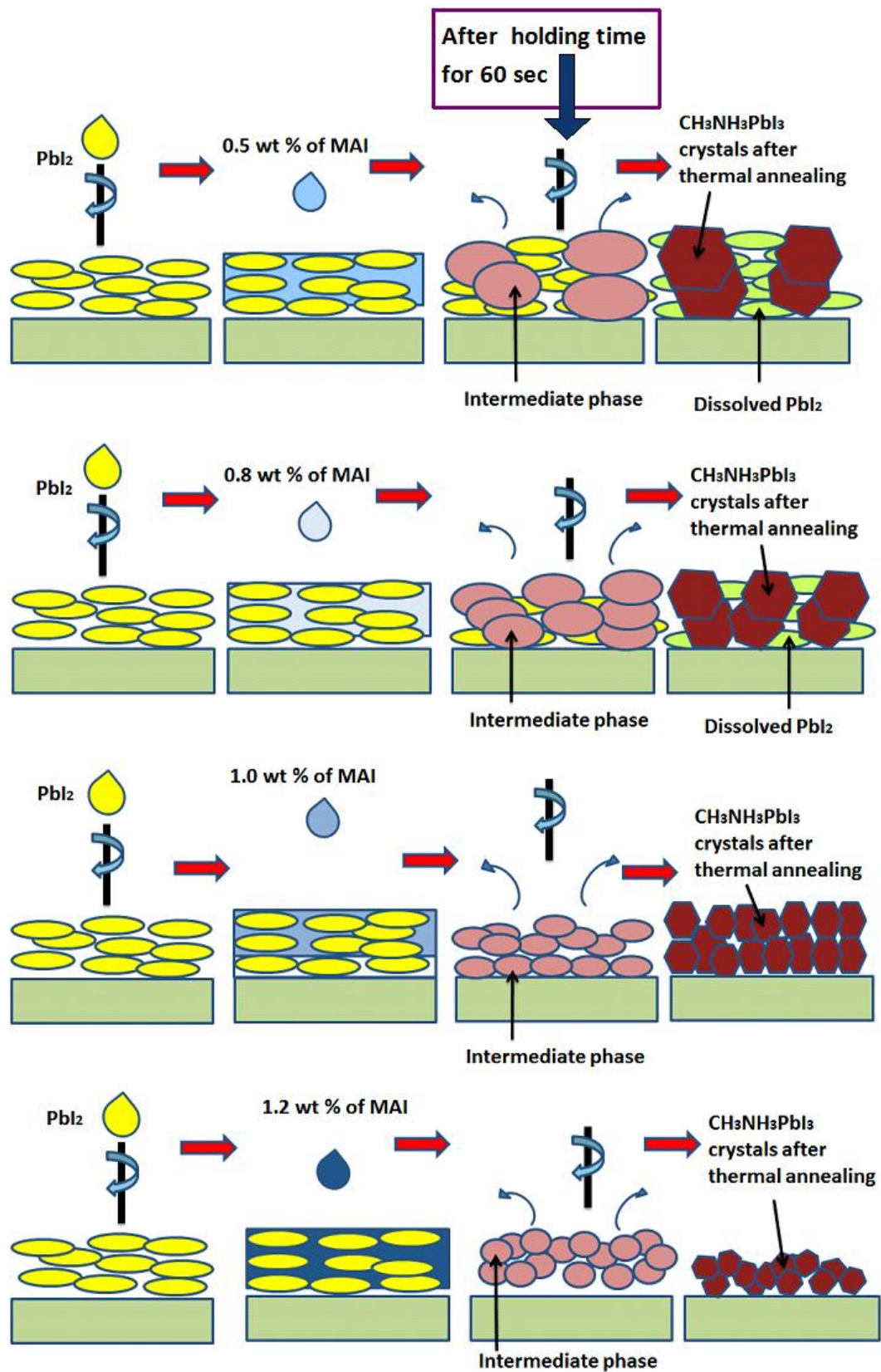
Figure 5.8 Schematic diagram of the processing model for the formation of the perovskite thin films with different concentration of the MAI solutions via TSSCM

Scanning electron microscopy (SEM) measurements were then used to characterise the morphologies of the perovskite films obtained by the TSSCM as shown in Figure 5.9 & and Figure 5.10. Different concentrations of the MAI solutions at 0.5 wt%, 0.8 wt%, 1.0 wt% and 1.2 wt% were separately utilized to apply onto the pre-coated PbI_2 thin film with different reaction time of 20 and 60 sec, and followed by thermal annealing of the perovskite films at 100°C for 2 hours. When the lowest concentration of 0.5 wt% MAI was added onto the pre-coated PbI_2 film, the size of the perovskite crystals increased from ~ 0.7 μm for a 20 sec reaction time to ~ 1.0 μm for a 60 sec reaction time as seen in Figure 5.9a &b.

Comparing Figure 5.9a with Figure 5.9b, the slightly dissolved PbI_2 film was observed except sporadically distributed perovskite crystals. The formed perovskite crystals did not cover the whole surface. In other words, most PbI_2 crystals were only slightly dissolved by the MAI solution. The low MAI concentration led to low nucleation density and thus low crystallisation for perovskites. Further increase in the reaction time between MAI and PbI_2 did not make any contributions to the enhancement of the nucleation density on the surface of the PbI_2 film. Interestingly, with the increase of the MAI concentration to 0.8 wt%, the crystallisation occurred with an increased surface coverage on the PbI_2 thin film as indicated in Figure 5.9c&d. However, the size of the perovskite crystals decreased to ~ 0.4 μm regardless of how long the reaction time would be.
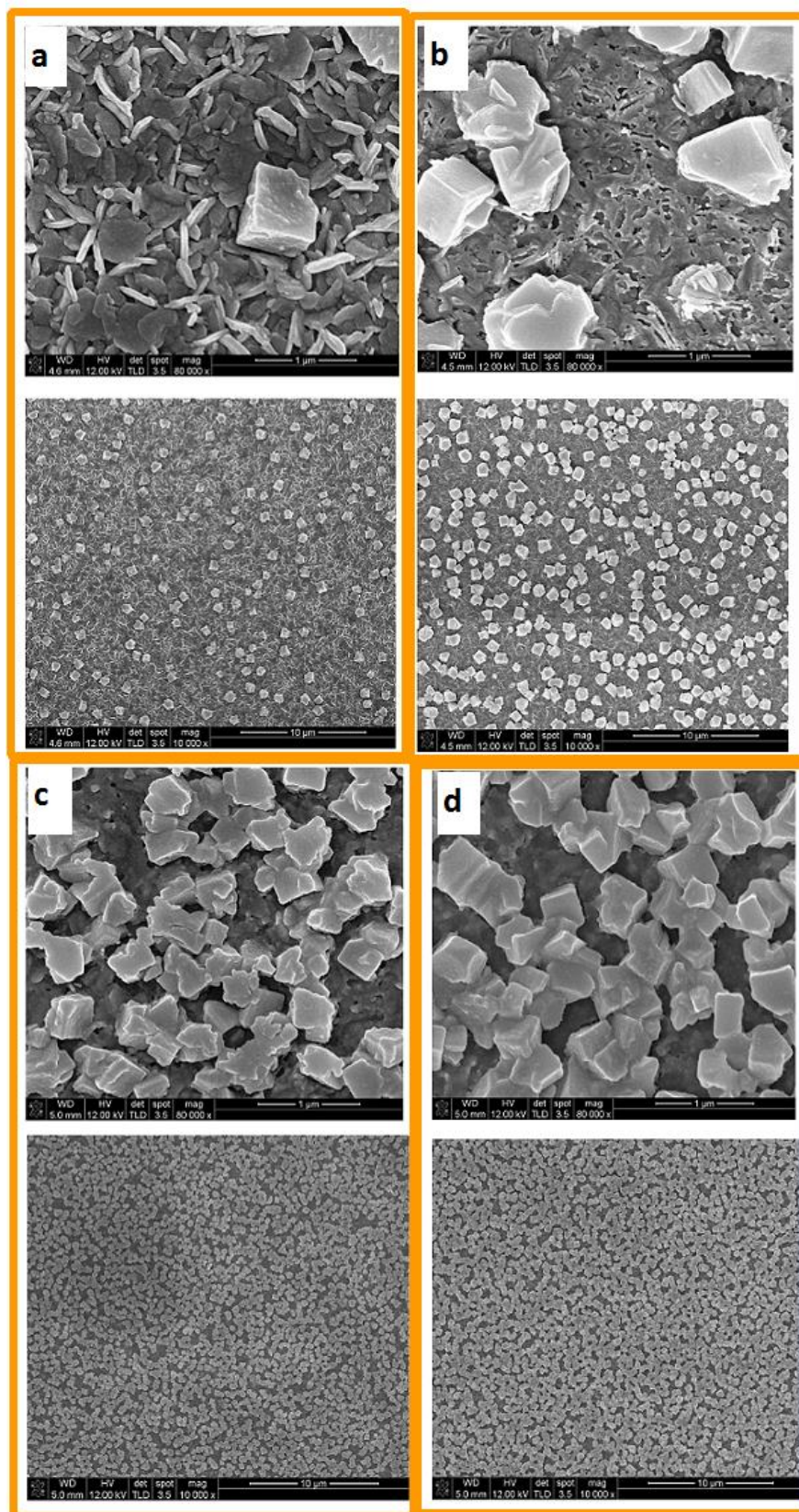
Figure 5.9 SEM images of the perovskite films fabricated via TSSCM at the 0.5 wt % MAI solution for reaction time: a) 20 sec; b) 60 sec.; and at the 0.8 wt % MAI solution at reaction time: c) 20 sec.; d) 60 sec. Two different measurement scales are used for each studied sample

With a further increase of the MAI concentration to 1.0 wt%, the coverage of the perovskite surface reached to all the pre-coated PbI_2 surface; meaning that all PbI_2 crystals have reacted with the MAI solution to form perovskites as shown in Figure 5.10a&b. Again, I have it was observed that the size of the perovskite crystals continued to decrease to about 0.2 μm. Nevertheless, when the concentration of the MAI solution further increased to 1.2 wt. %, pore defects among the smaller nano-sized perovskite crystals were revealed as shown in Figure 5.10c&d. According to SEM images in Figures 5.9&5.10, the size of the perovskite crystals in the film did not change with extended reaction time from 20 to 60 sec when using high concentrations of 0.8, 1 and 1.2 wt % MAI solutions. This confirms that the size of crystals in the perovskite film was determined in the initial reaction stage when the MAI solution came into contact with the pre-coated PbI_2.
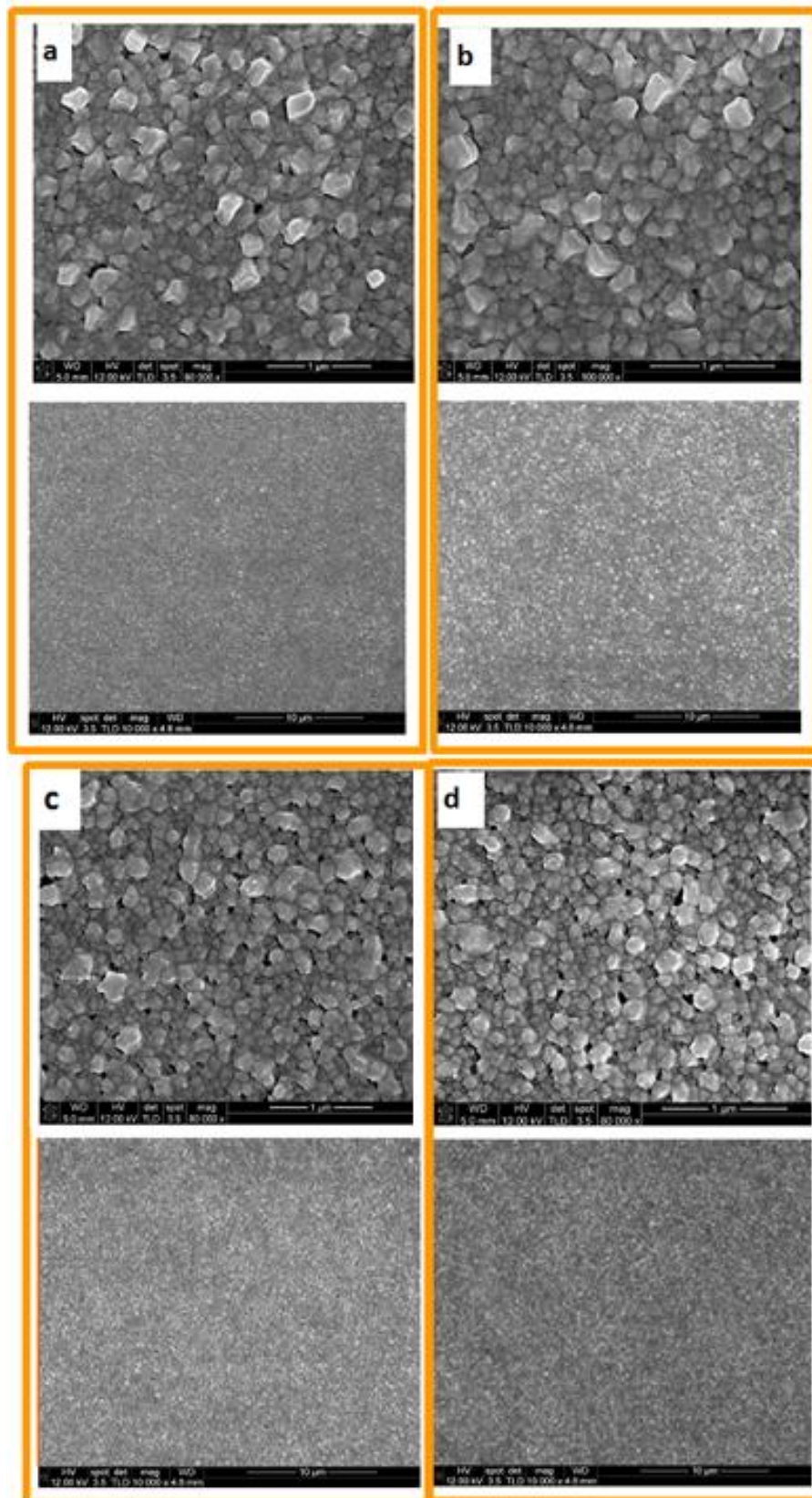
Figure 5.10 SEM images of the perovskite films fabricated via TSSCM at the 1 wt % MAI solution for reaction time: a) 20 sec.; b) 60 sec.; and at the 1.2 wt % MAI solution for reaction time: c) 20 sec.; d) 60 sec. Two different measurement scales are used for each studied sample

5.4.3 The impact of reaction time between MAI and PbI₂ on the morphology of the perovskite film produced from 1.0 wt% MAI solution

The growth behaviour of the perovskite crystals was then investigated according to different reaction times between MAI and PbI$_2$ at 5, 20, 60 and 180 sec respectively with the 1.0 wt % MAI solution as shown in Figure 5.11. Similarly, no change in the size of the perovskite crystals was observed when using different reaction times. The size of the perovskite crystals in the film was ~ 200 nm, however, at 5 sec reaction time, many porous defects existed in the perovskite film (Figure 5.11a) while for 20 sec reaction time, pores were significantly reduced (Figure 5.11b). A uniform and fully connected perovskite film without any pores or other defects was obtained when applying the 1.0 wt % MAI solution for 60 sec reaction time as shown in Figure 5.11c. Interestingly, the polycrystalline structures with clear grain boundaries in the perovskite film disappeared upon increasing the reaction time to 180 sec, resulting in poor quality perovksites (Figure 5.11d).
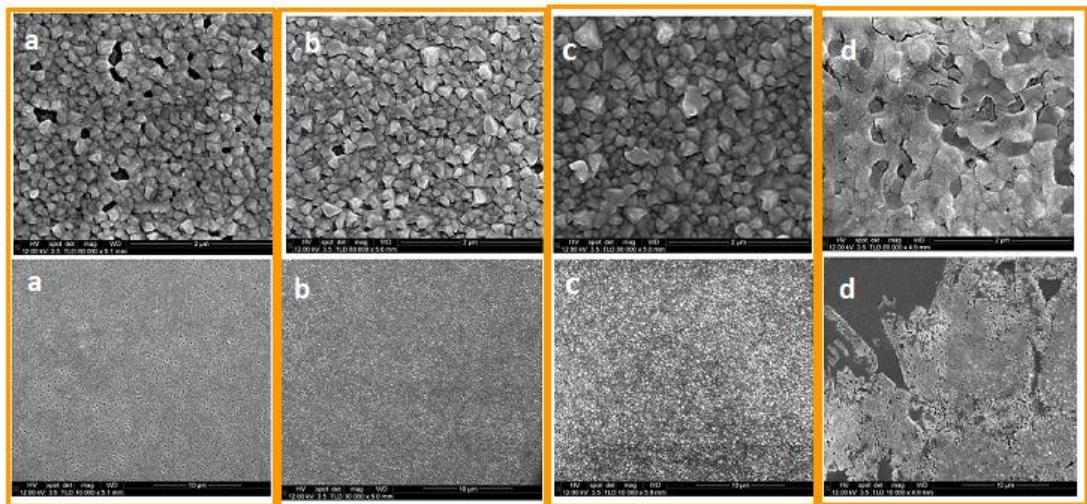
Figure 5.11 SEM images of the perovskite films fabricated via TSSCM at the 1.0 wt % MAI concentration with different reaction time for: (a) 5 sec; (b) 20 sec; (c) 60 sec; and (d) 180 sec

Based on these investigations, the best quality perovskite thin film was only achieved when the 1.0 wt% MAI solution was added on the pre-deposited PbI_2 thin film with 60 sec reaction time allowed between MAI and PbI_2 as shown in Figure 5.12.
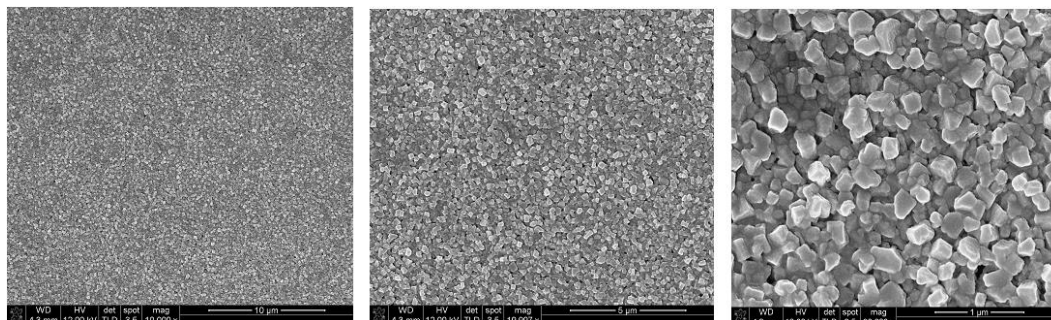
Figure 5.12 SEM images of the perovskite films fabricated via two-step method at fixed concentration of MAI at 1.0 wt% with loading time of MAI at 60 sec

5.4.4 The impact of reaction time between MAI and PbI_2 on the optical properties and crystal structures of the perovskite thin films

UV-Vis absorbance and X-ray diffraction patterns were used to further understand the effect of reaction time between MAI and PbI_2 on the formation of the perovskite thin films.

Figure 5.13 displays the UV-Vis spectra of the perovskite thin film produced from the 1.0 wt% MAI solution with different loading time. The same absorption onset was observed for all perovskite samples at ~ 780 nm. Furthermore, the absorbance increased gradually for the perovskite films after increasing reaction time from 5 to 60 sec between MAI and PbI_2 at the wavelength range of 420-780 nm. The fully-covered-surface and uniform morphology of the perovskite film by 60 sec reaction time was one of the main reasons to contribute to the improvement in the light absorption. However, a considerable reduction in the light absorption was observed for the perovskite film produced with further increased reaction time to 3 min.
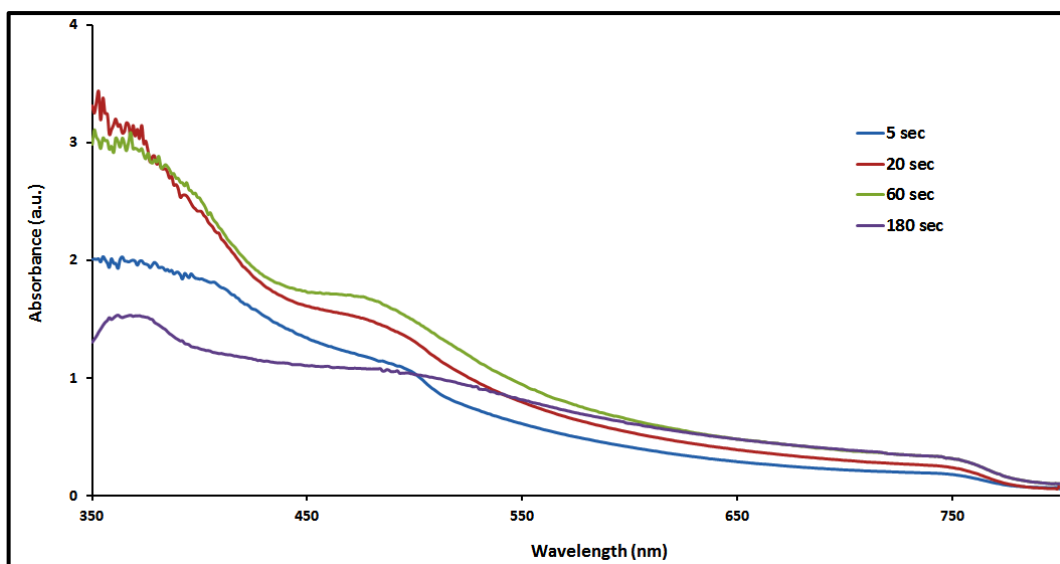
Figure 5.13 UV-Vis absorption spectra of the CH$_3$NH$_3$PbI$_3$ films fabricated with the 1.0 wt% MAI solution at different loading times

Figure 5.14 illustrates X-ray diffraction patterns for the perovskite films with different loading times. Two phases were obtained for the perovskite film with 5 sec reaction time, the residual PbI$_2$ phase "●" at 8.8° and 12.8° and the perovskite phase "■" at 14.2, 25, 28, 31, 41 and 51°, separately. Increasing reaction time between MAI and PbI$_2$ to 20 sec resulted in the significantly reduced peak intensity of the PbI$_2$ phase. Highly crystallised perovskites were obtained with reaction time at 60 sec without showing any residual PbI$_2$ phase in the XRD pattern shown in Figure 5.14. Furthermore, decomposition of the perovskite film was confirmed after further increasing the reaction time to 180 sec, showing two new peaks at 8.8° and 12.8° in the XRD pattern.
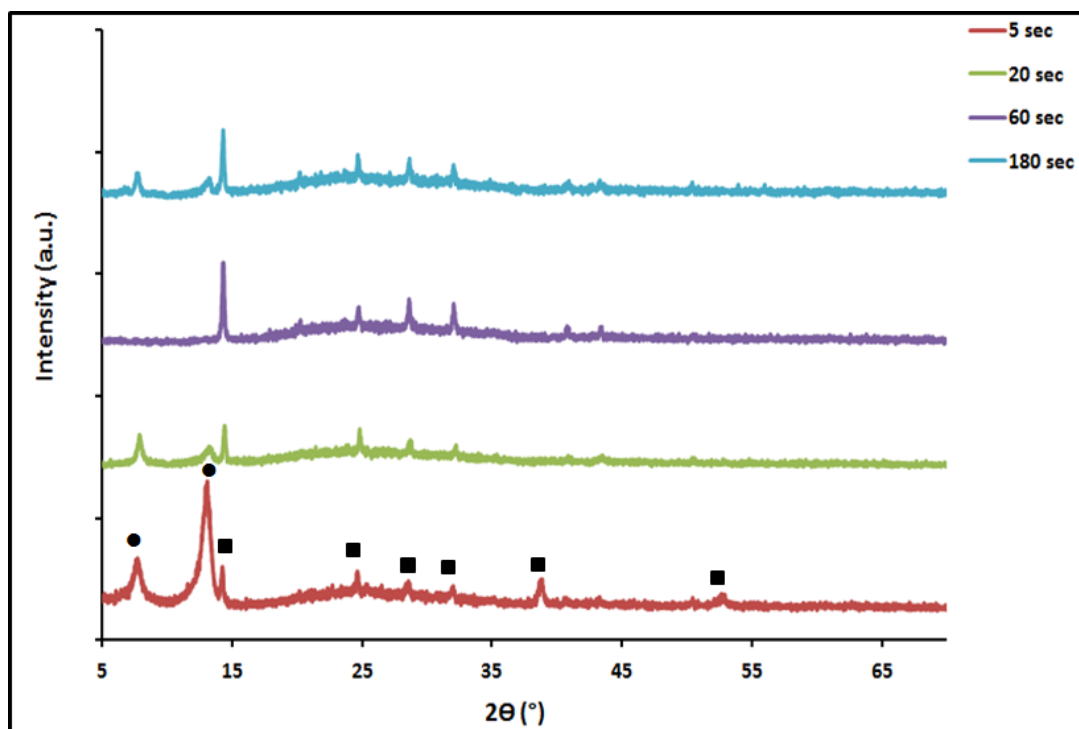
Figure 5.14 X-ray diffraction patterns of the CH₃NH₃PbI₃ film fabricated via the 0.1wt % MAI solution with different loading time

5.5 The impact of heat treatment on the perovskite films produced from 1.0 wt % MAI solution with 1 min reaction time between MAI and PbI₂

5.5.1 The impact of heat treatment on the morphology of the perovskite film

Thermal annealing is a crucial process to transform the formed intermediate phase into fully crystallised perovskites. In this experiment, different approaches to thermal annealing were used for the perovskite film growth. To demonstrate the effect of this variance, Figure 5.15 demonstrates the change in colour after annealing the perovskite films which were fabricated at same conditions and heated for 5, 30 and 120 minutes at 100^{0}C, respectively.
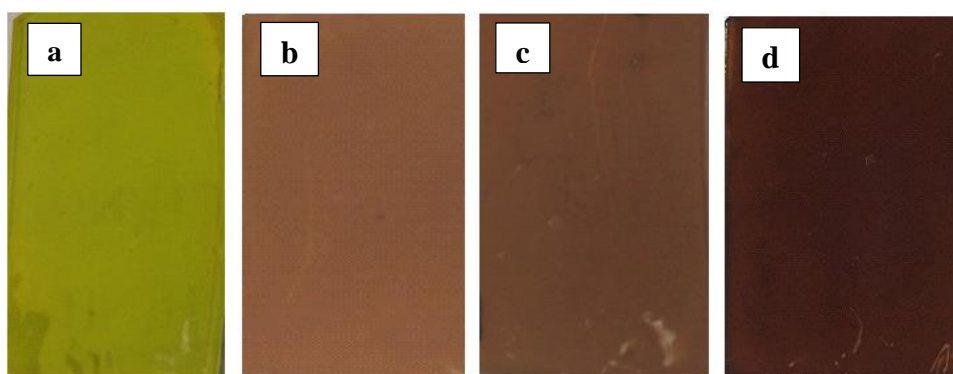
Figure 5.15 Pictures of PbI$_2$ and perovskite thin films after thermal annealing: a) PbI$_2$ film; perovskite thin films annealed for b) 5 min; c) 30 min; d) 120 min

SEM images of the perovskite films in Figure 5.16 show that the grain size of the perovskite crystals did not greatly change as thermal annealing time increased.

This result indicated that the size of the perovskite crystals was determined during the initial reaction stage between MAI and PbI$_2$. However, significant improvement in the morphology and an enhanced interconnection between the perovskite crystals was achieved when thermal annealing time gradually increased from 5 minutes to 120 minutes.
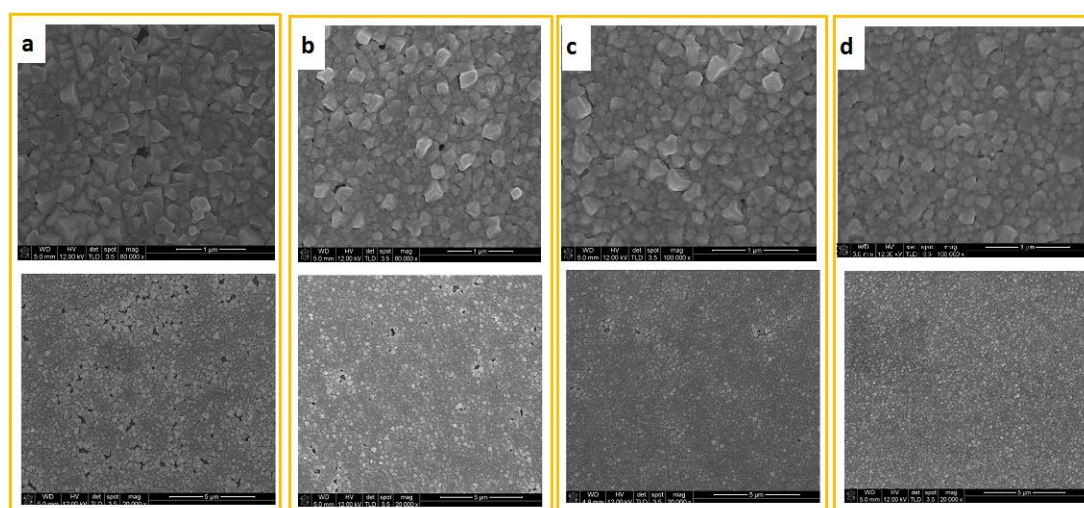
Figure 5.16 SEM images of the perovskite films fabricated via the two-step method at the 1.0 wt% MAI solution with 60 sec. loading time under various thermal annealing times: a) 5 min; b) 30 min; c) 60 min; d) 120 min

5.5.2 The impact of heat treatment on optical and crystalline structure properties of the perovskite film

To further understand the influence of thermal annealing on the formation of perovskite films, UV-vis absorbance and X-ray diffraction patterns were recorded for the perovskite films as shown in Figure 5.17 and Figure 5.18 respectively. A wide absorption band of the perovskite film was observed after 5 minutes thermal annealing, confirming the formation of perovskite structures as shown in Figure 5.17.

Additionally, it is also revealed that the absorbance of the perovskite film significantly increased in the wavelength range of 400-600 nm with increased thermal annealing times of 30, 60, to 120 min. This improvement in the light absorption is owing to the enhancement in the crystallinity of the perovskite structures and the improvement in the surface morphology. The onset in the light absorption is shown to occur at ~ 780 nm for all studied perovskite samples.
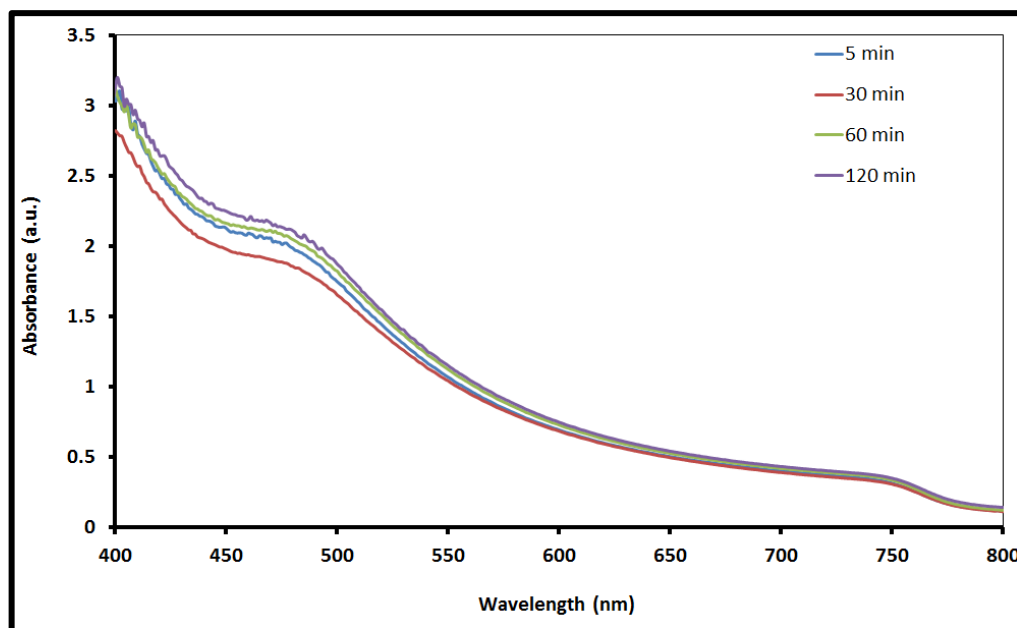
Figure 5.17 UV-Vis absorption spectra of the perovskite films annealed at 100 °C for 5, 30, 120, and 180 min, separately

X-ray diffraction (XRD) test was carried out to further explore the influence of thermal annealing on the degree of crystallinity of the perovskite films. As illustrated in Figure 5.18, the PbI_2 phase at 2Θ of $12.2°$ in X-ray diffraction pattern has disappeared after annealing the perovskite film for 5 minutes, which indicates a quick phase transformation. The same peaks in the diffraction pattern were observed for all the perovskite films that were annealed for a prolonged periods of 30, 60 and 120 minutes. However, the full width at half maximum (FWHM) of the diffraction peak at $14.2°$ decreased progressively with the gradually increased thermal annealing time for the perovskite films from 5 to 120 min. The FWHM value at $14.2°$ decreased from 0.251 for the perovskite film annealed for 5 min to 0.1571 after 2 hours thermal annealing as shown in table 2, indicating a high degree of crystallinity in the perovskite films.
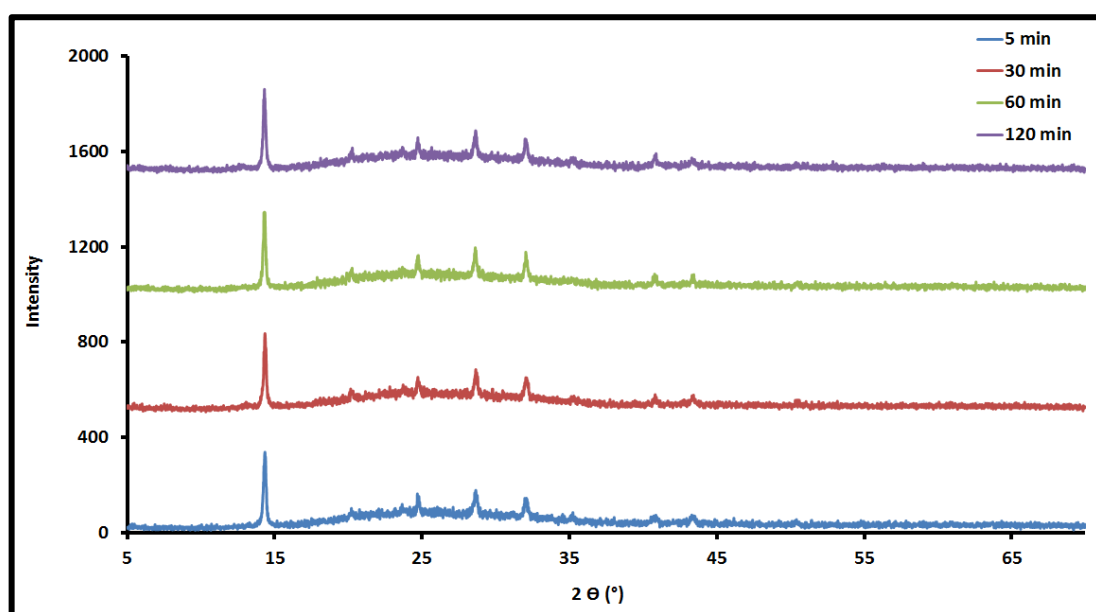
Figure 5.18 X-ray diffraction patterns of the CH₃NH₃PbI₃ thin films fabricated via TSSCM with different heat treatment times

Table 5-2 The full width at half maximum of the diffraction patterns at 14.2° for the perovskite film with different thermal annealing times

Heat treatment time	Full width at half maximum (FWHM)
5 min	0.251
30 min	0.228
60 min	0.203
120 min	0.157

5.6 Conclusions

OSSCM and TSSCM were utilized to fabricate thin films of $CH_3NH_3PbI_3$. Morphologies of the formed perovskite thin films by these methods were investigated. Without any additives from the mixed precursors of MAI and PbI_2, porous and fabric morphology of the perovskite film was obtained by OSSCM via SEM observation. This is mainly ascribed to the fast crystallisation of the intermediate phase in the blended precursors when thermally annealing the formed film. [134]. In the two-step method, different parameters for the perovskite film including different concentrations of the MAI solution different loading times (Art) and various thermal annealing conditions were used to investigate the crystallisation behaviour of the perovskite films. The best morphology of the perovskite film was obtained when the 1.0 wt % MAI solution was used with reaction time of 60 sec was allowed between MAI and PbI_2 and followed by thermal annealing at 100°C for 2 hours.

Chapter 6 - Highly reproducible perovskite solar cells via controlling the morphologies of the perovskite thin films by the solution-processed two-step method

6.1 Introduction

Organometal halide perovskites have received significant interests in the last few years due to their superior optical and electrical properties. They demonstrated highly-efficient capability in converting light into electricity with low cost precursors and cheap solution-processed methods in fabricating solar cells [47,150,161,210,216–218]. Power conversion efficiency (PCE) has considerably jumped from 3.8% in 2009 [77] to the certified efficiency of 22.1 % in 2016 [215] with two types of typical device architectures; i.e. solar cells based-on TiO_2 structures [219–224] or those based-on phenyl-C61-butyric acid methyl ester (PCBM) planar heterojunction (PHJ) structures [129,225–228]. In order to achieve high PCE solar cells, controlling the morphology of the perovskite thin films is one of the major challenges. In the published studies, perovskite films were produced via various methods such as vacuum thermal deposition and solution-processed deposition by either one-step or two-step processes. Good quality perovskite films were obtained by both aforementioned methods with high PCE solar cells. However, the major obstacle for the thermal evaporation method is due to its high-cost vacuum systems and complicated processes. Furthermore, in order to control the morphology of the perovskite thin films in the one-step solution-processed method, two main routes were utilised, i) adding additives into the precursor solution of perovskites; ii) by a so-called solvent engineering technology [215]. Nevertheless, it was found that uniform morphologies are difficult to re-produce in the one-step method owing to their uncontrollable crystallisation rate during the fabrication processes [22].

Therefore, the two-step method has been widely adopted as an efficient way to control the morphology of the perovskite layer for both TiO_2-based and the PCBM-based perovskite solar cells, mainly because the concentration in one of the precursors can be selected to control their reaction and crystallisation rates.

For the TiO_2-based perovskite solar cells, different techniques were used to control the morphologies including vapor-assisted solution-processes [138], the halide sources mixing method [229], low-temperature gas-solid crystallisation processes [230], solution chemistry engineering [142], anti-solvent vapour-assisted crystallisation processes [231], and the two-step ultrasonic spray deposition method [211]. However, these methods are complicated although high-performance solar cells were obtained in many cases and appeared in the published literature. Furthermore, the TiO_2 layer has to be sintered at around 500°C for the TiO_2-based solar cells [150]. Alternatively, the two-step fabrication method for the PCBM-based perovskite solar cells presents the low-temperature alternative processing route with the incredible benefit of simple procedure to control the morphologies of the perovskite films.

Different strategies have been used to control the crystallisation and to improve the morphologies of perovskite thin films in the PCBM-based perovskite solar cells. Shen *et al*. used the two-step annealing process to fabricate $CH_3NH_3PbI_3$ (assisted by doping with $PbCl_2$) perovskites films [148]. They found that thermal annealing improved the surface coverage and crystallisation of the perovskite films. A PCE of 9.1% was achieved for solar cells based on the perovskite obtained by this method [148]. Haung *et al*. claimed that solvent annealing used in the fabrication of the perovskite films is an efficient technique to enhance the crystallinity of perovskites, which results in obtaining 1 μm grain sizes of perovskites. They added the DMF

solvent at the edge of Petri dish where it contained the perovskite film sample during thermal annealing. They expected that the DMF vapour could penetrate into the perovskite film, achieving 15.6% PCE solar cells [153]. Dai's group used a technique (called layer-by-layer) to control the morphology of the perovskite film. The $PbCl_2$ thin film was deposited by thermal evaporation, followed by dipping the sample into a solution of CH_3NH_3I/IPA for several times to form the uniform perovskite layer [232].

Both solvent annealing and thermal annealing play their key roles in controlling the crystal growth of perovskites for the improvement of their morphologies in the two-step method. However, many other factors significantly affect the solvent annealing processes; these include type and vapour pressure of solvents, surroundings, and thermal annealing conditions such as annealing temperature, duration and ramping level [142]. On the other hand, the reaction time between the pre-coated metal halide after being dipped into the MAI solution requires accurate control [138].

In this chapter, we present a simple route to control the morphology of our perovskite films by the two-step deposition method in the fabrication of PCBM-based PHJ solar cells. Through wide investigations of alternating the concentration of MAI and its reaction time with the pre-deposited PbI_2 film, high-performance perovskite films were reproducibly obtained, resulting in solar cells with PCE of 15.01%. The morphology and crystallinity of perovskite films were extensively investigated by SEM and XRD, respectively. In addition, UV-Vis absorption spectra test was used to check the optical properties of the produced films.

6.2 Device structure and experimental methods

The structure of the produced PHJ PV devices is schematically presented in Figure 6.1; the structure encompasses thin film of ITO/PEDOT:PSS/CH$_3$NH$_3$PbI$_3$ /PCBM/BCP/Au, respectively. Pre-structured ITO-coated glass substrates with sizes of ~ 20 x 25 mm were cleaned according to a procedure which was described in section 3.2.8. The cleaned ITO substrates were spin-coated at 3000 rpm by the PEDOT:PSS solution and followed by heating at 140°C for 10 min. The PbI$_2$ thin film was deposited on top of the PEDOT:PSS film by the spin-coating method at 5000 rpm using the high-purity supersaturated hot solution and then annealed at 70°C for 8 min on a hotplate. The MAI solution with different concentrations (0.8, 1.0, 1.2 wt %) were added on top of the PbI$_2$ thin film and then was kept for a fixed time of 60 sec to allow for chemical reaction between PbI$_2$ and MAI, followed a rotation at 5000 rpm using the spin-coater. The obtained thin films were then heated at 100°C for 2 h. A thin film of PCBM was then deposited by the spin-coating method from the PCBM solution on top of the formed perovskite thin film at 2000 rpm and followed by heating at 100°C for 30 min. Thereafter, the thin film of BCP (about 10 nm thick) was spin-coated on top of the BCPM film as the buffer layer and finally a 100 nm thick Au film was applied as the top electrode on top of the BCP film using vacuum sputtering method.
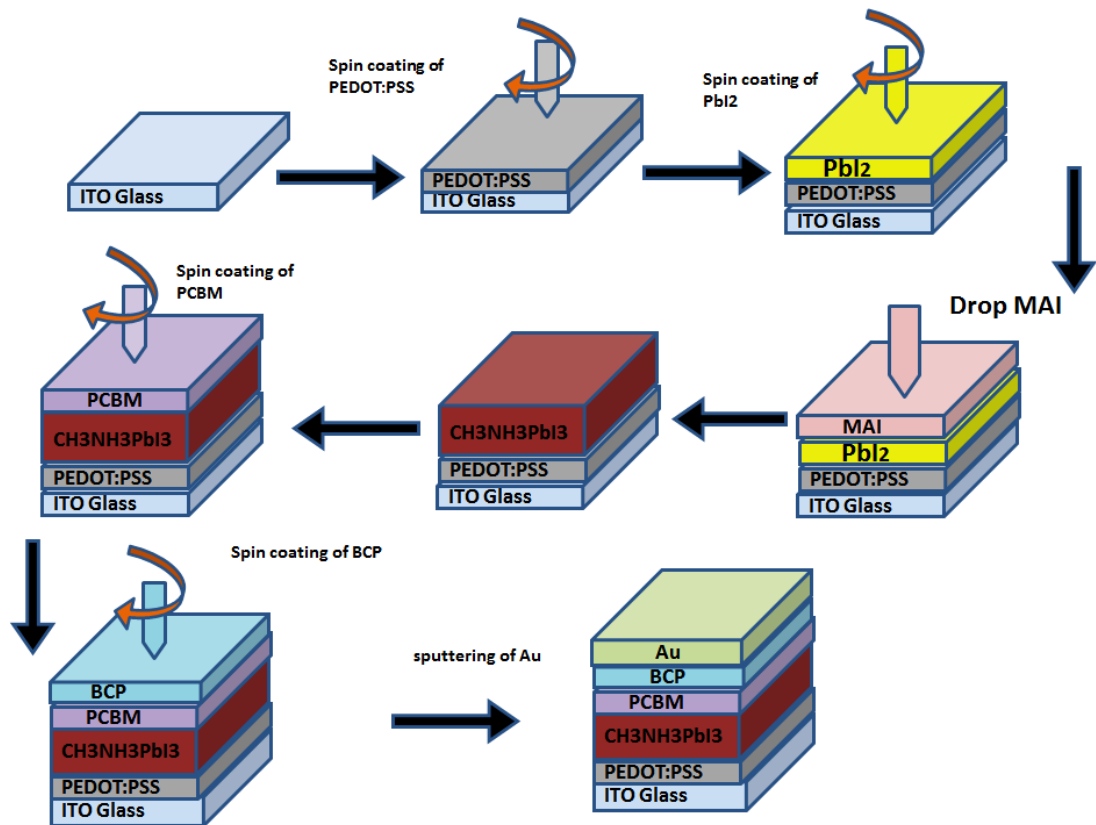
Figure 6.1 Schematic diagram of the fabrication process for each layer of the perovskite solar cells using TSSCM

6.3 Results and discussion

6.3.1 Cross section structures and surface morphologies of perovskite films with different concentrations of MAI

In order to disclose the mechanism, surface morphologies of the $CH_3NH_3PbI_3$ perovskite films have been widely examined in Chapter 5. To better compare with each other, typical morphologies by SEM were presented here again in Figure 6.2 (left side). Cross sectional images of the perovskite films with different concentration of MAI at fixed loading time of 60 sec are shown in Figure 6.2 (right side). The perovskite films were prepared as was explained in section 5.4.2 on normal glass slides. Figure 6.2a& b illustrate the SEM top-surface and cross section images of the final perovskite film fabricated by the 0.8 wt % MAI solution. Figure

6.2a shows block morphologies of the perovskite crystals measured at ~ 400 nm in addition to the PbI_2 crystals which were dissolved after applying 0.8 wt % MAI solution, this is due to the low concentration of MAI, where the corresponding thickness of the perovskite film was ~400 nm as shown in Figure 2b. These nano-sized $CH_3NH_3PbI_3$ polycrystals did not connect together and considerable residual PbI_2 phases existed in the film as it shown later by X-ray diffraction test in section 6.3.2. However, interconnected blocks of $CH_3NH_3PbI_3$ polycrystals without any residual PbI_2 phase were formed after applying the MAI solution at a concentration level of 1.0 wt % onto the pre-coated PbI_2 film as illustrated in Figure 6.2c & d. It was found that the intermediate perovskite phase was fully transferred to perovskite crystals after applying 1.0 wt % of MAI to the pre-coated PbI_2. The surface morphology of the cuboids $CH_3NH_3PbI_3$ polycrystals reveals a connected and uniform morphology of the perovskite film with a thickness of ~ 200-220 nm as illustrated in Figure 6.2d. Furthermore, when the concentration of the MAI solution was increased to 1.2 wt %, pores among smaller-sized $CH_3NH_3PbI_3$ polycrystals were revealed in Figure 6.2e &f. The measured thickness of the perovskite film showed a significant reduction to ~120 nm.
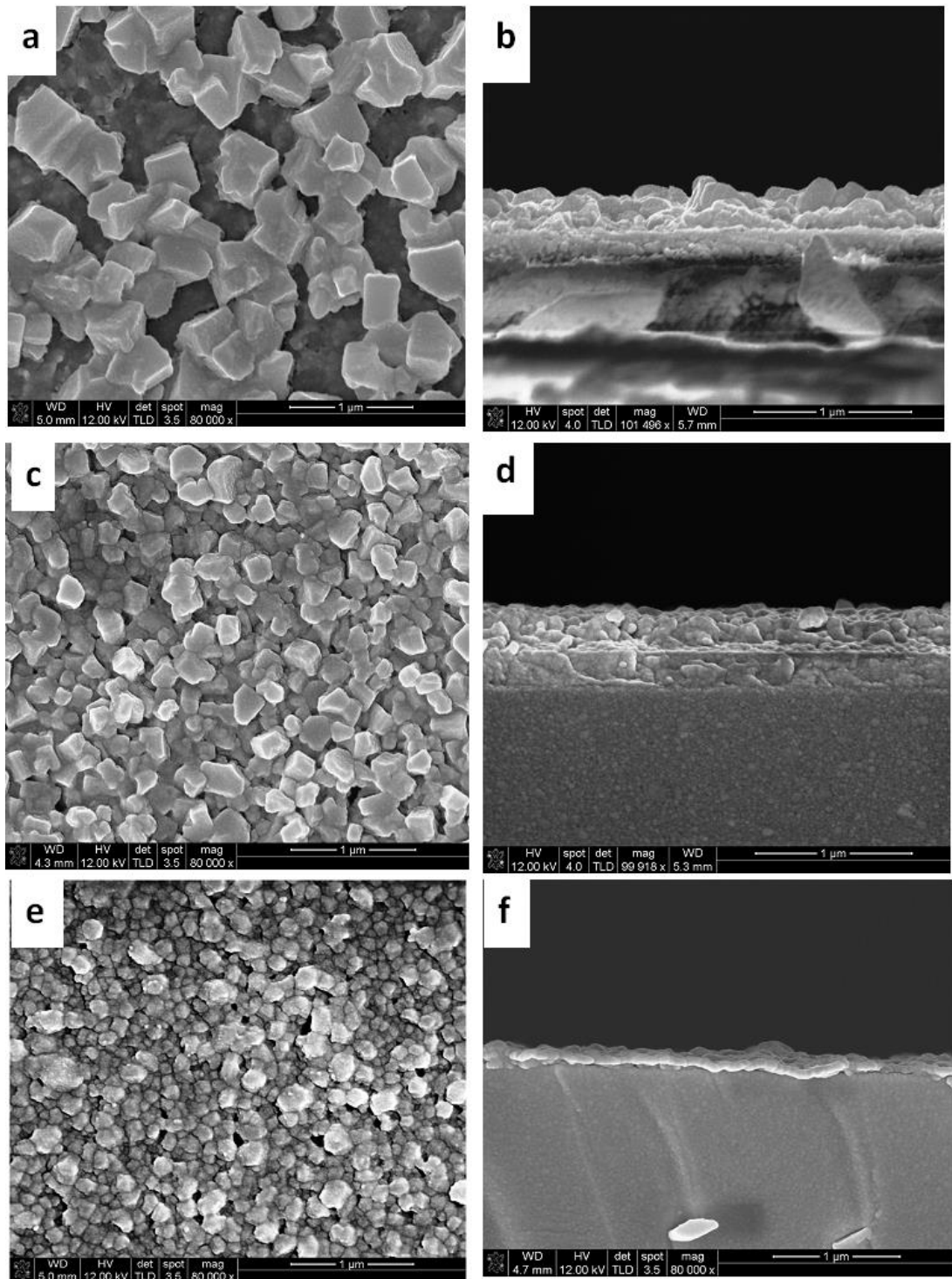
Figure 6.2 SEM top surface and cross section images of the perovskite films with different concentrations of MAI a& b) 0.8 wt %; c& d) 1.0 wt %; e& f) 1.2 wt %

6.3.2 Light absorption and crystal structures of the perovskite films with different MAI concentrations

Light absorption of the formed perovskites was examined to study the impact of the MAI concentrations on optical the properties of the perovskite films. All perovskite films with different MAI concentrations show absorption onset at ~ 780 nm as shown in Figure 6.3, which could confirm the band gap of perovskites at ~1.58 eV. The perovskite film produced by the low concentration of 0.8 wt% MAI solution presented the highest thickness as shown in Figure 6.2b and the highest light absorption was achieved by this film. On the contrast, the perovskite film obtained by the highest MAI concentration of 1.2 wt % resulted in the lowest thickness and therefore a significant reduction in the absorption intensity was observed as shown in Figure 6.3. The perovskite thin film from the 1.0 wt % MAI solution illustrated an excellent light absorbance between the perovskite films by 0.8 wt% and 1.2 wt% MAI solutions.
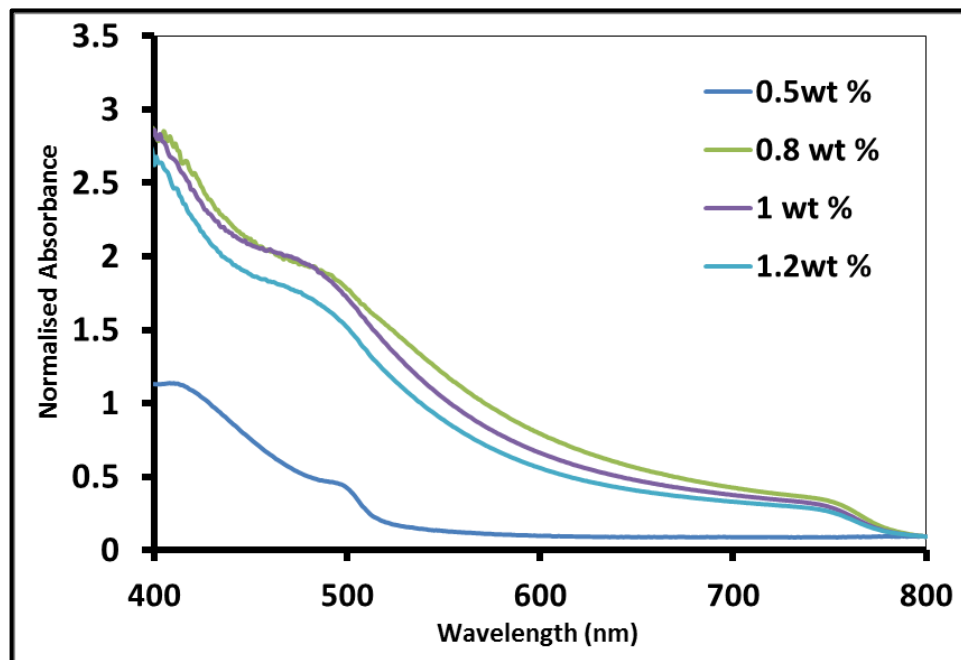
Figure 6.3 UV-Vis absorption spectra of CH$_3$NH$_3$PbI$_3$ films fabricated via TSSCM with different concentrations of MAI (0.5, 0.8, 1.0 and 1.2 wt %) at 60 sec loading time

X-ray diffraction (XRD) patterns were used to characterize the crystalline structures of the perovskite films as presented in Figure 6.4. All perovskite films were prepared under the same conditions on glass slides of exactly the same size. Diffraction peaks that belong to $CH_3NH_3PbI_3$ polycrystals were indicated by "■" while the main peaks being assigned to the residual PbI_2 phase were illustrated by "●". The XRD pattern of the sample from the lowest MAI concentration (0.5 wt%) reveals different peaks positions at 2Θ of 8.2, 12.8, 14.2, 20.09, 23.8, 28.4, 31.9, 40.7, 42.6 and 52 degrees. Most peaks belong to the perovskite structures except the peaks at 8.2 and 12.8 degrees which are due to the residual PbI_2 phase. The high intensity of these two peaks indicates that considerable residual PbI_2 phases are present in the sample. Increasing the MAI concentration to 0.8 wt % led to more perovskite phases in the film as it was shown in Figure 6.4, where the two peaks representing the residual PbI_2 phase have significantly reduced. When the MAI concentration reached to 1.0 wt %, only peaks representing the perovskite phase can be observed in the XRD pattern, suggesting that all PbI_2 phases have changed to perovskites via reaction.
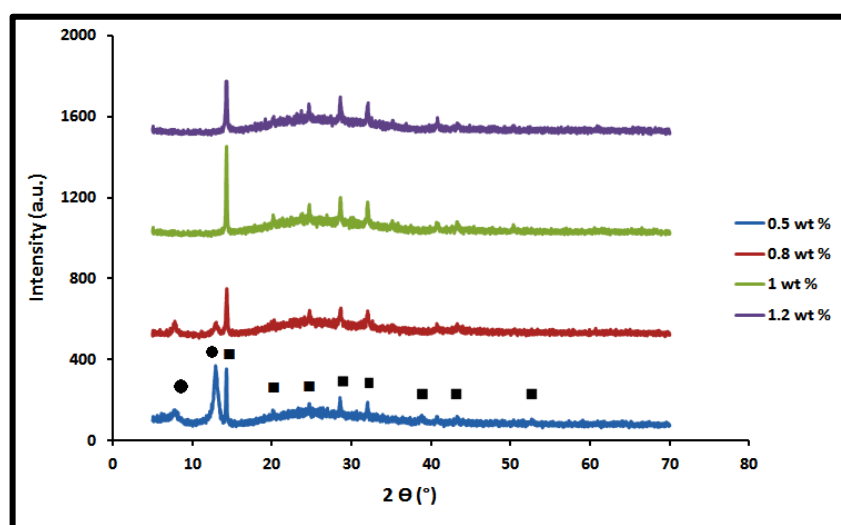
Figure 6.4 X-ray diffraction patterns of $CH_3NH_3PbI_3$ thin films fabricated via TSSCM with different concentrations of MAI (0.8, 1.0 and 1.2 wt %) at 60 sec loading time

For the sample produced by adding 1.2 wt % MAI concentration, the main peak at 2Θ of 14.2 with the highest intensity for the perovskite phase has further reduced due to the reduction in film thickness.

6.3.3 Performance of the perovskite solar cells

6.3.3.1 Effect of applying different MAI concentrations

The quality of perovskite thin films played a key role in determining the PCE of PV devices based on these films as the active layers. The concentration of the MAI solution and reaction time between MAI and PbI_2 are crucial to obtain high-quality perovskite thin films. We have found that reproducible solar cells were achieved when one minute reaction time was utilized. Therefore, different concentrations of the MAI solution and one minute reaction time were applied to fabricate perovskite thin films for our solar cells as was discussed in section 6.2 to compare their PCEs. As shown in Figure 6.5 for the J-V characteristics curves, the best performance measured among the PV devices was achieved using the perovskite film fabricated by the 1.0 wt. % MAI solution on the pre-coated PbI_2 thin film.

A summary of the performance of studied devices with the perovskites produced by different concentrations of MAI solutions is listed in Table 6.1.

Table 6-1 Device performance against different concentrations of the MAI solutions

Concentration of MAI (wt %)	V_{oc} (V)	J_{sc} (mA/cm^2)	FF	PCE (%)
0.8	0.95	11.4	0.38	4.19
1	0.945	20.25	0.64	12.39
1.2	0.93	14.2	0.54	7.2

Overall, the solar cells with the 1.0 wt % MAI concentration demonstrated a typical performance with PCE of 12.39%, short circuit current of 20.25 mA/cm², and fill factor of 0.70. The high performance was achieved due to the homogeneous and connected crystals of the perovskite structure and the pure perovskite phase. However, a reduction in the performance of the perovskite devices was observed when using 1.2 wt % of MAI solution to fabricate the perovskite layer compared to using 1.0 wt % of MAI solution. The solar cells presented a low PCE of 7.2%, owing to the low current density of 14.2 mA/cm^2 and low FF of 0.54. The smaller thickness of the perovskite film from the 1.2 wt % MAI solution and the perovskite's porous morphology are assigned as the main reasons for the decreased PCE.
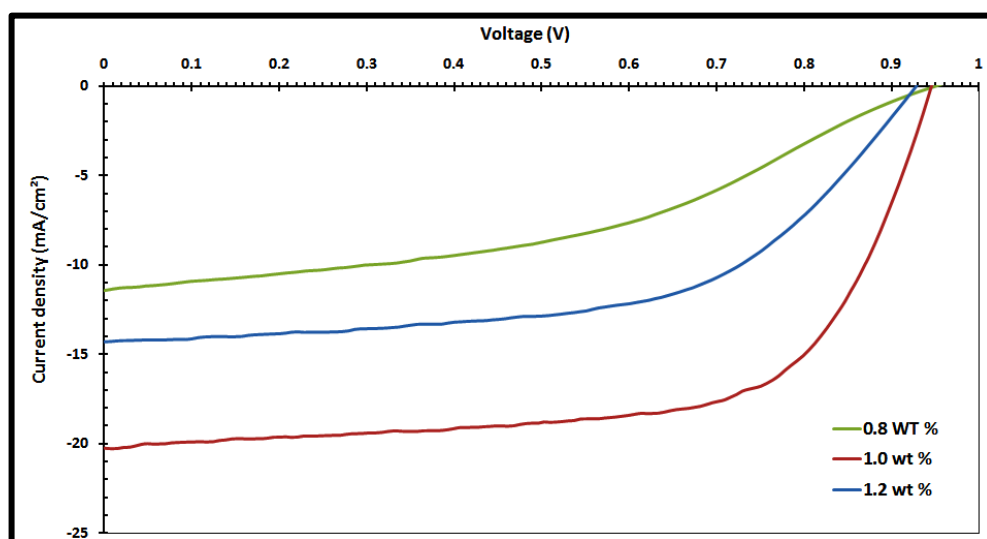
Figure 6.5 J-V characteristic curves of the CH$_3$NH$_3$PbI$_3$ solar cells fabricated via the two-step method with different concentrations of MAI at 60 sec loading time

By contrast, the PV devices with the perovskite film from the 0.8 wt. % MAI solution achieved the smallest PCE of 4.19%, presenting the lowest current density of 11.4 mA/cm^2 and very low FF of 0.38. The high portion of the residual PbI$_2$

phase in the perovskite thin film was blamed as the main culprit for the poor performance. Moreover, the second reason for the reduction of PCE was that the perovskite crystals did not cover the whole surface. All solar cells with the perovskite film by different MAI concentrations demonstrated reasonable open-circuit voltage of above 0.9 V.

6.3.3.2 Effects of using two different concentrations of PCBM solutions for the HTL with or without the BCP buffer layer

Three different perovskite devices were fabricated using the same procedures as described in Section 6.2. The PCBM layer however was produced with two different concentrations of 30 and 40 mg/1mL chlorobenzene solution. The solar cells were also fabricated either with a BCP buffer layer or without a BCP buffer layer. Table 6.2 demonstrates the performance of the perovskite solar cells with various concentrations of PCBM with or without BCP buffer layer.

Table 6-2 Performance of the perovskite devices with different concentrations of PCBM with or without BCP

Concentration of PCBM with or without BCP	V_{oc} (V)	J_{sc} (mA/cm²)	FF	PCE (%)
30 mg of PCBM with BCP	0.92	23.5	0.68	14.7
40 mg of PCBM with BCP	0.929	20.2	0.65	12.19
30 mg of PCBM without BCP	0.85	14.7	0.38	4.76

A significant enhancement in the PCEs of the perovskite solar cells with BCP, when PCBM thin film was deposited at a fixed spin rate of 1000 r.p.m from the 30 mg/1 mL chlorobenzene solution compared to the 40 mg/1 mL solution. The PCE has jumped from 12.19 % to 14.70 % after inserting a thin film of BCP with lower

concentration of PCBM as shown in Figure 6.6. This increase in PCE was due to the enhancement in fill factor and short circuit current from 0.65 to 0.68 and from 20.2 to 23.5 mA/cm^2 respectively. However, there was a substantial reduction in the performance of the perovskite solar cells when fabricated without a BCP buffer layer. The PCE is decreased to 4.35 as a result of the decreasing fill factor and short circuit current of 0.38 and 14.7 mA/cm^2 respectively.

The main benefit of using the BCP buffer layer is that it facilitates the collection of charge carriers from the electron transport layer to the corresponding electrode, and improves the interfacial layer between the PCBM and the top Au electrode.
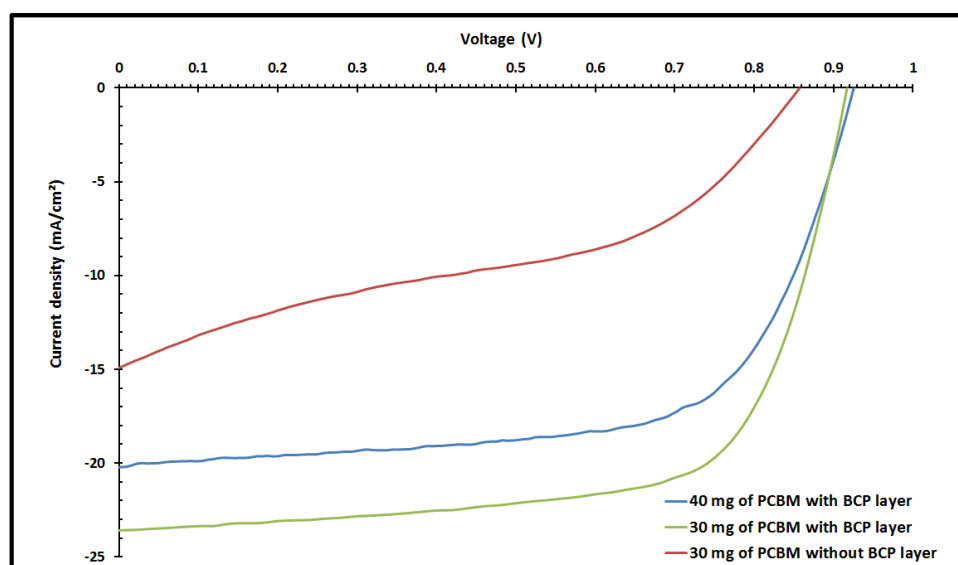
Figure 6.6 J-V characteristics of the perovskite devices with different concentrations of PCBM with or without BCP

The best performance of perovskite solar cells was obtained by using 1.0 wt% MAI solution, PCBM of 30 mg/1mL chlorobenzene solution with BCP buffer layer which was measured under illumination and under dark surroundings as shown in Figure 6.7. The PCE of 15.01% was attained with high short circuit current of 23.8 mA/cm², fill factor of 0.70, and open circuit voltage of 0.92 mV. Figure 6.8 presents the performance distribution of 135 solar cells fabricated from the 1.0 wt% MAI

solution, PCBM of 30 mg/1mL chlorobenzene solution with BCP buffer layer showing very good reproducibility.
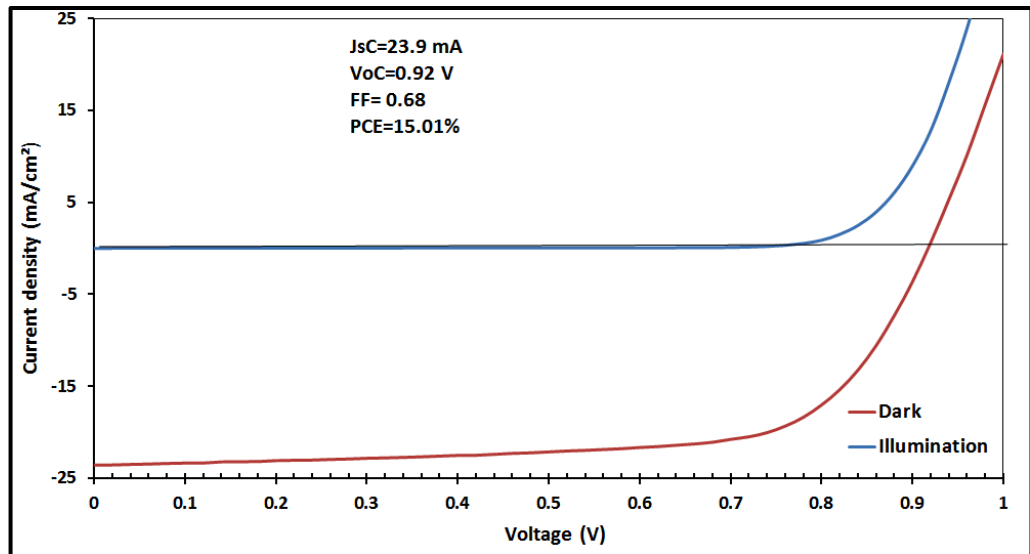
Figure 6.7 J-V characteristics for the best device under illumination and under the dark condition
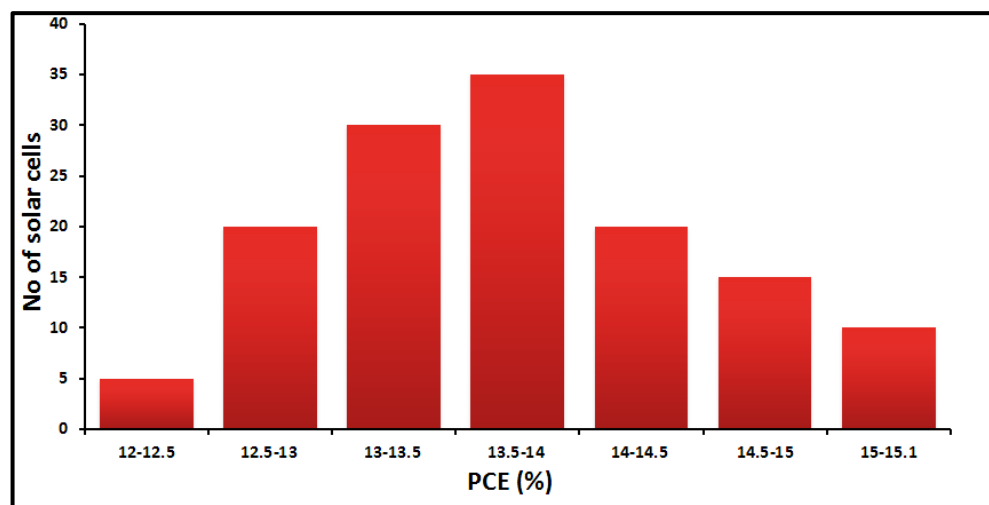
Figure 6.8 Performance distribution of 135 solar cells fabricated from the 1.0 wt % MAI solution

6.3.3.3 The hysteresis effect

It has recently been recognised that the phenomenon of hysteresis may occur in some perovskite solar cells at different scanning rates or at different directions [228]. The influence of hysteresis on the solar cells has also been investigated in this

work. Forward and reverse scanning in the measurements of J-V dependence were conducted as demonstrated in Figure 6.9. The studied solar cells exhibited convergent performance in PCE under both the forward and reverse scan directions, suggesting almost negligible hysteresis effect.
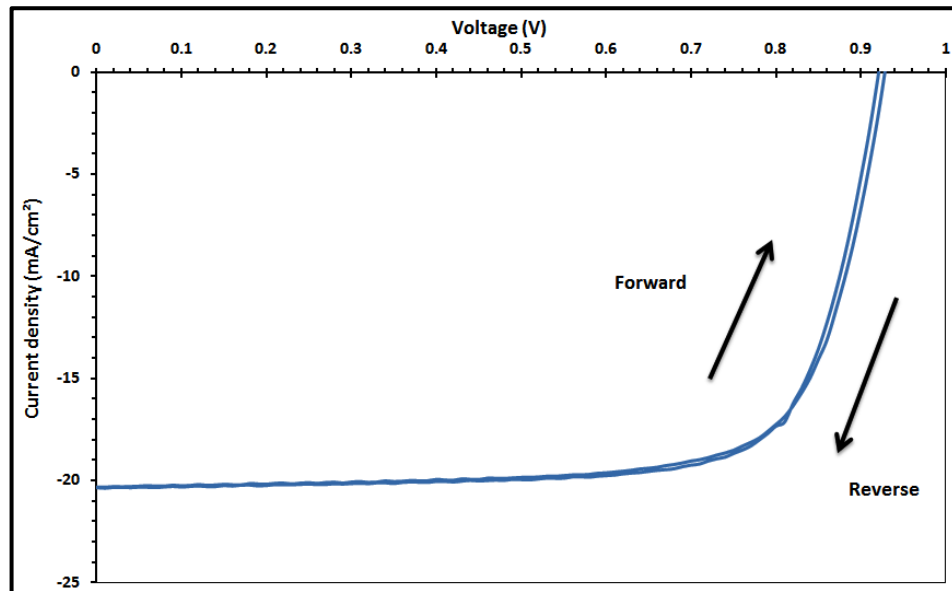
Figure 6.9 J-V characteristics measured under forward and reverse scan directions for the perovskite solar cells with the structure of ITO/PEDOT:PSS/CH$_3$NH$_3$PbI$_3$/PCBM/BCP/Au

The negligible hysteresis is accredited to the reduction in the density of defects due to the controlled morphologies of perovskite films produced by the two-step fabrication method [228]. The decent interface between the perovskite layer and the electron or hole transport layers can be another reason for the mitigation of the hysteresis effect in the perovskite solar cells [215].

6.4 Conclusions

A low-temperature two-step fabrication method was used to produce high quality CH$_3$NH$_3$PbI$_3$ thin films for PHJ solar cells. It was found that the concentration of the MAI solution and reaction time between MAI and PbI$_2$ have a significant impact on

the morphologies and crystal growth of the perovskite thin films. Highly replicable perovskite thin films were fabricated in this work and successfully applied for high performance solar cells.

For solar cells based on perovskite films produced by the 1.0 wt. % MAI solution and one minute reaction time, 110 out of 135 devices gave PCE above 13.0 %; the highest PCE was 15.01%.

Chapter 7 - Blending photoactive polymer with halide perovskite as light harvesting layer for solar cells to enhance stability of devices

7.1 Introduction

Polymer solar cells (PSCs) have received considerable interest in the past twenty years owing to their potentially low-cost roll-to-roll processing. The power conversion efficiency (PCE) has steadily increased to ~10% for a single BHJ photovoltaic device [62,233]. However, the PCE is still too low to occupy a large market share when competing with 1st generation Si-wafer-based and 2nd generation thin-film-based solar cells. The low PCE is mainly due to the short diffusion length of charge carriers within the photoactive conjugated polymer [234–236], which causes loss of free charge carriers due to recombination. Because of short charge-carrier diffusion length, planar heterojunction (PHJ) architectures only result in inefficient PSCs. High-efficiency however is achieved in BHJ PSCs via the blend of a photoactive polymer with an electron-acceptor material such as phenyl-C61-butyric acid methyl ester ($PC_{61}BM$) or phenyl C71 butyric acid methyl ester ($PC_{71}BM$) [31]. In addition, organolead halide perovskite-based solar cells more recently demonstrated highly-efficient capability of converting sunlight into electricity with low cost precursors and cheap solution-processing methods. The PCE has significantly increased from 3.8% in 2009 [77] to ~22.1% up to date [213]. The rapid increase in PCE has brought remarkable rise in interest in this fascinating class of materials. By combining different halides and altering their ratios in organolead halide perovskites, light absorbance can be tuned to cover a wide range of wavelengths [168]. However, their poor stability remains one of the main issues except containing toxic lead for the large-scale commercial deployment. Long term

stability is affected by several parameters including external factors of moisture, oxygen, temperature, UV light and internal intrinsic factors of ion migration, electro-migrations and interfacial reactions [237]. In terms of the PV devices, stability can be related to device architectures, type of electrodes, interfacial layers (hole- and electron-blocking layer), and active layers of the halide perovskites. Studies are widely carried out in these aspects and significant improvements have been achieved. For instance organic-inorganic hybrid combination of cesium (Cs) and formamidinium iodide (FAI) as A in ABX_3 perovskite structures demonstrated significant enhancement in thermal stability of organolead halide perovskites [238,239]. Moreover, by incorporating polyethylene glycol into the methylammonium lead iodide ($MAPbI_3$) perovskite active layer has not only increased its moisture resistance but also showed a "self-healing" effect on degradation of the PCE [172].

In the current research programme, it is reported for the first time on a fabrication method of organic-inorganic hybrid photoactive layers by blending a conjugated photoactive polymer with a halide perovskite to form a composite active material for light-harvesting in solar cells. The blend forms PHJ solar cells architecture with a PCBM layer, which can perform as a highly-efficient PV device with high PCE. This approach paves a new route to developing organic-inorganic hybrid solar cells. Photoactive conjugated polymers include a family of organic semiconductive materials that covers a full range of wavelengths for light absorption, among those are poly[3-hexylthiophene-2,5-diyl] (P3HT) with ~2.0 eV band gap, poly[[4,8-bis[(2-ethylhexyl)oxy]benzo[1,2-b:4,5-b′   ]dithiophene-2,6-diyl][3-fluoro-2-[(2-ethylhexyl)carbonyl] thieno[3,4-b]thiophenediyl]] (PTB-7) with ~1.81 eV band gap, and poly[diketopyrrolopyrrole-terthiophene] ($PDPP_3T$) with ~1.56 eV band gap.

This will allow more flexibility and of course better opportunity in synthesizing a photo-active layer to extend its light absorbance into full-range effective wavelengths without sacrificing other properties such as the stability of organometal halide perovskites. For example, organometal bromine-based perovskite has much better stability than iodide-based perovskite but suffers from narrow range wavelengths in light absorbance [160,240,241]. The conjugated polymer can also provide additional properties such as barrier protection to halide perovskites for stability enhancement of solar cells since the conjugated semiconductive polymers have better moisture resistance than organometal halide perovskites.

7.2 Experimental methods

7.2.1 Materials

MAI was synthesised according to the procedure which was described in section 3.2.3.1. The PbI_2 solution was prepared by dissolving 1 mole PbI_2 in 1 ml DMF solvent and stirred at 70 °C. 20 µl of DIO was added into the solution to promote the dissolution of PbI_2. Thereafter, 1.0 wt % MAI solution was then produced by adding MAI in 2-propanol and stirred for 10 min at 50 °C. The PTB7 and PCBM solutions were respectively prepared by dissolving 4 mg of PTB7 and 30 mg of PCBM in 1 ml of chlorobenzene separately. 2 mg of BCP was dissolved in 1 ml of methanol to form the BCP solution. The PEDOT:PSS solution was used as received from Ossila Ltd. UK (1.3-1.7 wt.% water solution).

7.2.2 Fabrication of the PV devices.

Pre-structured ITO-coated glass substrates (sheet resistance 15 Ω/□) with the size of ~20 × 25 mm were cleaned by following the procedure outlined in section 3.2.8. The cleaned ITO substrates were spin-coated at 3000 rpm by the PEDOT:PSS solution

and followed by heating at 140 °C for 10 min. The PbI_2 thin film was prepared on top of the PEDOT:PSS film by the spin-coating method at 5000 rpm using the supersaturated PbI_2 solution in DMF and then annealed at 70 °C for 8 min on a hotplate. Thereafter, the PTB7 film was spin-coated on top of the PbI_2 film and annealed at 70 °C for 2 min for the PTB7-$CH_3NH_3PbI_3$ based solar cells. The MAI solution was then added either on top of the PbI_2 for $CH_3NH_3PbI_3$ or on top of PTB7 film for PTB7-$CH_3NH_3PbI_3$ based solar cells respectively and was kept at 1 or 2.5 min respectively as loading times.

7.3 Optimising parameters of the composite perovskite layer with different PTB7 concentrations

The new composite perovskites were prepared using (THSSCM). After depositing the PbI_2 film onto the PEDOT:PSS, a PTB7 thin film was coated on top of the dried PbI_2 followed by dropping 120 μL of MAI (1.0 wt %) solution onto the PTB7 film. Three different concentrations of the PTB7 in chlorobenzene solutions (4, 6, and 8 mg in 1 mL chlorobenzene) were investigated and labelled as B1, B2 and B3 respectively as listed in Table 7.1. The loading times of MAI solution onto the pre-coated BTP7 were 150 sec for B1, 180 sec for B2 and 210 sec for B3 solutions separately.

Table 7-1 Concentrations of the PTB7 chlorobenzene solutions

Solution	Concentration of the BTP7 solution in chlorobenzene
B1	4 mg PTB7/1mL chlorobenzene
B2	6 mg PTB7/1mL chlorobenzene
B3	8 mg PTB7/1mL chlorobenzene

7.3.1 Structural properties of the composite perovskite layers with different PTB7 concentrations

XRD diffraction patterns were utilised to identify the effect of the PTB7 concentrations on the perovskite composites. The (THSSDM) was used to deposit all films. 25 μL of the PbI_2 solution was used to deposit the PbI_2 film on pre-cleaned glass slides of the same size (2 × 2.5 cm) which was then followed by thermal annealing at 80°C for 8 minutes. Different concentrations of the PTB7 polymer solution were applied onto the pre-coated PbI_2 thin film and followed by heating at 80°C for 60 sec.

Following this, a 120 μL of MAI (1.0 wt%) solution was applied onto either the PbI_2 or the PbI_2/PTB7 films and was allowed loading times of 1 min in the case of the pristine perovskite, 2.5 min for the PTB7 film produced by the B1 solution, 3 min for the PTB7 film produced by B2 solution and 3.5 min for the PTB7 film produced by the B3 solution. Samples were then thermally annealed at 100°C for 2 hours. Figure 7.1 shows that the pristine perovskite film exhibits diffraction peaks at 14.1°, 25°, 28°, 31°, 41.5°, and 51°, evidently confirming the pure phase of the perovskite.
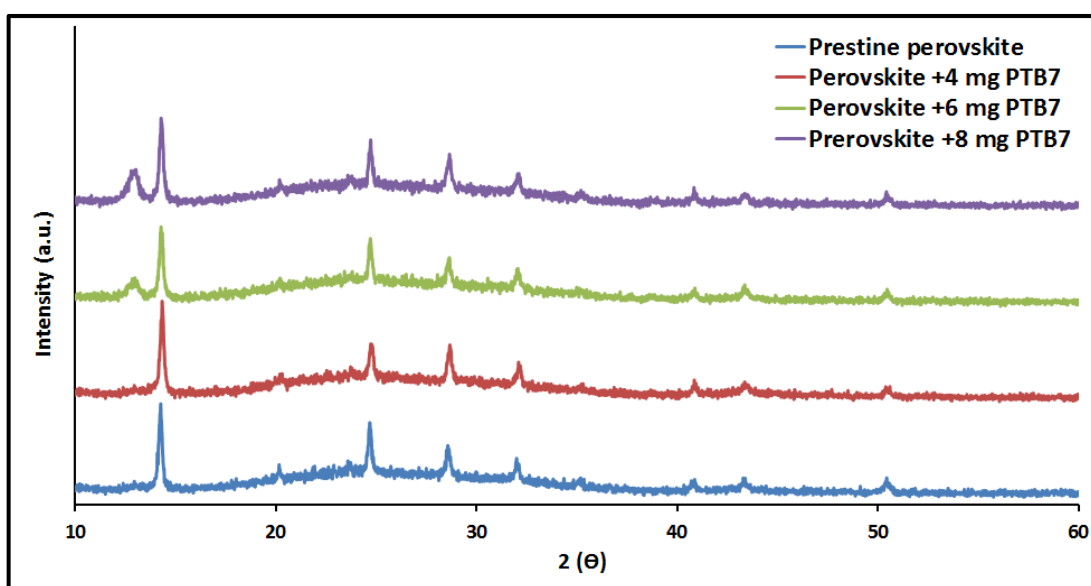
Figure 7.1 X-ray diffraction patterns of CH₃NH₃PbI₃ and CH₃NH₃PbI₃/PTB7 composite using different concentrations of the PTB7 polymer

Producing the PbI$_2$/PTB7 thin film by the B3 solution resulted in high residual PbI$_2$ phase at 2Θ of 12.8° in the composite-perovskite film, demonstrating that high thickness of the photoactive PTB7 thin film can hinder the completion of the reaction between MAI and PbI$_2$. Additionally, it was found that the residue of the PbI$_2$ peak reduced with the thickness decrease of the PTB7 thin film produced from the B3 solution to that of the B2 solution. This shows that the reaction between MAI and PbI$_2$ increased gradually with the decrease in the PTB7 thin film thickness. Diffraction peaks at 2Θ of around 14.1°, 25°, 28°, 31°, 41.5°, 51° were identified for the PTB7-perovskites. Finally, the pure CH$_3$NH$_3$PbI$_3$ phase in the PTB7-CH$_3$NH$_3$PbI$_3$ composite /thin film was obtained when the PTB7 film was produced by the B1 solution.

7.3.2 Optical properties of the PTB7-CH$_3$NH$_3$PbI$_3$ composite layer produced using different PTB7 solution concentrations

UV-Vis absorption spectra were utilised to further investigate the effect of using various concentrations of the PTB7 solution on the composite perovskite films as shown in Figure 7.2. A wide absorption band in the wavelength range of 570-720 nm was identified for the PTB7-CH$_3$NH$_3$PbI$_3$ composite thin film produced by the B3 solution. Compared to the pristine perovskite thin film, the wide absorption shoulder at 680 nm reduces gradually when the PTB7-CH$_3$NH$_3$PbI$_3$ composite thin film was produced from the B1 solution instead of B2 solution.
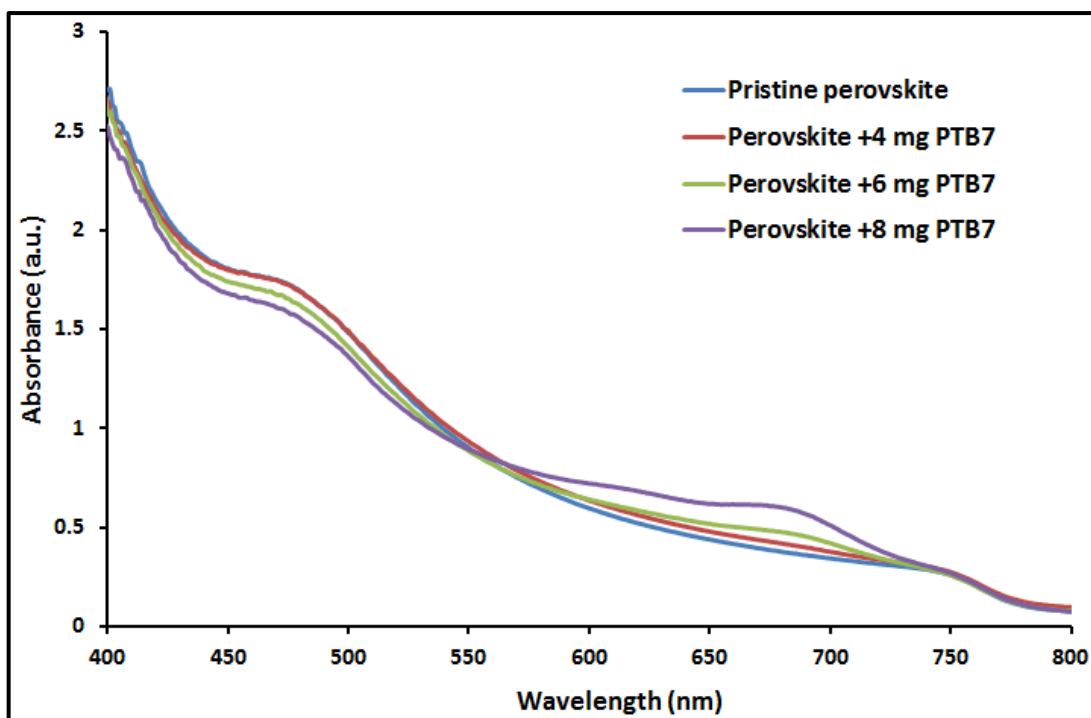
Figure 7.2 UV-Vis absorption spectra of $CH_3NH_3PbI_3$ and -PTB7-$CH_3NH_3PbI_3$ composite by different concentrations of the PTB7 solutions

7.3.3 Initial assessment of PV devices performance of PTB7-$CH_3NH_3PbI_3$ composite layers from different PTB7 solution concentrations

Figure 7.3 shows J-V characteristics of solar cells based on the PTB7-$CH_3NH_3PbI_3$ composites made with different concentrations of PTB7 solutions. A summary of the device parameters is given in Table 7.1. When solar cells were fabricated by the PTB7-$CH_3NH_3PbI_3$ composite produced from B3 solution, the device performance was very poor as shown in Figure 7.3. This can be ascribed to the high proportion of the residual PbI_2 phase within the composite perovskite and the high thickness of the $CH_3NH_3PbI_3$-PTB7 film. Consequently, this has generated the S-shaped J-V curve, increasing the recombination rate of negative and positive charges since the dissociated charge carriers must travel a long distance and be collected by electrodes. Furthermore, when a reduced concentration of the B2 solution was used to deposit the PTB7-$CH_3NH_3PbI_3$ composite layer for solar cells, a slight

improvement in the PCE was obtained due to the decreased PbI_2 residual and the smaller thickness of the $CH_3NH_3PbI_3$-PTB7 composite film compared to the composite film using B3 solution. The optimised device performance was finally achieved when B1 solution was utilized to fabricate the PTB7-$CH_3NH_3PbI_3$ composite for solar cells. Therefore, more detailed studies were carried out on solar cells based-on the PTB7-$CH_3NH_3PbI_3$ composite from the B1 solution.
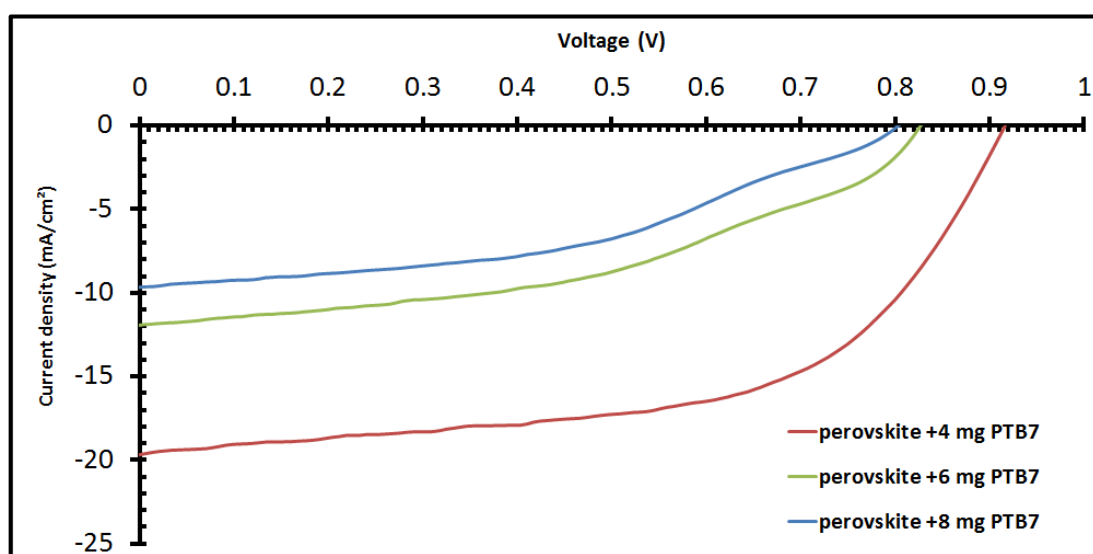
Figure 7.3 J–V characteristics of $CH_3NH_3PbI_3$/ PTB7 with different concentrations of PTB7 polymer

7.4 Results and discussion

7.4.1 Device architecture

The pristine $CH_3NH_3PbI_3$ perovskite and PTB7-$CH_3NH_3PbI_3$ composite films from B1 solution were used separately as photoactive layers to fabricate PV devices. The influence of PTB7 photoactive polymer on the PCE of the PV devices after it was introduced into $CH_3NH_3PbI_3$ perovskite were examined. Figure 7.4 presents the schematic device architecture of solar cells combined with cross-sectional scanning electron microscope (SEM) images of the integrated devices and their operational mechanism. The devices were constructed based on the planar-type architecture as

illustrated in Figure 7.4a; the device structure is comprised of indium tin oxide (ITO)/poly (3,4-ethylenedioxythiophene) polystyrene sulfonate (PEDOT:PSS)/ $CH_3NH_3PbI_3$ perovskite or PTB7-$CH_3NH_3PbI_3$ polymer-perovskite composite/ PCBM/bathocuproine (BCP)/Au, where the PEDOT:PSS and BCP layers act as the electron collecting and buffer layers respectively.
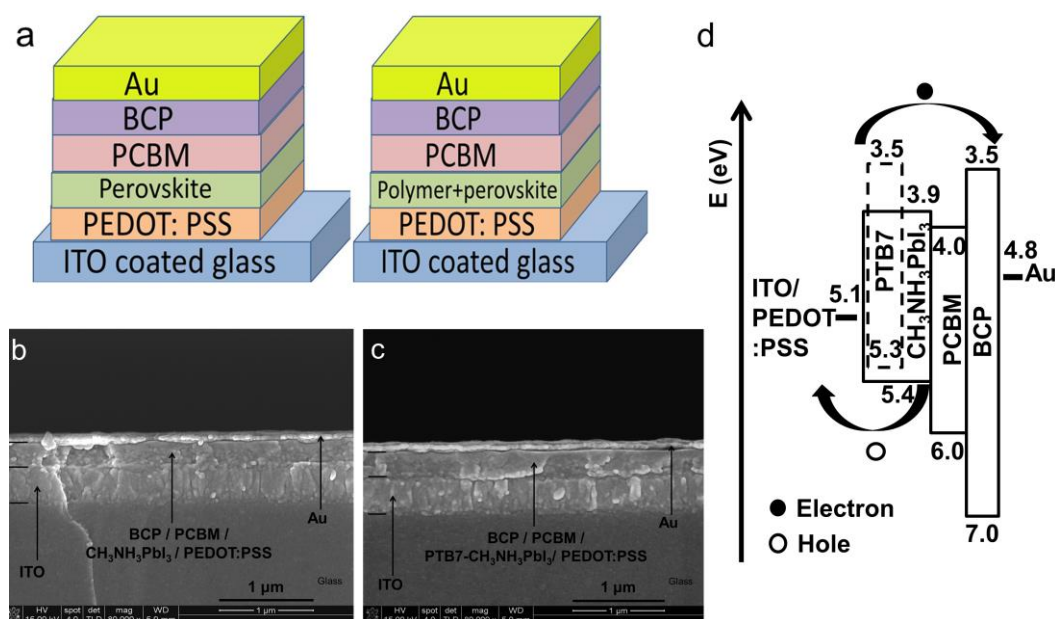
Figure 7.4 Device architecture and operational mechanism: (a) schematic architecture diagram of the PV devices fabricated from $CH_3NH_3PbI_3$ and PTB7-$CH_3NH_3PbI_3$ composite, respectively; (b&c) Cross-section SEM images of the real PV devices; (d) Energy level diagram of the PV device from PTB7-$CH_3NH_3PbI_3$ composite. Similar diagram for $CH_3NH_3PbI_3$ based PV devices can be drawn

Unfortunately, SEM cross section images shown in Figure 7.4b&c cannot provide sufficient contrast to differentiate the 4 layers of BCP, PCBM, $CH_3NH_3PbI_3$ or PTB7-$CH_3NH_3PbI_3$, and PEDOT:PSS. The estimated thicknesses of BCP, PCBM, and PEDOT:PSS are ~10 nm, ~50 nm, and ~30 nm, respectively. However, the combined four-layers illustrated in Figure 7.4b&c reveal the same thickness of ~300 nm for $CH_3NH_3PbI_3$ or PTB7-$CH_3NH_3PbI_3$ based solar cells, inferring that the photoactive layer of $CH_3NH_3PbI_3$ perovskite or PTB7-$CH_3NH_3PbI_3$ composite present the same thicknesses in both PV devices. Cross-section SEM images of a

single layer of $CH_3NH_3PbI_3$ perovskite or $PTB7-CH_3NH_3PbI_3$ composite on Si substrate, further confirm that the thickness of the photoactive layer is ~210 nm as shown in Figure 7.5 a &b.
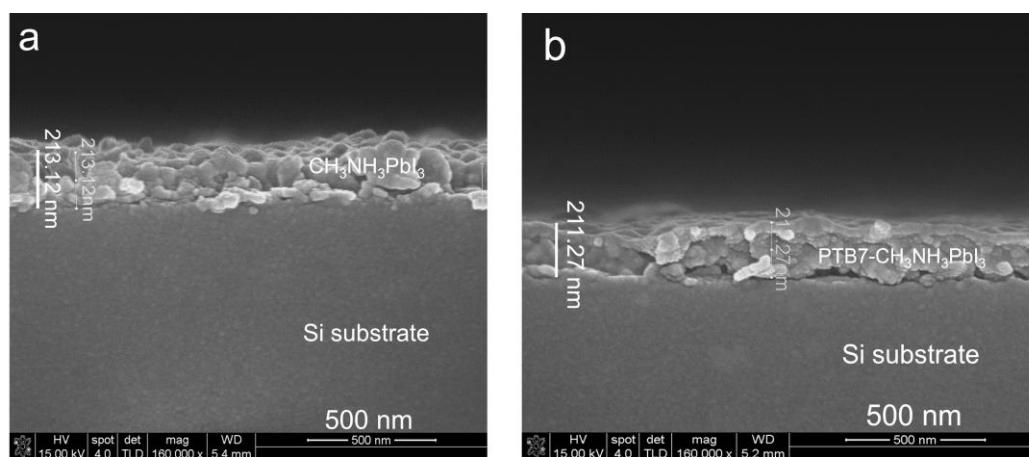
Figure 7.5 Cross-section SEM images of photoactive thin films on Si substrates, respectively: a) $CH_3NH_3PbI_3$ perovskite film; b) $PTB7-CH_3NH_3PbI_3$ composite film

Figure 7.4d illustrates the operation mode of the $PTB7-CH_3NH_3PbI_3$ composite-based PV device and the energy levels of each component layer in the device. PTB7 and $CH_3NH_3PbI_3$ absorb the UV−vis solar radiation and generate excitons, which can be dissociated into free holes and electrons at the interfaces of $PTB7-CH_3NH_3PbI_3$, $PEDOT:PSS/CH_3NH_3PbI_3$, and $CH_3NH_3PbI_3/PCBM$. The BCP layer is used as a buffer layer to form good contact with the Au electrode for electrons collection. Holes generated by PTB7 and $CH_3NH_3PbI_3$ are efficiently collected at the anode due to the high hole mobility of perovskite and the negligible energy level difference between the highest occupied molecular orbital of PTB7 and the valence band of $CH_3NH_3PbI_3$ perovskite.

7.4.2 UV- Visible light absorption and photoluminescence

Figure 7.6 presents photos of thin films and light absorbance of PTB7, $CH_3NH_3PbI_3$, and $PTB7-CH_3NH_3PbI_3$ composite films in the wavelength range of 400 to 800 nm

on glass substrates. A tremendous enhancement in the stability of $CH_3NH_3PbI_3$ perovskite due to forming the PTB7- $CH_3NH_3PbI_3$ composite material was verified after samples of PTB7, $CH_3NH_3PbI_3$, and PTB7-$CH_3NH_3PbI_3$ composite films were left in ambient environment for 168 hours with ~35% humidity.
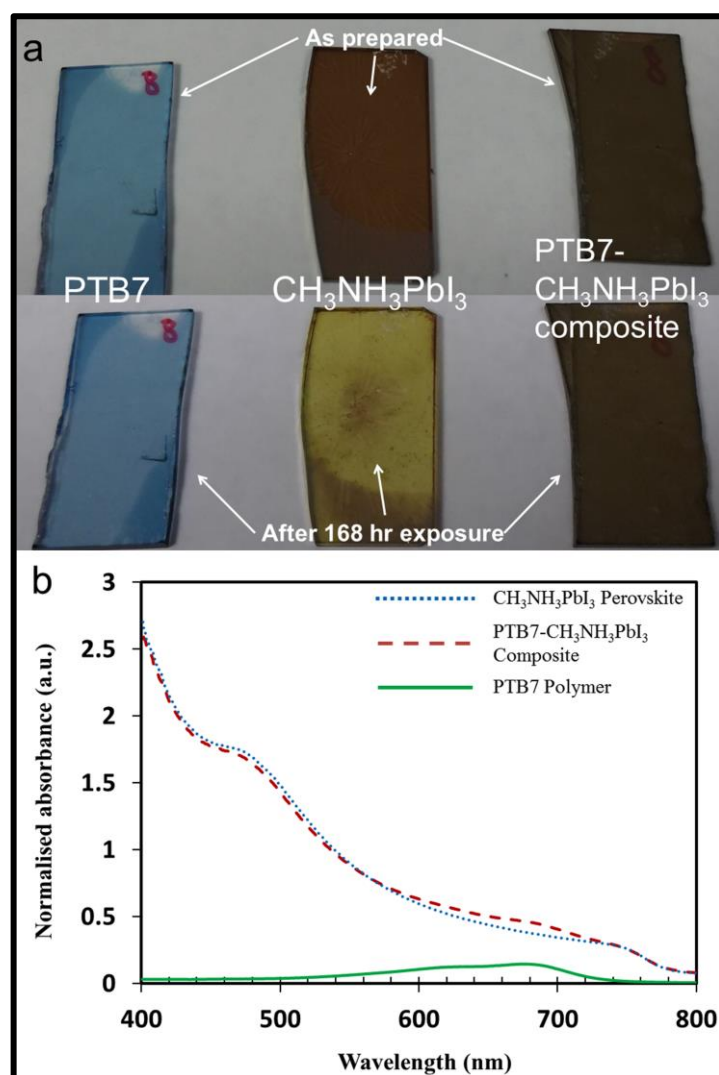
Figure 7.6 Photos of active layers at ambient environment with ~35% humidity and light absorbance after preparation: (a) Top: PTB7, $CH_3NH_3PbI_3$, and PTB7-$CH_3NH_3PbI_3$ composite films after preparation; Bottom: PTB7, $CH_3NH_3PbI_3$, and PTB7-$CH_3NH_3PbI_3$ composite films after 168 hours exposure to atmosphere; (b) Absorption spectra

As shown in Figure 7.6a, the initial dark-brown colour of the pristine $CH_3NH_3PbI_3$ perovskite changed to yellow colour after 168 hours of exposure to atmosphere due

to decomposition of $CH_3NH_3PbI_3$ into PbI_2 [242]. On the other hand PTB7-$CH_3NH_3PbI_3$ composite film has exhibited unaltered dark-brown colour after prolonged exposure to ambient atmosphere at RH of ~35%. The PTB7 polymer absorbs visible light mainly in the wavelength range of 550 to 750 nm as shown in Figure 7.6b. Contribution to harvesting of solar radiation via the incorporation of PTB7 into the $CH_3NH_3PbI_3$ perovskite film is evidenced in this wavelength range when compared with absorbance of the pristine $CH_3NH_3PbI_3$ film. The light absorption spectra of PTB7, $CH_3NH_3PbI_3$, and PTB7-$CH_3NH_3PbI_3$ composite are all illustrated in Figure 7.6b. A slightly lower light absorption for the PTB7-$CH_3NH_3PbI_3$ composite film against the pristine $CH_3NH_3PbI_3$ film is observed in the wavelength range of 400 to 550 nm, which is attributed to slightly smaller amount of $CH_3NH_3PbI_3$ by comparing the same thickness of photoactive layers with each other.

In addition, we have investigated the steady-state photoluminescence spectra of thin films for $CH_3NH_3PbI_3$ perovskite, PTB7-$CH_3NH_3PbI_3$ composite, and $CH_3NH_3PbI_3$ + PTB7 double-layer (i.e. a PTB7 thin film on top of the pristine $CH_3NH_3PbI_3$ film). Tests were performed under the same experimental conditions with the same size of samples on glass substrates.
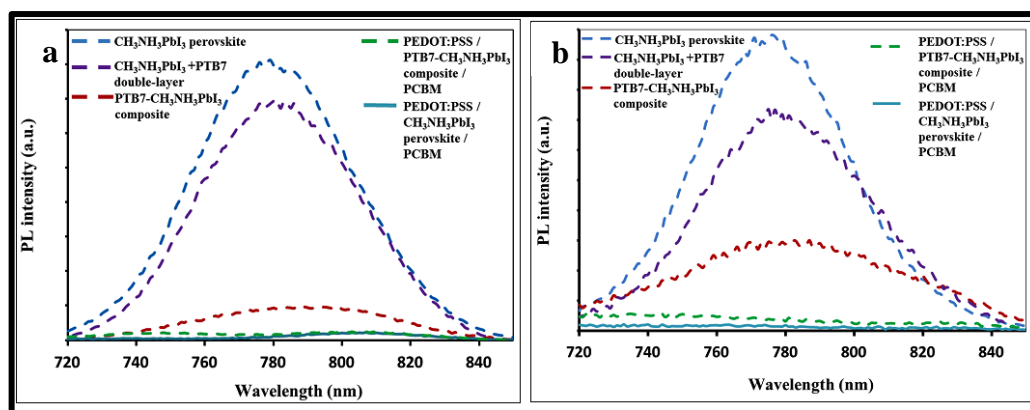
Figure 7.7 Emission peaks in steady-state photoluminescence spectra, under the same experimental conditions with the same size of samples on glass substrates upon excitation at: a) 400 nm, b) 600 nm

Emission peaks upon excitation at 400 nm in photoluminescence spectra for $CH_3NH_3PbI_3$, PTB7-$CH_3NH_3PbI_3$ composite films, and $CH_3NH_3PbI_3$ + PTB7 double-layer are shown separately in Figure 7.7. Thin films of the pristine $CH_3NH_3PbI_3$ and $CH_3NH_3PbI_3$ + PTB7 double-layers illustrate very close intensity for the photoluminescence peak at ~780 nm. Compared to thin films of $CH_3NH_3PbI_3$ and $CH_3NH_3PbI_3$ + PTB7 double-layer, the PTB7-$CH_3NH_3PbI_3$ composite film illustrates a clear quenching effect, confirming the effective charge transportation between PTB7 and $CH_3NH_3PbI_3$ within the blend. Steady-state photoluminescence spectra of triple layers of PEDOT:PSS, $CH_3NH_3PbI_3$ perovskite or PTB7-$CH_3NH_3PbI_3$ composite, and PCBM are also presented in Figure 7.7a, respectively. Again, significant quenching effects were observed. Photoluminescence peaks at ~780 nm nearly disappear after forming the planar-type architecture with PEDOT:PSS and PCBM. The same results in photoluminescence spectra were achieved in Figure 7.7b upon at excitation 600 nm except the smaller percentage of the quenching effect in comparison with those upon excitation 400 nm.

7.4.3 Morphological studying of perovskite layer with and without PTB7

Morphologies of $CH_3NH_3PbI_3$ and $PTB7$-$CH_3NH_3PbI_3$ composite thin films were investigated by SEM and atomic force microscope (AFM). Both thin films of $CH_3NH_3PbI_3$ perovskite and $PTB7$-$CH_3NH_3PbI_3$ composite illustrate morphologies with polycrystalline grains (perovskite phase) as shown in Figure 7.8. However, tiny gaps between some grains in the pristine $CH_3NH_3PbI_3$ film are observed in Figure 7.8a while fully connected grain phases appeared in the $PTB7$-$CH_3NH_3PbI_3$ composite film in Figure 7.8b. We also noticed that image contrast was reduced for the $PTB7$-$CH_3NH_3PbI_3$ composite film due to the addition of $PTB7$ into $CH_3NH_3PbI_3$ when compared with SEM images of the pristine $CH_3NH_3PbI_3$ film under the same operational parameters.
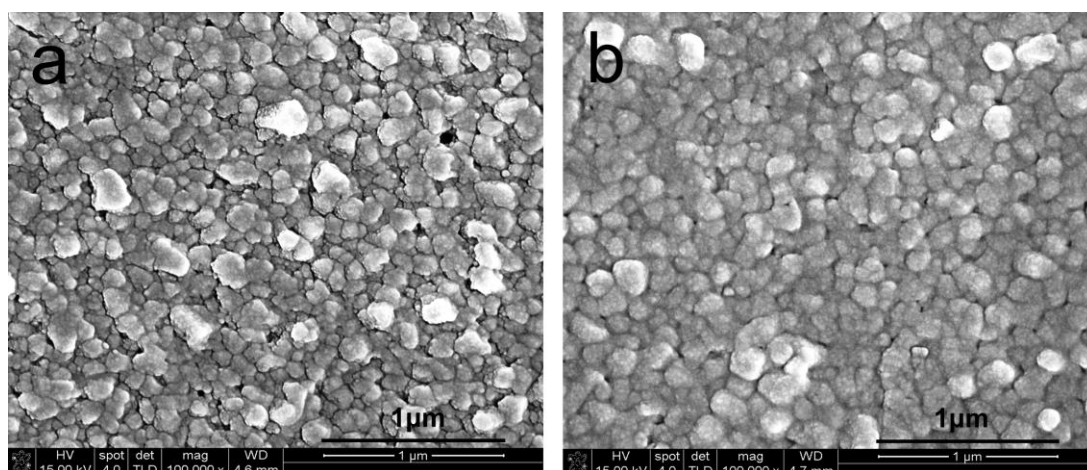
Figure 7.8 SEM images showing morphologies of photoactive thin films of: (a) $CH_3NH_3PbI_3$ perovskite; (b) $PTB7$-$CH_3NH_3PbI_3$ composite

Therefore, the investigation of morphologies by SEM inferred that the PTB7 polymer was blended into $CH_3NH_3PbI_3$ perovskite, forming nanocomposites with denser structures. AFM images are presented in Figure 7.9a-d, wherein different morphological structures were also revealed between $CH_3NH_3PbI_3$ perovskite and $PTB7$-$CH_3NH_3PbI_3$ composite thin films. The pristine $CH_3NH_3PbI_3$ perovskite film

has grains with the size of larger than 200 nm as shown in Figure 7.9a&c while the size of grains in the PTB7-$CH_3NH_3PbI_3$ composite film is less than 50 nm as illustrated in Figure 7.9b&d. Nevertheless, as observed in SEM images, grain sizes in the pristine $CH_3NH_3PbI_3$ and PTB7-$CH_3NH_3PbI_3$ composite films appeared to be very close at about 200 nm. Therefore, we assign that much smaller grain in AFM images for the PTB7-$CH_3NH_3PbI_3$ composite film was probably caused by the PTB7 polymer. This is because organic materials with light elements are difficult to obtain their direct high-contrast nano-structural images by SEM [243], and only larger grains of perovskites clearly appeared in morphologies in Figure 7.8. This may explain the difference in grain sizes by SEM and AFM separately.
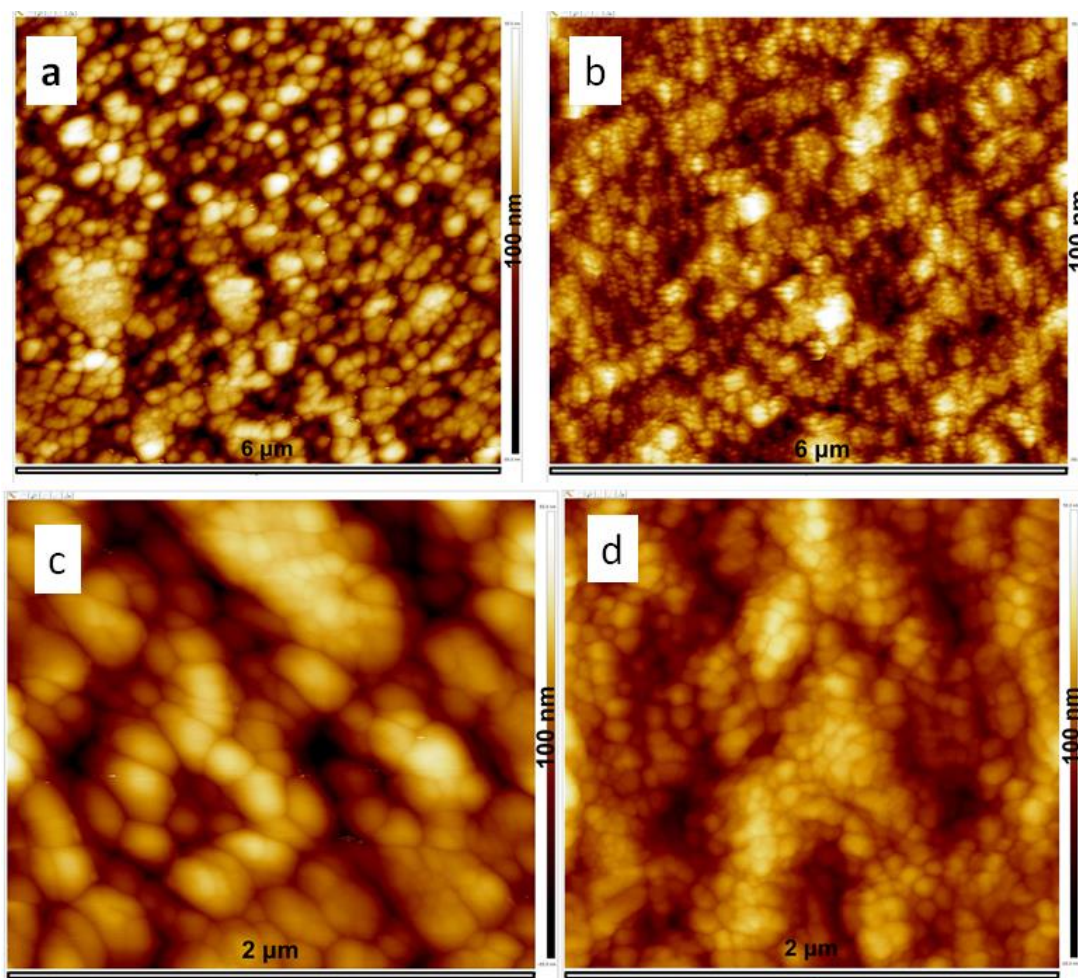
Figure 7.9 AFM images of photoactive thin films of: a) CH₃NH₃PbI₃ perovskites film; b) PTB7-CH₃NH₃PbI₃ composites films. Scale bars are 6 x 6 μm and height bars are 100 nm; and c) CH₃NH₃PbI₃ perovskite film, d) PTB7-CH₃NH₃PbI₃ composite film. Scale bars are 2 × 2 μ m and height bars are 100 nm

7.4.4 Structural study of perovskite films with and without PTB7

Structural characterisation of the photoactive layers has been carried out using XRD measurements. The XRD patterns obtained for both, $CH_3NH_3PbI_3$ and PTB7-$CH_3NH_3PbI_3$ composite films have verified their perovskite structures as presented in Figure 7.10.
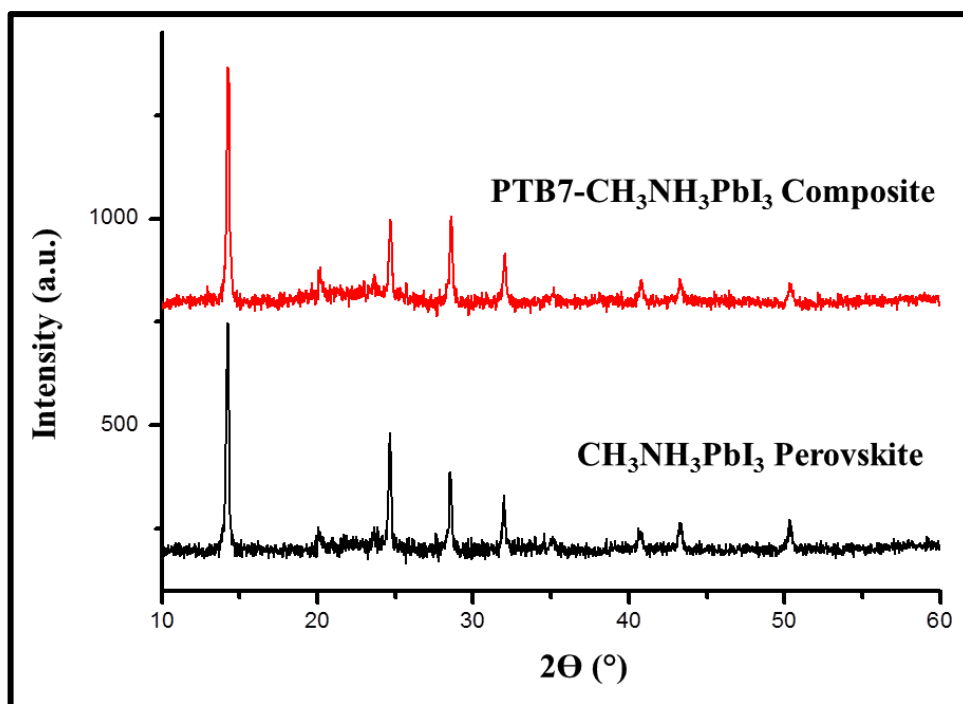
Figure 7.10 XRD patterns of $CH_3NH_3PbI_3$ perovskite and PTB7-$CH_3NH_3PbI_3$ composite thin films

7.4.5 FTIR analysis of the perovskite layers with and without PTB7

Figure 7.11 shows ATR-FTIR spectra of photoactive layers of $CH_3NH_3PbI_3$ perovskite and PTB7-$CH_3NH_3PbI_3$ composite thin films immediately after preparation. The measured spectra illustrate the main characteristic peaks of lead perovskite crystals specifically the wide strong peak at ~910 cm^{-1} for CH_3-NH_3 rock, a peak at ~989 cm^{-1} for C-N stretching band, peaks at ~1403 cm^{-1} and ~1439 cm^{-1} for C-H vibrational bands, and peaks at ~1482 cm^{-1} and ~1570 cm^{-1} for H-N vibration bands [242]. Most vibrational peaks for the pure $CH_3NH_3PbI_3$ perovskite either disappeared or became weak after exposure to ambient atmosphere for 3 hr although the dark colour of the film demonstrated no change. On the contrary, the PTB7-$CH_3NH_3PbI_3$ composite thin film maintained its vibrational peaks with only slightly reduced intensity after 48 hr exposure to ambient atmosphere. Its vibrational peaks however have disappeared after 168 hr exposure under ambient atmosphere,

159

presenting the same FTIR spectrum as that of the pure PTB7 film. However, no colour changed was revealed as previously shown in Figure 7.6a.
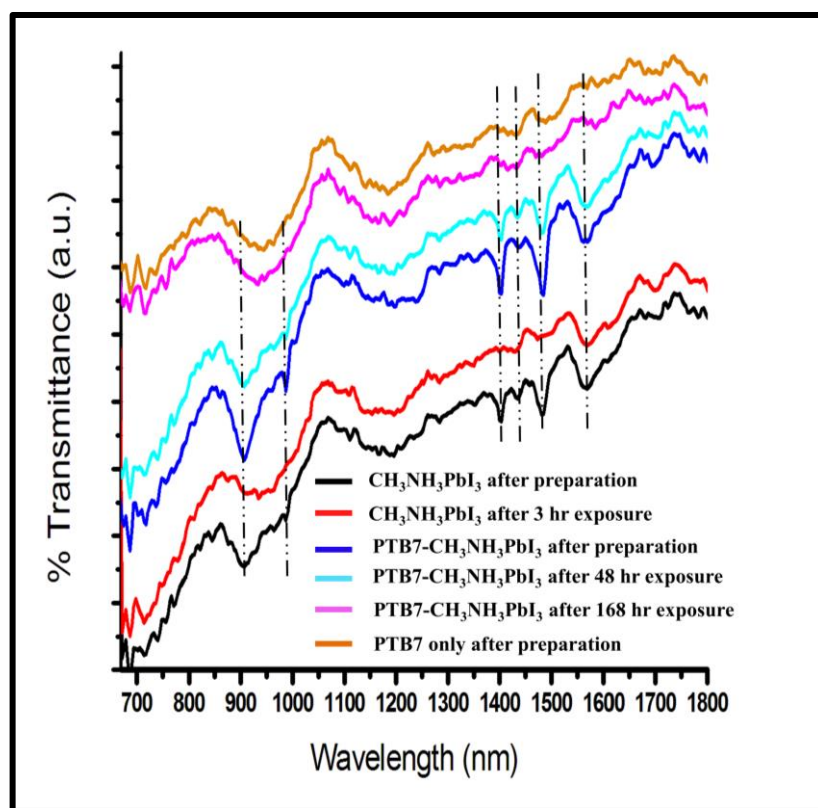
Figure 7.11 FTIR spectra of photoactive thin films at various conditions

7.4.6 Performance of the $CH_3NH_3PbI_3$ or PTB_7-$CH_3NH_3PbI_3$ based solar cells

The performance of solar cells based on $CH_3NH_3PbI_3$ or $PTB7$-$CH_3NH_3PbI_3$ composite photoactive layers has been studied by measuring their J-V characteristics and external quantum efficiency (EQE) spectra. The best J-V characteristics for both devices are separately shown in Figure 7.12a. The mean value for PCE of the PTB7-$CH_3NH_3PbI_3$ blend-based solar cells (the highest PCE = 14.4%) is 12.51% with the standard deviation of 0.99 and mean values of open circuit voltage (V_{oc}), short circuit current density (J_{sc}), and fill factor (FF) of 0.88 V, 22.28 mA/cm^2, and 63% with standard deviations of 0.028, 0.69, and 0.025 respectively as shown in Table 7.2. The mean PCE of $CH_3NH_3PbI_3$ based solar cells (the highest PCE = 14.3%) is

13.3% with standard deviation of 1.01 and the means of V_{oc}, J_{sc} and FF are 0.87 V, 21.7 mA/cm^2, and 70% with standard deviations of 0.02, 1.13, and 0.013 respectively, as presented in Table 7.3.
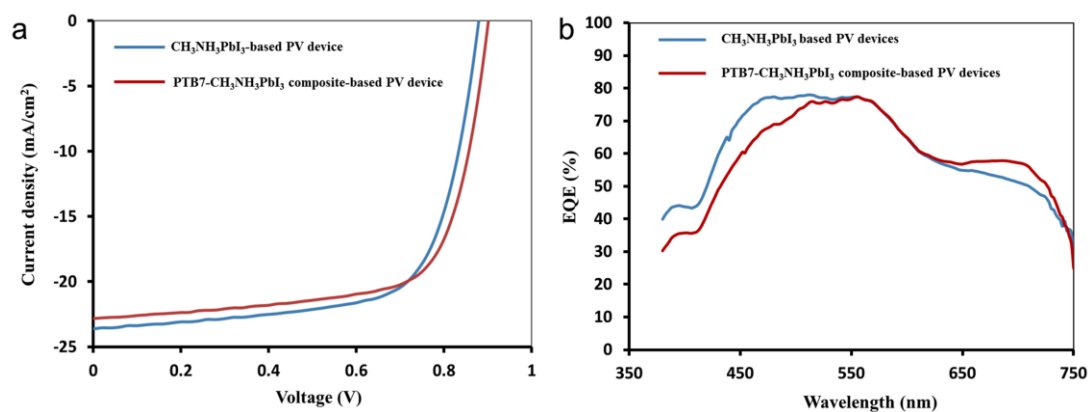
Figure 7.12 Performance of solar cells: (a) J-V curves of devices made with CH₃NH₃PbI₃ and PTB7-CH₃NH₃PbI₃ composite films; (b) EQE of devices with CH₃NH₃PbI₃ and PTB7-CH₃NH₃PbI₃ composite films

Table 7-2 Performance of solar cells based on PTB7-CH₃NH₃PbI₃ composite

No of device	V_{oc} (V)	J_{sc} (mA/cm²)	PCE (%)	FF
No 1	0.87	22.6	12.9	0.65
No 2	0.86	22.4	12.7	0.65
No 3	0.9	23.7	13.4	0.62
No 4	0.9	22.8	12.72	0.61
No 5	0.91	21.8	12.6	0.63
No 6	0.825	21.4	11.1	0.62
No 7	0.9	22.8	14.4	0.7
No 8	0.84	22	11.78	0.63
No 9	0.9	22.2	12.23	0.61
No 10	0.88	22.28	12.51	0.63
No 11	0.84	21.1	11.27	0.63
Mean range	0.88	22.28	12.51	0.63
Standard deviation	0.028	0.69	0.99	0.025

Table 7-3 Performance of solar cells based on CH$_3$NH$_3$PbI$_3$ perovskite

No of device	V$_{oc}$ (V)	J$_{sc}$ (mA/cm²)	PCE (%)	FF
No 1	0.9	22	13.9	0.7
No 2	0.88	23.6	14.3	0.69
No 3	0.87	22.7	14.02	0.7
No 4	0.86	20.2	12.72	0.73
No 5	0.87	22	13.6	0.71
No 6	0.84	21.9	13.09	0.71
No 7	0.86	20.88	12.76	0.70
No 8	0.91	21	13.02	0.68
No 9	0.88	23	14	0.69
No 10	0.85	20	12.07	0.71
Mean range	0.87	21.7	13.3	0.70
Standard deviation	0.02	1.13	1.01	0.013

The incorporation of PTB7 polymer into CH$_3$NH$_3$PbI$_3$ perovskite results in higher V$_{oc}$, more uniformly distributed higher J$_{sc}$ but slightly lower FF than those of the CH$_3$NH$_3$PbI$_3$ based devices when an equivalent thickness of the photoactive layer was fabricated in the solar cells, implying that charge transport and extraction can be more efficient in the composite photoactive layer. Since light absorbance of PTB7 mostly overlaps with CH$_3$NH$_3$PbI$_3$ in the wavelength range of ~550 to 750 nm, both solar cells present a close PCE. EQE spectra may provide additional information of

PTB7's contribution in charge generation and current output as shown in Figure 7.12b. One can clearly observe the difference between $CH_3NH_3PbI_3$ and PTB7-$CH_3NH_3PbI_3$ based solar cells in their EQE spectra. The $CH_3NH_3PbI_3$ based solar cells display higher EQE in the wavelength range of ~380 to 550 nm and more level curve in the wavelength range from ~480 to 550 nm than those of the PTB7-$CH_3NH_3PbI_3$ based solar cells. This is probably caused by alternation of microstructures and components in the photoactive materials due to the addition of PTB7 into the pristine $CH_3NH_3PbI_3$ when the same thickness of a photoactive layer was utilized in the solar cells. Contrary to that, a higher EQE is achieved for the PTB7-$CH_3NH_3PbI_3$ based solar cells in the wavelength range of about 610 to 750 nm and more level curve is presented in the wavelength range from ~650 to 700 nm.
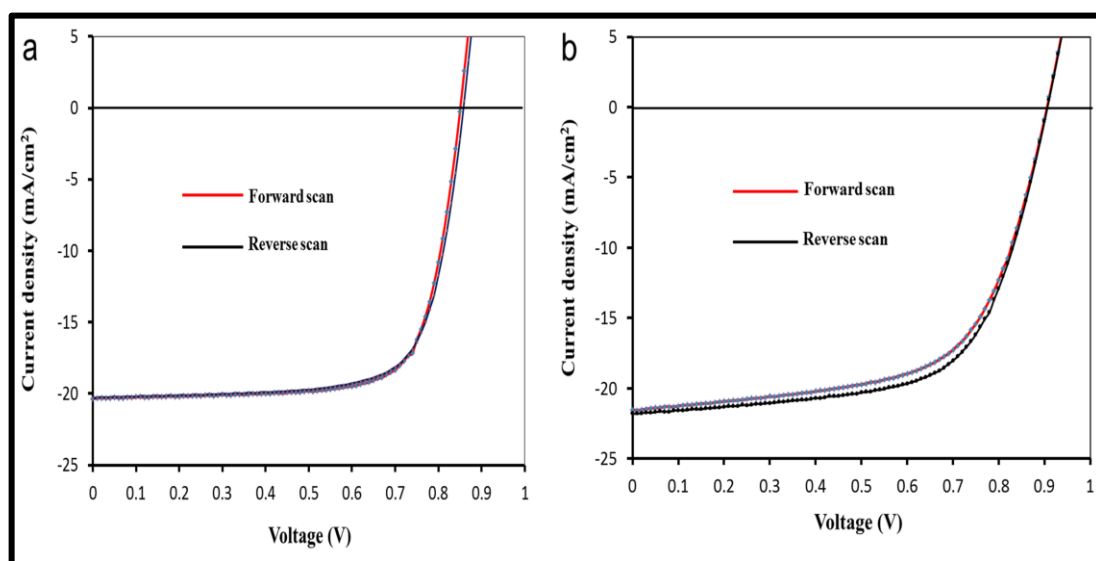
Figure 7.13 Hysteresis behavior of solar cells: a) J-V curves of $CH_3NH_3PbI_3$-based devices; b) J-V curves of PTB7-$CH_3NH_3PbI_3$-based devices. Both were measured under forward ($J_{sc} \rightarrow V_{oc}$) and reverse ($V_{oc} \rightarrow J_{sc}$) scan at the scan rate of 0.01 V/s

Moreover, the $CH_3NH_3PbI_3$ based solar cells have hysteresis-less behaviour as depicted in Figure 7.13a, indicating a good quality perovskite films and efficient charge extraction throughout the devices. Compared to the $CH_3NH_3PbI_3$ based PV

devices, the PTB7-$CH_3NH_3PbI_3$ based PV devices exhibits a tiny difference in the J-V curves between the forward scan and reverse scan at the scan rate of 0.01 V/s as shown in Figure 7.13b. Different hysteresis behaviour between $CH_3NH_3PbI_3$ and PTB7-$CH_3NH_3PbI_3$ based solar cells further evidences that the addition of the conjugated PTB7 polymer into $CH_3NH_3PbI_3$ perovskite may slightly change its property on charge extraction.

7.4.7 Life time study of the PV devices
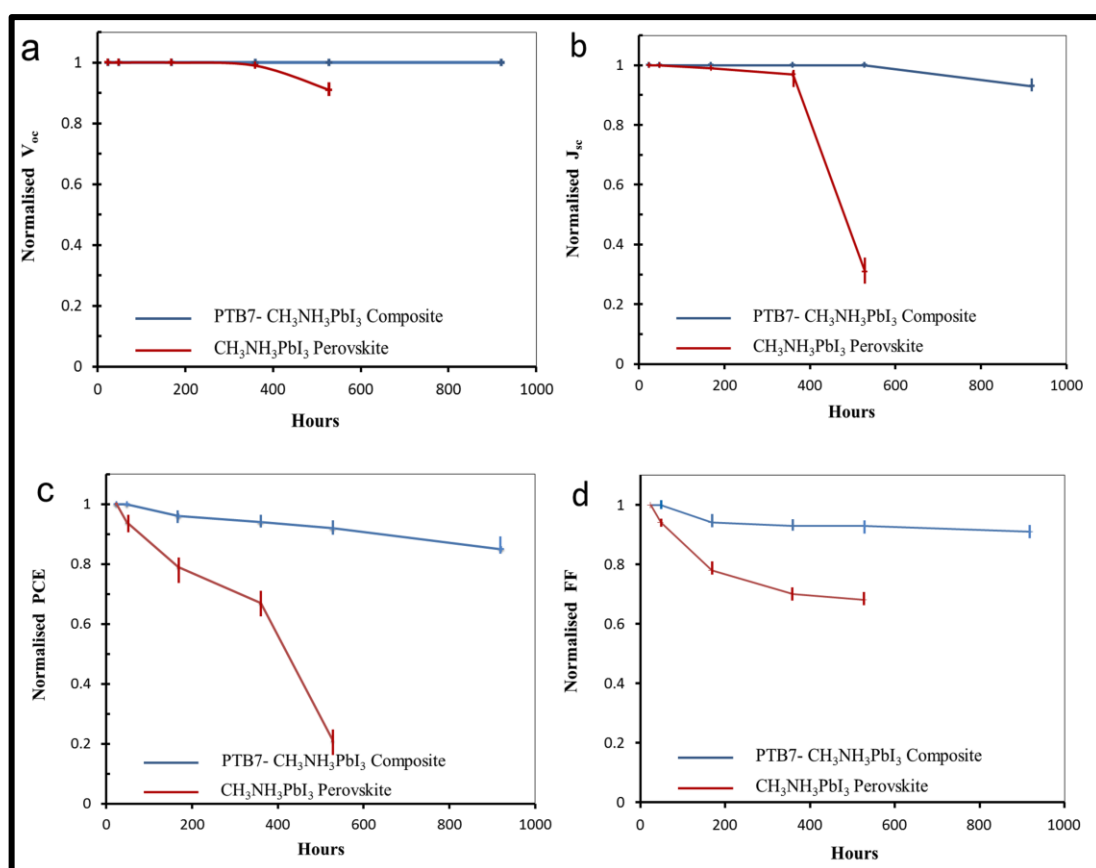
Figure 7.14 Performance variation of solar cells stored in the glovebox against time: (a) V_{oc} variation; (b) J_{sc} variation; (c) PCE variation; (d) FF variation

Solar cells of both types studied in section 7.4.6 were kept in the glovebox to investigate their stability under dark conditions before performing J-V characterisation under ambient environment. Figure 7.14a–d show that PTB7-$CH_3NH_3PbI_3$ based solar cells demonstrate significantly enhanced stability than the

CH$_3$NH$_3$PbI$_3$ based solar cells since the PTB7-CH$_3$NH$_3$PbI$_3$ composite film has exhibited a greatly increased resistance against decomposition of the CH$_3$NH$_3$PbI$_3$ perovskite as previously shown in Figure 7.6a. V$_{oc}$ of the PTB7-CH$_3$NH$_3$PbI$_3$ based solar cells maintained its original value after 920 hrs storage time while V$_{oc}$ of the CH$_3$NH$_3$PbI$_3$ based solar cells started to decrease after 360 hrs storage time and dropped to about 90% of its original value only after 528 hrs storage as illustrated in Figure 7.14a. Simultaneously, J$_{sc}$ of the PTB7-CH$_3$NH$_3$PbI$_3$ based solar cells exhibited no change before 528 hrs storage time and has retained about 93% of its original value after 920 hrs storage as shown in Figure 7.14b. Conversely, J$_{sc}$ of the CH$_3$NH$_3$PbI$_3$ based solar cells showed a noticeable decrease after 360 hrs storage while a sharply reduced value was measured at ~31% of its original value after 528 hrs storage. Changes in the PCE were calculated and obtained data are dipicted in Figure 7.14c. The PCE of the PTB7-CH$_3$NH$_3$PbI$_3$ based solar cells kept ~92% and ~85% of its original value respectively after 528 and 920 hrs storage time respectively. However, PCE of the CH$_3$NH$_3$PbI$_3$ based solar cells decreased to ~79% and ~21% of its original value only after 168 and 528 hrs storage time respectively. Figure 7.14d shows variation in the FF of PV devices of both types of active layers. FF of the PTB7-CH$_3$NH$_3$PbI$_3$ based solar cells stayed within more than 90% of its original value over the longest storage period of 920 hrs, while a gradually reduced FF of the CH$_3$NH$_3$PbI$_3$ based solar cells was observed, maintaining only about 47% of its original value after 528 hrs storage time. Therefore, one of the main factors on degrading performance of our solar cells is owing to the decrease of J$_{sc}$ that could be caused by alternation or decomposition of CH$_3$NH$_3$PbI$_3$ perovskite in the photoactive layer [244]. Performance degradation in ambient air with ~35% humidity for our solar cells were also recorded as shown in

Figure 7.15 a–d. Both devices showed nearly no change in the V_{oc} (Figure 7.15a)

after 172 hrs exposure to humid ambient. J_{sc}, PCE, and FF of both devices all

gradually reduced with exposure time. However, the PTB7-$CH_3NH_3PbI_3$ based solar

cells maintained ~68% J_{sc}, 64% PCE, and 75% FF of their original values after 172

hrs exposure while the $CH_3NH_3PbI_3$ based solar cells only kept ~37% J_{sc}, 18% PCE,

and 43% FF of their original values.
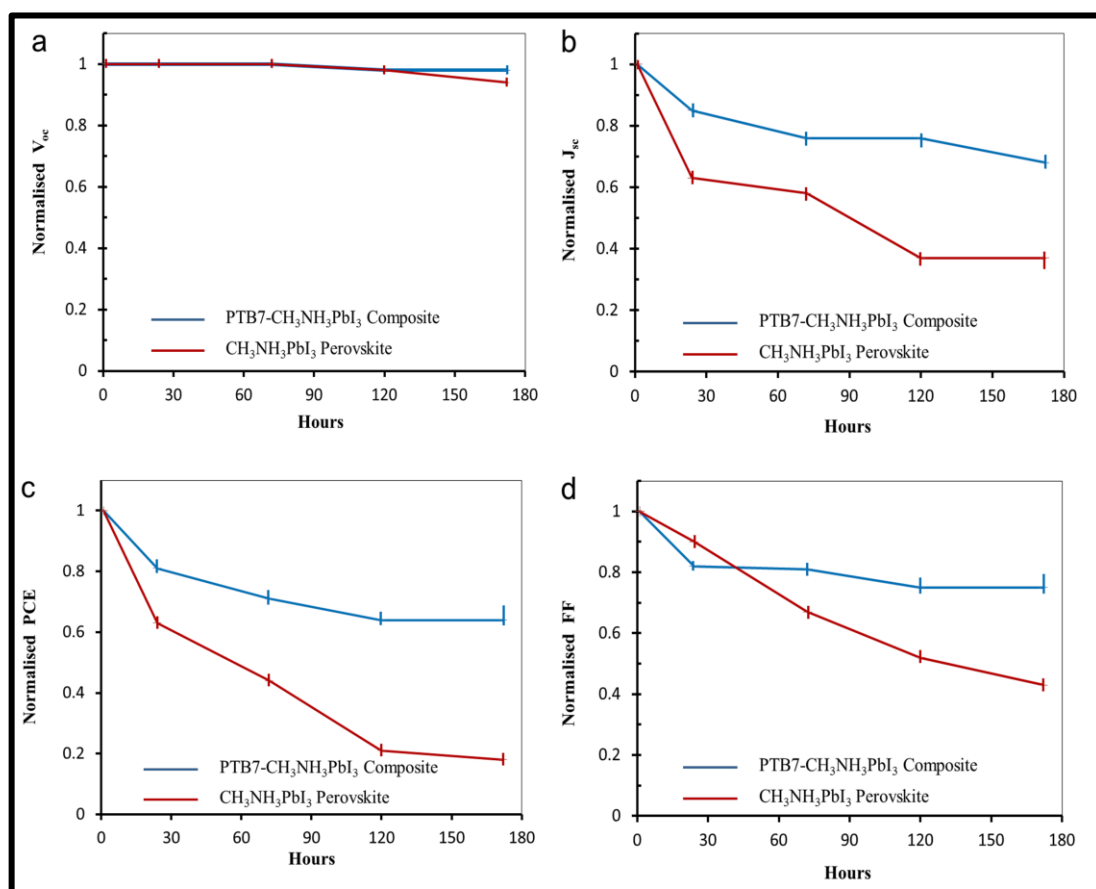
Figure 7.15   Performance degradation of solar cells under exposure to ambient air against time: a) V_{oc} variation; b) J_{sc} variation; c) PCE variation; d) FF variation

7.5 Conclusion

We have demonstrated the fabrication of organic-inorganic hybrid solution-

processed solar cells using blends of PTB7 polymer and $CH_3NH_3PbI_3$ perovskite as

the light-absorbing layer. The PHJ PV devices fabricated from $CH_3NH_3PbI_3$

perovskite or PTB7-CH$_3$NH$_3$PbI$_3$ composite with PCBM illustrated the same level of PCE. However, uniformly distributed high J$_{sc}$ in PV devices and significant improvement in stability against decomposition of CH$_3$NH$_3$PbI$_3$ perovskite were achieved in the PTB7-CH$_3$NH$_3$PbI$_3$ composite, leading to the stability enhancement of solar cells. Considering the existence of a variety of family materials either for photoactive conjugated polymers or organometal halide perovskites, various combinations are anticipated for exploring high performance and low-cost organic-inorganic hybrid solar cells.

Chapter 8 - Summary and outlook

8.1 Conclusion

The main purpose of this research is the development of three different types of active layer structures of photovoltaic devices and deduces the performance parameters of these devices and critically analyse the benefits arising from each structure. Numerous strategies have been introduced for each structure to enhance the performance of the solar cells. Low-temperature solution-processed methods were adopted in order to fabricate all the studied PV configurations. These configurations are summarised as below:

The first configuration:

❖ The dip coating technique was used to produce solution-processable inverted polymer solar cells. This is a promising method for the mass production of low-cost and large-scale PV devices due to its simplicity and high productivity in the lab. Power conversion efficiency of 3.4% was shown to be the best result for the currently studied dip-coated PV devices. Adding Petroleum ether was shown to play a key role in transforming the P3HT:PCBM blending to the gel which is compatible with the dip coating method.

❖ Thermal annealing and drying method of P3HT:PCBM has significantly impacted on the performance of the polymer solar cells after the sample was withdrawn from the solution. The self-organization of P3HT:PCBM layer can be improved by extending the time of film drying rate when it converted from the wet film to the dry film. The slow drying rate as shown to

contribute to the formation of self-organized and oriented structures of the P3HT:PCBM resulting in improvements in the morphology of the active layer and increasing the smoothness of the surface. Furthermore, thermal annealing improved the surface roughness of the active layer and enhanced its crystallinity.

❖ The spin- and dip- coated PEDOT:PSS thin films have demonstrated significantly different morphologies which might effect on the PCE of the PV devices.

The second configuration:

❖ OSSCM and TSSCM were employed to fabricate both perovskite films and solar cells at low temperature. Morphological studies and crystallisation behaviour of the $CH_3NH_3PbI_3$ films have been extensively studied using XRD, SEM and UV-vis absorption spectroscopy.

❖ Porous and fabric morphology of the $CH_3NH_3PbI_3$ films was observed by SEM when using OSSCM.

❖ Three major factors were shown to significantly impact on the crystallisation behaviour and control the morphology; these are the concentration of MAI solution, the reaction time between the MAI solution and the pre-coated PbI_2 and thermal annealing.

❖ The nucleation of the intermediate phase of perovskite was obtained in areas which have a concentration of MAI higher than concentration threshold (C_k). The growth of the intermediate phase of perovskite was determined by the reaction time between the MAI solution and PbI_2 film. Thermal annealing

170

played a key role in transforming the intermediate phase of the $CH_3NH_3PbI_3$ film to full perovskite phase after heating for 2 hours.

❖ It has been verified that the morphology of the $CH_3NH_3PbI_3$ films can be controlled when loaded 1 wt% MAI solution was loaded onto the pre-coated PbI_2 at allowed 60 sec of reaction time followed by thermal annealing at 100°C for 2 hours.

❖ The performance of the perovskite solar cells was examined using different concentrations of MAI solution to fabricate perovskite photoactive films. We have successfully fabricated highly reproducible PCE perovskite solar cells, with PCE of 12% was obtained. The hysteresis effect in the measured J-V characteristics was nearly negligible using TSSCM.

❖ The PCE of the perovskite solar cells was significantly enhanced up to 15 % by reducing the thickness of the PCBM layer.

❖ The impact of the buffer layer of BCP is essential to facilitate the transporting of the charge carriers and to improve the interfacial layer between the acceptor (PCBM) and the top electrode (Au).

The third configuration:

❖ We have developed a novel strategy to fabricate organic-inorganic hybrid perovskite solar cells via blending a conjugated polymer with a halide perovskite to produce a composite active material structure.

❖ Inserting the conjugated polymer into the perovskite layer has resulted in extending the light absorbance into full effective wavelengths range. Furthermore, the stability of the halide perovskite substantially enhanced

owing to the better moisture resistance of the conjugated polymer which provides a barrier protection to the halide perovskite.

❖ In order to optimise the photoactive composite material, different concentrations of photoactive polymer PTB7 (4mg, 6mg and 8mg in 1m L chlorobenzene) were applied between the PbI_2 and the MAI with the application of different reaction times of MAI onto the dried PTB7 film.

❖ The pure perovskite phase of the composite photoactive layer was obtained after the solution of 4 mg PTB7/1mL in chlorobenzene was applied onto the pre-coated PbI_2 followed by dropping 1 wt% MAI solution for 2.5 min onto PTB7 film.

❖ Although nearly the same performance was achieved for the composite perovskite and pristine perovskite devices, significant enhancement in the stability of the composite perovskite devices was achieved contrary to the normal perovskite which exhibited a decomposition of the perovskite film after 160 hours.

8.2 Future work

Despite the massive progress made on the development of highly performing perovskite solar cells, it is still far from industrial production. The stability issues and the toxicity of lead are still considered major concerns and finding solutions to solve these issues are vital to pave the way for commercialization. Therefore, the following routes for the fabrication of PV active layers may constitute parts of the solutions towards solving the above said issues:

❖ Using low band gap conjugated polymers in the composite halide perovskite to further enhance the light absorption and increase the stability of the perovskite devices will be one of our aims in future work.

❖ Replacing methylammonium (MA) with formamidinium (FA) using (THSSCM) will further enhance the stability of the perovskite devices.

❖ Replacing the Lead with non-toxic materials will be one of our aims in future work.

❖ Improving the scalability of the PV devices for all configurations studied in the current work and investigating the impacts of enlarging PV modules on the device performance.

❖ To continue the study of long term stability of perovskite-based PV devices using longer time periods (months, years).

Reference

[1]   J.   Staub,   International   Energy   Outlook,   2010. doi:10.1080/01636609609550217.

[2]   Faro, Price history of silicon PV cells, (2016). http://www.mena-forum.com/20929-2/price-history-of-silicon-pv-cells/.

[3]   World Energy Council, World Energy Resources: 2013 survey, World Energy Counc.   (2013)   11.   doi:http://www.worldenergy.org/wp-content/uploads/2013/09/Complete_WER_2013_Survey.pdf.

[4]   S. K. SOM, INTRODUCTION TO HEAT TRANSFER, 2008.

[5]   H. Wilsjire, J. Nielson, R. Hazlett, The American West at Risk: Science, Myths, and Politics of Land Abuse and Recovery, Oxford University Press, 2008.

[6]   Roland Hulstrom, Solar Resources, 1989.

[7]   S. G. N. Tiwari, Arvind Tiwari, Handbook of Solar Energy: Theory, Analysis and Applications, 2016.

[8]   Muhammad Iqbal, An Introduction To Solar Radiation, 2012.

[9]   Greg P. Smestad, Optoelectronics of Solar Cells, 2002.

[10] CHETAN   SINGH   SOLANKI,   Solar   Photovoltaics: Fundamentals, Technologies And Applications, 2015.

[11] A. Band, G. Inzelt, F. Scholz, Electrochemical Dictionary, Springer Science & Business Media, 2012.

[12]   Frederik C. Krebs, Polymeric Solar Cells: Materials, Design, Manufacture, 2010.

[13]   T.H. Han, H.-S. Moon, J.O. Hwang, S. Il Seok, S.H. Im, S.O. Kim, Peptide-templating dye-sensitized solar cells, Nanotechnology. 21 (2010) 185601. doi:10.1088/0957-4484/21/18/185601.

[14]   W. Yoon, J.E. Boercker, M.P. Lumb, D. Placencia, E.E. Foos, J.G. Tischler, Enhanced open-circuit voltage of PbS nanocrystal quantum dot solar cells., Sci. Rep. 3 (2013) 2225. doi:10.1038/srep02225.

[15]   G. Li, R. Zhu, Y. Yang, Polymer solar cells, Nat. Photonics. 6 (2012) 153–161. doi:10.1038/nphoton.2012.11.

[16]   P. Docampo, J.M. Ball, M. Darwich, G.E. Eperon, H.J. Snaith, Efficient organometal trihalide perovskite planar-heterojunction solar cells on flexible polymer substrates., Nat. Commun. 4 (2013) 2761. doi:10.1038/ncomms3761.

[17]   R. Sondergaard, M. Hosel, D. Angmo, T.T. Larsen-Olsen, F.C. Krebs, Roll-to-roll fabrication of polymer solar cells, Mater. Today. 15 (2012) 36–49. doi:10.1016/S1369-7021(12)70019-6.

[18]   R.R. Sondergaard, M. Hosel, F.C. Krebs, Roll-to-Roll fabrication of large area functional organic materials, J. Polym. Sci. Part B Polym. Phys. 51 (2013) 16–34. doi:10.1002/polb.23192.

[19]   F.C. Krebs, N. Espinosa, M. Hosel, R.R. Sondergaard, M. Jorgensen, 25th anniversary article: Rise to power - OPV-based solar parks, Adv. Mater. 26 (2014) 29–39. doi:10.1002/adma.201302031.

[20] M. Jorgensen, K. Norrman, F.C. Krebs, Stability/degradation of polymer solar cells, Sol. Energy Mater. Sol. Cells. 92 (2008) 686–714. doi:10.1016/j.solmat.2008.01.005.

[21] J. Zhao, Y. Li, G. Yang, K. Jiang, H. Lin, H. Ade, et al., Efficient organic solar cells processed from hydrocarbon solvents, Nat. Energy. 1 (2016) 15027. doi:10.1038/nenergy.2015.27.

[22] S. Shi, Y. Li, X. Li, H. Wang, Advancements in all-solid-state hybrid solar cells based on organometal halide perovskites, Mater. Horizons. 0 (2015) 1–28. doi:10.1039/C4MH00236A.

[23] A. Becquerel, Recherches sur les effets de la radiation chimique de la lumiere solaire au moyen des courants electriques, Comptes Rendus L´Academie Des Sci. 9 (1839) 145–149.

[24] R. Adams, WG, Day, The Action of Light on Selenium, Proc. R. Soc. London. A25 (1877) 113.

[25] A. Luque, S.S. Hegedus, Status, Trends, Challenges and the Bright Future of Solar Electricity from Photovoltaics, 2003. http://www3.interscience.wiley.com/cgi-bin/summary/109867793/SUMMARY.

[26] L.L. Kazmerski, Photovoltaics: A review of cell and module technologies, Renew. Sustain. Energy Rev. 1 (1997) 71–170. doi:10.1016/S1364-0321(97)00002-6.

[27] H. Spanggaard, F.C. Krebs, A brief history of the development of organic and polymeric photovoltaics, Sol. Energy Mater. Sol. Cells. 83 (2004) 125–146.

doi:10.1016/j.solmat.2004.02.021.

[28] M.A. Green, K. Emery, D.L. King, S. Igari, W. Warta, Solar cell efficiency tables (version 25), Prog. Photovoltaics Res. Appl. 13 (2005) 49–54. doi:10.1002/pip.598.

[29] Y. Zhou, M. Yang, W. Wu, A.L. Vasiliev, K. Zhu, N.P. Padture, Room-Temperature Crystallization of Hybrid-Perovskite Thin Films via Solvent-Solvent Extraction for High-Performance Solar Cells, J. Mater. Chem. A. 3 (2015) 8178–8184. doi:10.1039/C5TA00477B.

[30] C.W. Tang, Two-layer organic photovoltaic cell, Appl. Phys. Lett. 48 (1986) 183–185. doi:10.1063/1.96937.

[31] G. Yu, J. Gao, J.C. Hummelen, F. Wudl, A.J. Heeger, Polymer Photovoltaic Cells - Enhanced Efficiencies Via a Network of Internal Donor-Acceptor Heterojunctions, Science (80-.). 270 (1995) 1789–1791. doi:10.1126/science.270.5243.1789.

[32] C. Yumusak, D. a M. Egbe, Organic Bulk Heterojunction Solar Cells Based on Poly (p-Phenylene-Vinylene) Derivatives, Sol. Cells. (2010).

[33] Z.M. Schropp. R, Amorphous and Microcystalline Silicon Solar Cells: Modelling, Materials and Device Technology, 1998.

[34] Kumar. Pankaj, Organic Solar Cells: Device Physics, Processing, Degradation, and Prevention, 2016.

[35] R.W. Birkmire, E. Eser, Polycrystalline thin film solar cells: Present status and future potential, Ann. Rev. Mater. Sci. 27 (1997) 625–653.

[36] M. Fonrodona, J. Escarré, F. Villar, D. Soler, J.M. Asensi, J. Bertomeu, et al., PEN as substrate for new solar cell technologies, Sol. Energy Mater. Sol. Cells. 89 (2005) 37–47. doi:10.1016/j.solmat.2004.12.006.

[37] P. Schilinsky, C. Waldauf, C.J. Brabec, Performance analysis of printed bulk heterojunction solar cells, Adv. Funct. Mater. 16 (2006) 1669–1672. doi:10.1002/adfm.200500581.

[38] H. Hoppe, N. Sariciftci, Organic solar cells: An overview, J. Mater. Res. 19 (2004) 1924–1945. doi:10.1557/JMR.2004.0252.

[39] M. Saliba, T. Matsui, K. Domanski, J.-Y. Seo, A. Ummadisingu, S.M. Zakeeruddin, et al., Incorporation of rubidium cations into perovskite solar cells improves photovoltaic performance, Science (80-.). 354 (2016) 206. doi:10.1126/science.aah5557.

[40] R. a. J. Janssen, J.C. Hummelen, N.S. Sariciftci, Polymer–Fullerene Bulk Heterojunction Solar Cells, MRS Bull. 30 (2005) 33–36. doi:10.1557/mrs2005.6.

[41] J.-M. Nunzi, Organic photovoltaic materials and devices, Comptes Rendus Phys. 3 (2002) 523–542. doi:10.1016/S1631-0705(02)01335-X.

[42] F. Hao, C.C. Stoumpos, D.H. Cao, R.P.H. Chang, M.G. Kanatzidis, Lead-free solid-state organic-inorganic halide perovskite solar cells, Nat. Photonics. 8 (2014) 489–494. doi:10.1038/nphoton.2014.82.

[43] S. Gu, H. Neugebauer, N.S. Sariciftci, Conjugated Polymer-Based Organic Solar Cells, (2007) 1324–1338. doi:10.1021/cr050149z.

[44]   S. Brittman, G.W.P. Adhyaksa, E.C. Garnett, The expanding world of hybrid perovskites: materials properties and emerging applications, MRS Commun. 5 (2015) 7–26. doi:10.1557/mrc.2015.6.

[45]   J. Xiao, J. Shi, D. Li, Q. Meng, Perovskite thin-film solar cell: excitation in photovoltaic science, Sci. China Chem. 58 (2015) 221–238. doi:10.1007/s11426-014-5289-2.

[46]   Q. Lin, A. Armin, R.C.R. Nagiri, P.L. Burn, P. Meredith, Electro-optics of perovskite solar cells, Nat. Photonics. 9 (2015) 106–112. doi:10.1038/nphoton.2014.284.

[47]   G. Xing, N. Mathews, S. Sun, S.S. Lim, Y.M. Lam, M. Gratzel, et al., Long-Range Balanced Electron- and Hole-Transport Lengths in Organic-Inorganic CH3NH3PbI3, Science (80-.). 342 (2013) 344–347. doi:10.1126/science.1243167.

[48]   S.D. Stranks, G.E. Eperon, G. Grancini, C. Menelaou, M.J.P. Alcocer, T. Leijtens, et al., Electron-Hole Diffusion Lengths Exceeding, 342 (2013) 341–345.

[49]   K.S. Marder, Seth. Lee, Photoresponsive polymers, Springer Science & Business Media, 2008.

[50]   J.H. Hui Huang, Organic and Hybrid Solar Cells, Psychology. (2012) 2012. doi:10.1007/978-3-319-10855-1.

[51]   T.L. Benanti, D. Venkataraman, Organic solar cells: An overview focusing on active layer morphology, Photosynth. Res. 87 (2006) 73–81. doi:10.1007/s11120-005-6397-9.

[52]   F.C. Krebs, Polymeric solar cells: materials, design, manufacture., 2010.

[53]   C. Wang, X. Xu, W. Zhang, J. Bergqvist, Y. Xia, X. Meng, et al., Low Band Gap Polymer Solar Cells With Minimal Voltage Losses, Adv. Energy Mater. 6 (2016). doi:10.1002/aenm.201600148.

[54]   S.E. Shaheen, C.J. Brabec, N.S. Sariciftci, F. Padinger, T. Fromherz, J.C. Hummelen, 2.5% Efficient Organic Plastic Solar Cells, Appl. Phys. Lett. 78 (2001) 841–843. doi:10.1063/1.1345834.

[55]   D. Chirvase, Z. Chiguvare, M. Knipper, J. Parisi, V. Dyakonov, J.C. Hummelen, Electrical and optical design and characterisation of regioregular poly(3-hexylthiophene-2,5diyl)/fullerene-based heterojunction polymer solar cells, Synth. Met. 138 (2003) 299–304. doi:10.1016/S0379-6779(03)00027-4.

[56]   F. Padinger, R.S. Rittberger, N.S. Sariciftci, F. Padinger, R.S. Rittberger, R.S. Rittberger, et al., Effects of postproduction treatment om plastic solar cells, Adv. Funct. Mater. 13 (2003) 85. doi:10.1002/adfm.200390011.

[57]   M.T. Dang, L. Hirsch, G. Wantz, P3HT:PCBM, best seller in polymer photovoltaic research, Adv. Mater. 23 (2011) 3597–3602. doi:10.1002/adma.201100792.

[58]   Y.-W. Su, S.-C. Lan, K.-H. Wei, Organic photovoltaics, Mater. Today (Oxford, U. K.). 15 (2012) 554–562. doi:10.1016/s1369-7021(13)70013-0.

[59]   X. Guo, N. Zhou, S.J. Lou, J. Smith, D.B. Tice, J.W. Hennek, et al., Polymer solar cells with enhanced fill factors, Nat. Photonics. 7 (2013) 825–833. doi:10.1038/nphoton.2013.207.

[60] J. You, L. Dou, K. Yoshimura, T. Kato, K. Ohya, T. Moriarty, et al., A polymer tandem solar cell with 10.6% power conversion efficiency., Nat. Commun. 4 (2013) 1446. doi:10.1038/ncomms2411.

[61] J.-D. Chen, C. Cui, Y.Y.-Q. Li, L. Zhou, Q.-D. Ou, C. Li, et al., Single-Junction Polymer Solar Cells Exceeding 10% Power Conversion Efficiency, Adv. Mater. 27 (2015) 1035–1041. doi:10.1002/adma.201404535.

[62] Z. He, B. Xiao, F. Liu, H. Wu, Y. Yang, S. Xiao, et al., Single-junction polymer solar cells with high efficiency and photovoltage, Nat. Photonics. 9 (2015) 174–179. doi:10.1038/nphoton.2015.6.

[63] S. Karuthedath, T. Sauermann, H.-J. Egelhaaf, R. Wannemacher, C.J. Brabec, L. Lüer, The effect of oxygen induced degradation on charge carrier dynamics in P3HT:PCBM and Si-PCPDTBT:PCBM thin films and solar cells, J. Mater. Chem. A. 3 (2015) 3399–3408. doi:10.1039/c4ta06719c.

[64] C.J. Brabec, N.S. Sariciftci, J.C. Hummenlen, Plastic solar cells, Adv. Mater. 11 (2001) 15–26.

[65] X. Yang, J. Loos, Toward high-performance polymer solar cells: The importance of morphology control, Macromolecules. 40 (2007) 1353–1362. doi:10.1021/ma0618732.

[66] Z. Zheng, S. Zhang, J. Zhang, Y. Qin, W. Li, R. Yu, et al., Over 11% Efficiency in Tandem Polymer Solar Cells Featured by a Low-Band-Gap Polymer with Fine-Tuned Properties, Adv. Mater. (2016) 5133–5138. doi:10.1002/adma.201600373.

[67] C.J. Brabec, J.R. Durrant, Solution-processed organic solar cells, MRS Bull.

33 (2008) 670–675. doi:10.1557/mrs2008.138.

[68] Y.H. Chang, S.R. Tseng, C.Y. Chen, H.F. Meng, E.C. Chen, S.F. Horng, et al., Polymer solar cell by blade coating, Org. Electron. Physics, Mater. Appl. 10 (2009) 741–746. doi:10.1016/j.orgel.2009.03.001.

[69] Y. Rahaq, H. Wang, V. Kumar, Fabricating the solution-processable inverted photovoltaic devices by the dip-coating method, Org. Electron. Physics, Mater. Appl. 15 (2014) 984–990. doi:10.1016/j.orgel.2014.02.006.

[70] F. Aziz, A.F. Ismail, Spray coating methods for polymer solar cells fabrication: A review, Mater. Sci. Semicond. Process. 39 (2015) 416–425. doi:10.1016/j.mssp.2015.05.019.

[71] J.H. Lee, T. Sagawa, S. Yoshikawa, Morphological and topographical characterizations in spray coated organic solar cells using an additional solvent spray deposition, Org. Electron. Physics, Mater. Appl. 12 (2011) 2165–2173. doi:10.1016/j.orgel.2011.09.009.

[72] E.B. W. Geffcken, Deutsches Reichs patent, Jenaer Glaswerk Schott & Gen, 1939.

[73] F.C. Krebs, Fabrication and processing of polymer solar cells: A review of printing and coating techniques, Sol. Energy Mater. Sol. Cells. 93 (2009) 394–412. doi:10.1016/j.solmat.2008.10.004.

[74] W. Tress, Organic Solar Cells: Theory, Experiment, and Device Simulation, 2014.

[75] K. Wang, C. Liu, P. Du, J. Zheng, X. Gong, Bulk heterojunction perovskite

hybrid solar cells with large fill factor, Energy Environ. Sci. 0 (2015). doi:10.1039/C5EE00222B.

[76]   Q. Chen, N. De Marco, Y. (Michael) Yang, T.-B. Song, C.-C. Chen, H. Zhao, et al., Under the spotlight: The organic–inorganic hybrid halide perovskite for optoelectronic applications, Nano Today. 10 (2015) 355–396. doi:http://dx.doi.org/10.1016/j.nantod.2015.04.009.

[77]   A. Kojima, K. Teshima, Y. Shirai, T. Miyasaka, Organometal Halide Perovskites as Visible-Light Sensitizers for Photovoltaic Cells, J. Am. Chem. Soc. 131 (2009) 6050–6051. doi:10.1021/ja809598r.

[78]   J.-H. Im, C.-R. Lee, J.-W. Lee, S.-W. Park, N.-G. Park, 6.5% Efficient Perovskite Quantum-Dot-Sensitized Solar Cell, Nanoscale. 3 (2011) 4088. doi:10.1039/c1nr10867k.

[79]   H.-S. Kim, C.-R. Lee, J.-H. Im, K.-B. Lee, T. Moehl, A. Marchioro, et al., Lead iodide perovskite sensitized all-solid-state submicron thin film mesoscopic solar cell with efficiency exceeding 9%., Sci. Rep. 2 (2012) 591. doi:10.1038/srep00591.

[80]   M.M. Lee, J. Teuscher, T. Miyasaka, T.N. Murakami, H.J. Snaith, Efficient Hybrid Solar Cells Based on Meso-Superstructured Organometal Halide Perovskite, Science (80-.). 338 (2012) 643–647. doi:10.1126/science.1228604.

[81]   P.P. Boix, K. Nonomura, N. Mathews, S.G. Mhaisalkar, Current progress and future perspectives for organic/inorganic perovskite solar cells, Mater. Today. 17 (2014) 16–23. doi:10.1016/j.mattod.2013.12.002.

[82] L. Etgar, P. Gao, Z. Xue, Q. Peng, A.K. Chandiran, B. Liu, et al., Mesoscopic CH3NH3PbI3/TiO2 Heterojunction Solar Cells, J. Am. Chem. Soc. 134 (2012) 17396–17399. doi:10.1021/ja307789s.

[83] J. Burschka, N. Pellet, S.-J. Moon, R. Humphry-Baker, P. Gao, M.K. Nazeeruddin, et al., Sequential deposition as a route to high-performance perovskite-sensitized solar cells., Nature. 499 (2013) 316–9. doi:10.1038/nature12340.

[84] M. Liu, M.B. Johnston, H.J. Snaith, Efficient planar heterojunction perovskite solar cells by vapour deposition., Nature. 501 (2013) 395–8. doi:10.1038/nature12509.

[85] P. Gao, M. Grätzel, M.K. Nazeeruddin, Organohalide lead perovskites for photovoltaic applications, Energy Environ. Sci. 7 (2014) 2448. doi:10.1039/C4EE00942H.

[86] M. Saliba, T. Matsui, K. Domanski, J.-Y. Seo, A. Ummadisingu, S.M. Zakeeruddin, et al., Incorporation of rubidium cations into perovskite solar cells improves photovoltaic performance, Science (80-.). 354 (2016) 206. doi:10.1126/science.aah5557.

[87] Z. Cheng, J. Lin, Layered organic–inorganic hybrid perovskites: structure, optical properties, film preparation, patterning and templating engineering, CrystEngComm. 12 (2010) 2646. doi:10.1039/c001929a.

[88] M.A. Loi, J.C. Hummelen, Hybrid solar cells: Perovskites under the Sun, Nat Mater. 12 (2013) 1087–1089. doi:10.1038/nmat3815.

[89] S. Gamliel, L. Etgar, Organo-metal perovskite based solar cells: sensitized

versus planar architecture, RSC Adv. 4 (2014) 29012. doi:10.1039/C4RA03981E.

[90] V.A. Online, S. Luo, W. a Daoud, Recent progress in organic – inorganic halide perovskite solar cells : mechanisms and material, J. Mater. Chem. A Mater. Energy Sustain. 3 (2015) 8992–9010. doi:10.1039/c4ta04953e.

[91] C.K. Møller, Crystal Structure and Photoconductivity of Cæsium Plumbohalides, Nature. 182 (1958) 1436–1436. doi:10.1038/1821436a0.

[92] D. Weber, CH3NH3SnBrxI3-x (x=0-3), a Sn(II)-System with the Cubic Perovskite Structure, Zeitschrift Für Naturforsch. 33b (1978) 862–865. http://zfn.mpdl.mpg.de/data/Reihe_B/33/ZNB-1978-33b-0862.pdf.

[93] Y. Ma, S. Wang, L. Zheng, Z. Lu, D. Zhang, Z. Bian, et al., Recent research developments of perovskite solar cells, Chinese J. Chem. 32 (2014) 957–963. doi:10.1002/cjoc.201400435.

[94] W. Yin, J. Yang, J. Kang, Y. Yan, S.-H. Wei, Halide Perovskite Materials for Solar Cells: A Theoretical Review, J. Mater. Chem. A. 3 (2015) Advance. doi:10.1039/C4TA05033A.

[95] W.H. Zhang, B. Cai, Organolead halide perovskites: A family of promising semiconductor materials for solar cells, Chinese Sci. Bull. 59 (2014) 2092–2101. doi:10.1007/s11434-014-0259-9.

[96] X. Liu, W. Zhao, H. Cui, Y. Xie, Y. Wang, T. Xu, et al., Organic–inorganic halide perovskite based solar cells – revolutionary progress in photovoltaics, Inorg. Chem. Front. 2 (2015) 315–335. doi:10.1039/C4QI00163J.

[97] X. Huang, T.R. Paudel, P.A. Dowben, S. Dong, E.Y. Tsymbal, Electronic Structure and Stability of the CH 3 NH 3 PbBr 3 (001) Surface, 3 (n.d.) 1–25. doi:10.1103/PhysRevB.94.195309.

[98] T. Umebayashi, K. Asai, T. Kondo, A. Nakao, Electronic structures of lead iodide based low-dimensional crystals, Phys. Rev. B. 67 (2003) 155405. doi:10.1103/PhysRevB.67.155405.

[99] L.I.P. Ch, N.H. Pbx, C.X. Cl, Y.H. Chang, C.H. Park, First-Principles Study of the Structural and the Electronic Properties of the, 44 (2004) 889–893.

[100] T. Baikie, Y. Fang, J.M. Kadro, M. Schreyer, F. Wei, S.G. Mhaisalkar, et al., Synthesis and crystal chemistry of the hybrid perovskite (CH3NH3)PbI3 for solid-state sensitised solar cell applications, J. Mater. Chem. A. 1 (2013) 5628. doi:10.1039/c3ta10518k.

[101] N. Onoda-Yamamuro, T. Matsuo, H. Suga, Dielectric study of CH3NH3PbX3 (X = Cl, Br, I), J. Phys. Chem. Solids. 53 (1992) 935–939. doi:10.1016/0022-3697(92)90121-S.

[102] F. Brivio, A.B. Walker, A. Walsh, Structural and electronic properties of hybrid perovskites for high-efficiency thin-film photovoltaics from first-principles, APL Mater. 1 (2013) 42111. doi:10.1063/1.4824147.

[103] C. Bernal, K. Yang, First-Principles Hybrid Functional Study of the Organic–Inorganic Perovskites CH 3 NH 3 SnBr 3 and CH 3 NH 3 SnI 3, J. Phys. Chem. C. 118 (2014) 24383–24388. doi:10.1021/jp509358f.

[104] H.S. Jung, N.G. Park, Perovskite Solar Cells: From Materials to Devices, Small. 11 (2014) 10–25. doi:10.1002/smll.201402767.

[105] F. Hao, C.C. Stoumpos, R.P.H. Chang, M.G. Kanatzidis, Anomalous band gap behavior in mixed Sn and Pb perovskites enables broadening of absorption spectrum in solar cells, J. Am. Chem. Soc. 136 (2014) 8094–8099. doi:10.1021/ja5033259.

[106] Y.-C. Hsiao, T. Wu, M. Li, Q. Liu, W. Qin, B. Hu, Fundamental Physics behind High-Efficiency Organo-Metal Halide Perovskite Solar Cells, J. Mater. Chem. A. 3 (2015) 1–14. doi:10.1039/C5TA01376C.

[107] M. Hu, C. Bi, Y. Yuan, Z. Xiao, Q. Dong, Y. Shao, et al., Distinct exciton dissociation behavior of organolead trihalide perovskite and excitonic semiconductors studied in the same system, Small. 11 (2015) 2164–2169. doi:10.1002/smll.201402905.

[108] E. Zhou, J. Cong, K. Hashimoto, K. Tajima, Control of miscibility and aggregation via the material design and coating process for high-performance polymer blend solar cells, Adv. Mater. 25 (2013) 6991–6996. doi:10.1002/adma.201303170.

[109] I.B. Koutselas, L. Ducasse, G.C. Papavassiliou, Electronic properties of three- and low-dimensional semiconducting materials with Pb halide and Sn halide units, J. Phys. Condens. Matter. 8 (1999) 1217–1227. doi:10.1088/0953-8984/8/9/012.

[110] N.M. M. Hirasawa , T. Ishihara , T. Goto , K. Uchida, Magnetoabsorption of the lowest exciton in perovskite-type compound (CH3NH3)PbI3, Physica. 201 (1994) 427–430.

[111] S. Sun, T. Salim, N. Mathews, M. Duchamp, C. Boothroyd, G. Xing, et al.,

The origin of high efficiency in low-temperature solution-processable bilayer organometal halide hybrid solar cells, Energy Environ. Sci. 7 (2014) 399. doi:10.1039/c3ee43161d.

[112] R. Po, C. Carbonera, A. Bernardi, N. Camaioni, The role of buffer layers in polymer solar cells, Energy Environ. Sci. 4 (2011) 285. doi:10.1039/c0ee00273a.

[113] J. Even, L. Pedesseau, C. Katan, Analysis of multivalley and multibandgap absorption and enhancement of free carriers related to exciton screening in hybrid perovskites, J. Phys. Chem. C. 118 (2014) 11566–11572. doi:10.1021/jp503337a.

[114] S. Bai, Z. Wu, X. Wu, Y. Jin, N. Zhao, Z. Chen, et al., High-performance planar heterojunction perovskite solar cells: Preserving long charge carrier diffusion lengths and interfacial engineering, Nano Res. (2014) Ahead of Print. doi:10.1007/s12274-014-0534-8.

[115] G. Hodes, P. V. Kamat, Understanding the Implication of Carrier Diffusion Length in Photovoltaic Cells, J. Phys. Chem. Lett. 6 (2015) 4090–4092. doi:10.1021/acs.jpclett.5b02052.

[116] A. Kojima, K. Teshima, Y. Shirai, T. Miyasaka, Novel Photoelectrochemical Cell with Mesoscopic Electrodes Sensitized by Lead-halide Compounds (11), Meet. Abstr. MA2008-02 (2008) 27. http://ma.ecsdl.org/content/MA2008-02/1/27.abstract.

[117] T.C. Sum, N. Mathews, Advancements in perovskite solar cells: photophysics behind the photovoltaics, Energy Environ. Sci. 7 (2014) 2518–2534.

doi:10.1039/C4EE00673A.

[118] T. Salim, S. Sun, Y. Abe, A. Krishna, A.C. Grimsdale, Y.M. Lam, Perovskite-based solar cells: impact of morphology and device architecture on device performance, J. Mater. Chem. A Mater. Energy Sustain. 3 (2015) 8943–8969. doi:10.1039/c4ta05226a.

[119] T. Leijtens, G.E. Eperon, S. Pathak, A. Abate, M.M. Lee, H.J. Snaith, Overcoming ultraviolet light instability of sensitized TiO_2 with meso-superstructured organometal tri-halide perovskite solar cells., Nat. Commun. 4 (2013) 2885. doi:10.1038/ncomms3885.

[120] S. Guarnera, A. Abate, W. Zhang, J.M. Foster, G. Richardson, A. Petrozza, et al., Improving the long-term stability of perovskite solar cells with a porous Al2O3 buffer layer, J. Phys. Chem. Lett. 6 (2015) 432–437. doi:10.1021/jz502703p.

[121] J. Jang, S.H. Hwang, J. Roh, J. Lee, J. Ryu, J. Yun, Size-controlled SiO2 nanoparticles as scaffold layers in thin-film perovskite solar cells, J. Mater. Chem. A. (2014) Ahead of Print. doi:10.1039/C4TA03087G.

[122] V. Gonzalez-Pedro, E.J. Juarez-Perez, W.-S. Arsyad, E.M. Barea, F. Fabregat-Santiago, I. Mora-Sero, et al., General Working Principles of $CH_3NH_3PbX_3$ Perovskite Solar Cells, Nano Lett. 14 (2014) 888–893. doi:10.1021/nl404252e.

[123] D. Liu, T.L. Kelly, Perovskite solar cells with a planar heterojunction structure prepared using room-temperature solution processing techniques, Nat. Photonics. 8 (2013) 133–138. doi:10.1038/nphoton.2013.342.

[124] L. Yang, A.T. Barrows, D.G. Lidzey, T. Wang, Recent progress and challenges of organometal halide perovskite solar cells, Reports Prog. Phys. 79 (2016) 26501. doi:10.1088/0034-4885/79/2/026501.

[125] C.-H. Chiang, Z.-L. Tseng, C.-G. Wu, Planar heterojunction perovskite/PC71BM solar cells with enhanced open-circuit voltage via a (2/1)-step spin-coating process, J. Mater. Chem. A. 2 (2014) Ahead of Print. doi:10.1039/C4TA03674C.

[126] K. Sun, J. Chang, F.H. Isikgor, P. Li, J. Ouyang, Efficiency enhancement of planar perovskite solar cells by adding zwitterion/LiF double interlayers for electron collection, Nanoscale. 7 (2015) 896–900. doi:10.1039/C4NR05975A.

[127] J.-Y. Jeng, Y.-F. Chiang, M.-H. Lee, S.-R. Peng, T.-F. Guo, P. Chen, et al., $CH_3NH_3PbI_3$ Perovskite/Fullerene Planar-Heterojunction Hybrid Solar Cells, Adv. Mater. 25 (2013) 3727–3732. doi:10.1002/adma.201301327.

[128] C.W. Chen, H.W. Kang, S.Y. Hsiao, P.F. Yang, K.M. Chiang, H.W. Lin, Efficient and uniform planar-type perovskite solar cells by simple sequential vacuum deposition, Adv. Mater. 26 (2014) 6647–6652. doi:10.1002/adma.201402461.

[129] C.-H. Chiang, Z.-L. Tseng, C.-G. Wu, Planar heterojunction perovskite/PC_{71}BM solar cells with enhanced open-circuit voltage via a (2/1)-step spin-coating process, J. Mater. Chem. A. 2 (2014) 15897–15903. doi:10.1039/C4TA03674C.

[130] Chien-Hung Chiang & Chun-Guey Wu, Bulk heterojunction perovskite–

PCBM solar cells with high fill factor, Nat. Photonics. 10 (2016) 196–200.

[131] Y. Liu, Y.M. Yang, J. You, G. Li, Y. Yang, Integrated Perovskite/Bulk-Heterojunction toward E ffi cient Solar Cells, Nano Lett. (2014).

[132] C. Zuo, L. Ding, Bulk heterojunctions push the photoresponse of perovskite solar cells to 970 nm, J. Mater. Chem. A. 3 (2015) 9063–9066. doi:10.1039/C4TA04482G.

[133] Y. Liu, L.A. Renna, M. Bag, Z.A. Page, P.Y. Kim, J. Choi, et al., High Efficiency Tandem Thin-Perovskite/Polymer Solar Cells with a Graded Recombination Layer, ACS Appl. Mater. Interfaces. (2016) acsami.5b12740. doi:10.1021/acsami.5b12740.

[134] G.E. Eperon, V.M. Burlakov, P. Docampo, A. Goriely, H.J. Snaith, Morphological Control for High Performance, Solution-Processed Planar Heterojunction Perovskite Solar Cells, Adv. Funct. Mater. 24 (2014) 151–157. doi:10.1002/adfm.201302090.

[135] M. Xiao, F. Huang, W. Huang, Y. Dkhissi, Y. Zhu, J. Etheridge, et al., A Fast Deposition-Crystallization Procedure for Highly Efficient Lead(supporting), Angew. Chemie. 126 (2014) 10056–10061. doi:10.1002/ange.201405334.

[136] J.Y. Jeng, K.C. Chen, T.Y. Chiang, P.Y. Lin, T. Da Tsai, Y.C. Chang, et al., Nickel oxide electrode interlayer in CH3NH3PbI 3 perovskite/PCBM planar-heterojunction hybrid solar cells, Adv. Mater. 26 (2014) 4107–4113. doi:10.1002/adma.201306217.

[137] W. Yoon, J.E. Boercker, M.P. Lumb, J.G. Tischler, P.P. Jenkins, R.J. Walters, Vapor deposition of organic-inorganic hybrid perovskite thin-films

for photovoltaic applications, 2014 IEEE 40th Photovolt. Spec. Conf. (2014) 1577–1580. doi:10.1109/PVSC.2014.6925219.

[138] Q. Chen, H. Zhou, Z. Hong, S. Luo, H.-S. Duan, H.-H. Wang, et al., Planar heterojunction perovskite solar cells via vapor assisted solution process., J. Am. Chem. Soc. (2013) 3–6. doi:10.1021/ja411509g.

[139] M. Era, T. Hattori, T. Taira, T. Tsutsui, Self-organized growth of PbI-based layered perovskite quantum well by dual-source vapor deposition, Chem. Mater. 9 (1997) 8-. doi:10.1021/cm960434m.

[140] O. Malinkiewicz, A. Yella, Y.H. Lee, G.M.M. Espallargas, M. Graetzel, M.K. Nazeeruddin, et al., Perovskite solar cells employing organic charge-transport layers, Nat. Photonics. 8 (2014) 128–132. doi:10.1038/nphoton.2013.341.

[141] J.-H. Im, H.-S. Kim, N.-G. Park, Morphology-photovoltaic property correlation in perovskite solar cells: One-step versus two-step deposition of CH3NH3PbI3, Apl Mater. 2 (2014) 81510. doi:10.1063/1.4891275.

[142] Y. Zhao, K. Zhu, Solution Chemistry Engineering toward High-E ffi ciency Perovskite Solar Cells, J. Phys. Chem. Lett. 5 (2014) 4175–4186.

[143] Y. Ma, L. Zheng, Y.-H. Chung, S. Chu, L. Xiao, Z. Chen, et al., A highly efficient mesoscopic solar cell based on CH$_3$NH$_3$PbI$_{3-x}$Cl$_x$ fabricated via sequential solution deposition, Chem. Commun. 50 (2014) 12458–12461. doi:10.1039/C4CC01962H.

[144] H.-S. Ko, J.-W. Lee, N.-G. Park, 15.76% efficiency perovskite solar cells prepared under high relative humidity: importance of PbI2 morphology in two-step deposition of CH3NH3PbI3, J. Mater. Chem. A. 3 (2015) 8808–15.

doi:10.1039/C5TA00658A.

[145] P.-W. Liang, C.-Y. Liao, C.-C. Chueh, F. Zuo, S.T. Williams, X.-K. Xin, et al., Additive Enhanced Crystallization of Solution-Processed Perovskite for Highly Efficient Planar-Heterojunction Solar Cells, Adv. Mater. 26 (2014) 3748–3754. doi:10.1002/adma.201400231.

[146] A. Dualeh, N. Tétreault, T. Moehl, P. Gao, M.K. Nazeeruddin, M. Grätzel, Effect of annealing temperature on film morphology of organic-inorganic hybrid pervoskite solid-state solar cells, Adv. Funct. Mater. 24 (2014) 3250–3258. doi:10.1002/adfm.201304022.

[147] N.-G. Park, Perovskite solar cells: an emerging photovoltaic technology, Mater. Today. 18 (2015) 65–72. doi:10.1016/j.mattod.2014.07.007.

[148] H.-L. Hsu, C.-P. Chen, J.-Y. Chang, Y.-Y. Yu, Y.-K. Shen, Two-step thermal annealing improves the morphology of spin-coated films for highly efficient perovskite hybrid photovoltaics, Nanoscale. 6 (2014) 10281. doi:10.1039/C4NR02751E.

[149] Y. Xu, L. Zhu, J. Shi, S. Lv, X. Xu, J. Xiao, et al., Efficient Hybrid Mesoscopic Solar Cells with Morphology-Controlled $CH_3NH_3PbI_{3-x}Cl_x$ Derived from Two-Step Spin Coating Method, ACS Appl. Mater. Interfaces. 7 (2015) 2242–2248. doi:10.1021/am5057807.

[150] C. Bi, Y. Shao, Y. Yuan, Z. Xiao, C. Wang, Y. Gao, et al., Understanding the formation and evolution of interdiffusion grown organolead halide perovskite thin films by thermal annealing, J. Mater. Chem. A. 2 (2014) 18508–18514. doi:10.1039/C4TA04007D.

[151] J.-H. Im, I.-H. Jang, N. Pellet, M. Grätzel, N.-G. Park, Growth of CH3NH3PbI3 cuboids with controlled size for high-efficiency perovskite solar cells., Nat. Nanotechnol. 9 (2014) 927–932. doi:10.1038/nnano.2014.181.

[152] Y.-J. Jeon, S. Lee, R. Kang, J.-E. Kim, J.-S. Yeo, S.-H. Lee, et al., Planar heterojunction perovskite solar cells with superior reproducibility, Sci. Rep. 4 (2014) 6953. doi:10.1038/srep06953.

[153] Z. Xiao, Q. Dong, C. Bi, Y. Shao, Y. Yuan, J. Huang, Solvent Annealing of Perovskite-Induced Crystal Growth for Photovoltaic-Device Efficiency Enhancement, Adv. Mater. 26 (2014) n/a-n/a. doi:10.1002/adma.201401685.

[154] S.R.& S.I.S. Nam Joong Jeon, Jun Hong Noh, Young Chan Kim, Woon Seok Yang, Solvent engineering for high-performance inorganic–organic hybrid perovskite solar cells, Nat. Mater. 13 (2014) 897–903.

[155] J. Seo, S. Park, Y. Chan Kim, N.J. Jeon, J.H. Noh, S.C. Yoon, et al., Benefits of very thin PCBM and LiF layers for solution-processed p–i–n perovskite solar cells, Energy Environ. Sci. 7 (2014) 2642. doi:10.1039/C4EE01216J.

[156] H.-B. Kim, H. Choi, J. Jeong, S. Kim, B. Walker, S. Song, et al., Mixed solvents for the optimization of morphology in solution-processed, inverted-type perovskite/fullerene hybrid solar cells., Nanoscale. 6 (2014) 6679–83. doi:10.1039/c4nr00130c.

[157] A. Dualeh, P. Gao, S. Il Seok, M.K. Nazeeruddin, M. Gr??tzel, Thermal behavior of methylammonium lead-trihalide perovskite photovoltaic light harvesters, Chem. Mater. 26 (2014) 6160–6164. doi:10.1021/cm502468k.

[158] G. Niu, W. Li, F. Meng, L. Wang, H. Dong, Y. Qiu, Study on the stability of $CH_3NH_3PbI_3$ films and the effect of post-modification by aluminum oxide in all-solid-state hybrid solar cells, J. Mater. Chem. A. 2 (2014) 705–710. doi:10.1039/C3TA13606J.

[159] D. Bryant, N. Aristidou, S. Pont, I. Sanchez-Molina, T. Chotchunangatchaval, S. Wheeler, et al., Light and oxygen induced degradation limits the operational stability of methylammonium lead triiodide perovskite solar cells, Energy Environ. Sci. 9 (2016) DOI: 10.1039/c6ee00409a. doi:10.1039/C6EE00409A.

[160] S. Aharon, B. El Cohen, L. Etgar, Hybrid Lead Halide Iodide and Lead Halide Bromide in Efficient Hole Conductor Free Perovskite Solar Cell, J. Phys. Chem. C. (2014). doi:10.1021/jp5023407.

[161] J.H. Noh, S.H. Im, J.H. Heo, T.N. Mandal, S. Il Seok, Chemical Management for Colorful, E ffi cient, and Stable Inorganic − Organic Hybrid Nanostructured Solar Cells, Nano Lett. 13 (2013) 1764–1769. doi:dx.doi.org/10.1021/nl400349b.

[162] N. Pellet, P. Gao, G. Gregori, T.Y. Yang, M.K. Nazeeruddin, J. Maier, et al., Mixed-organic-cation perovskite photovoltaics for enhanced solar-light harvesting, Angew. Chemie - Int. Ed. 53 (2014) 3151–3157. doi:10.1002/anie.201309361.

[163] J.A. Chang, J.H. Rhee, S.H. Im, Y.H. Lee, H.J. Kim, S.I. Seok, et al., High-performance nanostructured inorganic??-organic heterojunction solar cells, Nano Lett. 10 (2010) 2609–2612. doi:10.1021/nl101322h.

[164] J.H. Kim, S.T. Williams, N. Cho, C.C. Chueh, A.K.Y. Jen, Enhanced Environmental Stability of Planar Heterojunction Perovskite Solar Cells Based on Blade-Coating, Adv. Energy Mater. 5 (2015) 2–7. doi:10.1002/aenm.201401229.

[165] D. Bi, G. Boschloo, S. Schwarzmüller, L. Yang, E.M.J. Johansson, A. Hagfeldt, Efficient and stable CH3NH3PbI3-sensitized ZnO nanorod array solid-state solar cells., Nanoscale. 5 (2013) 11686–91. doi:10.1039/c3nr01542d.

[166] Y.S. Kwon, J. Lim, H.-J. Yun, Y.-H. Kim, T. Park, A diketopyrrolopyrrole-containing hole transporting conjugated polymer for use in efficient stable organic–inorganic hybrid solar cells based on a perovskite, Energy Environ. Sci. 7 (2014) 1454. doi:10.1039/c3ee44174a.

[167] S.N. Habisreutinger, T. Leijtens, G.E. Eperon, S.D. Stranks, R.J. Nicholas, H.J. Snaith, Carbon nanotube / polymer composite as a highly stable charge collection layer in perovskite solar cells, (2014).

[168] G.E. Eperon, S.D. Stranks, C. Menelaou, M.B. Johnston, L.M. Herz, H.J. Snaith, Formamidinium lead trihalide: a broadly tunable perovskite for efficient planar heterojunction solar cells, Energy Environ. Sci. 7 (2014) 982. doi:10.1039/c3ee43822h.

[169] M. a. Green, A. Ho-Baillie, H.J. Snaith, The emergence of perovskite solar cells, Nat. Photonics. 8 (2014) 506–514. doi:10.1038/nphoton.2014.134.

[170] A. Mei, X. Li, L. Liu, Z. Ku, T. Liu, Y. Rong, et al., A hole-conductor–free, fully printable mesoscopic perovskite solar cell with high stability, Science

(80-.). 345 (2014) 295–298. doi:10.1126/science.1254763.

[171] J.W. Jo, M.-S. Seo, M. Park, J.-Y. Kim, J.S. Park, I.K. Han, et al., Improving Performance and Stability of Flexible Planar-Heterojunction Perovskite Solar Cells Using Polymeric Hole-Transport Material, Adv. Funct. Mater. (2016) 1–8. doi:10.1002/adfm.201600746.

[172] Y. Zhao, J. Wei, H. Li, Y. Yan, W. Zhou, D. Yu, et al., A polymer scaffold for self-healing perovskite solar cells, Nat. Commun. 7 (2016) 10228. doi:10.1038/ncomms10228.

[173] G. Niu, W. Li, F. Meng, L. Wang, H. Dong, Y. Qiu, Study on the stability of CH3NH3PbI3 films and the effect of post-modification by aluminum oxide in all-solid-state hybrid solar cells, J. Mater. Chem. A. 2 (2014) 705. doi:10.1039/c3ta13606j.

[174] C. Bernal, K. Yang, J. Accepted, First-principles hybrid functional study of the organic–inorganic perovskites CH3NH3SnBr3 and CH3NH3SnI3, (2014). doi:10.1021/jp509358f.

[175] N.K. Noel, S.D. Stranks, A. Abate, C. Wehrenfennig, S. Guarnera, A.-A. Haghighirad, et al., Lead-Free Organic-Inorganic Tin Halide Perovskites for Photovoltaic Applications, Energy Environ. Sci. 7 (2014) 3061–3068. doi:10.1039/C4EE01076K.

[176] F. Garnier, Field-Effect Transistors Based on Conjugated Materials, Electron. Mater. Oligomer Approach. (1998) 559–583.

[177] W.C. Choy, Organic Solar Cells. Materials and Device Physics, 2013.

[178] Y. Kim, S. Cook, S.M. Tuladhar, S.A. Choulis, J. Nelson, J.R. Durrant, et al., A strong regioregularity effect in self-organizing conjugated polymer films and high-efficiency polythiophene:fullerene solar cells, Nat. Mater. 5 (2006) 197–203. doi:10.1038/nmat1574.

[179] T. Ameri, P. Khoram, J. Min, C.J. Brabec, Organic ternary solar cells: A review, Adv. Mater. 25 (2013) 4245–4266. doi:10.1002/adma.201300623.

[180] A. Ng, X. Liu, W.Y. Jim, A.B. Djuri??ic??, K.C. Lo, S.Y. Li, et al., P3HT: PCBM solar cells - The choice of source material, J. Appl. Polym. Sci. 131 (2014) 1–9. doi:10.1002/app.39776.

[181] C.-C. Chen, Z. Hong, G. Li, Q. Chen, H. Zhou, Y. Yang, One-step, low-temperature deposited perovskite solar cell utilizing small molecule additive, J. Photonics Energy. 5 (2015) 57405. doi:10.1117/1.JPE.5.057405.

[182] X. Wang, Wang Zhiming, High-Efficiency Solar Cells: Physics, Materials, and Devices, Springer Science & Business Media, 2013.

[183] J. Lü, K. Huang, X. Chen, J. Zhu, F. Meng, X. Song, et al., Reversible wettability of nanostructured ZnO thin films by sol-gel method, Appl. Surf. Sci. 256 (2010) 4720–4723. doi:10.1016/j.apsusc.2010.02.080.

[184] W.R. Wei, M.L. Tsai, S. Te Ho, S.H. Tai, C.R. Ho, S.H. Tsai, et al., Above-11%-efficiency organic-inorganic hybrid solar cells with omnidirectional harvesting characteristics by employing hierarchical photon-trapping structures, Nano Lett. 13 (2013) 3658–3663. doi:10.1021/nl401540h.

[185] C. Waldauf, M. Morana, P. Denk, P. Schilinsky, K. Coakley, S.A. Choulis, et al., Highly efficient inverted organic photovoltaics using solution based

titanium oxide as electron selective contact, Appl. Phys. Lett. 89 (2006) 1–4. doi:10.1063/1.2402890.

[186] S. Lattante, Electron and Hole Transport Layers: Their Use in Inverted Bulk Heterojunction Polymer Solar Cells, Electronics. 3 (2014) 132–164. doi:10.3390/electronics3010132.

[187] S.F. Sun, Physical Chemistry of Macromolecules: Basic Principles and Issues, John Wiley & Sons, 2004.

[188] N. Colthup, Introduction to Infrared and Raman Spectroscopy, Elsevier, 2012.

[189] G. Gilliland, Photoluminescence Spectroscopy of Crystalline Semiconductors, Elsevier, 1997.

[190] L. Bergman, J. McHale, Handbook of luminescent semiconductor materials, CRC Press, 2011.

[191] Richard J. D. Tilley, Crystals and Crystal Structures, 2006.

[192] P.S. To, Chapter 7 : Basics of X-ray Diffraction, Solutions. (1999) 1–25. http://epswww.unm.edu/xrd/xrdbasics.pdf.

[193] C. Hammond, The Basics of Crystallography and Diffraction, Oxford University Press, 2015.

[194] P. Cherry, A. Duxbury, Practical Radiotherapy: Physics and Equipment, John Wiley & Sons, 2009.

[195] B.H. Stuart, Infrared Spectroscopy: Fundamentals and Applications, 2004. doi:10.1002/0470011149.

[196] R. Brendel, Thin-Film Crystalline Silicon Solar Cells: Physics and Technology, John Wiley & Sons, 2011.

[197] J. Mack, N. Kobayashi, Low symmetry phthalocyanines and their analogues, Chem. Rev. 111 (2011) 281–321. doi:10.1021/cr9003049.

[198] J. Lund, T. Larsen, Polymer solar cells, J. Alloys Compd. 7 (2006) 9. doi:10.1038/nphoton.2012.11.

[199] L. Valentini, D. Bagnis, J.M. Kenny, Nanofibrillar self-organization of regioregular poly(3-hexylthiophene) and [6,6]-phenyl C(61)-butyric acid methyl ester by dip-coating: a simple method to obtain efficient bulk heterojunction solar cells., Nanotechnology. 20 (2009) 95603. doi:10.1088/0957-4484/20/9/095603.

[200] M. Helgesen, R. Sondergaard, F.C. Krebs, Advanced materials and processes for polymer solar cell devices, J. Mater. Chem. 20 (2010) 36–60. doi:10.1039/B913168J.

[201] C.J. Brinker, Chemical Solution Deposition of Functional Oxide Thin Films, (2013) 233–261. doi:10.1007/978-3-211-99311-8.

[202] Y. Liang, Z. Xu, J. Xia, S.T. Tsai, Y. Wu, G. Li, et al., For the bright future-bulk heterojunction polymer solar cells with power conversion efficiency of 7.4%, Adv. Mater. 22 (2010). doi:10.1002/adma.200903528.

[203] R.F. Service, Outlook Brightens for Plastic Solar Cells, Science (80-.). 332 (2011) 293–293. doi:10.1126/science.332.6027.293.

[204] C.E. Small, S. Chen, J. Subbiah, C.M. Amb, S.-W. Tsang, T.-H. Lai, et al.,

High-efficiency inverted dithienogermole–thienopyrrolodione-based polymer solar cells, Nat. Photonics. 6 (2011) 115–120. doi:10.1038/nphoton.2011.317.

[205] Z. He, C. Zhong, S. Su, M. Xu, H. Wu, Y. Cao, et al., Enhanced power-conversion efficiency in polymer solar cells using an inverted device structure, Nat. Photonics. 25 (2013) 593–597. doi:10.1038/nphoton.2012.190.

[206] P.S. and V.P. R. Dabirian, X. Feng, L. Ortolani, A. Liscio, V. Morandi, K. Mu¨llen, Micron-sized [6,6]-phenyl C61 butyric acid methyl ester crystals grown by dip coating in solvent vapour atmosphere: interfaces for organic photovoltaics, Phys. Chem. Chem. Phys. (2010) 4473–4480.

[207] L. Xue, X. Gao, K. Zhao, J. Liu, X. Yu, Y. Han, The formation of different structures of poly(3-hexylthiophene) film on a patterned substrate by dip coating from aged solution, Nanotechnology. 21 (2010) 145303. doi:10.1088/0957-4484/21/14/145303.

[208] Z. Hu, J. Zhang, S. Xiong, Y. Zhao, Performance of polymer solar cells fabricated by dip coating process, Sol. Energy Mater. Sol. Cells. 99 (2012) 221–225. doi:10.1016/j.solmat.2011.12.002.

[209] V. Kumar, H. Wang, Plasmonic Au nanoparticles for enhanced broadband light absorption in inverted organic photovoltaic devices by plasma assisted physical vapour deposition, Org. Electron. Physics, Mater. Appl. 14 (2013) 560–568. doi:10.1016/j.orgel.2012.11.027.

[210] Y. Hou, H. Zhang, W. Chen, S. Chen, C.O.R. Quiroz, H. Azimi, et al., Inverted, Environmentally Stable Perovskite Solar Cell with a Novel Low-Cost and Water-Free PEDOT Hole-Extraction Layer, Adv. Energy Mater. 5

(2015) 1–7. doi:10.1002/aenm.201500543.

[211] H. Huang, J. Shi, L. Zhu, D. Li, Y. Luo, Q. Meng, Two-step ultrasonic spray deposition of CH3NH3PbI3 for efficient and large-area perovskite solar cell, Nano Energy. 27 (2016) 352–358. doi:10.1016/j.nanoen.2016.07.026.

[212] W. Geng, C.-J. Tong, J. Liu, W. Zhu, W.-M. Lau, L.-M. Liu, Structures and Electronic Properties of Different CH3NH3PbI3/TiO2 Interface: A First-Principles Study, Sci. Rep. 6 (2016) 20131. doi:10.1038/srep20131.

[213] Y. Zhou, K. Zhu, Perovskite Solar Cells Shine in the "Valley of the Sun," ACS Energy Lett. (2016) 64–67. doi:10.1021/acsenergylett.6b00069.

[214] M. He, D. Zheng, M. Wang, C. Lin, Z. Lin, High efficiency perovskite solar cells: from complex nanostructure to planar heterojunction, J. Mater. Chem. A. 2 (2014) 5994. doi:10.1039/c3ta14160h.

[215] L. Zheng, D. Zhang, Y. Ma, Z. Lu, Z. Chen, S. Wang, et al., Morphology control of the perovskite films for efficient solar cells, Dalt. Trans. 44 (2015) 10582–10593. doi:10.1039/C4DT03869J.

[216] K.G. Lim, H.B. Kim, J. Jeong, H. Kim, J.Y. Kim, T.W. Lee, Boosting the power conversion effi ciency of perovskite solar cells using self-organized polymeric hole extraction layers with high work function, Adv. Mater. 26 (2014) 6461–6466. doi:10.1002/adma.201401775.

[217] H. Zhang, H. Azimi, Y. Hou, T. Ameri, T. Przybilla, E. Spiecker, et al., Improved High-Efficiency Perovskite Planar Heterojunction Solar Cells via Incorporation of a Polyelectrolyte Interlayer, Chem. Mater. 26 (2014) 5190–5193. doi:10.1021/cm502864s.

[218] S. a. Kulkarni, T. Baikie, P.P. Boix, N. Yantara, N. Mathews, S. Mhaisalkar, Band-gap tuning of lead halide perovskites using a sequential deposition process, J. Mater. Chem. A. 2 (2014) 9221. doi:10.1039/c4ta00435c.

[219] H. Zhou, Q. Chen, G. Li, S. Luo, T.-B. Song, H.-S. Duan, et al., Interface engineering of highly efficient perovskite solar cells, Science (80-.). 27 (2013) 238–242. doi:10.1126/science.1254050.

[220] K. Wojciechowski, M. Saliba, T. Leijtens, A. Abate, H.J. Snaith, Sub-150 [degree]C processed meso-superstructured perovskite solar cells with enhanced efficiency, Energy Environ. Sci. 7 (2014) 1142–1147. doi:10.1039/C3EE43707H.

[221] J.T. Wang, J.M. Ball, E.M. Barea, A. Abate, J.A. Alexander-webber, J. Huang, et al., Low-Temperature Processed Electron Collection Layers of Graphene/ TiO 2 Nanocomposites in Thin Film Perovskite Solar Cells, (2014). doi:10.1021/nl403997a.

[222] P. Qin, A.L. Domanski, A.K. Chandiran, R. Berger, H.-J. Butt, M.I. Dar, et al., Yttrium-substituted nanocrystalline TiO_2 photoanodes for perovskite based heterojunction solar cells., Nanoscale. 6 (2014) 1508–14. doi:10.1039/c3nr05884k.

[223] J.-W. Lee, S.H. Lee, H.-S. Ko, J. Kwon, J.H. Park, S.M. Kang, et al., Opto-electronic properties of TiO2 nanohelices with embedded HC(NH2)2PbI3 perovskite solar cells, J. Mater. Chem. A. 3 (2015) 9179–9186. doi:10.1039/C4TA04988H.

[224] N.-G. Park, Organometal Perovskite Light Absorbers Toward a 20%

Efficiency Low-Cost Solid-State Mesoscopic Solar Cell, J. Phys. Chem. Lett. 4 (2013) 2423–2429. doi:10.1021/jz400892a.

[225] J.H. Kim, C.-C. Chueh, S.T. Williams, A.K.-Y. Jen, Room-temperature, solution-processable organic electron extraction layer for high-performance planar heterojunction perovskite solar cells, Nanoscale. (2015). doi:10.1039/C5NR04250J.

[226] S. Ryu, J. Seo, S.S. Shin, Y.C. Kim, N.J. Jeon, J.H. Noh, et al., Fabrication of metal-oxide-free $CH_3NH_3PbI_3$ perovskite solar cells processed at low temperature, J. Mater. Chem. A. 3 (2015) 3271–3275. doi:10.1039/C5TA00011D.

[227] W.-Y. Chen, L.-L. Deng, S.-M. Dai, X. Wang, C.-B. Tian, X.-X. Zhan, et al., Low-cost solution-processed copper iodide as an alternative to PEDOT: PSS hole transport layer for efficient and stable inverted planar heterojunction perovskite solar cells, J. Mater. Chem. A. 3 (2015) 19353–19359. doi:10.1039/C5TA05286F.

[228] J. Seo, S. Park, Y. Chan Kim, N.J. Jeon, J.H. Noh, S.C. Yoon, et al., Benefits of very thin PCBM and LiF layers for solution-processed p–i–n perovskite solar cells, Energy Environ. Sci. 7 (2014) 2642. doi:10.1039/C4EE01216J.

[229] M. Jiang, J. Wu, F. Lan, Q. Tao, D. Gao, G. Li, Enhancing the performance of planar organo-lead halide perovskite solar cells by using a mixed halide source, J. Mater. Chem. A. 3 (2015) 963–967. doi:10.1039/C4TA05373G.

[230] F. Hao, C.C. Stoumpos, Z. Liu, R.P.H. Chang, M.G. Kanatzidis, Hole Conductor-Free Solar Cells with Steady Power Conversion, J. Am. Chem.

Soc. 136 (2014) 16411–16419. doi:10.1021/ja509245x.

[231] D. Shi, V. Adinolfi, R. Comin, M. Yuan, E. Alarousu, A. Buin, et al., Low trap-state density and long carrier diffusion in organolead trihalide perovskite single crystals., Science. 347 (2015) 519–22. doi:10.1126/science.aaa2725.

[232] Y. Chen, T. Chen, L. Dai, Layer-by-Layer Growth of $CH_3NH_3PbI_{3-x}Cl_x$ for Highly Efficient Planar Heterojunction Perovskite Solar Cells, Adv. Mater. 27 (2015) 1053–1059. doi:10.1002/adma.201404147.

[233] J.-D. Chen, C. Cui, Y.-Q. Li, L. Zhou, Q.-D. Ou, C. Li, et al., Polymer solar cells: single-junction polymer solar cells exceeding 10% power conversion efficiency, Adv. Mater. 27 (2015) 1132. doi:10.1002/adma.201570040.

[234] J.J.M. Halls, K. Pichler, R.H. Friend, S.C. Moratti, A.B. Holmes, J.J.M. Halls, et al., Exciton diffusion and dissociation in a poly (p - phenylenevinylene)/ C60 heterojunction photovoltaic cell Exciton diffusion and dissociation in a poly (p-phenylenevinylene)/ C 60 heterojunction photovoltaic cell, Appl. Phys. Lett. 3120 (1996) 206–209. doi:10.1063/1.115797.

[235] P.E. Shaw, A. Ruseckas, I.D.W. Samuel, Exciton diffusion measurements in poly(3-hexylthiophene), Adv. Mater. 20 (2008) 3516–3520. doi:10.1002/adma.200800982.

[236] D. Vacar, E.S. Maniloff, D.W. McBranch, A.J. Heeger, Charge-transfer range for photoexcitations in conjugated polymer/fullerene bilayers and blends, Phys. Rev. B. 56 (1997) 4573–4577.

[237] T.A. Berhe, W.-N. Su, C.-H. Chen, C.-J. Pan, J.-H. Cheng, H.-M. Chen, et al.,

Organometal halide perovskite solar cells: degradation and stability, Energy Environ. Sci. 9 (2016) Advance Article. doi:10.1039/C5EE02733K.

[238] C. Yi, J. Luo, S. Meloni, A. Boziki, N. Ashari-Astani, C. Grätzel, et al., Entropic stabilization of mixed A-cation ABX 3 metal halide perovskites for high performance perovskite solar cells, Energy Environ. Sci. 9 (2016) 656–662. doi:10.1039/C5EE03255E.

[239] H.J.S. David P. McMeekin1, Golnaz Sadoughi1, Waqaas Rehman1, Giles E. Eperon1, Michael Saliba1, Maximilian T. Hörantner1, Amir Haghighirad1, Nobuya Sakai1, Lars Korte2, Bernd Rech2, Michael B. Johnston1, Laura M. Herz1, A mixed-cation lead mixed-halide perovskite absorber for tandem solar cells, Science (80-.). 351 (n.d.) 151–155.

[240] A. Buin, R. Comin, J. Xu, A.H. Ip, E.H. Sargent, Halide-Dependent Electronic Structure of Organolead Perovskite Materials, Chem. Mater. 27 (2015) 4405–4412.

[241] M.-C. Jung, S.R. Raga, Y. Qi, Properties and solar cell applications of Pb-free perovskite films formed by vapor deposition, RSC Adv. 6 (2016) 2819–2825. doi:10.1039/C5RA21291J.

[242] T. Glaser, C. Müller, M. Sendner, C. Krekeler, O.E. Semonin, T.D. Hull, et al., Infrared Spectroscopic Study of Vibrational Modes in Methylammonium Lead Halide Perovskites, J. Phys. Chem. Lett. (2015) 2913–2918. doi:10.1021/acs.jpclett.5b01309.

[243] R.C. Masters, A.J. Pearson, T.S. Glen, F.-C. Sasam, L. Li, M. Dapor, et al., Sub-nanometre resolution imaging of polymer–fullerene photovoltaic blends

using energy-filtered scanning electron microscopy, Nat. Commun. 6 (2015) 6928. doi:10.1038/ncomms7928.

[244] B. Conings, J. Drijkoningen, N. Gauquelin, A. Babayigit, J. D'Haen, L. D'Olieslaeger, et al., Intrinsic Thermal Instability of Methylammonium Lead Trihalide Perovskite, Adv. Energy Mater. 5 (2015) 1–8. doi:10.1002/aenm.201500477.